Quantum computing based on low-dimensional systems in germanium and silicon

Inauguraldissertation

zur

Erlangung der Würde eines Doktors der Philosophie

vorgelegt der

Philosophisch-Naturwissenschaftlichen Fakultät

der Universität Basel

von

Christoph Adelsberger

Basel, 2023

Genehmigt von der Philosophisch-Naturwissenschaftlichen Fakultät auf Antrag von

Erstbetreuer: Prof. Dr. Daniel Loss

Zweitbetreuerin: Prof. Dr. Jelena Klinovaja

Externer Experte: Prof. Dr. Georgios Katsaros

Basel, 19. September 2023

Prof. Dr. Marcel Mayor
Dekan

Summary

Condensed matter physics revolutionized our lives in the first half of the 20th century by providing the tools for the development of the transistor which is the building block of any modern classical computer. The working principle of transistors is based on quantum mechanics indirectly since it relies on the electronic band structures of the used semiconductors. However, the computations performed on a computer built of transistors are purely classical.

In the 1980s, Richard Feynman proposed a groundbreaking idea for the simulation of physics: the use of quantum computers that obey the rules of quantum mechanics rather than classical mechanics to unleash full computational power[1]. Since then, physicists have been trying to build a quantum computer that is predicted to be capable of solving complex problems like prime factorization of large numbers[2], the search in large unsorted databases[3], and solving linear systems of equations[4] much faster than a classical computer.

Though a universal quantum computer with millions of quantum bits (qubits) remains a distant goal, significant progress has been made in the past four decades. Demonstrations of quantum advantage over a classical computer for specific tasks have been achieved with superconducting quantum chips hosting $\sim 10 - 100$ qubits[5]. However, scaling up to millions of qubits with superconducting devices faces challenges due to the relatively large size of individual superconducting qubits, approximately $10\,\mu$m.

A promising alternative realization comes from condensed matter physics as well: the spin qubit. In the original proposal of the so-called Loss-DiVincenzo qubit[6] it was suggested to utilize the spin-1/2 degree of freedom of an electron confined in a quantum dot (QD) as a quantum mechanical two-level system, forming the qubit. It is about two orders of magnitude smaller than superconducting qubits and thus raises hope for better scalability. The number of realized spin qubits stands behind superconducting systems, but the wealth of experience from the advanced semiconductor industry for Si promises fast development in spin qubit research. The integration of industrial processes in spin qubit fabrication has become possible, but electrons in Si come with a disadvantage that could possibly spoil the advantages for scalability: they exhibit only weak intrinsic spin-orbit interaction (SOI). Consequently, fast, all-electrical qubit control relies on stray fields from micromagnets on the quantum device. This encouraged research on holes in Si and

[1] R. P. Feynman, "Simulating physics with computers", Int. J. Theor. Phys. **21**, 467 (1982).

[2] P. W. Shor, "Scheme for reducing decoherence in quantum computer memory", Phys. Rev. A **52**, R2493 (1995).

[3] L. K. Grover, "Quantum mechanics helps in searching for a needle in a haystack", Phys. Rev. Lett. **79**, 325 (1997).

[4] A. W. Harrow et al., "Quantum algorithm for linear systems of equations", Phys. Rev. Lett. **103**, 150502 (2009).

[5] F. Arute et al., "Quantum supremacy using a programmable superconducting processor", Nature **574**, 505 (2019), Y. Wu et al., "Strong quantum computational advantage using a superconducting quantum processor", Phys. Rev. Lett. **127**, 180501 (2021), Q. Zhu et al., "Quantum computational advantage via 60-qubit 24-cycle random circuit sampling", Sci. Bull. **67**, 240 (2022).

[6] D. Loss and D. P. DiVincenzo, "Quantum computation with quantum dots", Phys. Rev. A **57**, 120 (1998).

Ge with very strong SOI enabling ultrafast qubit control without large additional elements on the chip.

The small size of spin qubits comes at the cost of lower connectivity between qubits compared to superconducting systems. While exchange interaction allows for two-qubit gates, its short-range nature makes it incapable of coupling far-distant qubits which is desirable, e.g., for multi-qubit entanglement[7] or quantum error correction[8]. One solution for long-range coupling involves the use of circuit quantum electrodynamics, where the spin qubits in semiconductor QDs interact strongly with the photons in a superconducting cavity.

Furthermore, coupling semiconductors and superconductors (SCs) opens up a whole field of interesting physical phenomena among which are Andreev spin qubits (ASQs) and topological superconductivity with associated Majorana bound states (MBSs). ASQs have the potential to combine the advantages of superconducting and spin qubits in QDs and MBSs promise a new approach towards quantum computing relying on topological protection.

Motivated by these developments, this thesis delves into theoretical studies of low-dimensional hole and electron systems in Ge and Si. Chapter 1 introduces the field of quantum computing with spin qubits. After introducing some basic concepts of quantum computing in general, we discuss the properties of group-IV semiconductors, in particular Si and Ge. We explain what a spin qubit is, how it is implemented in a semiconductor QD, how it is controlled via single- and two-qubit operations, how it can be initialized and read out, and how it interacts with the environment. In the final part of this chapter, we pick two phenomena arising in hybrid SC-semiconductor devices, namely the Andreev bound state which can be harnessed to implement ASQs, and the MBS as an example of a topological state.

In Chapter 2, we analyze in detail one-dimensional Ge hole device designs that optimize SOI. We provide a new analytical approach for the estimation of SOI in the presence of transversal electric and magnetic fields where we treat orbital magnetic fields exactly. Assisted by numerical calculations we analyze the electric and magnetic field dependence as well as the dependence on strain and anisotropies of SOI, g factor, and effective masses. These quantities enter the one-dimensional, low-energy effective model that we derive. In particular, we stress the importance of orbital magnetic fields for the g factor. Considering electrostatic confinement of a QD in the one-dimensional system we predict the existence of a g-factor sweet spot that is tunable by strain and confinement potential. We expect highly coherent qubits and fast Rabi frequencies at low power for realistic device parameters. Eventually, we identify a regime of flat bands with promising potential for the simulation of strongly correlated matter.

Whereas in the previously discussed model the magnetic field was pointing in perpendicular direction to the nanowire (NW) axis, in Chapter 3 we analyze similar one-dimensional Ge hole structures with a magnetic field aligned along the NW axis. Also for this case we provide an analytical solution and derive an effective one-dimensional model. Among our core results is the strong renormalization of the effective g factor due to orbital magnetic fields even at weak magnetic fields. Furthermore, we provide a detailed discussion of strain, growth direction, energetically higher-lying valence bands, and different designs of one-dimensional systems. We raise special attention to the large effective g factor and SOI in curved quantum wells at weak electric fields suggesting the applicability of such devices as ideal hosts for MBSs. The same device design exhibits a g factor and SOI independent of the electric field at stronger electric fields, ideal for the optimization of the spin qubit coherence time.

In Chapter 4, we investigate the proximity-induced superconductivity and metallization effects in SC-Ge hole NWs. Taking into account the three-dimensional nature of the NW we predict

[7] A. Fedorov et al., "Implementation of a Toffoli gate with superconducting circuits", Nature **481**, 170 (2012).

[8] N. Ofek et al., "Extending the lifetime of a quantum bit with error correction in superconducting circuits", Nature **536**, 441 (2016).

a strong dependence of the induced gap and metallization effects on the proximity of the hole wavefunction in the Ge part to the SC. Most interestingly, by employing an external electric field the SOI and the proximity-induced pairing potential can be tuned to large values at the same time, making SC-Ge hole NWs a promising platform for quantum information processing via, e.g., ASQs or MBSs.

Finally, in Chapter 5, we propose a novel approach to lifting the valley degeneracy of the Si conduction band edge, which is a major hurdle on the way to large-scale Si-based quantum processors. In experimentally relevant fin field-effect transistor devices shear strain enhances the gap to non-computational valley states to values $\sim 1\,\mathrm{meV} - 10\,\mathrm{meV}$. This proposal does not rely on atomic-size interface details as predicted for planar Si/SiGe heterostructures in previous works and is robust against interface disorder. We show that the effect remains large for realistic values of applied electric fields and is largely independent of the fin shape.

Contents

CHAPTER 1

Introduction

In this introduction, we recall the basic concepts relevant to our work and put our research into a broader context. Additionally, we offer a motivation for the research projects presented in the subsequent chapters, focusing on quantum computing with spin quantum bits (qubits) based on one-dimensional electron and hole systems in Si and Ge. While most concepts presented apply to both holes and electrons, we will emphasize their differences when relevant. Moreover, many statements are not restricted to these specific platforms but are true also for different materials and device designs. Certain general considerations hold for any type of quantum computing.

In Sec 1.1, we review the concept of quantum computing, motivate its critical importance for future applications and give a short overview of semiconductor quantum systems harnessed nowadays for this purpose. Sec. 1.2 provides a concise review of the properties of the group-IV semiconductors Si and Ge. Here, we point out the differences and commonalities of electrons and holes and particularly focus on their properties in zero and one dimensions. In Sec. 1.3, we give an overview of the physics of spin qubits. We start by demonstrating how single qubit rotations can be achieved in the presence of spin-orbit interaction. Subsequently, we show the basic concepts behind two-qubit gates and discuss initialization and readout of spin qubits. Furthermore, we briefly review the decoherence of spin qubits due to their interactions with the environment. Lastly, in Sec. 1.4, we show how Andreev bound states emerge in hybrid superconductor-semiconductor structures due to Andreev reflections, forming the basis for Andreev spin qubits. In the topological regime, these hybrid devices can host Majorana bound states which are the prerequisite for topological qubits and topological quantum computing.

1.1 Quantum computing

Quantum computing is a revolutionary field that harnesses the principles of quantum mechanics to perform powerful computations. At the heart of quantum computing are quantum bits, or short qubits, which are quantum mechanical two-level systems. Conventionally, the two states of a qubit are denoted as $|0\rangle$ and $|1\rangle$, and they span a two-dimensional Hilbert space $\mathcal{H}$. A general qubit state can be described as a superposition of these basis states

$$|\psi\rangle = \alpha\,|0\rangle + \beta\,|1\rangle\,, \tag{1.1}$$

where α and β are complex-valued coefficients that satisfy the normalization condition $|\alpha|^2+|\beta|^2 = 1$. When a measurement is performed on the qubit, it collapses into one of the basis states, and the probability of obtaining $|0\rangle$ or $|1\rangle$ is given by $|\alpha|^2$ and $|\beta|^2$, respectively.

To visualize a qubit state geometrically, we can use the Bloch sphere (see Fig. 1.1). By defining the polar angle as $|\alpha| = \cos(\theta/2)$ with $0 \leq \theta \leq \pi$, and neglecting a non-measurable global phase, we can express the qubit state as

$$|\psi\rangle = \cos\left(\frac{\theta}{2}\right)|0\rangle + e^{i\phi}\sin\left(\frac{\theta}{2}\right)|1\rangle\,, \tag{1.2}$$

where ϕ $(0 \leq \phi < 2\pi)$ represents the azimuthal angle. These states lie on the surface of the Bloch sphere and are called pure states. More generally the Bloch vector, representing the quantum state, is the expectation value of the vector of Pauli matrices, which can have a length smaller than one. The states within the interior of the Bloch sphere are called mixed states.

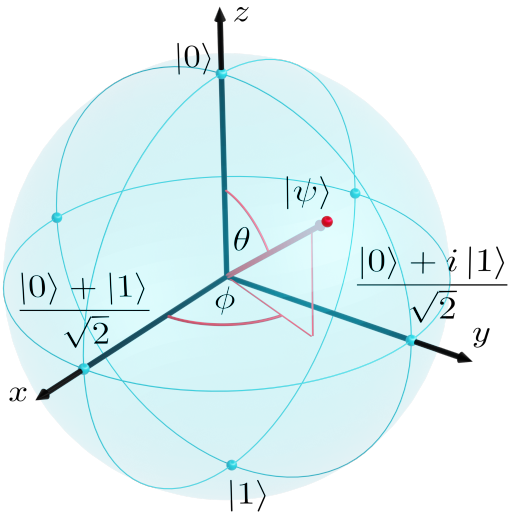

Figure 1.1: State $|\psi\rangle = \cos\left(\frac{\theta}{2}\right)|0\rangle + e^{i\phi}\sin\left(\frac{\theta}{2}\right)$ of a two-level quantum system visualized on the Bloch sphere. The south (north) pole represents the eigenstate $|1\rangle$ ($|0\rangle$) of the Pauli operator σ_z and states of equal superposition of $|1\rangle$ and $|0\rangle$ ($\theta = \pi/2$) are found on the equator. The dots at the equator represent the eigenstates of the Pauli operator σ_x (σ_y) where the x (y) axis pierces through the surface of the Bloch sphere. The states on the surface of the Bloch sphere are pure states and the states within its interior are mixed states.

Now, let us consider the scenario of having two qubits instead of just one. In this case, the basis of the Hilbert space is formed by the four states $\{|00\rangle, |01\rangle, |10\rangle, |11\rangle\}$, and an arbitrary two-qubit state can be written as

$$|\psi\rangle = \alpha_{00}|00\rangle + \alpha_{01}|01\rangle + \alpha_{10}|10\rangle + \alpha_{11}|11\rangle, \tag{1.3}$$

where α_x ($x = 00$, 01, 10, or 11) are complex coefficients that must be normalized. The notation for a two-qubit state is defined as the Kronecker product of single-qubit states, such as $|00\rangle = |0\rangle \otimes |0\rangle$. Particularly significant two-qubit states are the Bell states

$$\psi_{x,y} = \frac{|0, y\rangle + (-1)^x |1, \bar{y}\rangle}{\sqrt{2}}, \tag{1.4}$$

where $x, y = 0, 1$ and $\bar{y}$ is the negation of y [1]. Bell states are examples of entangled states and, in particular, they are maximally entangled. Entangled states cannot be decomposed into a Kronecker product of single-qubit states and they exhibit the classically counter-intuitive property that the measurement of one qubit determines the state of the other qubit, regardless of the physical distance between them. This correlation between qubits has important implications, such as in quantum teleportation [2, 3] or superdense coding [4, 5]. Quantum teleportation is a protocol that allows transferring quantum information, which in general does not need to be known, over a long distance by exploiting the entanglement between two qubits in a Bell state. Superdense coding on the other hand can be thought of as the opposite of quantum teleportation. While in quantum teleportation one needs to transfer two classical bits to convey the information of one qubit, in superdense coding one sends one qubit and transmits the information of two classical bits.

The notation for a two-qubit state can be straightforwardly extended to n qubits, with the basis states denoted as $|x_1 x_2 ... x_n\rangle$, where each x_i can take on the values 0 or 1 ($i = 1, 2, ..., n$). An n-qubit state is specified by 2^n complex coefficients, and even for a few hundreds of qubits, the number of coefficients becomes astronomically large. Storing such a vast number of complex coefficients on a classical computer is practically impossible, illustrating the potential advantage that quantum mechanical states offer for computation.

Manipulations of qubit states are achieved through quantum gates, analogous to classical logic gates that operate on classical bits. They enable the transformation and manipulation of information encoded in qubits. Quantum gates can be categorized as single-qubit gates, which act on a single qubit, and multi-qubit gates, which involve two or more qubits. They are represented by unitary operations U that transform an initial state $|\psi_i\rangle$ to a final state $|\psi_f\rangle = U|\psi_i\rangle$. Notably, unlike classical computing, quantum gates are always reversible due to the unitary property $U^\dagger U = I$, where I represents the identity matrix.

Single-qubit gates are generated by the Hamiltonian $H(t) = \sum_{i=0}^{3} a_i(t)\sigma_i$ where σ_0 is the identity, σ_j are the Pauli matrices ($j = 1, 2, 3 = x, y, z$), and $a_i(t)$ are time-dependent complex coefficients. Then the single-qubit gate becomes

$$U = \mathcal{T} e^{-i \int_0^t \mathrm{d}t H(t)/\hbar}, \tag{1.5}$$

where $\mathcal{T}$ is the time-ordering operator and $\hbar$ is the reduced Planck constant. Thus, any single-qubit gate can be interpreted as a rotation of the state vector on the Bloch sphere. Common examples of single-qubit gates include the Hadamard gate

$$H = \frac{1}{\sqrt{2}} \begin{pmatrix} 1 & 1 \\ 1 & -1 \end{pmatrix}, \tag{1.6}$$

which creates superposition by mapping the basis states as $|0\rangle \rightarrow \frac{|0\rangle+|1\rangle}{\sqrt{2}}$ and $|1\rangle \rightarrow \frac{|0\rangle-|1\rangle}{\sqrt{2}}$, the Pauli gates ($X$, Y, Z), which correspond to π-rotations around the x, y, and z axes of the Bloch sphere and are represented by the Pauli matrices, and the phase gate

$$P(\phi) = \begin{pmatrix} 1 & 0 \\ 0 & e^{i\phi} \end{pmatrix}, \tag{1.7}$$

which modifies the phase of the quantum state by a rotation about the z axis of the Bloch sphere by the angle ϕ.

In addition to single-qubit gates, multi-qubit gates are crucial for quantum computing. These gates act on multiple qubits simultaneously, allowing for complex interactions and entanglement between qubits. One notable example is the Controlled-NOT (CNOT) gate, which operates on two qubits. In the basis $\{|00\rangle, |01\rangle, |10\rangle, |11\rangle\}$ it reads

$$\mathrm{CNOT} = \begin{pmatrix} 1 & 0 & 0 & 0 \\ 0 & 1 & 0 & 0 \\ 0 & 0 & 0 & 1 \\ 0 & 0 & 1 & 0 \end{pmatrix}. \tag{1.8}$$

It performs a NOT operation on the target qubit (flipping the state from $|0\rangle$ to $|1\rangle$ and vice versa) if and only if the control qubit is in the state $|1\rangle$[1]. The CNOT gate is an essential component in building entangling operations and forms the basis for various quantum algorithms. In particular, by combining the Hadamard gate and the CNOT gate one can create a Bell state out of a two-qubit basis state.

An important concept in quantum computing is the universal set of quantum gates. This set comprises both single-qubit and multi-qubit gates that allow for the composition of any quantum gate by combining gates from the universal set. Surprisingly, it has been proven that there is no need for any further multi-qubit gate than the CNOT gate since the CNOT gate plus the set of arbitrary single-qubit rotation gates is universal [6]. Universal gate sets serve as the building blocks for quantum circuits and algorithms, enabling the execution of complex computations on a quantum computer.

While the theoretical framework of quantum computing is promising, it is important to consider the challenges posed by the real world. In practice, perfect qubits that can be initialized, manipulated, coupled, and read out without any errors are not achievable. Quantum systems are inherently sensitive to interactions with their environment, leading to decoherence of the quantum states. Coherent errors can cause uncontrolled rotations of the state vector around the Bloch sphere, while incoherent errors result in the loss of quantum information, transforming the pure quantum state on the surface of the Bloch sphere into a mixed state within its interior. One might think that complete isolation of the qubits from the environment would counteract decoherence. However, the very nature of quantum computation requires qubit manipulation, which inevitably involves interactions and compromises isolation. Thus, on the path to a functioning, fault-tolerant quantum computer, it is crucial to improve the initialization, manipulation, and readout of qubits to minimize error rates, ensuring they remain below the threshold for quantum error correction. This threshold depends strongly on the number of available qubits, the connectivity between the qubits, and chosen quantum error correction code [7–9].

Quantum error correction, distinct from classical error correction, cannot rely on redundancy due to the no-cloning theorem [10], which forbids the creation of an exact copy of an arbitrary

[1] In this notation the first qubit is the control and the second the target qubit.

quantum state. Instead, it relies on the entanglement of several physical qubits to form an error-corrected logical qubit [11]. Quantum error correction requires a significant number (at least a million [12] for useful computations) of high-quality physical qubits, posing a major challenge in scaling up quantum systems. The scaling of qubit counts is currently one of the most daunting tasks in the pursuit of a fault-tolerant quantum computer. Overcoming the hurdles of decoherence, error rates, and scalability is crucial for advancing quantum computing. Ongoing research and engineering efforts aim to develop robust error correction techniques, innovative qubit designs, and effective error mitigation strategies to pave the way for practical quantum computing applications.

Many proposals for quantum mechanical two-level systems that can be employed as qubits have been successfully realized so far. The most advanced quantum processors up to this point are based on superconducting qubits, which utilize Josephson junctions as key elements. Examples of superconducting quantum processors include Google's 53-qubit Sycamore processor [13] and the Zuchongzhi quantum processor from the University of Science and Technology of China [14, 15], for both of which quantum supremacy [16] was claimed, and IBM's 433-qubit processor Osprey[2] announced in 2022 [17]. However, one inherent limitation of superconducting qubits is their scalability, as they tend to be relatively large ($\sim 10\,\mu m$) [18, 19].

An alternative approach to qubit design that has attracted significant attention in recent years is the utilization of the spin degree of freedom of an electron (or a hole) to form a semiconductor spin qubit [20, 21]. An electron with spin states $|\pm 1/2\rangle$, which can be split in energy by an external magnetic field, serves as a natural two-level quantum system. Advances in semiconductor spin qubits in recent years have demonstrated their potential to fulfill DiVincenzo's criteria for quantum computation [22, 23]:

1. Scalability of the system and well-characterized qubits.
2. Initialization of a simple state like the ground state of the system.
3. Low decoherence, where the coherence time is much longer than the gate operation, readout, and initialization time.
4. Universal set of quantum gates.
5. Measurement of the qubit state.

Spin qubits are promising candidates to fulfill all of these criteria, driving the vision of large-scale quantum computing. Regarding the number of spin qubits the most advanced processors to date are a six-qubit processor with electrons in ^{28}Si/SiGe [24], a four-qubit processor based on hole spin qubits in Ge/SiGe [25], and two-qubit processors with gate fidelities overcoming the threshold for fault-tolerant operation ($> 99\,\%$) [26–28]. Despite being behind superconducting devices in terms of the number of qubits, spin qubits show promise for scalability due to their small size of $\sim 100\,nm$ which is about two orders of magnitude smaller than a typical superconducting qubit [18, 19]. However, there are still challenges to address, such as long-distance qubit coupling and cross-talk mitigation. One hope is to leverage the extensive experience gained from advanced complementary metal-oxide-semiconductor (CMOS) technology used for computer chips in the industry and apply it to quantum technology [29–31]. First attempts to realize spin qubit systems with industrial methods were successful [32] and Intel industrially produces 12-spin-qubit chips and makes them available to the research community [33].

Semiconductor spin qubits can be realized in various systems. As mentioned earlier, electron and hole quantum dots (QDs) in different planar heterostructures can serve as qubit platforms.

[2] So far there has no data been published that proves the functionality of all 433 qubits.

Additionally, electrons or holes in nanowires (NWs) [34–36] or other quasi-one-dimensional (1D) systems [37] can be confined to QDs. Spin qubits can also be realized in self-assembled QDs [38, 39], color-centers in diamond [40, 41] or silicon carbide [42], gate-defined QDs in graphene [43, 44] or carbon nanotubes [45], and donor qubits [46, 47]. Furthermore, it is possible to harness the nuclear spin instead of the spin of electrons or holes [47, 48]. In some cases, encoding a single qubit in more than one QD with one or more electrons or holes has proven advantageous [49–61].

1.2 Group-IV semiconductors

In this thesis, our focus lies on spin qubits in Si and Ge, which are semiconductor materials from group IV. More specifically, we analyze quasi-1D systems such as NWs, core/shell NWs [62, 63], gate-defined 1D channels [64, 65], curved quantum wells [62, 65, 66], hut wires [35], and fin structures [37, 67]. By employing electrostatic confinement [35, 63] or growing barrier sections as part of an NW [68, 69] it is possible to define QDs in these 1D systems. However, the physics of electrons and holes in 1D systems is inherently fascinating and non-trivial, as their properties depend on numerous factors that cannot be straightforwardly predicted from their bulk counterparts. Moreover, the coupling of 1D semiconductor systems to a superconductor (SC) opens up an entirely new field of phenomena to explore. Examples of such include proximity-induced superconductivity [70, 71], metallization of NWs [72–74], Andreev bound states [75, 76], and topological superconductivity with associated Majorana bound states [77–80], all of which warrant thorough investigation.

1.2.1 Electrons and holes

There are many reasons for the attractiveness of Si and Ge for spin qubit devices. In the early days of semiconductor-based gate-defined spin qubits, GaAs was the most popular material because of its ease of fabrication, single conduction band edge, and small effective mass [81]. However, the presence of $\sim 10^6$ nuclear spins that interact with the electron spin in a QD severely limits the coherence time of GaAs-based spin qubits [49] (see Sec. 1.3.4). Si and Ge can be isotopically purified such that the material becomes virtually nuclear spin free [82–84]. An undeniable proof of the high quality of the materials is the reported mobility of up to $4.3 \times 10^6\,\mathrm{cm^2\,V^{-1}\,s^{-1}}$ for holes in Ge [85–87] and $2.4 \times 10^6\,\mathrm{cm^2\,V^{-1}\,s^{-1}}$ for electrons in Si. [88]. Moreover, as already mentioned above, there are efforts to employ the highly developed CMOS industry for scaling up Si- and Ge-based spin qubit devices [29–32] which was made possible by the high quality and easy to grow silicon oxide [89]. The spin-orbit interaction (SOI) of electrons in Si is weak compared to other materials which, on the one hand, can be beneficial for a long coherence time [90–92]. However, efficient spin-to-charge conversion (see Sec. 1.3.3) requires a coupling of the spin and orbital degrees of freedom, which can be enhanced by the magnetic field gradient of micromagnets [24, 26, 27, 93]. In contrast, holes come with a naturally strong and tunable SOI as well as electrically tunable g factor and thus enable ultrafast qubit control [35–37, 89, 94–97]. Especially in Ge it is very natural to work with holes since almost any metal's Fermi level is pinned close to the valence band resulting in ohmic contact to the holes [98].

Before we dive into the physics of low-dimensional Si and Ge systems we recall some basic bulk properties of these materials. Si and Ge crystals have a diamond lattice structure which is a face-centered cubic (fcc) lattice with a diatomic basis. The lattice constants are $a^{\mathrm{Si}} = 5.430\,\text{Å}$ and $a^{\mathrm{Ge}} = 5.652\,\text{Å}$ [99]. Since the reciprocal lattice to an fcc lattice is a body-centered cubic (bcc) lattice, the Brillouin zone for Si and Ge looks like a truncated octahedron as shown in Fig. 1.2(a). The high symmetry points in the Brillouin zone are denoted as Γ for the center point, X for the center of a quadratic face, and L for the center of a hexagonal face. Fig. 1.2(b) shows schematically

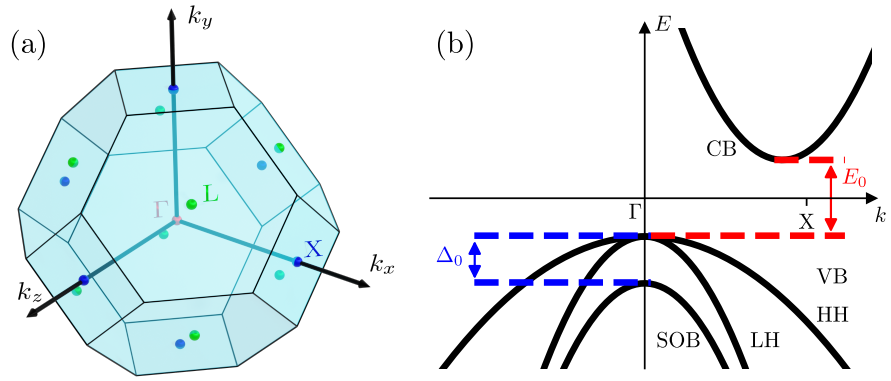

Figure 1.2: (a) The first Brillouin zone (BZ) of the fcc lattice is a truncated octahedron. The Γ point lies in the center of the BZ, the X points in the center of the square faces of the BZ, and the L points in the center of the hexagonal faces. The conduction band (CB) of Si has its minimum close to the X point (six-fold degeneracy) while the CB of Ge has its minimum at the L point (four-fold degeneracy since each valley is shared between neighboring BZs). (b) Schematic picture of the band structure of Si. The CB edge is close to the X point and the maximum of the valence band (VB) is at the Γ point at $k = 0$. The fundamental band gap is denoted as E_0 and the gap at $k = 0$ between the heavy/light hole (HH/LH) bands and the SO split-off band (SOB) as Δ_0. At $k = 0$ the HHs and LHs are degenerate.

the band structure of Si close to the fundamental band gap which is denoted as E_0 ($E_0^{\mathrm{Si}} = 1.17\,\mathrm{eV}$ and $E_0^{\mathrm{Ge}} = 0.744\,\mathrm{eV}$ at $0\,\mathrm{K}$ [100]). The conduction band (CB) of Si has its minimum close to the X point at $k_{\langle 100\rangle} = 0.85\frac{2\pi}{a^{\mathrm{Si}}}$ [101] [see Fig. 1.2(b)] while the CB edge of Ge is at the L point at $k_{\langle \frac{1}{2}\frac{1}{2}\frac{1}{2}\rangle} = \frac{2\pi}{a^{\mathrm{Ge}}}$ [100]. The CB is of s-type, meaning the orbital angular momentum is $l = 0$ and the spin is $s = 1/2$. Both materials have their valence band (VB) maximum at the Γ point at $k = 0$. The VB is of p-type with orbital angular momentum $l = 1$ and spin $s = 1/2$. This results in a total of six states of which four have total angular momentum $j = l + s = 3/2$ and two have $j = l - s = 1/2$. The former can be categorized as heavy holes (HHs) with z component of the total angular momentum $j_z = \pm 3/2$ and light holes (LHs) with $j_z = \pm 1/2$[3]. The names come from the larger effective mass of the HHs in the bulk that is characterized by the smaller curvature of the HH band in the dispersion relation as schematically shown in Fig. 1.2(b). At $k = 0$ the HH and LH bands are degenerate and they split at finite k due to SOI. The remaining two states with $j = 1/2$ and $j_z = \pm 1/2$ are split away from the HHs and LHs at $k = 0$ by the spin-orbit (SO) gap Δ_0 ($\Delta_0^{\mathrm{Si}} = 44.1\,\mathrm{meV}$ and $\Delta_0^{\mathrm{Ge}} = 296\,\mathrm{meV}$ [102]). As the name already tells us, the splitting arises due to SOI, and thus, the band is called the SO split-off band (SOB). The SOI for electrons arises perturbatively from the coupling of the CB to the VB and is therefore suppressed by the band gap. In contrast to that, the SOI for holes originates directly in a coupling of $\boldsymbol{k}$ to the effective spin degree of freedom in the VB and is thus much larger than for electrons. Note that there is no Dresselhaus SOI in Si and Ge due to the presence of bulk inversion symmetry, but a Dresselhaus-like term can appear in a quantum well due to interface inversion asymmetry [103–105]. All these bands are two-fold spin degenerate in the absence of a magnetic field.

[3]The z direction refers here to the direction of motion of the holes determined by $\boldsymbol{k}$. In the bulk it can be chosen arbitrarily.

In this thesis, we want to analyze simple Hamiltonians that describe the dynamics of electrons close to the CB edge or holes close to the VB edge rather than computationally heavy ab-initio models that describe the full band structure. A very powerful approximate approach is the $\boldsymbol{k}\cdot\boldsymbol{p}$ method, which allows to calculate the dispersion relation of a semiconductor to arbitrary precision in the vicinity of a given point $\boldsymbol{k}_0$ in reciprocal space [102, 106]. The great advantage of this method lies in the possibility to account for magnetic and electric fields as well as strain. It is based on the Schrödinger equation for the Bloch functions $e^{i\boldsymbol{k}\cdot\boldsymbol{r}}u_{n\boldsymbol{k}}(\boldsymbol{r}) \equiv e^{i\boldsymbol{k}\cdot\boldsymbol{r}}\langle\boldsymbol{r}|n\boldsymbol{k}\rangle$ accounting for the microscopic crystal lattice by the lattice periodic potential $V_0(\boldsymbol{r})$. The Bloch functions consist of a plane wave part $e^{i\boldsymbol{k}\cdot\boldsymbol{r}}$ and the functions $u_{n\boldsymbol{k}}(\boldsymbol{r}) = u_{n\boldsymbol{k}}(\boldsymbol{r}+m\boldsymbol{R})$ which have the same periodicity $\boldsymbol{R}$ as the lattice potential $V_0(\boldsymbol{r}) = V_0(\boldsymbol{r}+m\boldsymbol{R})$ where m is an integer. The index n is called band index in the absence of SOI and in the presence of SOI it is a common index for the mixed orbital and spin degrees of freedom. Including Pauli SOI, which comes from a non-relativistic approximation of the Dirac equation, the Schrödinger equation reads

$$\left[\frac{p^2}{2m} + V_0(\boldsymbol{r}) + \frac{\hbar^2k^2}{2m} + \frac{\hbar}{m}\boldsymbol{k}\cdot\boldsymbol{\pi} + \frac{\hbar}{4m^2c^2}\boldsymbol{p}\cdot\boldsymbol{\sigma}\times\nabla V_0(\boldsymbol{r})\right]|n\boldsymbol{k}\rangle = E_n(\boldsymbol{k})\,|n\boldsymbol{k}\rangle\,, \tag{1.9}$$

where m is the free electron mass, c is the speed of light, $\boldsymbol{\sigma}$ is the vector of Pauli matrices and $\boldsymbol{\pi} = \boldsymbol{p} + \frac{\hbar}{4mc^2}\boldsymbol{\sigma}\times\nabla V_0(\boldsymbol{r})$. In the absence of SOI $\boldsymbol{\pi} = \boldsymbol{p}$ which is where the name $\boldsymbol{k}\cdot\boldsymbol{p}$ method comes from. In this context, it is important to strictly distinguish between the wavevector $\boldsymbol{k}$ and the momentum operator $\boldsymbol{p}$. The lattice periodic functions $\{|n\boldsymbol{k}_0\rangle\}$ for a given k_0 form a complete orthonormal basis for Eq. (1.9) and the kets $\{|n\boldsymbol{k}\rangle\}$ for arbitrary $\boldsymbol{k}$ can be expressed as an expansion in terms of this basis. This yields an infinitely-dimensional matrix and diagonalizing this matrix gives the exact dispersion relation and expansion coefficients for any n and $\boldsymbol{k}$. However, in practice one is typically interested in only a few adjacent bands ($n = 1,\ldots,N$) and their dispersion relation around the expansion point $\boldsymbol{k}_0$. Thus, the exact $\boldsymbol{k}\cdot\boldsymbol{p}$ and SO interactions are taken into account only for the N bands of interest and the coupling to the remaining bands is treated perturbatively. To derive an effective $\boldsymbol{k}\cdot\boldsymbol{p}$ Hamiltonian one resorts to quasi-degenerate perturbation theory [102] which in this context is often referred to as Löwdin partitioning [107, 108]. For a simple dispersion of an electron in the case of the CB edge at the Γ point we obtain in second-order perturbation theory the parabolic dispersion relation

$$E_n(\boldsymbol{k}) = E_n(0) + \frac{\hbar^2k^2}{2m_n^*}, \tag{1.10}$$

where the effective mass m_n^* is proportional to the fundamental band gap E_0.

However, as we have already seen, the CB edge of Si and Ge is not at the Γ point. In the following, we want to focus on electrons in Si. As discussed above the CB edge of Si is close to the X point at $k_{\langle 100\rangle} = 0.85\frac{2\pi}{a^{\mathrm{Si}}}$ [101] and we define the distance of the minimum to the X point as $k_0 = 0.15\frac{2\pi}{a^{\mathrm{Si}}}$. Since there are six equivalent X points [see Fig. 1.2(a)], there are in total six CB minima in the Brillouin zone. Because all these minima are at the same energy they are degenerate, which is often referred to as valley degeneracy and the minima are called valleys. A simple $\boldsymbol{k}\cdot\boldsymbol{p}$ Hamiltonian from an expansion around the X point describing two adjacent valleys (neglecting spin) is given in the local valley basis (l, t_1, t_2) by [109, 110]

$$H = \frac{\hbar^2}{2m_t}(k_{t_1}^2 + k_{t_2}^2) + \frac{\hbar^2}{2m_l}k_l^2 + \frac{\hbar^2}{m_l}k_0k_l\sigma_x - \frac{\hbar^2}{M}k_{t_1}k_{t_2}\sigma_z, \tag{1.11}$$

where l is the longitudinal direction and t_1 and t_2 are the transversal directions. The longitudinal and transversal masses of Si are $m_l = 0.19m$ and $m_t = 0.91m$, respectively, and the band coupling

mass is $1/M \approx 1/m_t - 1/m$ [109, 111]. The other four valleys can be described by the same Hamiltonian by rotation.

The description of holes is more intricate than that of electrons due to the SOI in a p-type band. In what follows, we focus on holes in Ge, but except for material-specific numbers the description holds also for holes in other diamond-lattice semiconductors, explicitly also for Si. In Ge, the SO gap between the VB edge and the SOB is rather large ($\Delta_0^{\mathrm{Ge}} = 296\,\mathrm{meV}$ [102]). Thus, it is well justified to neglect the SOB when one is interested in the dynamics at the VB edge. The $\boldsymbol{k}\cdot\boldsymbol{p}$ Hamiltonian describing the dispersion relation close to the Γ point accounting for the HH and LH nature is the Luttinger-Kohn (LK) Hamiltonian [102, 108, 112]

$$H_{\mathrm{LK}} = -\frac{\hbar^2}{2m}\left[\left(\gamma_1 + \frac{5\gamma_2}{2}\right)k^2 - 2\gamma_2\left(k_x^2 J_x^2 + k_y^2 J_y^2 + k_z^2 J_z^2\right) - 4\gamma_3\left(\{k_x, k_y\}\{J_x, J_y\} + \mathrm{c.p.}\right)\right], \tag{1.12}$$

where $\gamma_1 = 13.35$, $\gamma_2 = 4.25$, and $\gamma_3 = 5.69$ are the material-dependent Luttinger parameters for Ge [113], J_i ($i = x, y, z$) are the standard spin-3/2 matrices, "c.p." stands for cyclic permutations, and the anti-commutator is defined as $\{A, B\} = (AB + BA)/2$. The global minus sign of the LK Hamiltonian stems from the fact that holes live in the VB and their energy is negative with respect to the energy of electrons in the conduction band. However, without loss of generality, we assume that holes have a positive energy and use a positive sign in the LK Hamiltonian as long as the conduction band is not accounted for explicitly. If not stated differently the coordinates x, y, and z are along the main crystallographic directions $\langle 100\rangle$. In many cases, when analytical solutions for the eigenvalues and eigenvectors of the LK Hamiltonian in Eq. (1.12) are required, it is necessary to make approximations. A prominent example, for which an exact solution is known, is the spherical or isotropic approximation where $\gamma_2 = \gamma_3$ [114]. However, the neglected anisotropies can lead to interesting effects as discussed in Chapters 2 and 3.

If the focus is on understanding the qualitative features of the Hamiltonian, rather than obtaining exact coefficients, the theory of invariants [115] provides a valuable approach to determine which terms are allowed and which should vanish based solely on symmetry arguments. This relies on the fact that the Hamiltonian must remain invariant under all symmetry operations of the problem determined, e.g., by the point group of the lattice[4]. Utilizing the theory of invariants allows for a much simpler derivation of the structure of the Hamiltonian compared to explicitly performing the Löwdin partitioning.

1.2.2 Low-dimensional systems: nanowires and quantum dots

Based on the Hamiltonians presented above for bulk electrons and holes, which in the following we generally refer to as particles, we can investigate the properties of low-dimensional systems by introducing a confinement potential $V(\boldsymbol{r})$ [$\boldsymbol{r} = (x, y, z)$]. Our particular interest lies in analyzing quasi-1D systems that can be modeled by, e.g., hard-wall confinement in transverse directions. This description is suitable for epitaxially grown NWs where a substantial potential difference exists between the material that hosts particles and a surrounding shell that could be a different semiconductor or a dielectric. Further confinement to a QD is typically achieved through electrostatic gates, which provide a harmonic confinement potential.

Moreover, gates serve the purpose of applying homogeneous electric fields to the particles. In a confined system, the electric field leads to structural inversion symmetry breaking and thus gives rise to Rashba SOI. Furthermore, the electric field induces a shift in the position of the

[4]The point group of the diamond lattice is O_h and has 48 symmetry elements.

wave function for the confined particle. Defining a spin qubit requires lifting the Kramers spin degeneracy through a magnetic field, leading to the well-controllable Zeeman splitting proportional to the g factor. It turns out that the g factor in hole NWs and QDs strongly deviates from the free electron g factor, is anisotropic, and strongly depends on the electric field. Coupling the magnetic field to the orbital motion of the particles via the vector potential induces orbital effects that cause a renormalization of the g factor and SOI strength, especially in hole NWs, as we will discuss in Chapters 2 and 3.

In many systems, strain arises due to the lattice mismatch at the interface between two different materials. For example, strain can be caused by the shell around an NW, the different layers in a planar heterostructure, or by gates deposited on the device to enable electric control. Strain becomes especially interesting in 1D hole systems leading to an increase of the subband gap and renormalization of the g factor and SOI strength, as we will show in Chapters 2 and 3. For electrons in 1D Si structures shear strain is a promising tool to lift the valley degeneracy as we propose in Chapter 5.

To describe the lowest energy states of a low-dimensional system one typically employs an effective model taking higher subbands into account perturbatively. For instance, for the lowest two states of a particle in a quasi 1D system (parallel to the z direction) with Rashba SOI, magnetic field B_z along the NW, and electric field E_x perpendicular to the NW the effective Hamiltonian up to order k_z^2 is given by

$$H_{\mathrm{NW}}(k_z) = \frac{\hbar^2}{2m_{\mathrm{eff}}}k_z^2 + \frac{1}{2}g_{\mathrm{eff}}\mu_B B_z\sigma_z - \alpha\hbar k_z E_x\sigma_y, \tag{1.13}$$

where m_{eff} is the effective mass, g_{eff} the effective g factor, and α the effective Rashba SOI coefficient. These parameters depend on confinement details and external electric and magnetic fields. The momentum parallel to the NW is denoted by $\hbar k_z$. In principle, the effective mass can depend on the spin, and orbital effects of the magnetic field are accounted for in the magnetic field dependence of the effective parameters. For strong electric and magnetic fields it might be necessary to take higher-order terms in E_x and B_z into account. The SOI is characterized by the SO length $l_{so} = \hbar/m_{\mathrm{eff}}\alpha E_x$, indicating that after a distance of $l_{so}\pi/2$ along the NW, the spin of the particle rotates in the plane spanned by the NW axis and the electric field direction from "up" to "down" or vice versa.

Notably, in hole NWs, the Rashba SOI originating in the direct dipolar coupling to an external electric field is unusually strong [94, 95]. Consequently, it is referred to as direct Rashba SOI. Unlike the standard Rashba SOI, which is suppressed by the fundamental band gap of the semiconductor, the direct Rashba SOI is only suppressed by a subband gap, making it 10 to 100 times larger. This direct coupling to the electric field is only strong if there is a strong HH-LH mixing as in systems with two axes of strong confinement. However, in planar structures and QDs therein, the ground state is primarily of HH-type, leading to the suppression of direct Rashba SOI.

The most common way to define a QD in an NW is to make use of gates and apply a smooth electrostatic confinement potential, which can be approximated by a harmonic potential $V_c = \frac{1}{2}m_{\mathrm{eff}}\omega^2 z^2$ along the quasi-1D system. The harmonic confinement is characterized by the orbital confinement frequency ω, which depends on the electric field gradient provided by the gates. The confinement along the NW is much weaker than the hard-wall confinement in transverse directions. By performing the unitary local spin rotation $U_s = e^{i\sigma_y z/l_{so}}$, we switch from the Hamiltonian in Eq. (1.13) including V_c to the rest frame of the spin. Averaging over the quantum harmonic oscillator ground state wave function results in the simple effective QD Hamiltonian

$$H_{\mathrm{QD}} = \frac{\hbar\omega}{2} - E_{so} + \frac{\mu_B B_z}{2}g_{\mathrm{eff}}e^{-l_z^2/l_{so}^2}\sigma_z, \tag{1.14}$$

where we assume that the Zeeman energy $g_{\text{eff}}\mu_B B_z$ is much smaller than the orbital confinement $\hbar\omega$. The SO energy is defined as $E_{so} = \hbar^2/2m_{\text{eff}}l_{so}^2$, and the harmonic confinement length along the NW is $l_z = \sqrt{\hbar/m_{\text{eff}}\omega}$. The g factor of the QD is renormalized by the exponential that depends on the confinement and SO length.

1.3 Spin qubits

A spin qubit can be encoded in the two states described by the effective Hamiltonian in Eq. (1.14). However, it is essential to recognize that the qubit states are not pure spin states due to the presence of SOI. As discussed in Sec. 1.1, universal quantum computing not only requires the definition of the qubit states but also qubit manipulation. In the following, we will present the mechanisms behind single- and two-qubit gates for spin qubits.

1.3.1 Single qubit rotations

Initial attempts to perform single-qubit rotations involved using a transversal ac magnetic field $B_x(t)$. If the frequency of the ac magnetic field ω_{ac} matches the Larmor frequency ω_L of the spin in the static magnetic field B_z, the spin will rotate about an axis in the $x-z$ plane at the Rabi frequency Ω_R, which depends on the amplitude of the ac magnetic field. This driving protocol is called electron spin resonance (ESR) and the qubit rotations are referred to as Rabi oscillations [116]. However, ESR proved challenging in practice due to several reasons. For instance, fast driving requires a large amplitude of the ac magnetic field that can only be produced by strong ac currents close to the QD [20, 117] accompanied by considerable heating effects. This can have disastrous effects on the qubits which require low temperatures to mitigate thermal decoherence processes. Additionally, creating strong local magnetic fields for selective qubit manipulation in multi-qubit devices turns out to be very difficult.

Fortunately, SOI provides an alternative way to perform single-qubit rotations without the need for an ac magnetic field. The mechanism is very similar, but an ac electric field is required which is much easier to control locally. All-electrical control of spin qubits is achieved through the electric-dipole-induced spin resonance (EDSR) scheme [118, 119]. In this method, an ac electric field $E_z(t)$ is applied along the NW. We consider again the Hamiltonian in Eq. (1.13) with additional harmonic confinement along the NW

$$H_{1\text{D}}(k_z) = \frac{\hbar^2}{2m_{\text{eff}}}k_z^2 + \frac{1}{2}g_{\text{eff}}\mu_B B_z\sigma_z - \alpha\hbar k_z E_x\sigma_y + \frac{m_{\text{eff}}\omega^2}{2}z^2 - eE_z(t)z. \tag{1.15}$$

In analogy to the QD Hamiltonian in Eq. (1.14) we can derive an effective EDSR Hamiltonian of the spin qubit. By completing the square we see that the ac electric field leads to a time-dependent shift of the center of mass of the QD

$$H_{1\text{D}}(k_z) = \frac{\hbar^2}{2m_{\text{eff}}}k_z^2 + \frac{1}{2}g_{\text{eff}}\mu_B B_z\sigma_z - \alpha\hbar k_z E_x\sigma_y + \frac{m_{\text{eff}}\omega^2}{2}\left[z - d(t)\right]^2, \tag{1.16}$$

where the periodical shift is defined as $d(t) = eE_z(t)l_z^2/\hbar\omega$ and we neglect a global energy shift of $-m_{\text{eff}}\omega^2 d(t)^2/2$. Moving to the orbital rest frame by the time-dependent unitary transformation $e^{-i\hbar k_z d(t)/\hbar}$ shifts the coordinates such that $z \to z + d(t)$. The resulting Hamiltonian is

$$\tilde{H}_{1\text{D}}(k_z) = \frac{\hbar^2}{2m_{\text{eff}}}k_z^2 + \frac{1}{2}g_{\text{eff}}\mu_B B_z\sigma_z - \alpha\hbar k_z E_x\sigma_y + \frac{m_{\text{eff}}\omega^2}{2}z^2 - \hbar k_z\frac{\mathrm{d}}{\mathrm{d}t}d(t). \tag{1.17}$$

As before, we perform the unitary local spin rotation $U_s = e^{i\sigma_y z/l_{so}}$ and average over the quantum harmonic oscillator ground state assuming the Zeeman energy and driving frequency to be much smaller than the orbital frequency, $g_{\text{eff}}\mu_B B_z/\hbar, \omega_{ac} \ll \omega$. The result we obtain is the effective EDSR Hamiltonian

$$H_{\text{EDSR}} = \frac{\hbar\omega}{2} - \frac{\hbar}{l_{so}}\frac{\mathrm{d}}{\mathrm{d}t}d(t)\sigma_y + \frac{\mu_B B_z}{2}g_{\text{eff}}e^{-l_z^2/l_{so}^2}\sigma_z. \tag{1.18}$$

Driving with the harmonic ac electric field $E_z(t) = E_{ac}\sin(\omega_{ac}t)$ gives the periodic shift of the QD position $d(t) = d_0\sin(\omega_{ac}t)$ with $d_0 = eE_{ac}l_z^2/\hbar\omega$. Then the resonance condition for achieving full Rabi oscillations is given by

$$\hbar\omega_{ac} = g_{\text{eff}}\mu_B B_z e^{-l_z^2/l_{so}^2} \tag{1.19}$$

and the Rabi frequency at resonance is determined by $\Omega_R = g_{\text{eff}}e^{-l_z^2/l_{so}^2}\mu_B B_z d_0/l_{so}$. Note that d_0 depends on E_{ac} and thus the Rabi frequency is controlled by the ac electric field. Another important remark is that the Rabi frequency depends via l_{so} on the SOI coefficient α meaning that stronger SOI allows for faster Rabi oscillations which set the operation speed for single-qubit gates. For cases where the intrinsic SOI is weak, such as for electrons in silicon, enhancing the effect by a magnetic field gradient as provided by micromagnets [120–122] can be advantageous. This is sometimes called artificial SOI since the inhomogeneous magnetic field mimics the effect of intrinsic SOI. Additionally, the coupling to the magnetic field gradient can be further enhanced by delocalizing one electron over two QDs because of the larger dipole coupling in such a setup which is referred to as flopping mode qubit [57, 58].

In the following, let us discuss how the EDSR Hamiltonian in Eq. (1.18) induces rotations of the qubit. To simplify the notation we neglect the global energy shift $\hbar\omega/2$, define the effective Zeeman energy $\Delta_Z = \mu_B B_z g_{\text{eff}}e^{-l_z^2/l_{so}^2}$, and write $\nu = \hbar\omega_{ac}d_0/l_{so}$. Then, the EDSR Hamiltonian becomes

$$H(t) = -\nu\cos(\omega_{ac}t + \varphi_0)\sigma_y + \frac{\Delta_Z}{2}\sigma_z, \tag{1.20}$$

where we introduce the phase φ_0 that allows us to control the rotation axis. Since there is no simple analytical solution for the Schrödinger equation

$$i\hbar\frac{\mathrm{d}}{\mathrm{d}t}|\psi(t)\rangle = H(t)|\psi(t)\rangle \tag{1.21}$$

to this time-dependent Hamiltonian, we have to make an approximation. First, we move to the rotating frame by the unitary $U_R(t) = e^{-i\omega_R t\sigma_z/2}$ which leaves us with

$$\tilde{H}(t) = \frac{1}{2}\begin{pmatrix} \Delta_Z - \hbar\omega_R & i\nu\left(e^{i[(\omega_R+\omega_{ac})t+\varphi_0]} + e^{i[(\omega_R-\omega_{ac})t-\varphi_0]}\right) \\ -i\nu\left(e^{-i[(\omega_R+\omega_{ac})t+\varphi_0]} + e^{-i[(\omega_R-\omega_{ac})t-\varphi_0]}\right) & -(\Delta_Z - \hbar\omega_R) \end{pmatrix}, \tag{1.22}$$

where the energy shift comes from the term $-i\hbar\left(U_R^\dagger(t)\frac{\mathrm{d}}{\mathrm{d}t}U_R(t)\right)$. By choosing the rotating frame frequency $\omega_R = \omega_{ac}$, the slowly oscillating terms in the off-diagonal matrix elements become time-independent. Thus, we obtain a time-independent Hamiltonian plus fast oscillating, also called counter-rotating, terms which we will neglect in the following. This is the often applied rotating wave approximation (RWA) [123] which relies on the conditions that the oscillating coupling is

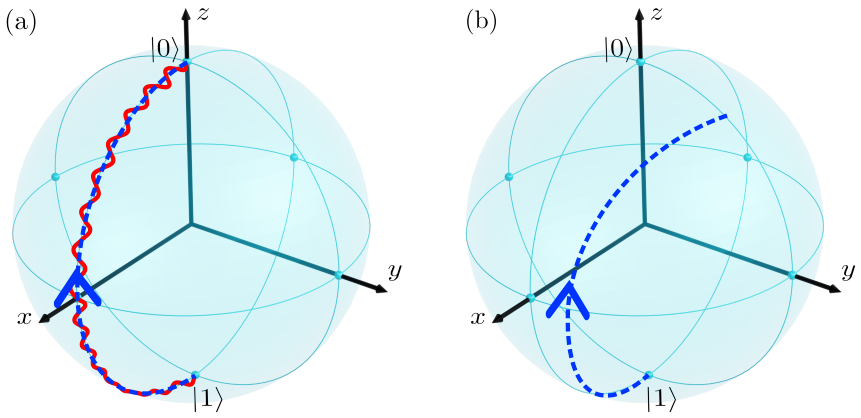

Figure 1.3: Schematic illustration of qubit rotations on the Bloch sphere via EDSR for $\varphi_0 = 0$. (a) At resonance, the initial state $|1\rangle$ is rotated about the y axis (dashed-blue line). After time $T_{\text{flip}} = \pi/\Omega_R$ the qubit is flipped completely to the state $|0\rangle$. The solid-red line shows the fast oscillations that are neglected by the RWA with exaggerated amplitude. (b) At off-resonant driving the rotation axis is tilted away from the y axis and the initial state $|1\rangle$ is not completely flipped to $|0\rangle$.

much smaller than the energy gap, $\nu/\Delta_Z \ll 1$, and the driving frequency is close to resonance, $\delta = |\Delta_Z| - |\hbar\omega_{ac}| \ll \Delta_Z$. The remaining Hamiltonian is time-independent

$$H_{\text{RWA}} = \frac{\hbar\Omega_R}{2}\boldsymbol{n}_R \cdot \boldsymbol{\sigma}, \tag{1.23}$$

where $\Omega_R = \sqrt{\delta^2 + \nu^2}/\hbar$ is the Rabi frequency and $\boldsymbol{n}_R = [\nu\sin(\varphi_0)/\hbar\Omega_R, -\nu\cos(\varphi_0)/\hbar\Omega_R, \delta/\hbar\Omega_R]$ determines the rotation axis. At resonance ($\delta = 0$) for $\varphi_0 = 0$ we obtain rotations about the y axis, leading to a full spin flip after the time $T_{\text{flip}} = \pi/\Omega_R$. Fig. 1.3(a) provides a schematic visualization of the qubit rotation with RWA and with the fast oscillations that are neglected in the RWA. For driving at frequencies slightly away from resonance the oscillations become faster, but the spin-flip probability drops below one, see Fig. 1.3(b).

Maintaining the regime of $\nu/\Delta_Z \ll 1$ is crucial to ensure that the counter-rotating terms are negligible. If this condition is violated, every single-qubit rotation is fraught with errors that accumulate over time reducing the gate fidelity. Additionally, driving the qubit beyond the validity of the RWA results in the Bloch-Siegert shift, a shift of the resonance frequency. To account for higher-order effects, corrections can be calculated using a higher-order Magnus expansion [124]. Moreover, the shape of the driving pulse turns out to play a vital role in achieving high-fidelity gates. Proper pulse shaping has proven to be a successful technique in optimizing gate speed and fidelity [26, 125]. Further optimization approaches are the driving of the qubit by higher-harmonic excitations [126] or phase driving [127]. The fastest Rabi oscillations up to now exceeding frequencies of 540 MHz have been realized experimentally by exploiting the strong SOI in hole systems [36, 128].

1.3.2 Two qubit gates

SOI not only enables single-qubit rotations, as discussed above, but also paves the way to fast two-qubit gates by inducing a strong anisotropy in the exchange interaction between two qubits. In what follows, we present the theory behind a simple two-qubit gate for two electrons in a double QD (DQD). Although we describe the situation for electrons, the results can easily be generalized for holes.

A single electron in a DQD can be described by the effective Hamiltonian

$$H_1 = \frac{\varepsilon}{2}\tau_z - t_0\tau_x + \frac{g\mu_B B_z}{2}\sigma_z + \frac{\delta g\mu_B B_z}{2}\tau_z\sigma_z - t_{so}\tau_y\sigma_y, \tag{1.24}$$

where ε represents the energy detuning between the left (L) and right (R) QD, $t_0 > 0$ is the energy associated with the conventional spin-conserving tunneling between the dots, g is the average g factor of the QDs, δg is the g factor difference between the QDs (important for individual addressability), and t_{so} is the spin-flip tunneling arising due to SOI. The Pauli operators τ_i and σ_i ($i = x, y, z$) refer to the position (L, R) and spin space, respectively. We assume strong confinement of the electron to the QDs, weak tunneling between them, and small detuning.

To consider two-qubit gates, we introduce a second particle for a second qubit which is also described by a Hamiltonian like the one in Eq. (1.24). Since electrons, which are spin-1/2 particles, have to obey the Pauli principle, there are six possible states the two electrons can occupy in the DQD, of which three are singlet ($|S_0\rangle$, $|S_{LL}\rangle$, $|S_{RR}\rangle$) and three are triplet states ($|T_0\rangle$, $|T_{\uparrow\uparrow}\rangle$, $|T_{\downarrow\downarrow}\rangle$) [129]. The singlet states are characterized by a symmetric orbital and an antisymmetric spin part of the wave function while the triplet states exhibit the opposite symmetries. In the $|S_0\rangle$ state and all the triplet states, the two electrons are delocalized in the DQD, while in the $|S_{LL}\rangle$ ($|S_{RR}\rangle$) state, both electrons are in the left (right) QD. Similarly, the spins are not polarized in the singlet states and $|T_0\rangle$, while the total spin-z component is one for $|T_{\uparrow\uparrow}\rangle$ and $|T_{\downarrow\downarrow}\rangle$. In the singlet-triplet basis, $\{|S_{LL}\rangle, |S_{RR}\rangle, |S_0\rangle, |T_{\uparrow\uparrow}\rangle, |T_{\downarrow\downarrow}\rangle, |T_0\rangle\}$ the DQD Hamiltonian can be written in a Hund-Mulliken approach in matrix form:

$$H_{\mathrm{DQD}} = \begin{pmatrix} U+\varepsilon & 0 & -\sqrt{2}t_0 & -t_{so} & -t_{so} & 0 \\ 0 & U-\varepsilon & -\sqrt{2}t_0 & -t_{so} & -t_{so} & 0 \\ -\sqrt{2}t_0 & -\sqrt{2}t_0 & 0 & 0 & 0 & \delta g\mu_B B_z \\ -t_{so} & -t_{so} & 0 & g\mu_B B_z & 0 & 0 \\ -t_{so} & -t_{so} & 0 & 0 & -g\mu_B B_z & 0 \\ 0 & 0 & \delta g\mu_B B_z & 0 & 0 & 0 \end{pmatrix}, \tag{1.25}$$

where U is the Coulomb repulsion between two electrons when confined to the same QD. This term is called Hubbard or charging energy and it makes a double occupation of one QD energetically unfavorable [21]. Although symmetry allows Coulomb interactions between any of the singlet states [130], in a typical QD, U is the dominant term, and we neglect the other couplings. The orbital part of the Hamiltonian, i.e. the terms containing ε and t_0, couples only singlet states because only their wave functions exhibit a symmetric orbital part. On the other hand, the Zeeman Hamiltonian couples only triplet states because of the symmetric spin part of the wave function. Magnetic fields in x and y direction would further couple the $|T_0\rangle$ state to $|T_{\uparrow\uparrow}\rangle$ and $|T_{\downarrow\downarrow}\rangle$, but for simplicity we keep assuming $B_x = B_y = 0$. SOI and the inhomogeneous g factor couple the orbital and spin degrees of freedom and thus induce the mixing of the singlet and triplet sectors of the Hamiltonian in Eq. (1.25).

In the following discussion, we outline the ideas of implementing a CNOT gate based on the Hamiltonian in Eq. (1.25) where we follow important steps provided in Ref. [131]. We assume

that U is much larger than all other energies and aim to derive an effective two-qubit Hamiltonian by decoupling the doubly occupied singlet states $|S_{LL}\rangle$ and $|S_{RR}\rangle$. In analogy to the derivation of the EDSR Hamiltonian, we perform a unitary local spin-flip rotation $U_s = e^{iL\tau_z\sigma_y/2l_{so}}$, that mixes spin and orbital degrees of freedom, where $L/l_{so} = \arctan(t_{so}/t)$ and $t = \sqrt{t_0^2 + t_{so}^2}$. This transformation already decouples $|S_{LL}\rangle$ and $|S_{RR}\rangle$ from the triplet states. However, they are still coupled to $|S_0\rangle$. To address this coupling, we treat it in second-order perturbation theory and introduce the exchange energy $J = \frac{2t^2}{U-\varepsilon} + \frac{2t^2}{U+\varepsilon} \approx \frac{4t^2}{U}\left[1 + \frac{\varepsilon^2}{U^2}\right]$.

Now, dropping the singlet states which are far away in energy, the DQD Hamiltonian becomes

$$\tilde{H}_{\mathrm{DQD}} = \begin{pmatrix} -J & -\frac{g}{\sqrt{2}}\sin(\theta) & \frac{g}{\sqrt{2}}\sin(\theta) & \delta g\cos(\theta) \\ -\frac{g}{\sqrt{2}}\sin(\theta) & g\cos(\theta) & 0 & \frac{\delta g}{\sqrt{2}}\sin(\theta) \\ \frac{g}{\sqrt{2}}\sin(\theta) & 0 & -g\cos(\theta) & \frac{\delta g}{\sqrt{2}}\sin(\theta) \\ \delta g\cos(\theta) & \frac{\delta g}{\sqrt{2}}\sin(\theta) & \frac{\delta g}{\sqrt{2}}\sin(\theta) & 0 \end{pmatrix} \tag{1.26}$$

in the basis $\{|S_0\rangle, |T_{\uparrow\uparrow}\rangle, |T_{\downarrow\downarrow}\rangle, |T_0\rangle\}$. To simplify the notation we define $\theta = L/l_{so}$ and set $\mu_B B_z = 1$. Due to the exchange energy, the singlet is the ground state for $B_z = 0$. To analyze the effect of the exchange interaction, we move to the computational frame where the single-qubit Hamiltonians are diagonal. This is justified because in experiments J is typically small compared to the Zeeman energy. By simple unitary transformations[5], we arrive at the two-qubit Hamiltonian

$$H_{2Q} \approx \begin{pmatrix} \frac{E_Z^{(1)}+E_Z^{(2)}}{2} & \nu^{(2)}\cos(\omega_{ac}t) & 0 & 0 \\ \nu^{(2)}\cos(\omega_{ac}t) & \frac{E_Z^{(1)}-E_Z^{(2)}-J_\parallel}{2} & \frac{J}{2}\cos^2(\theta) & 0 \\ 0 & \frac{J}{2}\cos^2(\theta) & \frac{-E_Z^{(1)}+E_Z^{(2)}-J_\parallel}{2} & \nu^{(2)}\cos(\omega_{ac}t) \\ 0 & 0 & \nu^{(2)}\cos(\omega_{ac}t) & \frac{-E_Z^{(1)}-E_Z^{(2)}}{2} \end{pmatrix} \tag{1.27}$$

in the computational frame $\{|\uparrow\uparrow\rangle, |\uparrow\downarrow\rangle, |\downarrow\uparrow\rangle, |\downarrow\downarrow\rangle\}$, where we neglect couplings to the high-energy states split away by the sum of Zeeman energies. The Zeeman energies of the two qubits are given by $E_z^{(1)/(2)} = (g \pm \delta g)\mu_B B_z$, $J_\parallel = J\cos(2\theta)$, and the term $\nu^{(2)}\cos(\omega_{ac}t)$ with the Rabi frequency $\nu^{(2)}$ appears when we drive qubit two via EDSR, see Eq. (1.20)[6].

For the realization of a CNOT gate, the off-diagonal matrix elements containing J need to vanish, which happens when $\theta = L/l_{so} = \pi/2$. This is experimentally achievable in the presence of strong SOI, e.g., with holes in Si fin field-effect transistors [131]. The possibility to tune these terms to zero is remarkable since they enable fast two-qubit gates, which are not limited by the difference of Zeeman energies $\left|E_Z^{(1)} - E_Z^{(2)}\right|$, which is typically small in experiments. When $\theta = 0$, the two-qubit Hamiltonian in Eq. (1.27) can be separated into two decoupled blocks and the diagonal exchange coupling terms become $J_\parallel = -J$. Then the two blocks can be driven independently, as their resonance frequencies are at $\omega_{ac} = (E_Z^{(2)} \pm J/2)/\hbar$, differing exactly by the exchange coupling. By driving the lower block at resonance ($\hbar\omega_{ac} = E_Z^{(2)} - J/2$) for the time $t = \pi\hbar/\nu^{(2)}$, the upper

[5] For the transformation we first rearrange the basis to $\left\{\left|T_{\uparrow\uparrow}\right\rangle, |S_0\rangle, |T_0\rangle, \left|T_{\downarrow\downarrow}\right\rangle\right\}$ and apply the basis transformation $\{|\uparrow\uparrow\rangle, |\uparrow\downarrow\rangle, |\downarrow\uparrow\rangle, |\downarrow\downarrow\rangle\} = M\left\{\left|T_{\uparrow\uparrow}\right\rangle, |S_0\rangle, |T_0\rangle, \left|T_{\downarrow\downarrow}\right\rangle\right\}$ with $M = \begin{pmatrix} 1 & 0 & 0 & 0 \\ 0 & 1/\sqrt{2} & 1/\sqrt{2} & 0 \\ 0 & -1/\sqrt{2} & 1/\sqrt{2} & 0 \\ 0 & 0 & 0 & 1 \end{pmatrix}$ and $|ss'\rangle = \left|s^{(1)}s^{(2)\prime}\right\rangle$ $(s, s' = \uparrow, \downarrow)$. In this basis we diagonalize the single-qubit Hamiltonians for qubit 1 and qubit 2 individually by the unitary transformation $U_C = e^{-i\left(\sigma_y^{(1)} - \sigma_y^{(2)}\right)\theta/2}$.

[6] Note that the direction of the static electric field is y here and x in Eq. (1.20) which is why we have a Pauli x matrix here.

block stays idle and the lower block performs a full spin flip corresponding to the CNOT gate, see Eq. (1.8). Note that due to the SOI, the exchange interaction is anisotropic and becomes $J_{\parallel} = J\boldsymbol{e}_B \cdot R_y(2\theta)\boldsymbol{e}_B$ for an arbitrary direction of the Zeeman field $\boldsymbol{e}_B$, where R_y is the standard Euler rotation matrix for a rotation about the y axis. This demonstrates the potential of using SOI in achieving high-fidelity and fast two-qubit gates for quantum information processing.

1.3.3 Initialization and readout

The tiny magnetic moment of an electron or a hole presents a challenge for directly measuring the state of a spin qubit. On the other hand, the development of quantum point contacts (QPCs) opened the path to highly sensitive charge measurements [103] even before the first proposal for a spin qubit [20]. In a QPC, the conductance is quantized and at the transition between two conductance plateaus, it becomes very susceptible to nearby charges [132, 133]. By measuring the conductance of the QPC the number of charges in a single QD [134] or DQD [135] can be determined.

Since the inception of spin qubits, the question of how to read them out has been addressed and a successful proposal involves converting the spin information to a charge signal for measurement [20, 48]. One routinely used method for single-shot readout of a spin qubit is energy-selective readout [136], which is schematically illustrated in Fig. 1.4(a,b). The idea is to couple a QD to a reservoir and a charge sensor, e.g., a QPC. In the QD two spin states are separated by the Zeeman energy Δ_Z and the chemical potential of the reservoir μ is located in between the energy of the two states. All the other states in the QD are far away in energy and a double-occupation is prevented by the charging energy U. If the spin in the QD is in the ground state $|\downarrow\rangle$, it cannot tunnel to the reservoir because of the lack of unoccupied states [see Fig. 1.4(a)], and the signal at the charge sensor is constant. Conversely, if the spin is in the excited state $|\uparrow\rangle$, it can tunnel to the reservoir and a new spin can tunnel from the reservoir to the ground state of the QD [see Fig. 1.4(b)], which manifests in a peak in the charge sensor signal. Since the quantum state is destroyed by the measurement, high visibility is necessary to successfully apply this type of readout. Nowadays a visibility $> 99\,\%$ is achieved [93, 137] and it became a common readout method. At finite temperatures, it requires sufficiently large magnetic fields to split the spin states more than the thermal broadening to distinguish the spin states, $\Delta_Z \gg k_B T$. Because an excited state always escapes to the reservoir and the ground state is refilled, this scheme can also be used to initialize the spin qubit in the ground state.

Despite its success, energy-selective readout has some drawbacks. The readout speed for a full measurement cycle is proportional to the spin relaxation time [93, 137], which can be slow. Furthermore, the tunneling rates need to be within a certain range: If the tunneling is too slow, the spin might relax before it tunnels, while if it is too fast, the charge sensor might miss the signal [138]. Therefore, a different approach is required for fast spin qubit readout.

Exploiting the Pauli spin blockade (PSB) [21, 103] as illustrated in Fig. 1.4(c,d) for spin-to-charge conversion is one such approach. The setup comprises a DQD where initially each QD is occupied by a single spin. The initial state can either be a singlet $|S_0\rangle$ or a triplet $|T_0\rangle$. The other triplet states $|T_{\downarrow\downarrow}\rangle$ and $|T_{\uparrow\uparrow}\rangle$ with single occupied QDs are split away in energy by a magnetic field [see Eq. (1.25)]. By electrostatic gates, the DQD detuning ε can be swept from the situation where the initial state is lower in energy than the singlet state $|S_{RR}\rangle$ to a situation where $|S_{RR}\rangle$ is lower in energy than the initial state.[7]. If the sweeping is slow compared to the tunneling time, adiabatic tunneling from the initial state to the state $|S_{RR}\rangle$ can happen around the singlet anticrossing point.

[7] We choose here the singlet state $|S_{RR}\rangle$, but the same protocol can be realized equivalently with the two spins on the left dot, $|S_{LL}\rangle$.

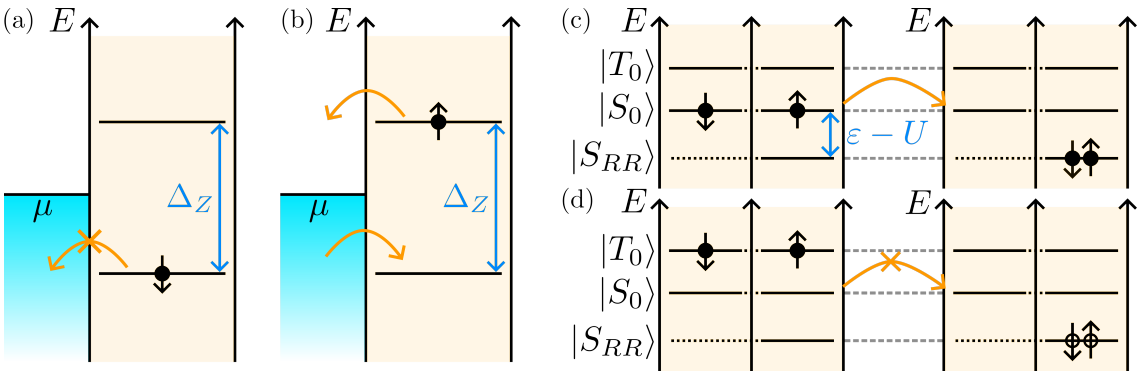

Figure 1.4: Schematic illustration of energy-selective readout and Pauli spin blockade (PSB). (a, b) In a QD the two spin states are separated in energy by the Zeeman gap Δ_Z due to a magnetic field. The chemical potential μ of a reservoir coupled to the QD is in between the two states. (a) If the spin in the QD is in the ground state ($|\downarrow\rangle$), it cannot tunnel to the reservoir because of the absence of unoccupied states. (b) A spin in the excited state ($|\uparrow\rangle$) can tunnel to the reservoir because its energy is larger than μ and it can be replaced by a spin from the reservoir that tunnels to the ground state. (c, d) By tuning ε the singlet state $|S_{RR}\rangle$ with both spins on the right QD can be brought to lower energy than the states $|S_0\rangle$ and $|T_0\rangle$, where the spins are delocalized over the DQD. (c) If the two spins are originally in the singlet state $|S_0\rangle$ they can localize at one QD. (d) If the spins form the triplet state $|T_0\rangle$, they cannot tunnel such that they end up at one QD because of the PSB.

Only if the initial state is $|S_0\rangle$ the spin on the left QD can tunnel to the right QD, forming the state $|S_{RR}\rangle$ [see Fig. 1.4(c)]. If the initial state is $|T_0\rangle$ the spin cannot tunnel because that would require a change of the symmetry of the wave function [see Fig. 1.4(d)] or the occupation of an excited orbital state which is excluded in the adiabatic limit [139]. This forbidden tunneling is referred to as the PSB. As before the difference of charge in the QDs can be measured by a nearby charge sensor. Also, the PSB method is suitable for the qubit initialization [49, 140, 141]. Both spins can be forced to locate in the right QD by electrostatic gates where they relax to the $|S_{RR}\rangle$ state. Tuning ε such that $|S_{RR}\rangle$ lies at higher energy than the states of single QD occupation causes one spin to tunnel to the left QD ending up in the $|S_0\rangle$ state. A subsequent single-qubit rotation enables the transition to one of the triplet states $|T_{\downarrow\downarrow}\rangle$ or $|T_{\uparrow\uparrow}\rangle$, which relax into the state $|T_0\rangle$. Particular caution is required if, in addition to the spin degree of freedom, there is also a valley degree of freedom as for electrons in Si. In this case, the doubly occupied QD state can be a spin triplet allowing for spin tunneling events that are forbidden in the valley-free situation [142]. However, accounting for the total symmetry of the wave functions enables the formulation of a generalized PSB theory in the presence of valleys.

A different approach to qubit readout is based on the dispersive shift of the resonance frequency of a resonator coupled to the qubit due to the change of the QD capacitance [143, 144]. In analogy to cavity quantum electrodynamics (QED) in atomic physics [145–147] and circuit QED with superconducting qubits [148–150], spin qubits are coupled to photons in a superconducting microwave resonator [21]. Measuring the cavity transmission or reflection in the dispersive regime means that the detuning between the QD transition and the cavity photon frequency is much larger than the cavity linewidth, i.e., away from the resonance. The cavity photon frequency is shifted by the dispersive shift depending on the state of the qubit. Strong resonator-spin qubit coupling has been achieved [151–155] and by exploiting an ancilla QD a readout fidelity of 99.2 % was

reported [156]. This technique exhibits low back action on the qubit because the measured operator commutes with the qubit Hamiltonian and the Hamiltonian that describes the interaction with the qubit-measurement apparatus [157]. This is referred to as quantum non-demolition measurement. In theory, this property allows for infinitely accurate measurements that, however, in practice are limited by decoherence due to coupling to the environment. Furthermore, it does not require a charge detector in the vicinity of the qubit. In addition to the high-fidelity readout, coupling the qubit to a microwave resonator also enables long-distance coupling of spin qubits. This is an advantage since inter-qubit connectivity beyond nearest neighbor interactions enables quantum information processing at higher fidelity [158].

To measure gate fidelities above the threshold for quantum error correction [26, 27] with readout fidelities far below the gate fidelity, advanced techniques are required. In practice randomized benchmarking [159, 160] and gate set tomography [161–163] are used for this purpose. The former allows for error characterization of arbitrarily large quantum processors by the implementation of a long sequence of random quantum gates and returns an error rate per gate. The latter, on the other hand, gives a full gate-resolved characterization of the errors.

1.3.4 Decoherence

Qubits, being quantum systems, inevitably interact with their environment, leading to decoherence, which results in the loss of quantum information. In the following, we provide a basic theoretical background for the description of noise including an introduction to the commonly reported relaxation time T_1, dephasing time T_2^*, coherence time T_2, and experiment-specific numbers like T_2^{Hahn} and T_2^{Rabi}. Subsequently, we discuss some important sources of noise for gate-defined spin qubits in semiconductors and give numbers for state-of-the-art experiments.

Theory of decoherence

The dynamics of a closed quantum system can be described by the time evolution of the density matrix of a quantum state given by the Liouville-von Neumann equation

$$\frac{\mathrm{d}}{\mathrm{d}t}\rho(t) = -\frac{i}{\hbar}\left[H(t), \rho(t)\right], \tag{1.28}$$

where the density matrix $\rho(t) = \sum_k p_k \left|\psi_k(t)\right\rangle \left\langle\psi_k(t)\right|$ is given by an ensemble of pure quantum states with the probability p_k for the state $\left|\psi_k(t)\right\rangle$ which fulfills $\sum_k p_k = 1$. However, when the quantum system interacts with its environment, decoherence processes occur and this simple description becomes insufficient. To account for these interactions, we extend Eq. (1.28) with a dissipator $\mathcal{D}[\rho(t)]$, leading to the Lindblad master equation

$$\frac{\mathrm{d}}{\mathrm{d}t}\rho(t) = -\frac{i}{\hbar}\left[H(t), \rho(t)\right] + \underbrace{\sum_{m,n} \Gamma_{|m\rangle\to|n\rangle}\left(\left|n\right\rangle\!\left\langle m\right| \rho(t) \left|m\right\rangle\!\left\langle n\right| - \frac{1}{2}\left|m\right\rangle\!\left\langle m\right| \rho(t) - \frac{1}{2}\rho(t)\left|m\right\rangle\!\left\langle m\right|\right)}_{=\mathcal{D}[\rho(t)]}, \tag{1.29}$$

where $\Gamma_{|m\rangle\to|n\rangle} \geq 0$ is the transition rate from state $|m\rangle$ to state $|n\rangle$ [164, 165]. Note that the validity of the Lindblad master equation relies on the Born approximation (weak coupling to the environment) and the Markov approximation (short memory for the noise). In the following, we assume a spin qubit described by the ground state $|0\rangle$ and the excited state $|1\rangle$. For the unitary time evolution we consider the time-independent Hamiltonian $H = \sigma_z \Delta/2$ in the $\{|0\rangle, |1\rangle\}$ basis. Relaxation is described in Eq. (1.29) by the process $|1\rangle \to |0\rangle$ with the associated relaxation

rate $\Gamma_{|1\rangle\to|0\rangle} = \Gamma_r$[8]. We can also include dephasing processes which are described by $|n\rangle \to |n\rangle$ and we choose $\Gamma_{|0\rangle\to|0\rangle} = \Gamma_{|1\rangle\to|1\rangle} = \Gamma_d$. By solving the differential equation in Eq. (1.29) with appropriate boundary conditions, one finds the relaxation time $T_1 = 1/\Gamma_r$ and the decoherence rate $1/T_2 = \Gamma_r/2 + \Gamma_d$. The pure dephasing time can be found by setting $\Gamma_r = 0$ as $T_2^* = 1/\Gamma_d$. This result also tells us the upper bound for the coherence time $T_2 \leq 2T_1$.

In the next paragraph, we will discuss charge noise[9] as an important source for decoherence of spin qubits which has the power spectral density $S_n(\omega) \propto \omega^{-1}$. However, the previous results for dephasing are only valid in the limit of white noise since we assume that the correlation time of the noise is much shorter than the lifetime of the qubit [167]. To provide a better description of dephasing due to charge noise, the filter function formalism is employed, which explicitly accounts for external control in the experiment, e.g., by gate pulses [21, 168, 169]. Let us consider the Hamiltonian $H = \sigma_z\Delta/2$ and the initial state $|0\rangle$. By applying a $\pi/2$ pulse about the y axis, i.e., letting the qubit evolve under the EDSR scheme for the time $T_{\pi/2} = \pi/2\Omega_R$ [see Eq. (1.23)], the initial state becomes $|+\rangle = (|0\rangle + |1\rangle)/2$ which is an eigenstate of σ_x. We assume here that the pulse initiates an instantaneous spin flip. Then we allow the state to evolve freely for a certain time Δt, which is referred to as free induction decay or Ramsey experiment. After a second $\pi/2$ pulse the qubit state is measured and one obtains a sinusoidal probability P_1 for the qubit to be in state $|1\rangle$ as a function of Δt. Due to dephasing, P_1 will be exponentially damped

$$\langle P_1\rangle = \frac{1}{2} + \frac{1}{2}e^{\frac{-\sigma_{\delta\phi}}{2}}\cos\left(\frac{\Delta t}{\hbar}\right), \tag{1.30}$$

where the decay is given by the variance

$$\sigma_{\delta\phi} = \frac{1}{2\pi\hbar}\int_{-\infty}^{\infty}\mathrm{d}\omega\frac{F(\omega t)}{\omega^2}S_n(\omega) \tag{1.31}$$

with the filter function [21, 169]

$$F(\omega t) = \left|\frac{\omega}{2}\int_0^t r(t')e^{i\omega t'}\mathrm{d}t'\right|^2. \tag{1.32}$$

The filter function depends on the experimental setup and the number of pulses that are applied to the qubit. For the Ramsey experiment described above, it takes the form

$$F(\omega t) = 4\sin^2\left(\frac{\omega t}{2}\right). \tag{1.33}$$

Even though the decay is exponential only for white noise with power spectral density $S_n(\omega) = \hbar^2/T_2^*$, the dephasing time T_2^* is commonly defined as the time after which the signal has decayed to $1/e$ for any type of noise. Another important type of noise is quasi-static noise, which models the slow dynamics of nuclear spins coupled to the spin qubit. It is characterized by the power spectral density $S_n(\omega) = 2\pi\hbar^2\delta(\omega)/(T_2^*)^2$. Solving the integral in Eq. (1.31) in this case yields $\sigma_{\delta\phi} = t^2/(T_2^*)^2$, which is a Gaussian decay. Returning to the original example of charge noise described by $1/f$ noise with the power spectral density $S_n(\omega) = \hbar^2/(T_2^*)^2|\omega|$, we need to introduce an infrared cutoff ω_{ir} because the integral in Eq. (1.31) diverges at $\omega = 0$. Then the decay can be

[8] We assume here that there is no spontaneous excitation, meaning $\Gamma_{|0\rangle\to|1\rangle} = 0$.

[9] A simple derivation of the $1/f$ power spectral density is based on classical random telegraph noise due to trapping and detrapping of charges [166].

approximated by

$$\sigma_{\delta\phi} \approx \frac{t^2}{\pi (T_2^*)^2} \ln\left(\frac{1}{\omega_{ir} t}\right), \tag{1.34}$$

which can be interpreted as Gaussian decay with a logarithmic correction. Commonly the notation T_2^* for the dephasing time is used for the decay time measured in a Ramsey experiment where the decay is dominated by dephasing. Thus, from Ramsey experiments, one typically sees $T_2^* \ll T_2$.

Dynamical decoupling techniques, such as the Hahn echo experiment, can significantly extend the coherence time of a spin qubit by reducing low-frequency noise through the application of additional, refocusing pulses [170]. In a Hahn echo experiment, the same principle as the Ramsey experiment is employed, but with an additional π pulse applied after a time $\Delta t/2$. Thus, the weight of the filter function is no longer peaked at low frequency but shifted to higher frequency. The filter function is given by

$$F(\omega t) = 16 \sin^4\left(\frac{\omega t}{4}\right) \tag{1.35}$$

with the immediate consequence that $\sigma_{\delta\phi}$ obtains a natural cutoff at low frequencies $F(\omega t)/\omega^2 \to 0$. The effects of static noise are filtered out completely by the Hahn echo pulse sequence and the coherence time measured is commonly reported as T_2^{Hahn}. By applying sequences of refocusing pulses, the coherence time of a spin qubit can be further enhanced [169]. However, it is essential to note that echo pulses only shift the weight of the filter function to different frequencies, leading to higher sensitivity to high-frequency noise.

The last important timescale we want to discuss is the Rabi decay time T_2^{Rabi}. In contrast to the other timescales that give a measure for the coherence time of an idle qubit, T_2^{Rabi} gives the coherence time of a driven qubit [171]. Due to the driving, the filter function is peaked at the Rabi frequency rather than at or close to $\omega = 0$, which results in $T_2^* < T_2^{\text{Rabi}}$ at dominant low-frequency noise.

Sources of noise

One of the most prominent sources of noise are local electrical fluctuations known as charge noise. It originates in fluctuations of the gate voltages, fluctuating defect states, phononic crystal deformation [172], or any other variations of charges close to the qubit. Its origin is not well understood, but experiments show a typical power spectral density $S_n(\omega) \propto \omega^{-1}$ [122, 151, 173, 174], hence the name $1/f$ or pink noise, although thermally activated white noise can also contribute to lesser extent [175, 176]. While charge noise does not affect the spin degree of freedom directly, the spin couples to charge fluctuations via the SOI or other mechanisms that couple orbital and spin degrees of freedom, which is necessary for the qubit manipulation and readout. However, certain geometries enable the electrical suppression of SOI at demand [67, 177] or tuning to a g factor minimum [58, 64, 178–180], creating a "sweet spot", where the dephasing is significantly reduced. Note that in the former situation, the charge noise is turned off completely while in the latter case, the qubit is protected from charge fluctuations only to some extent.

Especially in materials like GaAs, which was used extensively in the early days of spin qubits because of the simplicity of fabrication [81], the presence of nuclear spins and the associated hyperfine noise limits the coherence time of spin qubits $T_2^* \sim 10\,\text{ns}$ [49, 129, 181, 182]. Unlike charge noise, the power spectral density of hyperfine noise shows a sharp peak at ω_0 originating in the slow dynamics of nuclear spins [183–185]. The hyperfine noise can strongly be suppressed in isotopically purified Si or Ge which are virtually nuclear spin free [82–84] or by using holes

instead of electrons where the contact hyperfine interaction between nuclear spins and hole spins is stifled due to the p-type atomic orbitals [39, 89] and can even be tuned by appropriate QD design [186–192].

Noise associated with phonons primarily causes spin relaxation by energy exchange with the environment. This exchange is mediated for typical spin qubits by SOI, hyperfine interaction, or external magnetic field gradients [103, 193], and specifically in Si and Ge via the deformation potential [194]. In addition to the at low temperature dominant relaxation due to phonons [195, 196] also dephasing via two-phonon processes is possible [197].

In semiconductor spin qubits with long coherence time, the relaxation time T_1 is often not the limiting factor, although it can distort the readout when the readout time is comparable to T_1 [21]. State-of-the-art experiments with electrons in Si and holes in Ge report T_1 on the order of 10 ms [25–28, 198], with Si MOS QDs reaching timescales exceeding seconds [199]. The dephasing time T_2^* is $\sim 10\,\mu s$ for electrons in Si [26, 27] and $\sim 100\,ns$ for holes in Ge [25, 200] in the same experiments. Remarkably, the coherence time of holes in Ge can be extended by refocusing pulses to 100 µs [25]. Due to the valley degeneracy for electrons in Si, spin-valley relaxation hot spots emerge under the condition of equal valley and spin splitting resulting in vastly reduced relaxation times [201–203]. The spin-valley coupling causes the mixing of an excited spin state with valley states of opposite spin, facilitating relaxation to the ground state through phonon emission. This process is much faster than pure spin relaxation.

For comparison to the coherence times above, we also state here the gate speeds in the same experiments. The gate operation time is defined here as $T_{op} = 1/2f$ where f is the Rabi frequency[10] for single-qubit gates and the two-qubit gate operation frequency for two-qubit gates. Single qubit gates with electrons in Si are performed at operation times of $\sim 100\,ns$ [27, 28] and with holes in Ge at $\sim 20\,ns$ [200], which all exceed a fidelity of 99 %. Two qubit gates are operated at $\sim 40\,ns$ in Si [26, 28] and $\sim 10\,ns$ in Ge [25]. For holes in Si/Ge core/shell NW QDs a single-qubit gate operation time of 1.2 ns at a coherence time between 7 and 59 ns was reported [177] and holes in Ge hut wires reach $T_{op} \sim 0.92\,ns$ and a coherence time up to 82 ns [128]. An extensive overview and comparison between different spin qubits in semiconductor structures can be found in Ref. [171].

1.4 Superconductor-semiconductor devices

Recent advances have facilitated the growth of SC-semiconductor hybrid structures, characterized by clean interfaces of high transparency [70, 204–213]. These developments have paved the way for many applications, such as Andreev spin qubits (ASQs) [214–216], long-range coupling of spin qubits [19, 217–219], electrically controllable Josephson junctions [75, 220–222], and topological superconductivity, which is predicted to lead to the formation of Majorana bound states (MBSs) [77, 79, 223]. In addition to the emergence of proximity-induced superconductivity [224, 225], the SC has significant effects on the semiconductor, known as the metallization of the semiconductor [72]. These effects include the renormalization of the effective mass, g factor, and the SOI strength [72, 74, 226, 227]. A detailed analysis of these effects in Ge hole NWs is provided in Chapter 4. To motivate further interest in hybrid SC-semiconductor devices we review the physics of ASQs and MBSs in the subsequent sections.

1.4.1 Andreev spin qubits

ASQs have raised attention due to their potential to combine the advantages of superconducting qubits and spin qubits in QDs [215, 216, 228, 229]. The main idea is to exploit the small size

[10] Note that f here is not an angular frequency as the Rabi frequency in Eq. (1.23), meaning $f = \Omega_R/2\pi$.

of spin qubits which is advantageous for scaling up with the ease of coupling superconducting qubits through the supercurrent [228] or by effective wave function overlap [230–234] which both allow coupling over much longer distances than via the short-ranged exchange interaction. In this section, we briefly sketch the physics behind ASQs which are based on Andreev bound states (ABSs) in a SC-normal metal-SC (SNS) junction[11].

Let us begin by considering a normal metal-insulator junction. If a charge (we assume here an electron) in the metal approaches the insulator, it will be reflected specularly at the interface because it cannot enter the insulator due to the absence of states in the band gap, see Fig. 1.5(a). If we replace the insulator with a SC, the electron still cannot propagate through the interface if its energy is below the superconducting gap Δ_s because there are also no states in the gap. However, in addition to the specular reflection of the electron a retro-reflection of a hole of opposite spin and velocity can be observed and at the same time a Cooper pair forms[12] in the SC which is necessary to conserve charge and momentum [235], see Fig. 1.5(b). This process is called Andreev reflection [236, 237]. The probability of Andreev reflections depends on the transparency of the junction and the energy of the incident electron (or hole). It is higher for more transparent junctions, but is suppressed if the transparency is low.

A fascinating phenomenon emerges in a short SNS junction. An electron (or hole) in the normal metal with energy below the gap is coherently Andreev reflected back and forth at each of the junctions, forming an ABS in the normal region [238, 239], see Fig. 1.5(c). The energy of the ABS $E(\phi)$ depends on the transparency of the junctions and the difference of the superconducting phases ϕ of the two SCs. Similar to a particle in the box, the energy of ABSs is quantized. For a 1D SNS junction with perfectly transparent junctions, the quantization condition for the energy becomes

$$\phi - 2\arccos\left(\frac{E(\phi)}{\Delta_s}\right) - 2\frac{E(\phi)}{\Delta_s}\frac{L_N}{\xi} = 2\pi n, \tag{1.36}$$

where L_N is the length of the normal region, ξ is the superconducting coherence length, and n is an integer [239]. This formula is valid in the Andreev limit where the superconducting gap is much smaller than the chemical potential [240]. The emergence of ABSs in an SNS junction has important consequences as it allows the supercurrent to flow from one SC to the other through the junction, known as Josephson current [241, 242].

The effects observed in the case where the normal metal is replaced by a semiconductor are similar. Other mechanisms that can lead to the emergence of states within the superconducting gap, which are sometimes also called ABSs, include the trapping of states in magnetic flux vortices [243], at magnetic impurities [244–246], or at weak links between SCs.

Building on the physics of ABSs it was proposed to couple a superconductor to a QD to create an ASQ [228, 229]. In experiments, a semiconductor NW with SOI can be proximitized by a SC, leaving a short region in the normal state where ABSs emerge [216]. If there is an odd number of electrons in the QD or normal region, the ground state is a spin doublet. The key advantage over conventional spin qubits lies in the strong coupling of the ASQ to the superconducting leads and the fact that the Josephson current depends on the state of the enclosed spin via strong SOI. The difference in superconducting currents for the two spin states depends on the phase difference between the SCs

$$\Delta I = \pm\frac{2e}{\hbar}|\varepsilon_{so}||\cos(\phi)|, \tag{1.37}$$

[11] The normal metal section can also be a semiconductor.

[12] Equivalently a hole can be retro-reflected at the interface with the additional destruction of a Cooper pair in the SC.

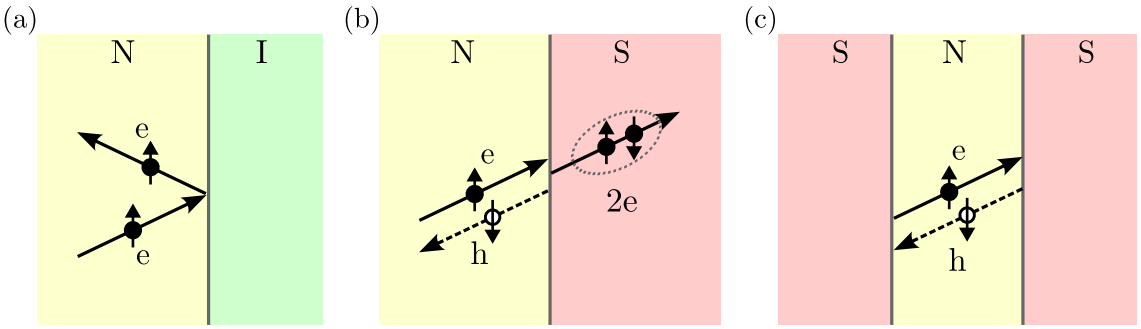

Figure 1.5: Schematic illustration of (a) specular reflection of an electron (e) at a normal metal-insulator (NI) junction, (b) Andreev reflection at a normal metal-SC (NS) junction, and (c) Andreev bound state (ABS) in the normal region of an SNS junction. (a) An incident electron with momentum $\boldsymbol{p}$ and energy below the energy gap of the insulator is reflected at the interface into an outgoing electron with momentum $\boldsymbol{p}' = \boldsymbol{p} - 2\hat{n}(\hat{n} \cdot \boldsymbol{p})$, where $\hat{n}$ is the unit vector normal to the interface. (b) If the insulator is replaced by a SC, the electron cannot propagate into the superconducting region if its energy is below the superconducting gap. However, a hole (h) of opposite spin and velocity can be retro-reflected with the simultaneous formation of a Cooper pair (2e) in the SC. (c) In a normal metal in between two superconducting regions, an electron can be Andreev reflected at one interface under the formation of a hole of opposite momentum. Subsequently, the hole is Andreev reflected at the other interface resulting in a so-called ABS.

where $\boldsymbol{\varepsilon_{so}}$ is a pseudovector that defines the spin-polarization axis [229]. The sign of the current is given by the spin projection along $\boldsymbol{\varepsilon_{so}}$ and thus enables readout of the qubit. In analogy to common spin qubits, ASQs can be driven electrically via gates as described in Sec. 1.3.1. Moreover, two-qubit gates can be realized by utilizing the magnetic interaction between the spin-dependent supercurrents through two qubits in a superconducting circuit. This is an Ising-type interaction allowing for CNOT operations.

The experimental realization of ASQs is far behind conventional spin qubits. State-of-the-art experiments have demonstrated a spin relaxation time of 17 µs and a spin coherence time of 52 ns in an Hahn echo experiment [216].

1.4.2 Majorana bound states in Rashba nanowires

A special type of ABSs that exhibits topologically non-trivial behavior is known as MBS. In the following, we provide a concise introduction to MBSs, explaining what they are, how they are predicted to form in semiconductor NWs with strong SOI proximitized by a SC, and why they are of interest for quantum computing. Our discussion is based on the comprehensive reviews in Refs. [239, 247].

A simple yet popular toy model used to describe the emergence of MBSs is the Kitaev chain [77]. Consider a discrete 1D chain of spinless fermions of length N, described by the following Hamiltonian in second quantization [248]

$$H = \sum_{j=1}^{N-1} \left(-t c_j^\dagger c_{j+1} + \Delta_s c_j c_{j+1} + \text{H.c.} \right) - \mu \sum_{j=1}^{N} c_j^\dagger c_j, \tag{1.38}$$

where $t \geq 0$ represents the nearest-neighbor hopping amplitude and μ is the chemical potential. In general, the p-wave superconducting pairing potential Δ_s can be a complex number, but for

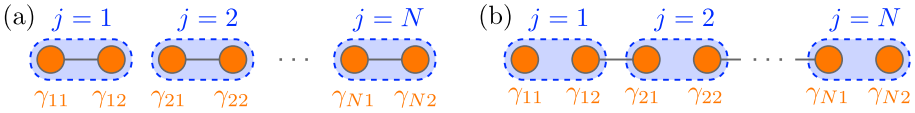

Figure 1.6: Schematic illustration of the two limiting cases of the Kitaev chain. (a) Trivial phase: $\Delta_s = t = 0$ and $\mu < 0$. Pairs of Majorana operators from the same site form a fermion. (b) Topological phase: $t = \Delta_s$ and $\mu = 0$. Majorana operators from neighboring sites pair up to form a fermion. The Majorana operators at the ends of the chain remain unpaired and do not enter the Hamiltonian.

simplicity is chosen to be real and positive here. The creation and annihilation operators for the spinless fermions at site j are $c_j^\dagger$ and c_j, respectively, and they satisfy the canonical commutation relations $\{c_j^\dagger, c_k^\dagger\} = \{c_j, c_k\} = 0$ and $\{c_j, c_k^\dagger\} = \delta_{jk}$ for $j, k = 1, \ldots, N$. For the description of the topological phase transition, we employ a mathematical trick and define the new, so-called Majorana operators $\gamma_{j1} = c_j^\dagger + c_j$ and $\gamma_{j2} = i(c_j^\dagger - c_j)$ following the commutation relations

$$\{\gamma_{j\alpha}, \gamma_{k\beta}\} = 2\delta_{jk}\delta_{\alpha\beta}, \;\; \gamma_{j\alpha}^\dagger = \gamma_{j\alpha}, \tag{1.39}$$

where $\alpha, \beta = 1, 2$. The second relation implies that quasiparticle excitations due to the new operators behave as their own antiparticles. Rewriting the Hamiltonian in Eq. (1.38) in terms of the Majorana operators yields

$$H = \frac{i}{2}\sum_{j=1}^{N-1}\left[(\Delta_s + t)\gamma_{j2}\gamma_{(j+1)1} + (\Delta_s - t)\gamma_{j1}\gamma_{(j+1)2}\right] - \frac{\mu}{2}\sum_{j=1}^{N}(i\gamma_{j1}\gamma_{j2} + 1)\,. \tag{1.40}$$

To gain insight, let us consider two limiting cases. The first one is the fully uncoupled chain where $\Delta_s = t = 0$ and $\mu < 0$. In this case, each pair of Majorana operators pairs up to form a physical fermion, see Fig. 1.6(a). It is clear that from the Hamiltonians in Eqs. (1.38) and (1.40) only the second sums remain. Thus, adding a fermion to the chain comes at the cost of the chemical potential $-\mu$ and the spectrum is fully gapped. This phase is referred to as the topologically trivial phase and it does not host MBSs.

The second limiting case occurs when $t = \Delta_s$ and $\mu = 0$, causing the Majorana operators from neighboring sites to pair up as shown in Fig. 1.6(b). In this situation, we introduce a new set of fermionic operators $d_j = 1/2(\gamma_{j2} + i\gamma_{(j+1)1})$ and $d_j^\dagger = 1/2(\gamma_{j2} - i\gamma_{(j+1)1})$ which lead to

$$H = 2t\sum_{j=1}^{N-1}\left(d_j^\dagger d_j - \frac{1}{2}\right) \tag{1.41}$$

in the given limit. Again, the spectrum is gapped, now with the energy cost of $2t$ for adding a fermion. However, there are two Majorana operators, γ_{11} and γ_{N2}, left at the ends of the chain that do not enter the Hamiltonian in Eq. (1.41), implying that they commute with H. Thus, there must be two modes at zero energy, which are the MBSs localized at the ends of the Kitaev chain in the topological phase. We can combine the two MBSs to a single fermionic mode $d_0 = 1/2(\gamma_{11} + i\gamma_{N2})$, $d_0^\dagger = 1/2(\gamma_{11} - i\gamma_{N2})$ which is delocalized over the ends of the chain. Since the excitation and deexcitation of these fermionic modes comes at no energy cost, the ground state at zero energy is twofold degenerate. This property, together with the non-Abelian commutation relations, makes MBSs highly interesting for topological quantum computing. Although we only considered the limiting case of $t = \Delta_s$ and $\mu = 0$, the MBSs remain upon deviations from these fine-tuned

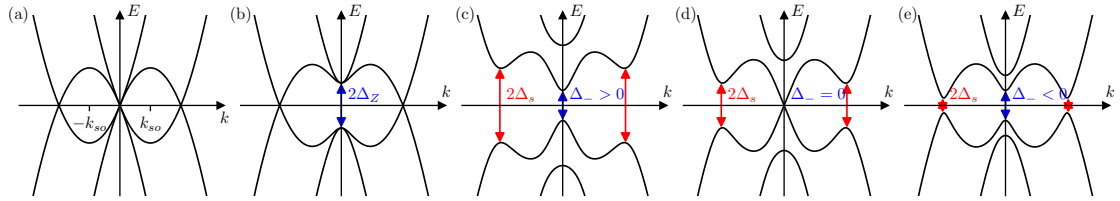

Figure 1.7: Bulk spectrum of a Rashba NW proximitized by a SC in the presence of a magnetic field at $\mu = 0$. (a) $\Delta_Z = \Delta_s = 0$: Two parabolas shifted by $\pm k_{so}$ with respect to each other. We depict both particle-hole symmetric bands. (b) $\Delta_Z > 0$, $\Delta_s = 0$: A Zeeman gap opens at $k = 0$ while the outer branches remain ungapped. (c) $\Delta_s > \Delta_Z > 0$: The superconducting pairing potential causes a gap opening at the outer branches and the gap at $k = 0$ is renormalized to $\Delta_- = \Delta_s - \Delta_Z > 0$. This is the topologically trivial regime. (d) $\Delta_s = \Delta_Z > 0$: The gap at $k = 0$ closes. This is the topological phase transition point. (e) $\Delta_Z > \Delta_s > 0$: Reopening of the gap at $k = 0$. This is the topologically non-trivial phase with $\Delta_- < 0$.

parameters. Continuous changes in the parameters will not destroy the MBSs as long as the bulk gap remains open, a phenomenon known as the topological protection of the MBSs.

Before reviewing the concept of topological quantum computing based on MBSs we shortly discuss one experimentally realizable platform that is predicted to host MBSs: the Rashba NW [249–252]. The great interest in this specific platform lies in the predicted experimental feasibility. In reality, it is hard to find a spinless p-wave superconductor as necessary for the direct implementation of the Kitaev chain. However, by combining a semiconducting NW with strong Rashba SOI, a magnetic field perpendicular to the SOI vector, and a s-wave SC in proximity to the NW, spin-momentum-locked, so-called helical, bands form. A conventional s-wave superconducting pairing projected onto such a helical band leads to an effective spinless p-wave SC [253]. Let us first consider the Rashba NW in its trivial phase in the absence of the superconducting pairing potential. The bulk spectrum consists of two parabolas of opposite spin that are shifted with respect to each other by the SO wavevector $\pm k_{so}$, see Fig. 1.7. The magnetic field opens up a Zeeman gap Δ_Z at $k = 0$, while the outer branches of the parabolas at $\pm 2k_{so}$ remain ungapped. The introduction of a superconducting pairing potential causes a gap opening also at the outer branches and leads to a renormalization of the gap at $k = 0$. A competition between Δ_s and Δ_Z eventually results in a topological phase transition. If $\Delta_Z^2 > \Delta_s^2 + \mu^2$, the system is in the topological phase and the ends of the Rashba NW host MBSs. Note that in a NW of finite length the MBSs hybridize into a fermion of finite energy that is exponentially suppressed by the length of the NW. Thus, the above considerations are only valid for long systems.

The accessibility of this platform has caused numerous experimental efforts to demonstrate the existence of MBSs. Measurements have shown zero-bias conductance peaks [254–259], which are expected to appear in the presence of MBSs. However, non-topological states like the aforementioned ABSs have turned out to mimic MBS signatures [76, 239, 260–267]. More advanced techniques to validate the existence of MBSs combine several signatures, such as the 'topological gap protocol', which demands correlated zero-bias conductance peaks at both ends of the NW simultaneously with bulk reopening signatures that support the interpretation as a transition between the trivial and topological phases [268]. State-of-the-art experiments have reported devices passing this protocol [269], but challenges remain as non-topological mechanisms can still explain the measured data [270]. Therefore, irrefutable proof of the existence of MBSs is still sought.

Assuming the existence of MBSs, we can exploit their properties for topological quantum computing. One proposed advantage of MBSs over other qubits is their potential to store quantum

information for a long time because their non-locality implies protection from dephasing [77, 271]. At the heart of the interest in MBSs for topological quantum computing lies their non-Abelian exchange statistics. In three dimensions, there are only two fundamental types of particles, fermions and bosons, which differ in their behavior under exchange. Let us assume two indistinguishable particles, one in state ψ_1 and the other in state ψ_2. Upon exchange of the two particles, their many-body wave function acquires a phase

$$|\psi_1\psi_2\rangle = e^{i\phi}\,|\psi_2\psi_1\rangle\,. \tag{1.42}$$

If the two particles are bosons the phase factor is $+1$ and if they are fermions it is -1, which is called Abelian exchange statistics. However, in condensed matter physics, it is possible to confine particles to two dimensions where the phase factor is not restricted to the values ± 1. Particles, or better quasiparticles, following such non-Abelian exchange statistics are referred to as anyons and MBSs are one specific type of anyons. By exchange or so-called braiding of MBSs, topologically protected single-qubit rotations by an angle $\pi/2$ can be performed. However, for universal quantum computing it is necessary to couple the MBSs to other types of qubits [272–274] or perform non-protected operations [78, 275].

The standard materials employed for the experimental realization of MBSs in Rashba NWs are InAs or InSb [254, 255, 257, 259, 261], because of their strong SOI. However, the presence of substantial disorder in these devices has so far hindered a definitive verification of the existence of MBSs [276]. In contrast, planar Ge structures exhibit hole mobility figures surpassing those of InAs by a factor of $50 - 100$ [86]. Moreover, as mentioned earlier, advances in the fabrication of SC-Ge devices enabled the measurement of a hard superconducting gap in Ge [209]. Thus, the prospect of harnessing gate-defined 1D hole channels within planar Ge heterostructures emerges as a highly promising avenue for realizing MBSs [80].

References

[1] M. A. Nielsen and I. L. Chuang, *Quantum computing and quantum information* (Cambridge University Press, Cambridge, 2010).

[2] C. H. Bennett, G. Brassard, C. Crépeau, R. Jozsa, A. Peres, and W. K. Wootters, "Teleporting an unknown quantum state via dual classical and Einstein-Podolsky-Rosen channels", Phys. Rev. Lett. **70**, 1895 (1993).

[3] D. Bouwmeester, J.-W. Pan, K. Mattle, M. Eibl, H. Weinfurter, and A. Zeilinger, "Experimental quantum teleportation", Nature **390**, 575 (1997).

[4] C. H. Bennett and S. J. Wiesner, "Communication via one- and two-particle operators on Einstein-Podolsky-Rosen states", Phys. Rev. Lett. **69**, 2881 (1992).

[5] T. Schaetz, M. D. Barrett, D. Leibfried, J. Chiaverini, J. Britton, W. M. Itano, J. D. Jost, C. Langer, and D. J. Wineland, "Quantum dense coding with atomic qubits", Phys. Rev. Lett. **93**, 040505 (2004).

[6] A. Barenco, C. H. Bennett, R. Cleve, D. P. DiVincenzo, N. Margolus, P. Shor, T. Sleator, J. A. Smolin, and H. Weinfurter, "Elementary gates for quantum computation", Phys. Rev. A **52**, 3457 (1995).

[7] E. Knill, "Quantum computing with realistically noisy devices", Nature **434**, 39 (2005).

[8] D. Gottesman, "An introduction to quantum error correction and fault-tolerant quantum computation", (2009), arXiv:0904.2557 [quant-ph].

[9] A. M. Stephens, "Fault-tolerant thresholds for quantum error correction with the surface code", Phys. Rev. A **89**, 022321 (2014).

[10] W. K. Wootters and W. H. Zurek, "A single quantum cannot be cloned", Nature **299**, 802 (1982).

[11] P. W. Shor, "Scheme for reducing decoherence in quantum computer memory", Phys. Rev. A **52**, R2493 (1995).

[12] A. G. Fowler, M. Mariantoni, J. M. Martinis, and A. N. Cleland, "Surface codes: towards practical large-scale quantum computation", Phys. Rev. A **86**, 032324 (2012).

[13] F. Arute, K. Arya, R. Babbush, D. Bacon, J. C. Bardin, R. Barends, R. Biswas, S. Boixo, F. G. S. L. Brandao, D. A. Buell, B. Burkett, Y. Chen, Z. Chen, B. Chiaro, R. Collins, W. Courtney, A. Dunsworth, E. Farhi, B. Foxen, A. Fowler, C. Gidney, M. Giustina, R. Graff, K. Guerin, S. Habegger, M. P. Harrigan, M. J. Hartmann, A. Ho, M. Hoffmann, T. Huang, T. S. Humble, S. V. Isakov, E. Jeffrey, Z. Jiang, D. Kafri, K. Kechedzhi, J. Kelly, P. V. Klimov, S. Knysh, A. Korotkov, F. Kostritsa, D. Landhuis, M. Lindmark, E. Lucero, D. Lyakh, S. Mandrà, J. R. McClean, M. McEwen, A. Megrant, X. Mi, K. Michielsen, M. Mohseni, J. Mutus, O. Naaman, M. Neeley, C. Neill, M. Y. Niu, E. Ostby, A. Petukhov, J. C. Platt, C. Quintana, E. G. Rieffel, P. Roushan, N. C. Rubin, D. Sank, K. J. Satzinger, V. Smelyanskiy, K. J. Sung, M. D. Trevithick, A. Vainsencher, B. Villalonga, T. White, Z. J. Yao, P. Yeh, A. Zalcman, H. Neven, and J. M. Martinis, "Quantum supremacy using a programmable superconducting processor", Nature **574**, 505 (2019).

[14] Y. Wu, W.-S. Bao, S. Cao, F. Chen, M.-C. Chen, X. Chen, T.-H. Chung, H. Deng, Y. Du, D. Fan, M. Gong, C. Guo, C. Guo, S. Guo, L. Han, L. Hong, H.-L. Huang, Y.-H. Huo, L. Li, N. Li, S. Li, Y. Li, F. Liang, C. Lin, J. Lin, H. Qian, D. Qiao, H. Rong, H. Su, L. Sun, L. Wang, S. Wang, D. Wu, Y. Xu, K. Yan, W. Yang, Y. Yang, Y. Ye, J. Yin, C. Ying, J. Yu, C. Zha, C. Zhang, H. Zhang, K. Zhang, Y. Zhang, H. Zhao, Y. Zhao, L. Zhou, Q. Zhu, C.-Y. Lu, C.-Z. Peng, X. Zhu, and J.-W. Pan, "Strong quantum computational advantage using a superconducting quantum processor", Phys. Rev. Lett. **127**, 180501 (2021).

[15] Q. Zhu, S. Cao, F. Chen, M.-C. Chen, X. Chen, T.-H. Chung, H. Deng, Y. Du, D. Fan, M. Gong, C. Guo, C. Guo, S. Guo, L. Han, L. Hong, H.-L. Huang, Y.-H. Huo, L. Li, N. Li, S. Li, Y. Li, F. Liang, C. Lin, J. Lin, H. Qian, D. Qiao, H. Rong, H. Su, L. Sun, L. Wang, S. Wang, D. Wu, Y. Wu, Y. Xu, K. Yan, W. Yang, Y. Yang, Y. Ye, J. Yin, C. Ying, J. Yu, C. Zha, C. Zhang, H. Zhang, K. Zhang, Y. Zhang, H. Zhao, Y. Zhao, L. Zhou, C.-Y. Lu, C.-Z. Peng, X. Zhu, and J.-W. Pan, "Quantum computational advantage via 60-qubit 24-cycle random circuit sampling", Sci. Bull. **67**, 240 (2022).

[16] A. Bouland, B. Fefferman, C. Nirkhe, and U. Vazirani, "On the complexity and verification of quantum random circuit sampling", Nat. Phys. **15**, 159 (2018).

[17] F. Lardinois, "IBM unveils its 433 qubit Osprey quantum computer", TechCrunch (2022).

[18] J. Clarke and F. K. Wilhelm, "Superconducting quantum bits", Nature **453**, 1031 (2008).

[19] G. Burkard, M. J. Gullans, X. Mi, and J. R. Petta, "Superconductor-semiconductor hybrid-circuit quantum electrodynamics", Nat. Rev. Phys. **2**, 129 (2020).

[20] D. Loss and D. P. DiVincenzo, "Quantum computation with quantum dots", Phys. Rev. A **57**, 120 (1998).

[21] G. Burkard, T. D. Ladd, J. M. Nichol, A. Pan, and J. R. Petta, "Semiconductor spin qubits", Rev. Mod. Phys. **95**, 025003 (2023).

[22] D. P. DiVincenzo, "Quantum gates and circuits", Proc. R. Soc. Lond. A **454**, 261 (1998).

[23] D. P. DiVincenzo, "The physical implementation of quantum computation", Fortschr. Phys. **48**, 771 (2000).

[24] S. G. J. Philips, M. T. Mądzik, S. V. Amitonov, S. L. de Snoo, M. Russ, N. Kalhor, C. Volk, W. I. L. Lawrie, D. Brousse, L. Tryputen, B. P. Wuetz, A. Sammak, M. Veldhorst, G. Scappucci, and L. M. K. Vandersypen, "Universal control of a six-qubit quantum processor in silicon", Nature **609**, 919 (2022).

[25] N. W. Hendrickx, W. I. L. Lawrie, M. Russ, F. van Riggelen, S. L. de Snoo, R. N. Schouten, A. Sammak, G. Scappucci, and M. Veldhorst, "A four-qubit germanium quantum processor", Nature **591**, 580 (2021).

[26] X. Xue, M. Russ, N. Samkharadze, B. Undseth, A. Sammak, G. Scappucci, and L. M. K. Vandersypen, "Quantum logic with spin qubits crossing the surface code threshold", Nature **601**, 343 (2022).

[27] A. Noiri, K. Takeda, T. Nakajima, T. Kobayashi, A. Sammak, G. Scappucci, and S. Tarucha, "Fast universal quantum gate above the fault-tolerance threshold in silicon", Nature **601**, 338 (2022).

[28] A. R. Mills, C. R. Guinn, M. J. Gullans, A. J. Sigillito, M. M. Feldman, E. Nielsen, and J. R. Petta, "Two-qubit silicon quantum processor with operation fidelity exceeding 99%", Sci. Adv. **8**, eabn5130 (2022).

[29] R. Maurand, X. Jehl, D. Kotekar-Patil, A. Corna, H. Bohuslavskyi, R. Laviéville, L. Hutin, S. Barraud, M. Vinet, M. Sanquer, and S. D. Franceschi, "A CMOS silicon spin qubit", Nat. Commun. **7**, 13575 (2016).

[30] M. Veldhorst, H. G. J. Eenink, C. H. Yang, and A. S. Dzurak, "Silicon CMOS architecture for a spin-based quantum computer", Nat Commun. **8**, 1766 (2017).

[31] L. M. K. Vandersypen, H. Bluhm, J. S. Clarke, A. S. Dzurak, R. Ishihara, A. Morello, D. J. Reilly, L. R. Schreiber, and M. Veldhorst, "Interfacing spin qubits in quantum dots and donors—hot, dense, and coherent", npj Quantum Inf. **3**, 34 (2017).

[32] A. M. J. Zwerver, T. Krähenmann, T. F. Watson, L. Lampert, H. C. George, R. Pillarisetty, S. A. Bojarski, P. Amin, S. V. Amitonov, J. M. Boter, R. Caudillo, D. Correas-Serrano, J. P. Dehollain, G. Droulers, E. M. Henry, R. Kotlyar, M. Lodari, F. Lüthi, D. J. Michalak, B. K. Mueller, S. Neyens, J. Roberts, N. Samkharadze, G. Zheng, O. K. Zietz, G. Scappucci, M. Veldhorst, L. M. K. Vandersypen, and J. S. Clarke, "Qubits made by advanced semiconductor manufacturing", Nat. Electron. **5**, 184 (2022).

[33] L. Stadler, "Intel's new chip to advance silicon spin qubit research for quantum computing", Business Wire (2023).

[34] Y. Hu, H. O. H. Churchill, D. J. Reilly, J. Xiang, C. M. Lieber, and C. M. Marcus, "A Ge/Si heterostructure nanowire-based double quantum dot with integrated charge sensor", Nat. Nanotechnol. **2**, 622 (2007).

[35] H. Watzinger, J. Kukučka, L. Vukušić, F. Gao, T. Wang, F. Schäffler, J.-J. Zhang, and G. Katsaros, "A germanium hole spin qubit", Nat. Commun. **9**, 3902 (2018).

[36] F. N. M. Froning, M. J. Rančić, B. Hetényi, S. Bosco, M. K. Rehmann, A. Li, E. P. A. M. Bakkers, F. A. Zwanenburg, D. Loss, D. M. Zumbühl, and F. R. Braakman, "Strong spin-orbit interaction and g-factor renormalization of hole spins in Ge/Si nanowire quantum dots", Phys. Rev. Res. **3**, 013081 (2021).

[37] L. C. Camenzind, S. Geyer, A. Fuhrer, R. J. Warburton, D. M. Zumbühl, and A. V. Kuhlmann, "A hole spin qubit in a fin field-effect transistor above 4 kelvin", Nat. Electron. **5**, 178 (2022).

[38] A. Bracker, E. Stinaff, D. Gammon, M. Ware, J. Tischler, A. Shabaev, A. Efros, D. Park, D. Gershoni, V. Korenev, and I. Merkulov, "Optical pumping of the electronic and nuclear spin of single charge-tunable quantum dots", Phys. Rev. Lett. **94**, 047402 (2005).

[39] R. J. Warburton, "Single spins in self-assembled quantum dots", Nat. Mater. **12**, 483 (2013).

[40] J. Wrachtrup, S. Y. Kilin, and A. P. Nizovtsev, "Quantum computation using the ^{13}C nuclear spins near the single NV defect center in diamond", Opt. Spectrosc. **91**, 429 (2001).

[41] L. Childress and R. Hanson, "Diamond NV centers for quantum computing and quantum networks", MRS Bull. **38**, 134 (2013).

[42] J. R. Weber, W. F. Koehl, J. B. Varley, A. Janotti, B. B. Buckley, C. G. V. de Walle, and D. D. Awschalom, "Defects in SiC for quantum computing", J. Appl. Phys. **109**, 102417 (2011).

[43] B. Trauzettel, D. V. Bulaev, D. Loss, and G. Burkard, "Spin qubits in graphene quantum dots", Nat. Phys. **3**, 192 (2007).

[44] L. M. Gächter, R. Garreis, J. D. Gerber, M. J. Ruckriegel, C. Tong, B. Kratochwil, F. K. de Vries, A. Kurzmann, K. Watanabe, T. Taniguchi, T. Ihn, K. Ensslin, and W. W. Huang, "Single-shot spin readout in graphene quantum dots", PRX Quantum **3**, 020343 (2022).

[45] E. A. Laird, F. Pei, and L. P. Kouwenhoven, "A valley–spin qubit in a carbon nanotube", Nat. Nanotechnol. **8**, 565 (2013).

[46] Y. He, S. K. Gorman, D. Keith, L. Kranz, J. G. Keizer, and M. Y. Simmons, "A two-qubit gate between phosphorus donor electrons in silicon", Nature **571**, 371 (2019).

[47] A. Morello, J. J. Pla, F. A. Zwanenburg, K. W. Chan, K. Y. Tan, H. Huebl, M. Möttönen, C. D. Nugroho, C. Yang, J. A. van Donkelaar, A. D. C. Alves, D. N. Jamieson, C. C. Escott, L. C. L. Hollenberg, R. G. Clark, and A. S. Dzurak, "Single-shot readout of an electron spin in silicon", Nature **467**, 687 (2010).

[48] B. E. Kane, "A silicon-based nuclear spin quantum computer", Nature **393**, 133 (1998).

[49] J. R. Petta, A. C. Johnson, J. M. Taylor, E. A. Laird, A. Yacoby, M. D. Lukin, C. M. Marcus, M. P. Hanson, and A. C. Gossard, "Coherent manipulation of coupled electron spins in semiconductor quantum dots", Science **309**, 2180 (2005).

[50] J. Levy, "Universal quantum computation with spin-1/2 pairs and Heisenberg exchange", Phys. Rev. Lett. **89**, 147902 (2002).

[51] D. M. Zajac, T. M. Hazard, X. Mi, E. Nielsen, and J. R. Petta, "Scalable gate architecture for a one-dimensional array of semiconductor spin qubits", Phys. Rev. Appl. **6**, 054013 (2016).

[52] D. P. DiVincenzo, D. Bacon, J. Kempe, G. Burkard, and K. B. Whaley, "Universal quantum computation with the exchange interaction", Nature **408**, 339 (2000).

[53] Y.-P. Shim and C. Tahan, "Charge-noise-insensitive gate operations for always-on, exchange-only qubits", Phys. Rev. B **93**, 121410 (2016).

[54] M. Russ and G. Burkard, "Asymmetric resonant exchange qubit under the influence of electrical noise", Phys. Rev. B **91**, 235411 (2015).

[55] J. V. Koski, A. J. Landig, M. Russ, J. C. Abadillo-Uriel, P. Scarlino, B. Kratochwil, C. Reichl, W. Wegscheider, G. Burkard, M. Friesen, S. N. Coppersmith, A. Wallraff, K. Ensslin, and T. Ihn, "Strong photon coupling to the quadrupole moment of an electron in a solid-state qubit", Nat. Phys. **16**, 642 (2020).

[56] M. Friesen, J. Ghosh, M. A. Eriksson, and S. N. Coppersmith, "A decoherence-free subspace in a charge quadrupole qubit", Nat. Commun. **8**, 15923 (2017).

[57] X. Croot, X. Mi, S. Putz, M. Benito, F. Borjans, G. Burkard, and J. R. Petta, "Flopping-mode electric dipole spin resonance", Phys. Rev. Res. **2**, 012006(R) (2020).

[58] M. Benito, X. Croot, C. Adelsberger, S. Putz, X. Mi, J. R. Petta, and G. Burkard, "Electric-field control and noise protection of the flopping-mode spin qubit", Phys. Rev. B **100**, 125430 (2019).

[59] D. Kim, Z. Shi, C. B. Simmons, D. R. Ward, J. R. Prance, T. S. Koh, J. K. Gamble, D. E. Savage, M. G. Lagally, M. Friesen, S. N. Coppersmith, and M. A. Eriksson, "Quantum control and process tomography of a semiconductor quantum dot hybrid qubit", Nature **511**, 70 (2014).

[60] M. Russ, J. R. Petta, and G. Burkard, "Quadrupolar exchange-only spin qubit", Phys. Rev. Lett. **121**, 177701 (2018).

[61] J. Kyriakidis and G. Burkard, "Universal quantum computing with correlated spin-charge states", Phys. Rev. B **75**, 115324 (2007).

[62] L. J. Lauhon, M. S. Gudiksen, D. Wang, and C. M. Lieber, "Epitaxial core–shell and core–multishell nanowire heterostructures", Nature **420**, 57 (2002).

[63] Y. Hu, F. Kuemmeth, C. M. Lieber, and C. M. Marcus, "Hole spin relaxation in Ge-Si core-shell nanowire qubits", Nat. Nanotechnol. **7**, 47 (2011).

[64] C. Adelsberger, M. Benito, S. Bosco, J. Klinovaja, and D. Loss, "Hole-spin qubits in Ge nanowire quantum dots: interplay of orbital magnetic field, strain, and growth direction", Phys. Rev. B **105**, 075308 (2022).

[65] C. Adelsberger, S. Bosco, J. Klinovaja, and D. Loss, "Enhanced orbital magnetic field effects in Ge hole nanowires", Phys. Rev. B **106**, 235408 (2022).

[66] S. Bosco and D. Loss, "Hole spin qubits in thin curved quantum wells", Phys. Rev. Appl. **18**, 044038 (2022).

[67] S. Bosco, B. Hetényi, and D. Loss, "Hole spin qubits in si FinFETs with fully tunable spin-orbit coupling and sweet spots for charge noise", PRX Quantum **2**, 010348 (2021).

[68] M. T. Björk, C. Thelander, A. E. Hansen, L. E. Jensen, M. W. Larsson, L. R. Wallenberg, and L. Samuelson, "Few-electron quantum dots in nanowires", Nano Lett. **4**, 1621 (2004).

[69] F. A. Zwanenburg, A. A. van Loon, G. A. Steele, C. E. W. M. van Rijmenam, T. Balder, Y. Fang, C. M. Lieber, and L. P. Kouwenhoven, "Ultrasmall silicon quantum dots", J. Appl. Phys. **105**, 124314 (2009).

[70] J. Ridderbos, M. Brauns, F. K. de Vries, J. Shen, A. Li, S. Kölling, M. A. Verheijen, A. Brinkman, W. G. van der Wiel, E. P. A. M. Bakkers, and F. A. Zwanenburg, "Hard superconducting gap and diffusion-induced superconductors in Ge-Si nanowires", Nano Lett. **20**, 122 (2020).

[71] Y.-J. Doh, J. A. van Dam, A. L. Roest, E. P. A. M. Bakkers, L. P. Kouwenhoven, and S. D. Franceschi, "Tunable supercurrent through semiconductor nanowires", Science **309**, 272 (2005).

[72] C. Reeg, D. Loss, and J. Klinovaja, "Metallization of a Rashba wire by a superconducting layer in the strong-proximity regime", Phys. Rev. B **97**, 165425 (2018).

[73] C. Reeg, D. Loss, and J. Klinovaja, "Proximity effect in a two-dimensional electron gas coupled to a thin superconducting layer", Beilstein J. Nanotechnol. **9**, 1263 (2018).

[74] C. Adelsberger, H. F. Legg, D. Loss, and J. Klinovaja, "Microscopic analysis of proximity-induced superconductivity and metallization effects in superconductor-germanium hole nanowires", (2023), arXiv:2306.06944 [cond-mat.mes-hall].

[75] J. Ridderbos, M. Brauns, A. Li, E. P. A. M. Bakkers, A. Brinkman, W. G. van der Wiel, and F. A. Zwanenburg, "Multiple Andreev reflections and Shapiro steps in a Ge-Si nanowire Josephson junction", Phys. Rev. Mater. **3**, 084803 (2019).

[76] R. Hess, H. F. Legg, D. Loss, and J. Klinovaja, "Local and nonlocal quantum transport due to Andreev bound states in finite Rashba nanowires with superconducting and normal sections", Phys. Rev. B **104**, 075405 (2021).

[77] A. Y. Kitaev, "Unpaired Majorana fermions in quantum wires", Phys. Usp. **44**, 131 (2001).

[78] C. Nayak, S. H. Simon, A. Stern, M. Freedman, and S. Das Sarma, "Non-Abelian anyons and topological quantum computation", Rev. Mod. Phys. **80**, 1083 (2008).

[79] F. Maier, J. Klinovaja, and D. Loss, "Majorana fermions in Ge/Si hole nanowires", Phys. Rev. B **90**, 195421 (2014).

[80] K. Laubscher, J. D. Sau, and S. Das Sarma, "Majorana zero modes in gate-defined germanium hole nanowires", (2023), arXiv:2305.14313 [cond-mat.mes-hall].

[81] A. Laucht, F. Hohls, N. Ubbelohde, M. F. Gonzalez-Zalba, D. J. Reilly, S. Stobbe, T. Schröder, P. Scarlino, J. V. Koski, A. Dzurak, C.-H. Yang, J. Yoneda, F. Kuemmeth, H. Bluhm, J. Pla, C. Hill, J. Salfi, A. Oiwa, J. T. Muhonen, E. Verhagen, M. D. LaHaye, H. H. Kim, A. W. Tsen, D. Culcer, A. Geresdi, J. A. Mol, V. Mohan, P. K. Jain, and J. Baugh, "Roadmap on quantum nanotechnologies", Nanotechn. **32**, 162003 (2021).

[82] K. Itoh, W. Hansen, E. Haller, J. Farmer, V. Ozhogin, A. Rudnev, and A. Tikhomirov, "High purity isotopically enriched ^{70}Ge and ^{74}Ge single crystals: isotope separation, growth, and properties", J. Mater. Res. **8**, 1341 (1993).

[83] K. M. Itoh and H. Watanabe, "Isotope engineering of silicon and diamond for quantum computing and sensing applications", MRS Commun. **4**, 143 (2014).

[84] A. Sigillito, R. Jock, A. Tyryshkin, J. Beeman, E. Haller, K. Itoh, and S. Lyon, "Electron spin coherence of shallow donors in natural and isotopically enriched germanium", Phys. Rev. Lett. **115**, 247601 (2015).

[85] M. Myronov, J. Kycia, P. Waldron, W. Jiang, P. Barrios, A. Bogan, P. Coleridge, and S. Studenikin, "Holes outperform electrons in group IV semiconductor materials", Small Sci. **3**, 2200094 (2023).

[86] L. E. A. Stehouwer, A. Tosato, D. D. Esposti, D. Costa, M. Veldhorst, A. Sammak, and G. Scappucci, "Germanium wafers for strained quantum wells with low disorder", Appl. Phys. Lett. **123**, 092101 (2023).

[87] A. Sammak, D. Sabbagh, N. W. Hendrickx, M. Lodari, B. P. Wuetz, A. Tosato, L. Yeoh, M. Bollani, M. Virgilio, M. A. Schubert, P. Zaumseil, G. Capellini, M. Veldhorst, and G. Scappucci, "Shallow and undoped germanium quantum wells: a playground for spin and hybrid quantum technology", Adv. Funct. Mater. **29**, 1807613 (2019).

[88] M. Y. Melnikov, A. A. Shashkin, V. T. Dolgopolov, S.-H. Huang, C. W. Liu, and S. V. Kravchenko, "Ultra-high mobility two-dimensional electron gas in a SiGe/Si/SiGe quantum well", Appl.Phys. Lett. **106**, 092102 (2015).

[89] G. Scappucci, C. Kloeffel, F. A. Zwanenburg, D. Loss, M. Myronov, J.-J. Zhang, S. D. Franceschi, G. Katsaros, and M. Veldhorst, "The germanium quantum information route", Nat. Rev. Mater. **6**, 926 (2021).

[90] T. Tanttu, B. Hensen, K. W. Chan, C. H. Yang, W. W. Huang, M. Fogarty, F. Hudson, K. Itoh, D. Culcer, A. Laucht, A. Morello, and A. Dzurak, "Controlling spin-orbit interactions in silicon quantum dots using magnetic field direction", Phys. Rev. X **9**, 021028 (2019).

[91] R. Ruskov, M. Veldhorst, A. S. Dzurak, and C. Tahan, "Electron g-factor of valley states in realistic silicon quantum dots", Phys. Rev. B **98**, 245424 (2018).

[92] P. Harvey-Collard, N. T. Jacobson, C. Bureau-Oxton, R. M. Jock, V. Srinivasa, A. M. Mounce, D. R. Ward, J. M. Anderson, R. P. Manginell, J. R. Wendt, T. Pluym, M. P. Lilly, D. R. Luhman, M. Pioro-Ladrière, and M. S. Carroll, "Spin-orbit interactions for singlet-triplet qubits in silicon", Phys. Rev. Lett. **122**, 217702 (2019).

[93] A. Mills, C. Guinn, M. Feldman, A. Sigillito, M. Gullans, M. Rakher, J. Kerckhoff, C. Jackson, and J. Petta, "High-fidelity state preparation, quantum control, and readout of an isotopically enriched silicon spin qubit", Phys. Rev. Appl. **18**, 064028 (2022).

[94] C. Kloeffel, M. Trif, and D. Loss, "Strong spin-orbit interaction and helical hole states in Ge/Si nanowires", Phys. Rev. B **84**, 195314 (2011).

[95] C. Kloeffel, M. J. Rančić, and D. Loss, "Direct Rashba spin-orbit interaction in Si and Ge nanowires with different growth directions", Phys. Rev. B **97**, 235422 (2018).

[96] N. Piot, B. Brun, V. Schmitt, S. Zihlmann, V. P. Michal, A. Apra, J. C. Abadillo-Uriel, X. Jehl, B. Bertrand, H. Niebojewski, L. Hutin, M. Vinet, M. Urdampilleta, T. Meunier, Y.-M. Niquet, R. Maurand, and S. D. Franceschi, "A single hole spin with enhanced coherence in natural silicon", Nat. Nanotechnol. **17**, 1072 (2022).

[97] D. Jirovec, A. Hofmann, A. Ballabio, P. M. Mutter, G. Tavani, M. Botifoll, A. Crippa, J. Kukucka, O. Sagi, F. Martins, J. Saez-Mollejo, I. Prieto, M. Borovkov, J. Arbiol, D. Chrastina, G. Isella, and G. Katsaros, "A singlet-triplet hole spin qubit in planar Ge", Nat. Mater. **20**, 1106 (2021).

[98] A. Dimoulas, P. Tsipas, A. Sotiropoulos, and E. K. Evangelou, "Fermi-level pinning and charge neutrality level in germanium", Appl. Phys. Lett. **89**, 252110 (2006).

[99] R. R. Reeber and K. Wang, "Thermal expansion and lattice parameters of group IV semiconductors", Mater. Chem. Phys. **46**, 259 (1996).

[100] C. Kittel, *Introduction to solid state physics* (Wiley, New York, 2005).

[101] G. Feher, "Electron spin resonance experiments on donors in silicon. I. electronic structure of donors by the electron nuclear double resonance technique", Phys. Rev. **114**, 1219 (1959).

[102] R. Winkler, *Spin-orbit coupling effects in two-dimensional electron and hole systems* (Springer, Berlin, Oct. 10, 2003).

[103] R. Hanson, L. P. Kouwenhoven, J. R. Petta, S. Tarucha, and L. M. K. Vandersypen, "Spins in few-electron quantum dots", Rev. Mod. Phys. **79**, 1217 (2007).

[104] M. O. Nestoklon, E. L. Ivchenko, J.-M. Jancu, and P. Voisin, "Electric field effect on electron spin splitting in sige/si quantum wells", Phys. Rev. B **77**, 155328 (2008).

[105] E. A. Rodríguez-Mena, J. C. Abadillo-Uriel, G. Veste, B. Martinez, J. Li, B. Sklénard, and Y.-M. Niquet, "Linear-in-momentum spin orbit interactions in planar Ge/GeSi heterostructures and spin qubits", (2023), arXiv:2307.10007 [cond-mat.mes-hall].

[106] P. Y. Yu and M. Cardona, *Fundamentals of semiconductors: physics and materials properties, Physics and materials properties* (Springer, Berlin, Heidelberg, 2010).

[107] P.-O. Löwdin, "A note on the quantum-mechanical perturbation theory", J.Chem. Phys. **19**, 1396 (1951).

[108] J. M. Luttinger and W. Kohn, "Motion of electrons and holes in perturbed periodic fields", Phys. Rev. **97**, 869 (1955).

[109] J. C. Hensel, H. Hasegawa, and M. Nakayama, "Cyclotron resonance in uniaxially stressed silicon. II. nature of the covalent bond", Phys. Rev. **138**, A225 (1965).

[110] Z. Stanojevic, O. Baumgartner, V. Sverdlov, and H. Kosina, "Electronic band structure modeling in strained Si-nanowires: two band k·p versus tight binding", in 2010 14th international workshop on computational electronics (Oct. 2010).

[111] V. Sverdlov, G. Karlowatz, S. Dhar, H. Kosina, and S. Selberherr, "Two-band k·p model for the conduction band in silicon: impact of strain and confinement on band structure and mobility", Solid-State Electron. **52**, 1563 (2008).

[112] J. M. Luttinger, "Quantum theory of cyclotron resonance in semiconductors: general theory", Phys. Rev. **102**, 1030 (1956).

[113] P. Lawaetz, "Valence-band parameters in cubic semiconductors", Phys. Rev. B **4**, 3460 (1971).

[114] R. Winkler, D. Culcer, S. J. Papadakis, B. Habib, and M. Shayegan, "Spin orientation of holes in quantum wells", Semicond. Sci. Technol. **23**, 114017 (2008).

[115] G. L. Bir and G. E. Pikus, *Symmetry and strain-induced effects in semiconductors* (Wiley, New York, 1974).

[116] I. I. Rabi, "Space quantization in a gyrating magnetic field", Phys. Rev. **51**, 652 (1937).

[117] F. H. L. Koppens, C. Buizert, K. J. Tielrooij, I. T. Vink, K. C. Nowack, T. Meunier, L. P. Kouwenhoven, and L. M. K. Vandersypen, "Driven coherent oscillations of a single electron spin in a quantum dot", Nature **442**, 766 (2006).

[118] V. N. Golovach, M. Borhani, and D. Loss, "Electric-dipole-induced spin resonance in quantum dots", Phys. Rev. B **74**, 165319 (2006).

[119] K. C. Nowack, F. H. L. Koppens, Y. V. Nazarov, and L. M. K. Vandersypen, "Coherent control of a single electron spin with electric fields", Science **318**, 1430 (2007).

[120] E. Kawakami, P. Scarlino, D. R. Ward, F. R. Braakman, D. E. Savage, M. G. Lagally, M. Friesen, S. N. Coppersmith, M. A. Eriksson, and L. M. K. Vandersypen, "Electrical control of a long-lived spin qubit in a Si/SiGe quantum dot", Nat. Nanotechnol. **9**, 666 (2014).

[121] M. Pioro-Ladrière, T. Obata, Y. Tokura, Y.-S. Shin, T. Kubo, K. Yoshida, T. Taniyama, and S. Tarucha, "Electrically driven single-electron spin resonance in a slanting Zeeman field", Nat. Phys. **4**, 776 (2008).

[122] J. Yoneda, K. Takeda, T. Otsuka, T. Nakajima, M. R. Delbecq, G. Allison, T. Honda, T. Kodera, S. Oda, Y. Hoshi, N. Usami, K. M. Itoh, and S. Tarucha, "A quantum-dot spin qubit with coherence limited by charge noise and fidelity higher than 99.9%", Nat. Nanotechnol. **13**, 102 (2018).

[123] F. Bloch and A. Siegert, "Magnetic resonance for nonrotating fields", Phys.l Rev. **57**, 522 (1940).

[124] D. Zeuch, F. Hassler, J. J. Slim, and D. P. DiVincenzo, "Exact rotating wave approximation", Ann. Phys. **423**, 168327 (2020).

[125] C. H. Yang, K. W. Chan, R. Harper, W. Huang, T. Evans, J. C. C. Hwang, B. Hensen, A. Laucht, T. Tanttu, F. E. Hudson, S. T. Flammia, K. M. Itoh, A. Morello, S. D. Bartlett, and A. S. Dzurak, "Silicon qubit fidelities approaching incoherent noise limits via pulse engineering", Nat. Electron. **2**, 151 (2019).

[126] P. Scarlino, E. Kawakami, D. Ward, D. Savage, M. Lagally, M. Friesen, S. Coppersmith, M. Eriksson, and L. Vandersypen, "Second-harmonic coherent driving of a spin qubit in a Si/SiGe quantum dot", Phys. Rev. Lett. **115**, 106802 (2015).

[127] S. Bosco, S. Geyer, L. C. Camenzind, R. S. Eggli, A. Fuhrer, R. J. Warburton, D. M. Zumbühl, J. C. Egues, A. V. Kuhlmann, and D. Loss, "Phase driving hole spin qubits", (2023), arXiv:2303.03350 [cond-mat.mes-hall].

[128] K. Wang, G. Xu, F. Gao, H. Liu, R.-L. Ma, X. Zhang, Z. Wang, G. Cao, T. Wang, J.-J. Zhang, D. Culcer, X. Hu, H.-W. Jiang, H.-O. Li, G.-C. Guo, and G.-P. Guo, "Ultrafast coherent control of a hole spin qubit in a germanium quantum dot", Nat. Commun. **13**, 206 (2022).

[129] G. Burkard, D. Loss, and D. P. DiVincenzo, "Coupled quantum dots as quantum gates", Phys. Rev. B **59**, 2070 (1999).

[130] D. Stepanenko, M. Rudner, B. I. Halperin, and D. Loss, "Singlet-triplet splitting in double quantum dots due to spin-orbit and hyperfine interactions", Phys. Rev. B **85**, 075416 (2012).

[131] S. Geyer, B. Hetényi, S. Bosco, L. C. Camenzind, R. S. Eggli, A. Fuhrer, D. Loss, R. J. Warburton, D. M. Zumbühl, and A. V. Kuhlmann, "Two-qubit logic with anisotropic exchange in a fin field-effect transistor", (2022), arXiv:2212.02308 [cond-mat.mes-hall].

[132] D. A. Wharam, T. J. Thornton, R. Newbury, M. Pepper, H. Ahmed, J. E. F. Frost, D. G. Hasko, D. C. Peacock, D. A. Ritchie, and G. A. C. Jones, "One-dimensional transport and the quantisation of the ballistic resistance", J. Phys. C **21**, L209 (1988).

[133] B. J. van Wees, H. van Houten, C. W. J. Beenakker, J. G. Williamson, L. P. Kouwenhoven, D. van der Marel, and C. T. Foxon, "Quantized conductance of point contacts in a two-dimensional electron gas", Phys. Rev. Lett. **60**, 848 (1988).

[134] D. Sprinzak, Y. Ji, M. Heiblum, D. Mahalu, and H. Shtrikman, "Charge distribution in a kondo-correlated quantum dot", Phys. Rev. Lett. **88**, 176805 (2002).

[135] J. M. Elzerman, R. Hanson, J. S. Greidanus, L. H. W. van Beveren, S. D. Franceschi, L. M. K. Vandersypen, S. Tarucha, and L. P. Kouwenhoven, "Few-electron quantum dot circuit with integrated charge read out", Phys. Rev. B **67**, 161308 (2003).

[136] J. M. Elzerman, R. Hanson, L. H. W. van Beveren, B. Witkamp, L. M. K. Vandersypen, and L. P. Kouwenhoven, "Single-shot read-out of an individual electron spin in a quantum dot", Nature **430**, 431 (2004).

[137] D. Keith, Y. Chung, L. Kranz, B. Thorgrimsson, S. K. Gorman, and M. Y. Simmons, "Ramped measurement technique for robust high-fidelity spin qubit readout", Sci. Adv. **8**, eabq0455 (2022).

[138] D. Keith, S. K. Gorman, L. Kranz, Y. He, J. G. Keizer, M. A. Broome, and M. Y. Simmons, "Benchmarking high fidelity single-shot readout of semiconductor qubits", New J. Phys. **21**, 063011 (2019).

[139] T. Fujisawa, D. G. Austing, Y. Tokura, Y. Hirayama, and S. Tarucha, "Allowed and forbidden transitions in artificial hydrogen and helium atoms", Nature **419**, 278 (2002).

[140] N. W. Hendrickx, W. I. L. Lawrie, L. Petit, A. Sammak, G. Scappucci, and M. Veldhorst, "A single-hole spin qubit", Nat. Commun. **11**, 3478 (2020).

[141] B. M. Maune, M. G. Borselli, B. Huang, T. D. Ladd, P. W. Deelman, K. S. Holabird, A. A. Kiselev, I. Alvarado-Rodriguez, R. S. Ross, A. E. Schmitz, M. Sokolich, C. A. Watson, M. F. Gyure, and A. T. Hunter, "Coherent singlet-triplet oscillations in a silicon-based double quantum dot", Nature **481**, 344 (2012).

[142] D. Culcer, Ł. Cywiński, Q. Li, X. Hu, and S. D. Sarma, "Quantum dot spin qubits in silicon: multivalley physics", Phys. Rev. B **82**, 155312 (2010).

[143] K. D. Petersson, C. G. Smith, D. Anderson, P. Atkinson, G. A. C. Jones, and D. A. Ritchie, "Charge and spin state readout of a double quantum dot coupled to a resonator", Nano Lett. **10**, 2789 (2010).

[144] J. I. Colless, A. C. Mahoney, J. M. Hornibrook, A. C. Doherty, H. Lu, A. C. Gossard, and D. J. Reilly, "Dispersive readout of a few-electron double quantum dot with fast rf gate sensors", Phys. Rev. Lett. **110**, 046805 (2013).

[145] H. Mabuchi and A. C. Doherty, "Cavity quantum electrodynamics: coherence in context", Science **298**, 1372 (2002).

[146] R. Miller, T. E. Northup, K. M. Birnbaum, A. Boca, A. D. Boozer, and H. J. Kimble, "Trapped atoms in cavity QED: coupling quantized light and matter", J. Phys. B: At. Mol. Opt. Phys. **38**, S551 (2005).

[147] H. Walther, B. T. H. Varcoe, B.-G. Englert, and T. Becker, "Cavity quantum electrodynamics", Rep. Prog. Phys. **69**, 1325 (2006).

[148] A. Wallraff, D. I. Schuster, A. Blais, L. Frunzio, R. S. Huang, J. Majer, S. Kumar, S. M. Girvin, and R. J. Schoelkopf, "Strong coupling of a single photon to a superconducting qubit using circuit quantum electrodynamics", Nature **431**, 162 (2004).

[149] A. Blais, S. M. Girvin, and W. D. Oliver, "Quantum information processing and quantum optics with circuit quantum electrodynamics", Nat. Phys. **16**, 247 (2020).

[150] A. Blais, A. L. Grimsmo, S. Girvin, and A. Wallraff, "Circuit quantum electrodynamics", Rev. Mod. Phys. **93**, 025005 (2021).

[151] X. Mi, M. Benito, S. Putz, D. M. Zajac, J. M. Taylor, G. Burkard, and J. R. Petta, "A coherent spin-photon interface in silicon", Nature **555**, 599 (2018).

[152] A. J. Landig, J. V. Koski, P. Scarlino, U. C. Mendes, A. Blais, C. Reichl, W. Wegscheider, A. Wallraff, K. Ensslin, and T. Ihn, "Coherent spin-photon coupling using a resonant exchange qubit", Nature **560**, 179 (2018).

[153] N. Samkharadze, G. Zheng, N. Kalhor, D. Brousse, A. Sammak, U. C. Mendes, A. Blais, G. Scappucci, and L. M. K. Vandersypen, "Strong spin-photon coupling in silicon", Science **359**, 1123 (2018).

[154] T. Cubaynes, M. R. Delbecq, M. C. Dartiailh, R. Assouly, M. M. Desjardins, L. C. Contamin, L. E. Bruhat, Z. Leghtas, F. Mallet, A. Cottet, and T. Kontos, "Highly coherent spin states in carbon nanotubes coupled to cavity photons", npj Quantum Inf. **5**, 47 (2019).

[155] T. Bonsen, P. Harvey-Collard, M. Russ, J. Dijkema, A. Sammak, G. Scappucci, and L. M. K. Vandersypen, "Probing the Jaynes-Cummings ladder with spin circuit quantum electrodynamics", Phys. Rev. Lett. **130**, 137001 (2023).

[156] F. Borjans, X. Mi, and J. Petta, "Spin digitizer for high-fidelity readout of a cavity-coupled silicon triple quantum dot", Phys. Rev. Appl. **15**, 044052 (2021).

[157] A. Blais, R.-S. Huang, A. Wallraff, S. M. Girvin, and R. J. Schoelkopf, "Cavity quantum electrodynamics for superconducting electrical circuits: an architecture for quantum computation", Phys. Rev. A **69**, 062320 (2004).

[158] N. M. Linke, D. Maslov, M. Roetteler, S. Debnath, C. Figgatt, K. A. Landsman, K. Wright, and C. Monroe, "Experimental comparison of two quantum computing architectures", Proc. Natl. Acad. Sci. **114**, 3305 (2017).

[159] J. Emerson, R. Alicki, and K. Życzkowski, "Scalable noise estimation with random unitary operators", J. Opt. B: Quantum and Semiclass. Opt. **7**, S347 (2005).

[160] E. Magesan, J. M. Gambetta, and J. Emerson, "Characterizing quantum gates via randomized benchmarking", Phys. Rev. A **85**, 042311 (2012).

[161] S. T. Merkel, J. M. Gambetta, J. A. Smolin, S. Poletto, A. D. Córcoles, B. R. Johnson, C. A. Ryan, and M. Steffen, "Self-consistent quantum process tomography", Phys. Rev. A **87**, 062119 (2013).

[162] R. Blume-Kohout, J. K. Gamble, E. Nielsen, K. Rudinger, J. Mizrahi, K. Fortier, and P. Maunz, "Demonstration of qubit operations below a rigorous fault tolerance threshold with gate set tomography", Nat. Commun. **8**, 14485 (2017).

[163] E. Nielsen, J. K. Gamble, K. Rudinger, T. Scholten, K. Young, and R. Blume-Kohout, "Gate set tomography", Quantum **5**, 557 (2021).

[164] H.-P. Breuer and F. Petruccione, *The theory of open quantum systems* (Oxford University Press, Oxford, 2002).

[165] L. Chirolli and G. Burkard, "Decoherence in solid-state qubits", Adv. Phys. **57**, 225 (2008).

[166] P. Dutta, P. Dimon, and P. M. Horn, "Energy scales for noise processes in metals", Phys. Rev. Lett. **43**, 646 (1979).

[167] Y. Makhlin, G. Schön, and A. Shnirman, "Dissipative effects in Josephson qubits", Chem. Phys. **296**, 315 (2004).

[168] G. Ithier, E. Collin, P. Joyez, P. J. Meeson, D. Vion, D. Esteve, F. Chiarello, A. Shnirman, Y. Makhlin, J. Schriefl, and G. Schön, "Decoherence in a superconducting quantum bit circuit", Phys. Rev. B **72**, 134519 (2005).

[169] Ł. Cywiński, R. M. Lutchyn, C. P. Nave, and S. D. Sarma, "How to enhance dephasing time in superconducting qubits", Phys. Rev. B **77**, 174509 (2008).

[170] E. L. Hahn, "Spin echoes", Phys. Rev. **80**, 580 (1950).

[171] P. Stano and D. Loss, "Review of performance metrics of spin qubits in gated semiconducting nanostructures", Nat. Rev. Phys. **4**, 672 (2022).

[172] X. Hu, "Two-spin dephasing by electron-phonon interaction in semiconductor double quantum dots", Phys. Rev. B **83**, 165322 (2011).

[173] P. Dutta and P. M. Horn, "Low-frequency fluctuations in solids: $\frac{1}{f}$ noise", Rev. Mod. Phys. **53**, 497 (1981).

[174] E. J. Connors, J. Nelson, H. Qiao, L. F. Edge, and J. M. Nichol, "Low-frequency charge noise in Si/SiGe quantum dots", Phys. Rev. B **100**, 165305 (2019).

[175] L. S. Langsjoen, A. Poudel, M. G. Vavilov, and R. Joynt, "Qubit relaxation from evanescent-wave Johnson noise", Phys. Rev. A **86**, 010301 (2012).

[176] S. B. Tenberg, S. Asaad, M. T. Mądzik, M. A. I. Johnson, B. Joecker, A. Laucht, F. E. Hudson, K. M. Itoh, A. M. Jakob, B. C. Johnson, D. N. Jamieson, J. C. McCallum, A. S. Dzurak, R. Joynt, and A. Morello, "Electron spin relaxation of single phosphorus donors in metal-oxide-semiconductor nanoscale devices", Phys. Rev. B **99**, 205306 (2019).

[177] F. N. M. Froning, L. C. Camenzind, O. A. H. van der Molen, A. Li, E. P. A. M. Bakkers, D. M. Zumbühl, and F. R. Braakman, "Ultrafast hole spin qubit with gate-tunable spin-orbit switch functionality", Nat. Nanotechnol. **16**, 308 (2021).

[178] D. Vion, A. Aassime, A.Cottet, P. Joyez, H. Pothier, C. Urbina, D. Esteve, and M. H. Devoret, "Manipulating the quantum state of an electrical circuit", Science **296**, 886 (2002).

[179] K. D. Petersson, J. R. Petta, H. Lu, and A. C. Gossard, "Quantum coherence in a one-electron semiconductor charge qubit", Phys. Rev. Lett. **105**, 246804 (2010).

[180] Z. Wang, E. Marcellina, A. R. Hamilton, J. H. Cullen, S. Rogge, J. Salfi, and D. Culcer, "Optimal operation points for ultrafast, highly coherent Ge hole spin-orbit qubits", npj Quantum Inf. **7**, 54 (2021).

[181] W. A. Coish and D. Loss, "Hyperfine interaction in a quantum dot: Non-Markovian electron spin dynamics", Phys. Rev. B **70**, 195340 (2004).

[182] W. A. Coish and D. Loss, "Singlet-triplet decoherence due to nuclear spins in a double quantum dot", Phys. Rev. B **72**, 125337 (2005).

[183] M. T. Mądzik, T. D. Ladd, F. E. Hudson, K. M. Itoh, A. M. Jakob, B. C. Johnson, J. C. McCallum, D. N. Jamieson, A. S. Dzurak, A. Laucht, and A. Morello, "Controllable freezing of the nuclear spin bath in a single-atom spin qubit", Sci. Adv. **6**, eaba3442 (2020).

[184] T. D. Ladd, D. Maryenko, Y. Yamamoto, E. Abe, and K. M. Itoh, "Coherence time of decoupled nuclear spins in silicon", Phys. Rev. B **71**, 014401 (2005).

[185] D. J. Reilly, J. M. Taylor, J. R. Petta, C. M. Marcus, M. P. Hanson, and A. C. Gossard, "Exchange control of nuclear spin diffusion in a double quantum dot", Phys. Rev. Lett. **104**, 236802 (2010).

[186] J. Fischer, W. A. Coish, D. V. Bulaev, and D. Loss, "Spin decoherence of a heavy hole coupled to nuclear spins in a quantum dot", Phys. Rev. B **78**, 155329 (2008).

[187] J. Fischer and D. Loss, "Hybridization and spin decoherence in heavy-hole quantum dots", Phys. Rev. Lett. **105**, 266603 (2010).

[188] F. Maier and D. Loss, "Effect of strain on hyperfine-induced hole-spin decoherence in quantum dots", Phys. Rev. B **85**, 195323 (2012).

[189] S. Bosco and D. Loss, "Fully tunable hyperfine interactions of hole spin qubits in Si and Ge quantum dots", Phys. Rev. Lett. **127**, 190501 (2021).

[190] J. H. Prechtel, A. V. Kuhlmann, J. Houel, A. Ludwig, S. R. Valentin, A. D. Wieck, and R. J. Warburton, "Decoupling a hole spin qubit from the nuclear spins", Nat. Mater. **15**, 981 (2016).

[191] C. Testelin, F. Bernardot, B. Eble, and M. Chamarro, "Hole–spin dephasing time associated with hyperfine interaction in quantum dots", Phys. Rev. B **79**, 195440 (2009).

[192] D. Klauser, W. A. Coish, and D. Loss, "Nuclear spin state narrowing via gate-controlled Rabi oscillations in a double quantum dot", Phys. Rev. B **73**, 205302 (2006).

[193] F. A. Zwanenburg, A. S. Dzurak, A. Morello, M. Y. Simmons, L. C. L. Hollenberg, G. Klimeck, S. Rogge, S. N. Coppersmith, and M. A. Eriksson, "Silicon quantum electronics", Rev. Mod. Phys. **85**, 961 (2013).

[194] C. Tahan and R. Joynt, "Relaxation of excited spin, orbital, and valley qubit states in ideal silicon quantum dots", Phys. Rev. B **89**, 075302 (2014).

[195] F. Maier, C. Kloeffel, and D. Loss, "Tunable g factor and phonon-mediated hole spin relaxation in Ge/Si nanowire quantum dots", Phys. Rev. B **87**, 161305(R) (2013).

[196] J. Li, B. Venitucci, and Y.-M. Niquet, "Hole-phonon interactions in quantum dots: effects of phonon confinement and encapsulation materials on spin-orbit qubits", Phys. Rev. B **102**, 075415 (2020).

[197] V. Kornich, C. Kloeffel, and D. Loss, "Phonon-mediated decay of singlet-triplet qubits in double quantum dots", Phys. Rev. B **89**, 085410 (2014).

[198] D. M. Zajac, A. J. Sigillito, M. Russ, F. Borjans, J. M. Taylor, G. Burkard, and J. R. Petta, "Resonantly driven CNOT gate for electron spins", Science **359**, 439 (2018).

[199] C. H. Yang, A. Rossi, R. Ruskov, N. S. Lai, F. A. Mohiyaddin, S. Lee, C. Tahan, G. Klimeck, A. Morello, and A. S. Dzurak, "Spin-valley lifetimes in a silicon quantum dot with tunable valley splitting", Nat. Commun. **4**, 2069 (2013).

[200] N. W. Hendrickx, D. P. Franke, A. Sammak, G. Scappucci, and M. Veldhorst, "Fast two-qubit logic with holes in germanium", Nature **577**, 487 (2020).

[201] P. Stano and J. Fabian, "Orbital and spin relaxation in single and coupled quantum dots", Phys. Rev. B **74**, 045320 (2006).

[202] P. Huang and X. Hu, "Spin relaxation in a Si quantum dot due to spin-valley mixing", Phys. Rev. B **90**, 235315 (2014).

[203] N. E. Penthorn, J. S. Schoenfield, L. F. Edge, and H. Jiang, "Direct measurement of electron intervalley relaxation in a Si/Si-Ge quantum dot", Phys. Rev. Appl. **14**, 054015 (2020).

[204] N. W. Hendrickx, D. P. Franke, A. Sammak, M. Kouwenhoven, D. Sabbagh, L. Yeoh, R. Li, M. L. V. Tagliaferri, M. Virgilio, G. Capellini, G. Scappucci, and M. Veldhorst, "Gate-controlled quantum dots and superconductivity in planar germanium", Nat. Commun. **9**, 2835 (2018).

[205] J. Ridderbos, M. Brauns, J. Shen, F. K. de Vries, A. Li, E. P. A. M. Bakkers, A. Brinkman, and F. A. Zwanenburg, "Josephson effect in a few-hole quantum dot", Adv. Mater **30**, 1802257 (2018).

[206] N. W. Hendrickx, M. L. V. Tagliaferri, M. Kouwenhoven, R. Li, D. P. Franke, A. Sammak, A. Brinkman, G. Scappucci, and M. Veldhorst, "Ballistic supercurrent discretization and micrometer-long Josephson coupling in germanium", Phys. Rev. B **99**, 075435 (2019).

[207] F. Vigneau, R. Mizokuchi, D. C. Zanuz, X. Huang, S. Tan, R. Maurand, S. Frolov, A. Sammak, G. Scappucci, F. Lefloch, and S. D. Franceschi, "Germanium quantum-well Josephson field-effect transistors and interferometers", Nano Lett. **19**, 1023 (2019).

[208] K. Aggarwal, A. Hofmann, D. Jirovec, I. Prieto, A. Sammak, M. Botifoll, S. Martí-Sánchez, M. Veldhorst, J. Arbiol, G. Scappucci, J. Danon, and G. Katsaros, "Enhancement of proximity-induced superconductivity in a planar Ge hole gas", Phys. Rev. Res. **3**, L022005 (2021).

[209] A. Tosato, V. Levajac, J.-Y. Wang, C. J. Boor, F. Borsoi, M. Botifoll, C. N. Borja, S. Martí-Sánchez, J. Arbiol, A. Sammak, M. Veldhorst, and G. Scappucci, "Hard superconducting gap in germanium", Commun. Mater. **4**, 23 (2023).

[210] E. Zhuo, Z. Lyu, X. Sun, A. Li, B. Li, Z. Ji, J. Fan, E. Bakkers, X. Han, X. Song, F. Qu, G. Liu, J. Shen, and L. Lu, "Hole-type superconducting gatemon qubit based on Ge/Si core/shell nanowires", npj Quantum Inf. **9**, 51 (2023).

[211] W. Chang, S. M. Albrecht, T. S. Jespersen, F. Kuemmeth, P. Krogstrup, J. Nygård, and C. M. Marcus, "Hard gap in epitaxial semiconductor-superconductor nanowires", Nat. Nanotechnol. **10**, 232 (2015).

[212] M. Kjaergaard, F. Nichele, H. J. Suominen, M. P. Nowak, M. Wimmer, A. R. Akhmerov, J. A. Folk, K. Flensberg, J. Shabani, C. J. Palmstrøm, and C. M. Marcus, "Quantized conductance doubling and hard gap in a two-dimensional semiconductor-superconductor heterostructure", Nat. Commun. **7**, 12841 (2016).

[213] A. Fornieri, A. M. Whiticar, F. Setiawan, E. Portolés, A. C. C. Drachmann, A. Keselman, S. Gronin, C. Thomas, T. Wang, R. Kallaher, G. C. Gardner, E. Berg, M. J. Manfra, A. Stern, C. M. Marcus, and F. Nichele, "Evidence of topological superconductivity in planar Josephson junctions", Nature **569**, 89 (2019).

[214] E. J. H. Lee, X. Jiang, M. Houzet, R. Aguado, C. M. Lieber, and S. D. Franceschi, "Spin-resolved Andreev levels and parity crossings in hybrid superconductor-semiconductor nanostructures", Nat. Nanotechnol. **9**, 79 (2014).

[215] S. Park and A. L. Yeyati, "Andreev spin qubits in multichannel Rashba nanowires", Phys. Rev. B **96**, 125416 (2017).

[216] M. Hays, V. Fatemi, D. Bouman, J. Cerrillo, S. Diamond, K. Serniak, T. Connolly, P. Krogstrup, J. Nygård, A. L. Yeyati, A. Geresdi, and M. H. Devoret, "Coherent manipulation of an Andreev spin qubit", Science **373**, 430 (2021).

[217] K. D. Petersson, L. W. McFaul, M. D. Schroer, M. Jung, J. M. Taylor, A. A. Houck, and J. R. Petta, "Circuit quantum electrodynamics with a spin qubit", Nature **490**, 380 (2012).

[218] M. Leijnse and K. Flensberg, "Coupling spin qubits via superconductors", Phys. Rev. Lett. **111**, 060501 (2013).

[219] T. W. Larsen, K. D. Petersson, F. Kuemmeth, T. S. Jespersen, P. Krogstrup, J. Nygård, and C. M. Marcus, "Semiconductor-nanowire-based superconducting qubit", Phys. Rev. Lett. **115**, 127001 (2015).

[220] J. Xiang, A. Vidan, M. Tinkham, R. M. Westervelt, and C. M. Lieber, "Ge/Si nanowire mesoscopic Josephson junctions", Nat. Nanotechnol. **1**, 208 (2006).

[221] L. Casparis, M. R. Connolly, M. Kjaergaard, N. J. Pearson, A. Kringhøj, T. W. Larsen, F. Kuemmeth, T. Wang, C. Thomas, S. Gronin, G. C. Gardner, M. J. Manfra, C. M. Marcus, and K. D. Petersson, "Superconducting gatemon qubit based on a proximitized two-dimensional electron gas", Nat. Nanotechnol. **13**, 915 (2018).

[222] T. W. Larsen, M. E. Gershenson, L. Casparis, A. Kringhøj, N. J. Pearson, R. P. G. McNeil, F. Kuemmeth, P. Krogstrup, K. D. Petersson, and C. M. Marcus, "Parity-protected superconductor-semiconductor qubit", Phys. Rev. Lett. **125**, 056801 (2020).

[223] R. M. Lutchyn, E. P. A. M. Bakkers, L. P. Kouwenhoven, P. Krogstrup, C. M. Marcus, and Y. Oreg, "Majorana zero modes in superconductor-semiconductor heterostructures", Nat. Rev. Mater. **3**, 52 (2018).

[224] W. S. Cole, S. Das Sarma, and T. D. Stanescu, "Effects of large induced superconducting gap on semiconductor Majorana nanowires", Phys. Rev. B **92**, 174511 (2015).

[225] T. D. Stanescu and S. Das Sarma, "Proximity-induced low-energy renormalization in hybrid semiconductor-superconductor Majorana structures", Phys. Rev. B **96**, 014510 (2017).

[226] C. Reeg and D. L. Maslov, "Transport signatures of topological superconductivity in a proximity-coupled nanowire", Phys. Rev. B **95**, 205439 (2017).

[227] C. Reeg, D. Loss, and J. Klinovaja, "Finite-size effects in a nanowire strongly coupled to a thin superconducting shell", Phys. Rev. B **96**, 125426 (2017).

[228] N. M. Chtchelkatchev and Y. V. Nazarov, "Andreev quantum dots for spin manipulation", Phys. Rev. Lett. **90**, 226806 (2003).

[229] C. Padurariu and Y. V. Nazarov, "Theoretical proposal for superconducting spin qubits", Phys. Rev. B **81**, 144519 (2010).

[230] M.-S. Choi, C. Bruder, and D. Loss, "Spin-dependent Josephson current through double quantum dots and measurement of entangled electron states", Phys. Rev. B **62**, 13569 (2000).

[231] K. L. Hur, P. Recher, É. Dupont, and D. Loss, "Mesoscopic resonating valence bond system on a triple dot", Phys. Rev. Lett. **96**, 106803 (2006).

[232] F. Hassler, G. Catelani, and H. Bluhm, "Exchange interaction of two spin qubits mediated by a superconductor", Phys. Rev. B **92**, 235401 (2015).

[233] L. G. Rosado, F. Hassler, and G. Catelani, "Long-range exchange interaction between spin qubits mediated by a superconducting link at finite magnetic field", Phys. Rev. B **103**, 035430 (2021).

[234] M. Spethmann, X.-P. Zhang, J. Klinovaja, and D. Loss, "Coupled superconducting spin qubits with spin-orbit interaction", Phys. Rev. B **106**, 115411 (2022).

[235] G. E. Blonder, M. Tinkham, and T. M. Klapwijk, "Transition from metallic to tunneling regimes in superconducting microconstrictions: excess current, charge imbalance, and supercurrent conversion", Phys. Rev. B **25**, 4515 (1982).

[236] A. F. Andreev, "Thermal conductivity of the intermediate state of superconductors", Sov. Phys. JETP **19**, 1228 (1964).

[237] A. F. Andreev, "Electron spectrum of the intermediate state of superconductors", Sov. Phys. JETP **22**, 18 (1966).

[238] J. A. Sauls, "Andreev bound states and their signatures", Phil. Trans. R. Soc. A **376**, 20180140 (2018).

[239] E. Prada, P. San-Jose, M. W. A. de Moor, A. Geresdi, E. J. H. Lee, J. Klinovaja, D. Loss, J. Nygård, R. Aguado, and L. P. Kouwenhoven, "From Andreev to Majorana bound states in hybrid superconductor–semiconductor nanowires", Nat. Rev. Phys. **2**, 575 (2020).

[240] C. W. J. Beenakker, "Three "universal" mesoscopic josephson effects", Proc. 14th Taniguchi Symposium, 235 (1992).

[241] B. Josephson, "Possible new effects in superconductive tunnelling", Phys. Lett. **1**, 251 (1962).

[242] B. Josephson, "Supercurrents through barriers", Adv. Phys. **14**, 419 (1965).

[243] C. Caroli, P. D. Gennes, and J. Matricon, "Bound Fermion states on a vortex line in a type II superconductor", Phys. Lett. **9**, 307 (1964).

[244] L. Yu, "Bound state in superconductors with paramagnetic impurities", Acta Phys. Sin. **21**, 75 (1965).

[245] H. Shiba, "Classical spins in superconductors", Prog. Theor. Phys. **40**, 435 (1968).

[246] A. I. Rusinov, "Superconductivity near a paramagnetic impurity", Sov. Phys. JETP **9** (1969).

[247] K. Laubscher and J. Klinovaja, "Majorana bound states in semiconducting nanostructures", J. Appl. Phys. **130**, 081101 (2021).

[248] E. Lieb, T. Schultz, and D. Mattis, "Two soluble models of an antiferromagnetic chain", Ann. Phys. **16**, 407 (1961).

[249] R. M. Lutchyn, J. D. Sau, and S. Das Sarma, "Majorana fermions and a topological phase transition in semiconductor-superconductor heterostructures", Phys. Rev. Lett. **105**, 077001 (2010).

[250] Y. Oreg, G. Refael, and F. von Oppen, "Helical liquids and Majorana bound states in quantum wires", Phys. Rev. Lett. **105**, 177002 (2010).

[251] J. D. Sau, S. Tewari, R. M. Lutchyn, T. D. Stanescu, and S. Das Sarma, "Non-Abelian quantum order in spin-orbit-coupled semiconductors: search for topological Majorana particles in solid-state systems", Phys. Rev. B **82**, 214509 (2010).

[252] T. D. Stanescu, R. M. Lutchyn, and S. D. Sarma, "Majorana fermions in semiconductor nanowires", Phys. Rev. B **84**, 144522 (2011).

[253] J. Alicea, "New directions in the pursuit of Majorana fermions in solid state systems", Rep. Prog. Phys. **75**, 076501 (2012).

[254] V. Mourik, K. Zuo, S. M. Frolov, S. R. Plissard, E. P. A. M. Bakkers, and L. P. Kouwenhoven, "Signatures of Majorana fermions in hybrid superconductor-semiconductor nanowire devices", Science **336**, 1003 (2012).

[255] A. Das, Y. Ronen, Y. Most, Y. Oreg, M. Heiblum, and H. Shtrikman, "Zero-bias peaks and splitting in an Al–InAs nanowire topological superconductor as a signature of Majorana fermions", Nat. Phys. **8**, 887 (2012).

[256] L. P. Rokhinson, X. Liu, and J. K. Furdyna, "The fractional a.c. Josephson effect in a semiconductor–superconductor nanowire as a signature of Majorana particles", Nat. Phys. **8**, 795 (2012).

[257] M. T. Deng, C. L. Yu, G. Y. Huang, M. Larsson, P. Caroff, and H. Q. Xu, "Anomalous zero-bias conductance peak in a Nb–InSb nanowire–Nb hybrid device", Nano Lett **12**, 6414 (2012).

[258] J. R. Williams, A. J. Bestwick, P. Gallagher, S. S. Hong, Y. Cui, A. S. Bleich, J. G. Analytis, I. R. Fisher, and D. Goldhaber-Gordon, "Unconventional Josephson effect in hybrid superconductor-topological insulator devices", Phys. Rev. Lett. **109**, 056803 (2012).

[259] H. O. H. Churchill, V. Fatemi, K. Grove-Rasmussen, M. T. Deng, P. Caroff, H. Q. Xu, and C. M. Marcus, "Superconductor-nanowire devices from tunneling to the multichannel regime: zero-bias oscillations and magnetoconductance crossover", Phys. Rev. B **87**, 241401 (2013).

[260] G. Kells, D. Meidan, and P. W. Brouwer, "Near-zero-energy end states in topologically trivial spin-orbit coupled superconducting nanowires with a smooth confinement", Phys. Rev. B **86**, 100503 (2012).

[261] E. J. H. Lee, X. Jiang, R. Aguado, G. Katsaros, C. M. Lieber, and S. D. Franceschi, "Zero-bias anomaly in a nanowire quantum dot coupled to superconductors", Phys. Rev. Lett. **109**, 186802 (2012).

[262] J. Cayao, E. Prada, P. San-Jose, and R. Aguado, "SNS junctions in nanowires with spin-orbit coupling: role of confinement and helicity on the subgap spectrum", Phys. Rev. B **91**, 024514 (2015).

[263] C.-X. Liu, J. D. Sau, T. D. Stanescu, and S. D. Sarma, "Andreev bound states versus Majorana bound states in quantum dot-nanowire-superconductor hybrid structures: trivial versus topological zero-bias conductance peaks", Phys. Rev. B **96**, 075161 (2017).

[264] C. Reeg, O. Dmytruk, D. Chevallier, D. Loss, and J. Klinovaja, "Zero-energy Andreev bound states from quantum dots in proximitized Rashba nanowires", Phys. Rev. B **98**, 245407 (2018).

[265] C. Jünger, R. Delagrange, D. Chevallier, S. Lehmann, K. A. Dick, C. Thelander, J. Klinovaja, D. Loss, A. Baumgartner, and C. Schönenberger, "Magnetic-field-independent subgap states in hybrid Rashba nanowires", Phys. Rev. Lett. **125**, 017701 (2020).

[266] M. Valentini, F. Peñaranda, A. Hofmann, M. Brauns, R. Hauschild, P. Krogstrup, P. San-Jose, E. Prada, R. Aguado, and G. Katsaros, "Nontopological zero-bias peaks in full-shell nanowires induced by flux-tunable Andreev states", Science **373**, 82 (2021).

[267] I. J. Califrer, P. H. Penteado, J. C. Egues, and W. Chen, "Proximity-induced zero-energy states indistinguishable from topological edge states", Phys. Rev. B **107**, 045401 (2023).

[268] D. I. Pikulin, B. van Heck, T. Karzig, E. A. Martinez, B. Nijholt, T. Laeven, G. W. Winkler, J. D. Watson, S. Heedt, M. Temurhan, V. Svidenko, R. M. Lutchyn, M. Thomas, G. de Lange, L. Casparis, and C. Nayak, "Protocol to identify a topological superconducting phase in a three-terminal device", (2021), arXiv:2103.12217 [cond-mat.mes-hall].

[269] M. Aghaee, A. Akkala, Z. Alam, R. Ali, A. A. Ramirez, M. Andrzejczuk, A. E. Antipov, P. Aseev, M. Astafev, B. Bauer, J. Becker, S. Boddapati, F. Boekhout, J. Bommer, T. Bosma, L. Bourdet, S. Boutin, P. Caroff, L. Casparis, M. Cassidy, S. Chatoor, A. W. Christensen, N. Clay, W. S. Cole, F. Corsetti, A. Cui, P. Dalampiras, A. Dokania, G. de Lange, M. de Moor, J. C. E. Saldaña, S. Fallahi, Z. H. Fathabad, J. Gamble, G. Gardner, D. Govender, F. Griggio, R. Grigoryan, S. Gronin, J. Gukelberger, E. B. Hansen, S. Heedt, J. H. Zamorano, S. Ho, U. L. Holgaard, H. Ingerslev, L. Johansson, J. Jones, R. Kallaher, F. Karimi, T. Karzig, C. King, M. E. Kloster, C. Knapp, D. Kocon, J. Koski, P. Kostamo, P. Krogstrup, M. Kumar, T. Laeven, T. Larsen, K. Li, T. Lindemann, J. Love, R. Lutchyn, M. H. Madsen, M. Manfra, S. Markussen, E. Martinez, R. McNeil, E. Memisevic, T. Morgan, A. Mullally, C. Nayak, J. Nielsen, W. H. P. Nielsen, B. Nijholt, A. Nurmohamed, E. O'Farrell, K. Otani, S. Pauka, K. Petersson, L. Petit, D. I. Pikulin, F. Preiss, M. Quintero-Perez, M. Rajpalke, K. Rasmussen, D. Razmadze, O. Reentila, D. Reilly, R. Rouse, I. Sadovskyy, L. Sainiemi, S. Schreppler, V. Sidorkin, A. Singh, S. Singh, S. Sinha, P. Sohr, T. Stankevič, L. Stek, H. Suominen, J. Suter, V. Svidenko, S. Teicher, M. Temuerhan, N. Thiyagarajah, R. Tholapi, M. Thomas, E. Toomey, S. Upadhyay, I. Urban, S. Vaitiekėnas, K. V. Hoogdalem, D. V. Woerkom, D. V. Viazmitinov, D. Vogel, S. Waddy, J. Watson, J. Weston, G. W. Winkler, C. K. Yang, S. Yau, D. Yi, E. Yucelen, A. Webster, R. Zeisel, and R. Z. and, "InAs-Al hybrid devices passing the topological gap protocol", Phys. Rev. B **107**, 245423 (2023).

[270] R. Hess, H. F. Legg, D. Loss, and J. Klinovaja, "Trivial Andreev band mimicking topological bulk gap reopening in the nonlocal conductance of long Rashba nanowires", Phys. Rev. Lett. **130**, 207001 (2023).

[271] C. Beenakker, "Search for Majorana fermions in superconductors", Annu. Rev. Condens. Matt. Phys. **4**, 113 (2013).

[272] F. Hassler, A. R. Akhmerov, C.-Y. Hou, and C. W. J. Beenakker, "Anyonic interferometry without anyons: how a flux qubit can read out a topological qubit", New J. Phys. **12**, 125002 (2010).

[273] M. Leijnse and K. Flensberg, "Quantum information transfer between topological and spin qubit systems", Phys. Rev. Lett. **107**, 210502 (2011).

[274] J. D. Sau, S. Tewari, and S. D. Sarma, "Universal quantum computation in a semiconductor quantum wire network", Phys.Rev. A **82**, 052322 (2010).

[275] A. Kitaev, "Fault-tolerant quantum computation by anyons", Annals of Physics **303**, 2 (2003).

[276] J. D. Sau, S. Tewari, and S. D. Sarma, "Experimental and materials considerations for the topological superconducting state in electron- and hole-doped semiconductors: searching for non-Abelian Majorana modes in 1D nanowires and 2D heterostructures", Phys. Rev. B **85**, 064512 (2012).

CHAPTER 2

Hole-spin qubits in Ge nanowire quantum dots: Interplay of orbital magnetic field, strain, and growth direction

Adapted from:
Christoph Adelsberger, Mónica Benito, Stefano Bosco, Jelena Klinovaja, and Daniel Loss
"Hole-spin qubits in Ge nanowire quantum dots: Interplay of orbital magnetic field, strain, and growth direction",
Phys. Rev. B **105**, 075308 (2022)

Hole-spin qubits in quasi-one-dimensional structures are a promising platform for quantum information processing because of the strong spin-orbit interaction (SOI). We present analytical results and discuss device designs that optimize the SOI in Ge semiconductors. We show that at the magnetic field values at which qubits are operated, orbital effects of magnetic fields can strongly affect the response of the spin qubit. We study one-dimensional hole systems in Ge under the influence of electric and magnetic fields applied perpendicular to the device. In our theoretical description, we include these effects exactly. The orbital effects lead to a strong renormalization of the g factor. We find a sweet spot of the nanowire (NW) g factor where charge noise is strongly suppressed and present an effective low-energy model that captures the dependence of the SOI on the electromagnetic fields. Moreover, we compare properties of NWs with square and circular cross sections with ones of gate-defined one-dimensional channels in two-dimensional Ge heterostructures. Interestingly, the effective model predicts a flat band ground state for fine-tuned electric and magnetic fields. By considering a quantum dot (QD) harmonically confined by gates, we demonstrate that the NW g-factor sweet spot is retained in the QD. Our calculations reveal that this sweet spot can be designed to coincide with the maximum of the SOI, yielding highly coherent qubits with large Rabi frequencies. We also study the effective g factor of NWs grown along different high-symmetry axes and find that our model derived for isotropic semiconductors is valid for the most relevant growth directions of nonisotropic Ge NWs. Moreover, a NW grown

along one of the three main crystallographic axes shows the largest SOI. Our results show that the isotropic approximation is not justified in Ge in all cases.

2.1 Introduction

Important challenges of the scalability of spin qubits defined in quantum dots (QD) [1] can be overcome by making qubits electrically controllable. In the case of electrons, one can take advantage of the small intrinsic spin-orbit interaction (SOI) [2] or gradients of magnetic field [3–8]. The physics of hole spins in semiconductors such as germanium [9] and silicon [10] has attracted much attention recently because it naturally enables stronger SOI than in electron systems [11–21], which allows for the realization of electrically controlled single- [18–20, 22] and two-qubit [21] gates. Furthermore, strong natural SOI or artificial SOI due to micro-magnets enables strong light-matter coupling to resonators [23–31]. Recent progress with Ge/SiGe heterostructures was made by demonstrating singlet-triplet encoding [32] and a four-qubit quantum processor [9]. While we focus on nanowires (NWs) in this work, our approach also holds for planar heterostructures with electrostatically defined channels. Another great advantage of hole spins is their tunable response to the hyperfine interactions [33–38], a major decoherence channel in spin qubits [39–44], which can be made far weaker than in electron QDs [45, 46]. Furthermore, in Si and Ge, the hyperfine interactions can also be minimized by isotopically purifying the material [47, 48]. The effective low-dimensional physics of hole systems depends strongly on the details of the confinement, the material strain, and the applied electromagnetic fields [11, 12, 46, 49–54]. In particular, the strongest SOI, enabling the fastest and most power-efficient operations, is reached in quasi-one-dimensional structures, which can be fabricated in different ways [11, 19, 52].

To define spin qubits, a magnetic field is necessary to energetically split different spin states. When a magnetic field is applied perpendicular to the axis of a one-dimensional NW, the magnetic orbital effects can strongly influence the performance of the qubit. In two-dimensional heterostructures with a magnetic field applied in plane, the influence of these orbital effects strongly depends on the width of the two-dimensional electron or hole gas. In this case one can observe a correction of the g factor [55] and a renormalization of the effective mass [56] depending on the design of the dot.

In this work, we analyze the SOI, the effective g factor, and the effective mass of the lowest-energy states in NWs with rectangular or circular cross section and in squeezed planar heterostructures. We compare different designs and fully account for the orbital effects in a moderate magnetic and electric field. In contrast to Ref. [11], we use here a different basis which allows us to treat these orbital effects exactly in our analytical calculations. Interestingly, we predict that, where the SOI is maximal, the g factor can be fine-tuned to be in a sweet spot at which the charge noise is negligible. Similar sweet spots have been predicted in Ref. [57] in hole systems possessing a SOI that is cubic in momentum. In these systems, because of the cubic SOI, the Rabi frequency in electric-dipole-induced spin resonance (EDSR) experiments is predicted to be two orders of magnitude smaller than in elongated QDs [52]. Furthermore, we find that the effective masses of the low-energy holes depend strongly on both electric and magnetic fields and become spin-dependent at finite magnetic fields. Interestingly, in an extreme case, the lowest-energy band can be tuned to be flat. We envision that this flatness potentially could promote hole NWs as a new playground for simulating strongly correlated matter. Also, by extending our analysis to include the cubic anisotropies of the valence band, we find that these corrections can strongly affect the g factor for certain growth directions of the NW, especially in the presence of strain.

This work is structured as follows. In Sec. 2.2 we introduce the model of low-energy holes. In Sec. 2.3 we focus on a NW with rectangular cross section and calculate the SOI that is linear in momentum and of the direct Rashba type due to strong heavy-hole (HH)-light-hole (LH) mixing [11, 12]. First, we derive analytic expressions for the dependence of the SOI on external electric fields with and without magnetic orbital effects and compare them with numerical results. The

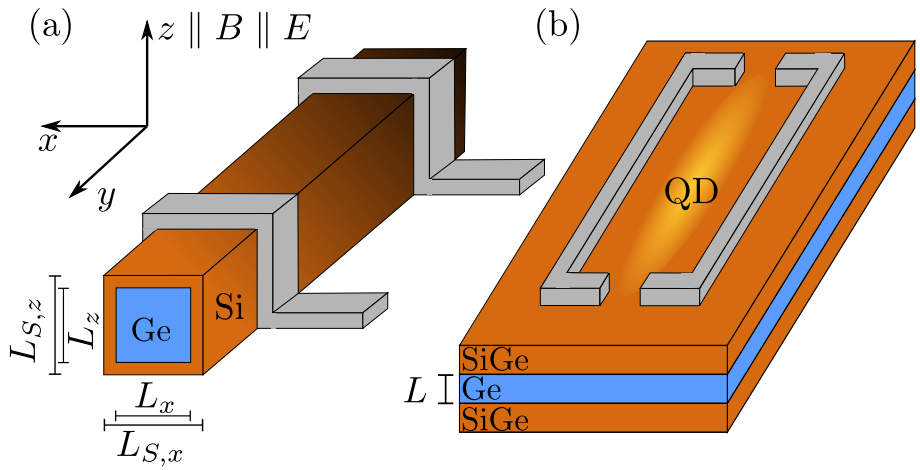

Figure 2.1: (a) Sketch of a rectangular Ge NW with side lengths L_x and L_z. The NW can be covered by a Si shell which induces strain in the Ge core. The NW including shell has total side lengths $L_{S,x}$ and $L_{S,z}$. The gates (gray) can be used to apply electric fields and to define an elongated QD. (b) Sketch of a planar Ge/SiGe heterostructure with a gate-defined one-dimensional channel. The height of the Ge layer in the center is L and the channel is electrostatically confined in the x direction with a harmonic confinement length l_x.

complete low-energy model, the effective g factor, and the effective masses are analyzed in Sec. 2.4. We show from a numerical analysis that the g factor is strongly renormalized by orbital effects. Moreover, we find a spin-dependent effective mass term that strongly depends on magnetic and electric fields. In Sec. 2.5 we compare NWs with square and circular cross-sections to squeezed dots in Ge/SiGe planar heterostructures, also including strain. In Sec. 2.6 we analyze the g factor of a QD formed by gate confinement along the NW. In these system, we predict fast Rabi frequencies at low power at electric field values compatible with ones needed for a g-factor sweet spot, thus enhancing the performance of the qubit. We conclude this section by showing that the effective model breaks down for certain fine-tuned electric and magnetic fields, where the lowest band in the NW spectrum becomes flat. In Sec. 2.7 we study NWs grown along different typical growth directions, and, in particular, we focus on the interplay of cubic anisotropies and orbital effects. In Sec. 2.8 we summarize our results. Details of our calculations are given in the Appendixes.

2.2 Model of the nanowire

The general Hamiltonian describing properties of low-energy holes in diamond-lattice semiconductors is written as

$$H = H_{\mathrm{LK}} + H_{\mathrm{BP}} + H_Z + H_E + V, \tag{2.1}$$

where H_{LK} is the Luttinger-Kohn (LK) Hamiltonian [58, 59] describing the spin-$\frac{3}{2}$ holes near the Γ point. In addition, H_{BP} is the Bir-Pikus (BP) Hamiltonian [60] capturing the strain of the lattice and H_Z is the Zeeman Hamiltonian describing the coupling of the spin to an external magnetic field. The term H_E includes the electric field generated by an externally applied gate potential. In order to define a quasi-one-dimensional channel, we consider a confinement potential V that models the cross section as depicted in Fig. 2.1(a) or the harmonic confinement along the x direction produced by gates in a planar Ge/SiGe heterostructure [see Fig. 2.1(b)].

In Ge, the material dependent LK parameters are $\gamma_1 = 13.35$, $\gamma_2 = 4.25$, and $\gamma_3 = 5.69$ [61]. Since $(\gamma_3 - \gamma_2)/\gamma_1 \approx 10.8\,\%$ is rather small, the isotropic LK Hamiltonian is commonly employed in literature [11, 12, 52, 62–64]. The isotropic LK Hamiltonian enables analytical calculations that provide results generally applicable for any NW. Corrections due to anisotropies are analyzed in detail in Sec. 2.7. The isotropic LK Hamiltonian H_{LK} is written as [11, 58, 59, 61, 62, 65, 66]

$$H_{\mathrm{LK}} = \frac{\hbar^2}{2m}\left[\gamma_k \boldsymbol{k}^2 - 2\gamma_s \left(\boldsymbol{k}\cdot\boldsymbol{J}\right)^2\right] + H_{\mathrm{orb}}, \tag{2.2}$$

where the orbital effects of the magnetic field are given by

$$\begin{aligned} H_{\mathrm{orb}} = \frac{\hbar e}{2m}\Bigg\{ & \gamma_k\left(\frac{e}{\hbar}\boldsymbol{A}^2 + 2\boldsymbol{k}\cdot\boldsymbol{A}\right) - \frac{2\gamma_s e}{\hbar}\left(\boldsymbol{A}\cdot\boldsymbol{J}\right)^2 \\ & - 4\gamma_s\left[k_x A_x J_x^2 + \left(\{k_x, A_y\} + \{k_y, A_x\}\right)\{J_x, J_y\} + \text{c.p.}\right]\Bigg\}, \end{aligned} \tag{2.3}$$

where γ_2 and γ_3 have been replaced by the effective parameter [1] $\gamma_s \approx 4.84$ and $\gamma_k = \gamma_1 + 5\gamma_s/2$. Here $\boldsymbol{J}$ is the vector of standard spin $\frac{3}{2}$ matrices, $\{A, B\} = (AB + BA)/2$ is the symmetrized anti-commutator, and by "c.p." we mean cyclic permutations. The orbital effects come from the kinematic momentum operator [59]

$$\boldsymbol{\pi} = \boldsymbol{k} + \frac{e}{\hbar}\boldsymbol{A}, \tag{2.4}$$

with the canonical momentum operator $\hbar k_j = -i\hbar\partial_j$, $j = x, y, z$, the positive elementary charge e, and the vector potential $\boldsymbol{A}$, which is related to the magnetic field by $\boldsymbol{B} = \nabla \times \boldsymbol{A}$. In the isotropic approximation, the LK Hamiltonian does not depend on the orientation of the crystallographic axes. We point out that although in this work our analysis is explicitly restricted to Ge, our analytical results are valid more generally also for holes in GaAs, InAs, and InSb where the isotropic approximation is applicable [67].

In Ge/Si core/shell NWs, the BP Hamiltonian is well approximated by [11, 60]

$$H_{\mathrm{BP}}^{\mathrm{NW}} = |b|\varepsilon_s J_y^2, \tag{2.5}$$

where $b = -2.5\,\mathrm{eV}$ [60] is the material-dependent deformation potential and $\varepsilon_s = \varepsilon_\perp - \varepsilon_{yy}$. The strain tensor elements $\varepsilon_\perp$ and ε_{yy} arising from the lattice mismatch between Si and Ge can be estimated following Ref. [51] by assuming an homogeneous strain in the core of the NW. With this assumption, the strain tensor elements depend only on the relative shell thickness [51, 68], and in a Ge core with a Si shell of relative shell thickness $\gamma = (L_{S,x} - L_x)/L_x = 0.1$, they are given by $\varepsilon_\perp = -2.1 \times 10^{-3}$ and $\varepsilon_{yy} = -8.3 \times 10^{-3}$. In this case, the total strain energy is $0.62\,\% \times |b| = 15.5\,\mathrm{meV} > 0$. In contrast, in a gate-defined one-dimensional channel [see Fig. 2.1(b)] the strain induced in the Ge layer by the lattice mismatch to the SiGe top and bottom layers is described by the BP Hamiltonian [16, 57]

$$H_{\mathrm{BP}}^{\mathrm{ch}} = |b|\varepsilon_s J_z^2. \tag{2.6}$$

Note that, in contrast to the NW, where the strain tends to favor LHs aligned parallel to the NW axis, here $|b|\varepsilon_s < 0$, meaning that the ground state tends to comprise HHs aligned perpendicular

[1] By trying to solve the LK Hamiltonian for arbitrary growth directions of the NW and averaging over the rotation angle, we find that the choice $\gamma_s = 4.25\sqrt{1 - \frac{3}{8}\left[1 - \left(\frac{\gamma_3}{\gamma_2}\right)^2\right]} = 4.84$ is most natural. The exact choice of γ_s is however irrelevant for the qualitative behavior of our results.

to the substrate. For our strain analysis we choose $|\varepsilon_s| = 0.62\%$ as in the NW setup, a value measured in typical Ge heterostructures [69].

In addition to the vector potential entering the momentum operators in Eq. (2.4), an external magnetic field $\boldsymbol{B}$ couples directly to the spin degree of freedom via the Zeeman Hamiltonian

$$H_Z = 2\kappa\mu_B \boldsymbol{B}\cdot\boldsymbol{J}, \tag{2.7}$$

where κ is a material-dependent parameter (for Ge $\kappa = 3.41$). We neglect here the anisotropic Zeeman term, which is less relevant in NWs [59, 61].

Finally, we include a homogeneous electric field via the Hamiltonian

$$H_E = -e\boldsymbol{E}\cdot\boldsymbol{r}. \tag{2.8}$$

When the hole wavefunction is strongly confined in two directions and there is an inversion-symmetry-breaking electric field, the system presents a strong so-called direct Rashba SOI [11, 12] that is linear in momentum and is important for fast all-electric manipulation of spin qubits via EDSR.

2.3 Direct Rashba spin-orbit coupling

In this section we calculate the strength of the effective direct Rashba SOI induced by an electric field applied parallel to the magnetic field (in our case, in the z direction) and perpendicular to the NW or quasi-one-dimensional structure, which extends in y direction, see Fig. 2.1. Here we first consider an infinitely long NW and later, in Sec. 2.6, we confine a QD by a harmonic potential. Since we choose the Landau gauge $\boldsymbol{A} = (0, x, 0)B$ for $\boldsymbol{B} \parallel z$, the translational invariance in the y direction is preserved and the canonical momentum k_y is a good quantum number.

2.3.1 Model

First, we assume hard-wall (HW) confinement

$$V(x,z) = \begin{cases} 0 & |x| < L_x/2 \text{ and } |z| < L_z/2 \\ \infty & \text{otherwise,} \end{cases} \tag{2.9}$$

which describes well a rectangular NW of the width L_z (L_x) in z (x) direction [see Fig. 2.1(a)]. We divide the isotropic LK Hamiltonian in Eq. (2.2) into three parts,

$$H^s_{\mathrm{LK}} = H_{zz} + H_{\mathrm{mix}} + H_{xy}, \tag{2.10}$$

where the addends are defined as

$$H_{zz} = \frac{\hbar^2}{2m}\begin{pmatrix} \gamma_z^{\mathrm{H}}\pi_z^2 & 0 & 0 & 0 \\ 0 & \gamma_z^{\mathrm{L}}\pi_z^2 & 0 & 0 \\ 0 & 0 & \gamma_z^{\mathrm{L}}\pi_z^2 & 0 \\ 0 & 0 & 0 & \gamma_z^{\mathrm{H}}\pi_z^2 \end{pmatrix}, \tag{2.11}$$

$$\begin{aligned} H_{\mathrm{mix}} = &\frac{\hbar^2\sqrt{3}\gamma_s}{m}\left[\begin{pmatrix} 0 & -\{\pi_z,\pi_x\} & 0 & 0 \\ -\{\pi_z,\pi_x\} & 0 & 0 & 0 \\ 0 & 0 & 0 & \{\pi_z,\pi_x\} \\ 0 & 0 & \{\pi_z,\pi_x\} & 0 \end{pmatrix}\right. \\ &\left. + i\begin{pmatrix} 0 & \{\pi_z,\pi_y\} & 0 & 0 \\ -\{\pi_z,\pi_y\} & 0 & 0 & 0 \\ 0 & 0 & 0 & -\{\pi_z,\pi_y\} \\ 0 & 0 & \{\pi_z,\pi_y\} & 0 \end{pmatrix}\right], \end{aligned} \tag{2.12}$$

$$H_{xy} = \frac{\hbar^2}{2m}\begin{pmatrix} \gamma_+\{\pi_+,\pi_-\} & 0 & -\sqrt{3}\gamma_s\pi_-^2 & 0 \\ 0 & \gamma_-\{\pi_+,\pi_-\} & 0 & -\sqrt{3}\gamma_s\pi_-^2 \\ -\sqrt{3}\gamma_s\pi_+^2 & 0 & \gamma_-\{\pi_+,\pi_-\} & 0 \\ 0 & -\sqrt{3}\gamma_s\pi_+^2 & 0 & \gamma_+\{\pi_+,\pi_-\} \end{pmatrix}, \tag{2.13}$$

with $\gamma_z^{\mathrm{H,L}} = \gamma_1 \mp 2\gamma_s$, $\gamma_\pm = \gamma_1 \pm \gamma_s$, $\pi_\pm = \pi_x \pm i\pi_y$. Here π_x, π_y, and π_z are the components of the kinematic momentum as defined in Eq. (2.4). The term H_{zz} is diagonal in the chosen spin basis $\{+\frac{3}{2}, +\frac{1}{2}, -\frac{1}{2}, -\frac{3}{2}\}$, whereas H_{xy} couples the spins $\pm\frac{3}{2}$ to the spins $\mp\frac{1}{2}$, and H_{mix} spin $\pm\frac{3}{2}$ to spin $\pm\frac{1}{2}$. In addition, we include the Zeeman term H_Z defined in Eq. (2.7) and the electric field term H_E defined in Eq. (2.8). We assume that the electric field $\boldsymbol{E}$ is applied along the z axis (parallel to the $\boldsymbol{B}$ field) and, for convenience, express H_E in terms of the electric length $l_E = (\hbar^2/2meE)^{1/3}$.

2.3.2 One-dimensional basis states

Let us now neglect orbital effects of the magnetic field by assuming $\boldsymbol{A} = 0$, hence $\pi_j = k_j, j = x, y, z$. We first focus on the x direction and as in our model there are no fields in this direction, we only consider

$$H_{xy}^{k_y=0} = \frac{\hbar^2}{2m}\begin{pmatrix} \gamma_+k_x^2 & 0 & -\sqrt{3}\gamma_sk_x^2 & 0 \\ 0 & \gamma_-k_x^2 & 0 & -\sqrt{3}\gamma_sk_x^2 \\ -\sqrt{3}\gamma_sk_x^2 & 0 & \gamma_-k_x^2 & 0 \\ 0 & -\sqrt{3}\gamma_sk_x^2 & 0 & \gamma_+k_x^2 \end{pmatrix} \tag{2.14}$$

in this direction and we choose the basis states

$$\phi_{n_x}^0(x) = \frac{\sqrt{2}}{\sqrt{L_x}}\sin\left[\frac{\pi n_x}{L_x}\left(x + \frac{L_x}{2}\right)\right], \tag{2.15}$$

which respect the HW boundary conditions in the x direction given in Eq. (2.9). We introduce the quantum number $n_x = 1, 2, \ldots$. The off-diagonal matrix elements of the Hamiltonian in Eq. (2.14) lead in this basis to superpositions between spin $\pm\frac{3}{2}$ and $\mp\frac{1}{2}$.

Next we consider the z direction and obtain the eigenstates of the Hamiltonian $H_{zz} + H_Z + H_E$. In the absence of electric fields the eigenfunctions are

$$\phi_{n_z}^0(z) = \frac{\sqrt{2}}{\sqrt{L_z}}\sin\left[\frac{\pi n_z}{L_z}\left(z + \frac{L_z}{2}\right)\right], \tag{2.16}$$

which again respect the HW boundary conditions along z given in Eq. (2.9). Here we also introduce the quantum number $n_z = 1, 2, \ldots$. The corresponding energy levels, including the Zeeman energy coming from the magnetic field $\boldsymbol{B} \parallel z$, are given by

$$\varepsilon_z^{0,\pm 3/2}(n_z) = \frac{\hbar^2 \gamma_z^{\mathrm{H}}}{2m} \left(\frac{\pi n_z}{L_z}\right)^2 \pm 3\kappa\mu_B B, \tag{2.17}$$

$$\varepsilon_z^{0,\pm 1/2}(n_z) = \frac{\hbar^2 \gamma_z^{\mathrm{L}}}{2m} \left(\frac{\pi n_z}{L_z}\right)^2 \pm \kappa\mu_B B. \tag{2.18}$$

In contrast, when an electric field $\boldsymbol{E}$ is applied along the z axis, the eigenfunctions can be written in terms of Airy functions,

$$\phi^{\mathrm{H(L)}}(z) = a\,\mathrm{Ai}\left[g^{\mathrm{H(L)}}(z)\right] + b\,\mathrm{Bi}\left[g^{\mathrm{H(L)}}(z)\right], \tag{2.19}$$

with

$$g^{\mathrm{H(L)}}(z) = (\gamma_z^{\mathrm{H(L)}})^{-1/3} \left(-\frac{z}{l_E} - \frac{2m}{\hbar^2}\varepsilon^{\mathrm{H(L)}} l_E^2\right). \tag{2.20}$$

The values of $\varepsilon^{\mathrm{H(L)}}(n_z)$ and the coefficients a and b are found numerically by imposing the HW boundary conditions. The lowest-energy solutions $\varepsilon^{\mathrm{H(L)}}(n_z)$, obtained by solving the equation $\phi^{\mathrm{H(L)}}(0) = \phi^{\mathrm{H(L)}}(L_z)$ numerically, are shown in Fig. 2.2(a).

As a result, the total low-energy spectrum of $H_{zz} + H_Z + H_E$ reads

$$\varepsilon_z^{\pm 3/2}(n_z) = \varepsilon^{\mathrm{H}}(n_z) \pm 3\kappa\mu_B B, \tag{2.21}$$

$$\varepsilon_z^{\pm 1/2}(n_z) = \varepsilon^{\mathrm{L}}(n_z) \pm \kappa\mu_B B. \tag{2.22}$$

The index n_z labels the solutions (from low to high energy). Importantly, in this case the wave function for spin $\pm\frac{3}{2}$ is not the same as for spin $\pm\frac{1}{2}$ [note the factor $\gamma_z^{\mathrm{H(L)}}$ in Eq. (2.20)]. This implies, as it will become clear below, that the total wave function cannot be factorized into z and x, y components. However, for low electric fields $\langle \phi^{\mathrm{H}}_{n_z' \neq n_z} | \phi^{\mathrm{L}}_{n_z} \rangle \ll \langle \phi^{\mathrm{H}}_{n_z} | \phi^{\mathrm{L}}_{n_z} \rangle$ and thus this factorization is a good approximation [see Figs. 2.2(b) and 2.2(c) below].

Weak electric field approximation

To estimate the weak electric field condition, for simplicity, we use variational solutions instead of the numerically exact Airy function solutions. We correct the wave functions corresponding to zero electric field with an exponential factor to write down the ansatz [57]

$$\phi_{n_z}^{\mathrm{H(L)}}(z) \propto \phi_{n_z}^0(z) \exp\left[-\rho_{n_z}^{\mathrm{H(L)}} \left(\frac{z}{L_z} + \frac{1}{2}\right)\right], \tag{2.23}$$

where the variational parameters $\rho_{n_z}^{\mathrm{H(L)}}$ minimize the energy of the subsequently orthogonalized states.

If the electric field is weak, meaning $L_z/\pi \ll \gamma_1^{1/3} l_E$, the minimal ground-state energy ($n_z = 1$) is found at

$$\rho_1^{\mathrm{H(L)}} = \frac{(L_z/l_E)^3}{12\pi^2 \left(\gamma_z^{\mathrm{H(L)}}\right)^2} \left(\pi^2 - 6\right), \tag{2.24}$$

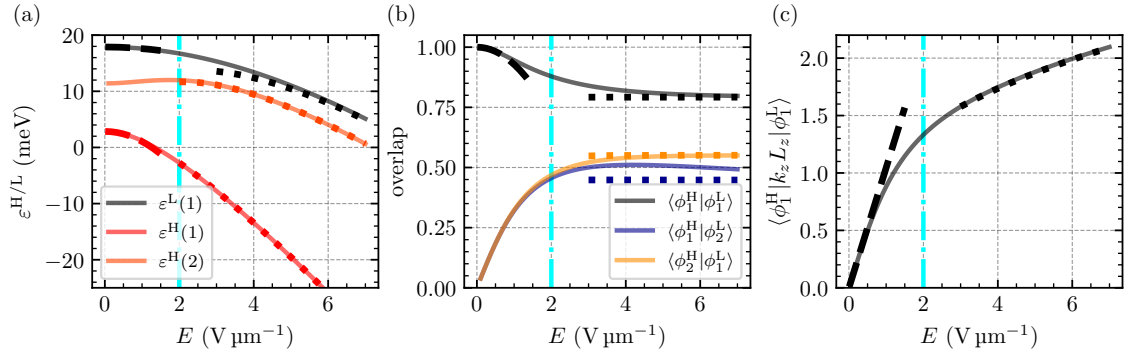

Figure 2.2: Solutions of $H_{zz} + H_E$ for the one-dimensional problem in the z direction. In all plots the solid lines are the numerically exact Airy function solutions. The dash-dotted cyan line at $E = 2\,\mathrm{V\,\mu m^{-1}}$ marks the transition from the weak to strong electric field regime. (a) Lowest-energy solutions for $\varepsilon^{\mathrm{H(L)}}(n_z)$ (independent of B) as function of electric field E applied in the z direction (perpendicular to the NW axis). The dashed lines correspond to the analytical solution defined by Eq. (2.25) (weak electric field) and the dotted lines to the one defined by Eq. (2.28) (strong electric field). (b) Overlap between wave functions of HH and LH states. The dashed line corresponds to the analytical solution given by Eq. (2.26) (weak electric field). The dotted lines represent the result obtained using the wave functions defined in Eq. (2.29). For weak electric field $\langle\phi^{\mathrm{H}}_{n_z'\neq n_z}|\phi^{\mathrm{L}}_{n_z}\rangle \ll \langle\phi^{\mathrm{H}}_{n_z}|\phi^{\mathrm{L}}_{n_z}\rangle$. (c) Matrix elements of k_z (in dimensionless units) between the lowest-energy HH and LH states. The dashed line (weak electric field) corresponds to the analytical solution given by Eq. (2.27), and the dotted line (strong electric field) represents the result obtained using the wave functions in Eq. (2.29). In all plots we use $L_z = 22\,\mathrm{nm}$. Generally, we find that both analytical approximations agree well with exact numerical results shown by the solid lines. These results are used in Sec. 2.3.3 to estimate the g factor in Eq. (2.38) and the SOI in Eq. (2.43) in the weak electric field case.

and the corresponding energy is

$$\varepsilon^{\mathrm{H(L)}}(1) \approx \frac{\hbar^2}{m}\left[\frac{\gamma_z^{\mathrm{H(L)}}\pi^2}{2L_z^2} - \frac{L_z^4\left(\pi^2-6\right)^2}{288\pi^4\gamma_z^{\mathrm{H(L)}}l_E^6} + \mathcal{O}\left(\frac{L_z^{10}}{l_E^{12}}\right)\right]. \tag{2.25}$$

We also give the expression for the overlap

$$\langle\phi_1^{\mathrm{H}}|\phi_1^{\mathrm{L}}\rangle \approx 1 - \frac{(L_z/l_E)^6\left(\pi^2-6\right)^3\gamma_s^2}{216\pi^6(\gamma_1^2-4\gamma_s^2)^2} + \mathcal{O}\left(\frac{L_z^{12}}{l_E^{12}}\right) \tag{2.26}$$

and for the matrix elements of k_z,

$$\langle\phi_1^{\mathrm{H}}|k_z|\phi_1^{\mathrm{L}}\rangle \approx -i\frac{L_z^2\left(\pi^2-6\right)\gamma_s}{6l_E^3\pi^2(\gamma_1^2-4\gamma_s^2)} + \mathcal{O}\left(\frac{L_z^8}{l_E^9}\right). \tag{2.27}$$

The dashed lines in Fig. 2.2(a), only shown for low electric field, correspond to Eq. (2.25). In analogy, we show the low-field approximation for the overlap amplitude between the HH and LH wave functions in Fig. 2.2(b). This overlap is important to estimate the SOI. Finally, the matrix elements of k_z between HH and LH states are also relevant [see Fig. 2.2(c)] and we show that the linear approximation used to derive Eq. (2.27) works well for weak electric field.

Strong electric field approximation

In the opposite limit of strong electric field, the wave function is strongly compressed to the edge. Thus, we approximate the solution by just one Airy function $\mathrm{Ai}(z)$. In this case, the energy spectrum reads

$$\varepsilon^{\mathrm{H(L)}}(n_z) \approx -\frac{\hbar^2}{m}\left(\frac{L_z}{4l_E^3} + \frac{\left[\gamma^{\mathrm{H(L)}}\right]^{1/3}}{2l_E^2}\mathrm{Ai0}(n_z)\right) \tag{2.28}$$

and is shown by a dotted line in Fig. 2.2(a). The corresponding wave functions is

$$\phi_{n_z}^{\mathrm{H(L)}} = \frac{\mathrm{Ai}\left[\frac{L_z-2z}{2l_E(\gamma^{\mathrm{H(L)}})^{1/3}} + \mathrm{Ai0}(n_z)\right]}{\sqrt{l_E(\gamma^{\mathrm{H(L)}})^{1/3}}\mathrm{Ai}'(\mathrm{Ai0}(n_z))}\,, \tag{2.29}$$

with the n_z^{th} zero of the Airy function denoted by $\mathrm{Ai0}(n_z)$. The overlap between wave functions of HH and LH states as well as matrix elements of k_z are shown with dotted lines in Figs. 2.2(b) and 2.2(c). Again, we find an excellent agreement with numerical results in the strong electric field regime.

2.3.3 Solution without orbital effects

In the following we use the one-dimensional wave functions derived above to study the SOI. At low magnetic fields, the orbital effects are not expected to give a large contribution to the SOI [52]. Thus, in this subsection we neglect them and calculate a simple formula for the SOI amplitude. First, we extend the solution of the Hamiltonian $H_{xy}^{k_y=0}$ at $k_y = 0$ [see Eq. (2.14)] by including the parity-mixing term

$$\frac{H_{\mathrm{mix}}^{k_y=0}}{\sqrt{3}\gamma_s} = \frac{\hbar^2}{m}\begin{pmatrix} 0 & -k_x & 0 & 0 \\ -k_x & 0 & 0 & 0 \\ 0 & 0 & 0 & k_x \\ 0 & 0 & k_x & 0 \end{pmatrix} k_z. \tag{2.30}$$

Later we will use perturbation theory to include the terms linear in k_y:

$$\frac{H_{k_y}}{\sqrt{3}\gamma_s} = \frac{\hbar^2}{m}\begin{pmatrix} 0 & ik_z & ik_x & 0 \\ -ik_z & 0 & 0 & ik_x \\ -ik_x & 0 & 0 & -ik_z \\ 0 & -ik_x & ik_z & 0 \end{pmatrix} k_y. \tag{2.31}$$

A good basis of wave functions is given by

$$\psi_{n_x,n_z}^{\mathrm{H(L)}}(x,z) = \phi_{n_z}^{\mathrm{H(L)}}(z)\phi_{n_x}^{0}(x), \tag{2.32}$$

where the functions $\phi_{n_z}^{\mathrm{H(L)}}(z)$ and $\phi_{n_x}^{0}(x)$ are introduced in Eqs. (2.19) and (2.15), respectively.

As a starting point for the following perturbation theory, we choose the Hamiltonian

$$H_0 = H_{zz} + H_Z + H_E + H_{xy}^{k_y=0}. \tag{2.33}$$

Its eigenstates can be approximated in position-space by

$$\langle x,z|n_x,n_z,\uparrow\rangle = \begin{pmatrix} \sin\left(\theta_{n_x,n_z}^{\uparrow}/2\right)\phi_{n_z}^{\mathrm{H}}(z) \\ 0 \\ \cos\left(\theta_{n_x,n_z}^{\uparrow}/2\right)\phi_{n_z}^{\mathrm{L}}(z) \\ 0 \end{pmatrix} \phi_{n_x}^{0}(x) \tag{2.34}$$

for the $\{\frac{3}{2},-\frac{1}{2}\}$ subspace, denoted by $S=\uparrow$ in the following, and by

$$\langle x,z|n_x,n_z,\downarrow\rangle = \begin{pmatrix} 0 \\ \cos\left(\theta^{\downarrow}_{n_x,n_z}/2\right)\phi^{\mathrm{L}}_{n_z}(z) \\ 0 \\ \sin\left(\theta^{\downarrow}_{n_x,n_z}/2\right)\phi^{\mathrm{H}}_{n_z}(z) \end{pmatrix} \phi^{0}_{n_x}(x) \tag{2.35}$$

for the $\{\frac{1}{2},-\frac{3}{2}\}$ subspace, denoted by $S=\downarrow$. Here we have introduced the angle

$$\theta^{\uparrow,\downarrow}_{n_x,n_z} = \arctan\left(\frac{\sqrt{3}\gamma_s\pi^2 n_x^2\,\langle\phi^{\mathrm{H}}_{n_z}|\phi^{\mathrm{L}}_{n_z}\rangle\,\hbar^2/(L_x^2 m)}{\pi^2 n_x^2\gamma_s\hbar^2/(L_x^2 m)\pm 4\kappa\mu_B B+\varepsilon^{\mathrm{H}}(n_z)-\varepsilon^{\mathrm{L}}(n_z)}\right). \tag{2.36}$$

The corresponding low-energy spectrum $E^{S}_{n_x,n_z}$ is given by

$$\begin{aligned} E^{\uparrow,\downarrow}_{n_x,n_z} =& \frac{\hbar^2\pi^2 n_x^2\gamma_1}{2mL_x^2} \pm \kappa\mu_B B + \frac{\varepsilon^{\mathrm{H}}(n_z)}{2} + \frac{\varepsilon^{\mathrm{L}}(n_z)}{2} \\ & - \frac{1}{2}\sqrt{\left(\frac{\pi^2 n_x^2\gamma_s\hbar^2}{L_x^2 m} \pm 4\kappa\mu_B B + \varepsilon^{\mathrm{H}}(n_z) - \varepsilon^{\mathrm{L}}(n_z)\right)^2 + \frac{3\gamma_s^2\pi^4 n_x^4 |\langle\phi^{\mathrm{H}}_{n_z}|\phi^{\mathrm{L}}_{n_z}\rangle|^2\hbar^4}{L_x^4 m^2}} \end{aligned} \tag{2.37}$$

and is shown in Fig. 2.3 for a NW with square cross section (dashed lines). Expanding $E^{\uparrow,\downarrow}_{n_x,n_z}$ in the regime of weak electric fields $L_z/\pi \ll \gamma_1^{1/3} l_E$, we obtain (for square cross section) an effective g factor in the z direction, given by the equation

$$\frac{E^{\uparrow}_{1,1}-E^{\downarrow}_{1,1}}{\mu_B B} = \left[4\kappa - \frac{3L_z^4 m^2\mu_B^2 B^2\kappa^3}{\hbar^4\pi^4\gamma_s^2} + \mathcal{O}\left(B^4\right)\right]\left[1+\mathcal{O}\left(\frac{L_z^6}{l_E^6}\right)\right]. \tag{2.38}$$

From Eq. (2.38) we observe that the effective g factor depends on the magnetic field even without accounting for magnetic orbital effects.

The states with $n_x=2$ and $n_z=1$ and with $n_x=1$ and $n_z=2$ are almost degenerate at $B=0$ in Fig. 2.3. This is due to the fact that $L_x=L_z$ and that here we use $E=1\,\mathrm{V\,\mu m^{-1}}$, which is in the weak field limit defined in Sec. 2.3.2. At larger electric fields the quasi-degeneracy is lifted, as expected from Eq. (2.28).

Finally, the parity-mixing term $H^{k_y=0}_{\mathrm{mix}}$ couples states with different parity in x (i.e., states with even and odd quantum number n_x) and different pseudo-spin $S=\uparrow,\downarrow$. More explicitly, the states depicted in blue in Fig. 2.3 couple to the ones in green, and we define the perturbed states

$$|1,1,S\rangle' = |1,1,S\rangle + \frac{\langle 2,1,\bar{S}|H^{k_y=0}_{\mathrm{mix}}|1,1,S\rangle}{E^{S}_{1,1}-E^{\bar{S}}_{2,1}}|2,1,\bar{S}\rangle, \tag{2.39}$$

where $\bar{S}$ is the opposite pseudospin to S, and the overlap

$$\langle 2,1,\bar{S}|H^{k_y=0}_{\mathrm{mix}}|1,1,S\rangle = \pm - i\frac{8\hbar^3}{3L_x m}\sqrt{3}\gamma_s\sin\left(\frac{\theta^{S}_{1,1}+\theta^{\bar{S}}_{2,1}}{2}\right)\langle\phi^{\mathrm{H}}_1|k_z|\phi^{\mathrm{L}}_1\rangle. \tag{2.40}$$

In the absence of electric fields, the leading correction to the states $|1,1,S\rangle$ comes from couplings to the states with $n_x=2$ and $n_z=2$.

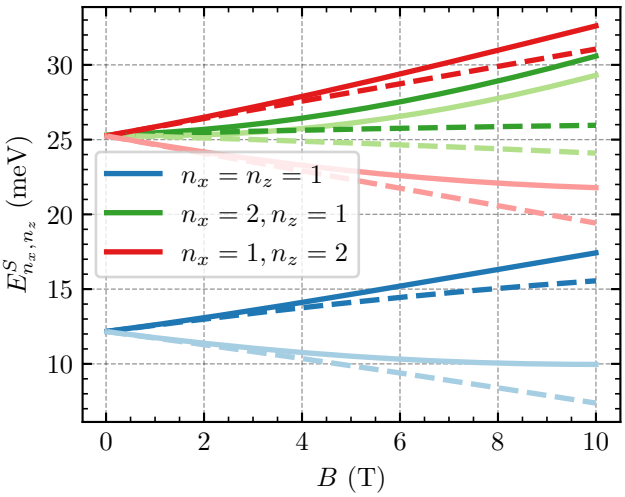

Figure 2.3: The energy levels $E^{\uparrow,\downarrow}_{n_x,n_z}$ of H_0, defined in Eq. (2.33), of a Ge NW as a function of the perpendicular magnetic field B in the z direction. Here the parity-mixing term [see Eq. (2.30)] is neglected. The dashed lines correspond to Eq. (2.37), in which we also neglect orbital effects. The solid lines are obtained by the approach developed in Sec. 2.3.4, where we include orbital effects. The Zeeman splitting is large ($\approx 1\,\mathrm{meV}$) at $B = 1\,\mathrm{T}$. The strong renormalization of the g factor due to orbital effects can be observed by comparing the solid and dashed lines. Here $L_x = L_z = 22\,\mathrm{nm}$ and $E = 1\,\mathrm{V\,\mu m^{-1}}$. We also note that because $L_x = L_z$ the states shown with red and green lines are close in energy at $B = 0$. This quasidegeneracy is a result of the small value of E used here and is lifted in the strong E field limit.

From the Hamiltonian term linear in k_y [see Eq. (2.31)], we obtain a direct SOI term because the eigenstates defined in Eq. (2.34) and Eq. (2.35) (for $n_x = n_z = 1$) are directly connected via the terms proportional to $k_z k_y$,

$$H^{(1)}_{\alpha_{so}} = i\frac{\hbar^2}{m}\sqrt{3}\gamma_s \sin\left(\frac{\theta^{\uparrow}_{1,1} + \theta^{\downarrow}_{1,1}}{2}\right)\langle\phi^{\mathrm{H}}_1|k_z|\phi^{\mathrm{L}}_1\rangle k_y\sigma_x, \tag{2.41}$$

where the Pauli matrix σ_x acts in the pseudospin space $S = \uparrow, \downarrow$.

There is however another sizeable SOI term, that is induced by the linear term proportional to $k_x k_y$ and is assisted by the parity-mixing Hamiltonian $H^{k_y=0}_{\mathrm{mix}}$. This term is given by

$$H^{(2)}_{\alpha_{so}} = -i\frac{64\hbar^6}{3m^2L_x^2}\gamma_s^2\langle\phi^{\mathrm{H}}_1|\phi^{\mathrm{L}}_1\rangle\langle\phi^{\mathrm{H}}_1|k_z|\phi^{\mathrm{L}}_1\rangle k_y\sigma_x\left[\frac{\sin\frac{\theta^{\uparrow}_{1,1}+\theta^{\downarrow}_{2,1}}{2}\sin\frac{\theta^{\downarrow}_{1,1}-\theta^{\downarrow}_{2,1}}{2}}{E^{\uparrow}_{1,1}-E^{\downarrow}_{2,1}} + \frac{\sin\frac{\theta^{\downarrow}_{1,1}+\theta^{\uparrow}_{2,1}}{2}\sin\frac{\theta^{\uparrow}_{1,1}-\theta^{\uparrow}_{2,1}}{2}}{E^{\downarrow}_{1,1}-E^{\uparrow}_{2,1}}\right]. \tag{2.42}$$

The full SOI amplitude is given by $H_{\alpha_{so}} = H^{(1)}_{\alpha_{so}} + H^{(2)}_{\alpha_{so}} = \alpha_{so}\sigma_x k_y$.

To lowest order in the electric field and while the Zeeman term is small compared to the difference of confinement energies, $4\kappa\mu_B B \ll \pi^2\gamma_s\hbar^2/(L_x^2 m)$, the SOI strength is effectively described by

$$\alpha_{so} \approx \frac{\hbar^2}{m} \frac{L_z^2\left(\pi^2-6\right)\gamma_s^2}{4l_E^3\pi^2(\gamma_1^2-4\gamma_s^2)r_1}\left[1+\frac{128\gamma_s\left[r_2-4r_1+2(r_1-r_2)L_x^2/L_z^2\right]}{9\pi^2 r_2\left[2\gamma_s(-r_1+r_2)-3\gamma_1\right]}\right], \tag{2.43}$$

where we define $r_1=\sqrt{1+L_x^4/L_z^4-L_x^2/L_z^2}$ and $r_2=\sqrt{16+L_x^4/L_z^4-4L_x^2/L_z^2}$. In particular, in a Ge NW with a square crosssection, we find $\alpha_{so}\approx 0.094\, eEL_z^2$.

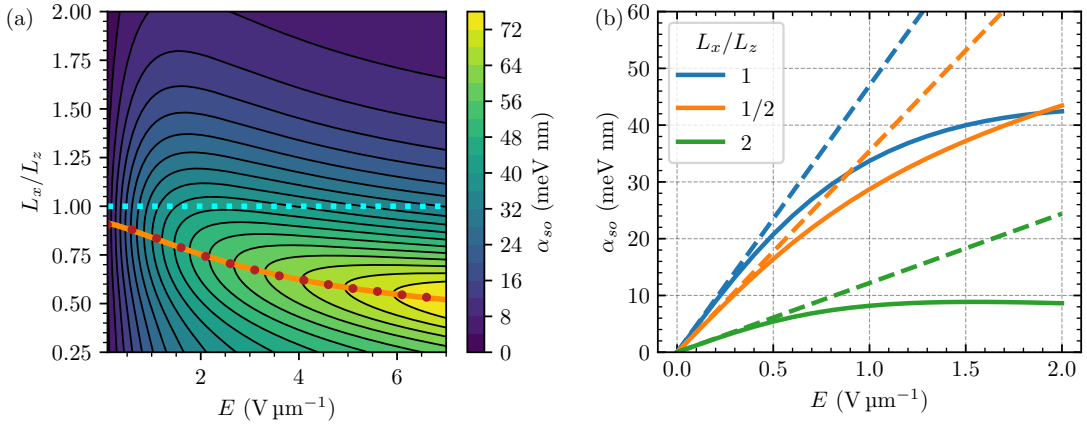

Figure 2.4: (a) Color code and contour plot of the SOI strength α_{so} obtained from Eqs. (2.41) and (2.42) as a function of perpendicular electric field E and the confinement length L_x/L_z. We fix $L_z=22\,\text{nm}$ and $B=1\,T$. The red dots mark the maximal SOI and the solid orange line shows the fitting function discussed in the text. With the dotted cyan line we mark the case $L_x=L_z$, where the cross section is a square. The plot shows a strong dependence on the geometry of the cross section, where the SOI increases for decreasing ratio L_x/L_z and increasing E-field. (b) Cuts of the plot in (a) for specific side length ratios L_x/L_z. The solid lines show the SOI strength according to Eqs. (2.41) and (2.42) and the dashed lines depict the small electric field approximation according to Eq. (2.43). The approximation captures very well the linear dependence on E at low field and yields the correct slope for all the considered ratios of side lengths.

In Fig. 2.4(a), we fix the side length $L_z=22\,\text{nm}$ and show a contour plot of the SOI strength α_{so} as a function of the side length L_x and the perpendicular electric field E. We see that the square cross section is not maximizing the SOI strength. In fact, in the figure, the maximal SOI is marked by red dots and lies on the curve $L_x^m=2.74 l_E\gamma_1^{1/3}\sqrt{\text{erf}\left(0.10L_z^2/(\gamma_1^{2/3}l_E^2)\right)}$ (orange solid line). This fitting function is similar to the one used in Ref. [52] for the gate-defined Ge one-dimensional channel shown in Fig. 2.1(b), where the optimal length is found to be $(L_x^m)_{1D}=0.81 l_E\gamma_1^{1/3}\sqrt{\text{erf}\left(0.12L_z^2/(\gamma_1^{2/3}l_E^2)\right)}$ [52]. Note that for strong electric field ($E>3\,\text{V}\,\mu\text{m}^{-1}$) we can neglect the error function and $L_x^m=2.74 l_E\gamma_1^{1/3}$ has a simple $E^{-1/3}$ dependence. We interpret this dependence as follows. The electric field gives rise to the new length scale l_E which determines the optimal side length of the cross section in the x direction. Only for weak electric field, this simple dependence is corrected by the square root of the error function. We also find that in the range of parameters considered, our analytical results for the SOI are in good agreement to the more general numerical calculation explained in Sec. 2.4, also including magnetic orbital effects.

Moreover, in Fig. 2.4(b) we show cuts of the contour plot in Fig. 2.4(a) at certain ratios of the NW side lengths. We compare the result for the SOI strength α_{so} given by Eqs. (2.41) and (2.42) to the low field approximation in Eq. (2.43) and we observe an excellent agreement at low electric fields. In this case, the SOI strength increases linearly and the approximation yields the correct slope.

2.3.4 Solution with orbital effects

In this section we account for the orbital effects of the magnetic field. As stated before, we work in the Landau gauge, resulting in $\tilde{\pi}_x = \tilde{k}_x$, $\tilde{\pi}_y = \tilde{k}_y + \tilde{x}$, and $\tilde{\pi}_z = \tilde{k}_z$. To simplify the notation in the following we express the lengths in units of the magnetic length $l_B = \sqrt{\hbar/eB}$, i.e. $\tilde{z} = z/l_B$ and $\tilde{\mathbf{k}} = l_B\mathbf{k}$, and we introduce the cyclotron energy $\hbar\omega_c = e\hbar B/m$. Orbital effects renormalize the SOI at large values of B, when the side length of the cross section is comparable to the magnetic length. Here we discuss a procedure to treat these orbital effects exactly, in contrast to perturbative approaches in other works such as Ref. [54], where a slab geometry is analyzed, or Refs. [63, 64], where a cylindrical NW is analyzed. Our results reproduce the effects captured in these works and extend them to the limits examined here.

First, we introduce the ladder operators

$$a = \frac{\tilde{k}_x - i\tilde{x}}{\sqrt{2}}, \tag{2.44}$$

which satisfy the canonical commutation relation $\left[a, a^\dagger\right] = 1$. The Hamiltonian $H_{xy}^{k_y=0}$ [see Eq. (2.14)] can be rewritten as

$$H_{xy}^{k_y=0} = \hbar\omega_c \begin{pmatrix} \gamma_+\left(a^\dagger a + \frac{1}{2}\right) & 0 & -\sqrt{3}\gamma_s a^2 & 0 \\ 0 & \gamma_-\left(a^\dagger a + \frac{1}{2}\right) & 0 & -\sqrt{3}\gamma_s a^2 \\ -\sqrt{3}\gamma_s (a^\dagger)^2 & 0 & \gamma_-\left(a^\dagger a + \frac{1}{2}\right) & 0 \\ 0 & -\sqrt{3}\gamma_s (a^\dagger)^2 & 0 & \gamma_+\left(a^\dagger a + \frac{1}{2}\right) \end{pmatrix}, \tag{2.45}$$

$$H_{\text{mix}}^{k_y=0} = \sqrt{3}\gamma_s \hbar\omega_c \begin{pmatrix} 0 & -\sqrt{2}a & 0 & 0 \\ -\sqrt{2}a^\dagger & 0 & 0 & 0 \\ 0 & 0 & 0 & \sqrt{2}a \\ 0 & 0 & \sqrt{2}a^\dagger & 0 \end{pmatrix} \tilde{k}_z. \tag{2.46}$$

In analogy with the preceding section, we now find the eigenstates of H_0 [see Eq. (2.33)] and then analyze the effect of H_{mix} and calculate the SOI strength. In the Landau gauge, the operator

$$a^\dagger a = \frac{1}{2}\left(-\partial_{\tilde{x}}^2 + \tilde{x}^2 - 1\right) \tag{2.47}$$

has two eigenfunctions, one even and one odd, with real-valued eigenvalue η

$$\psi_\eta^e(\tilde{x}) = e^{-\frac{\tilde{x}^2}{2}}\, {}_1F_1\left(-\frac{\eta}{2}; \frac{1}{2}; \tilde{x}^2\right), \tag{2.48}$$

$$\psi_\eta^o(\tilde{x}) = i\sqrt{2}\,\tilde{x}\, e^{-\frac{\tilde{x}^2}{2}}\, {}_1F_1\left(-\frac{\eta}{2} + \frac{1}{2}; \frac{3}{2}; \tilde{x}^2\right), \tag{2.49}$$

given in terms of confluent hypergeometric functions ${}_1F_1(a,b,\tilde{x})$. The annihilation and creation operators act on these eigenfunctions as

$$a\psi_\eta^e = \eta\psi_{\eta-1}^o, \tag{2.50}$$
$$a\psi_\eta^o = \psi_{\eta-1}^e, \tag{2.51}$$
$$a^\dagger\psi_\eta^e = (\eta+1)\psi_{\eta+1}^o, \tag{2.52}$$
$$a^\dagger\psi_\eta^o = \psi_{\eta+1}^e. \tag{2.53}$$

The parity quantum number $\lambda = e, o$ is a good quantum number at $k_y = 0$, when the parity-mixing term $H_{\text{mix}}^{k_y=0}$ is neglected. In this case, we can express the general solutions for the wave functions in a similar way to Eqs. (2.34) and (2.35) with the hypergeometric functions from Eqs. (2.48) and (2.49) substituting the trigonometric functions in the x direction. By using these functions, we solve exactly the Schrödinger equation $H_0\Psi = \epsilon\Psi$, with $H_0 = H_{zz} + H_Z + H_E + H_{xy}^{k_y=0}$ and with the spinor Ψ being dependent on the general real-valued eigenvalue ε. The energy of the system is then found by computing the values of ε for which each component of the wave functions satisfies HW boundary conditions, i.e., $\Psi^\lambda_{\uparrow/\downarrow,\text{H/L}}(L_x/2) = 0$. For more technical details on this analysis and on the wave functions, we refer to App. 2.A.

We introduce the new notation $|n_x, n_z, S\rangle$ for these exact solutions. The quantum number n_x labels the possible solutions and determines the parity and, as before, $S = \uparrow, \downarrow$ is the pseudospin. In Fig. 2.3 the solid lines depict the energy levels at $k_y = 0$ obtained with this approach.

In analogy to the analysis in Sec. 2.3.3, the parity-mixing term $H_{\text{mix}}^{k_y=0}$ couples states with different pseudospin and different parity. The corrected lowest-energy eigenstates are then

$$|1,1,S\rangle' = |1,1,S\rangle + \frac{\langle 2,1,\bar{S}|H_{\text{mix}}^{k_y=0}|1,1,S\rangle}{E_{1,1}^S - E_{2,1}^{\bar{S}}}|2,1,\bar{S}\rangle, \tag{2.54}$$

and the SOI can be estimated by treating the terms linear in k_y,

$$H_{k_y}^{\text{orb}} = H_{k_y} + \hbar\omega_c \begin{pmatrix} \gamma_+\tilde{x} & 0 & \sqrt{3}\gamma_s\tilde{x} & 0 \\ 0 & \gamma_-\tilde{x} & 0 & \sqrt{3}\gamma_s\tilde{x} \\ \sqrt{3}\gamma_s\tilde{x} & 0 & \gamma_-\tilde{x} & 0 \\ 0 & \sqrt{3}\gamma_s\tilde{x} & 0 & \gamma_+\tilde{x} \end{pmatrix} \tilde{k}_y, \tag{2.55}$$

perturbatively. Because the extra terms proportional to $\tilde{x}$ couple states within the same spin subspace states but with different parity in x, they contribute to the term assisted by parity mixing $H_{\alpha_{so}}^{(2)}$ [see Eqs. (2.41) and (2.42)]. In this case, we find the direct contribution to the SOI,

$$\begin{aligned} H_{\alpha_{so}}^{(1)} &= \langle 1,1,\downarrow|H_{k_y}|1,1,\uparrow\rangle\sigma_x \\ &= i\hbar\omega_c\sqrt{3}\gamma_s\left(\langle\Psi_{\downarrow,L}^e|\Psi_{\uparrow,H}^e\rangle + \langle\Psi_{\downarrow,H}^e|\Psi_{\uparrow,L}^e\rangle\right)\langle\phi_1^H|\tilde{k}_z|\phi_1^L\rangle\tilde{k}_y\sigma_x, \end{aligned} \tag{2.56}$$

and the term assisted by parity mixing,

$$
\begin{aligned}
H^{(2)}_{\alpha_{so}} =& \left(\langle 1,1,\downarrow | H^{\mathrm{orb}}_{k_y} | 2,1,\downarrow \rangle \frac{\langle 2,1,\downarrow | H^{k_y=0}_{\mathrm{mix}} | 1,1,\uparrow \rangle}{E^{\uparrow}_{1,1} - E^{\downarrow}_{2,1}} \right. \\
&\left. + \langle 2,1,\uparrow | H^{\mathrm{orb}}_{k_y} | 1,1,\uparrow \rangle \frac{\langle 1,1,\downarrow | H^{k_y=0}_{\mathrm{mix}} | 2,1,\uparrow \rangle}{E^{\downarrow}_{1,1} - E^{\uparrow}_{2,1}} \right) \sigma_x \\
=& i\sqrt{3}(\hbar\omega_c)^2 \gamma_s \Bigg\{ \frac{\langle \phi^{\mathrm{H}}_1 | \tilde{k}_z | \phi^{\mathrm{L}}_1 \rangle}{E^{\uparrow}_{1,1} - E^{\downarrow}_{2,1}} \left(\langle \Psi^{o}_{\downarrow,\mathrm{H}} | a^\dagger | \Psi^{e}_{\uparrow,\mathrm{L}} \rangle + \langle \Psi^{o}_{\downarrow,\mathrm{L}} | a^\dagger | \Psi^{e}_{\uparrow,\mathrm{H}} \rangle \right) \\
&\times \Big[\gamma_+ \langle \Psi^{e}_{\downarrow,\mathrm{H}} | a - a^\dagger | \Psi^{o}_{\downarrow,\mathrm{H}} \rangle + \gamma_- \langle \Psi^{e}_{\downarrow,\mathrm{L}} | a - a^\dagger | \Psi^{o}_{\downarrow,\mathrm{L}} \rangle \\
&+ 2\sqrt{3}\gamma_s \langle \phi^{\mathrm{H}}_1 | \phi^{\mathrm{L}}_1 \rangle \left(\langle \Psi^{e}_{\downarrow,\mathrm{L}} | a | \Psi^{o}_{\downarrow,\mathrm{H}} \rangle - \langle \Psi^{e}_{\downarrow,\mathrm{H}} | a^\dagger | \Psi^{o}_{\downarrow,\mathrm{L}} \rangle \right) \Big] \\
&+ \frac{\langle \phi^{\mathrm{H}}_1 | \tilde{k}_z | \phi^{\mathrm{L}}_1 \rangle}{E^{\downarrow}_{1,1} - E^{\uparrow}_{2,1}} \left(\langle \Psi^{e}_{\downarrow,\mathrm{H}} | a^\dagger | \Psi^{o}_{\uparrow,\mathrm{L}} \rangle + \langle \Psi^{e}_{\downarrow,\mathrm{L}} | a^\dagger | \Psi^{o}_{\uparrow,\mathrm{H}} \rangle \right) \\
&\times \Big[\gamma_+ \langle \Psi^{o}_{\uparrow,\mathrm{H}} | a - a^\dagger | \Psi^{e}_{\uparrow,\mathrm{H}} \rangle + \gamma_- \langle \Psi^{o}_{\uparrow,\mathrm{L}} | a - a^\dagger | \Psi^{e}_{\uparrow,\mathrm{L}} \rangle \\
&+ 2\sqrt{3}\gamma_s \langle \phi^{\mathrm{H}}_1 | \phi^{\mathrm{L}}_1 \rangle \left(\langle \Psi^{o}_{\uparrow,\mathrm{H}} | a | \Psi^{e}_{\uparrow,\mathrm{L}} \rangle - \langle \Psi^{o}_{\uparrow,\mathrm{L}} | a^\dagger | \Psi^{e}_{\uparrow,\mathrm{H}} \rangle \right) \Big] \Bigg\} \tilde{k}_y \sigma_x .
\end{aligned} \tag{2.57}
$$

The function $\Psi^{\lambda}_{\uparrow/\downarrow,\mathrm{H/L}}$ is defined in App. 2.A and $\phi^{\mathrm{H/L}}_{n_z}$ is given by Eq. (2.19). The sum of these two terms yields the total SOI strength α_{so} with effective Rashba-type Hamiltonian, $H_{\alpha_{so}} = H^{(1)}_{\alpha_{so}} + H^{(2)}_{\alpha_{so}} = \alpha_{so}\sigma_x k_y$.

As shown in Fig. 2.5, the SOI strength α_{so} now decreases with magnetic field and the maximum moves towards stronger electric fields. This decrease can be explained by orbital effects that start to become very relevant at $B \approx 1.4\,\mathrm{T}$, where the magnetic length is comparable to the NW side length. The second term in Eq. (2.55) leads to a negative contribution in Eq. (2.57) and thus reduces the total SOI α_{so} with increasing magnetic field. In the figure we plot the analytical result (dashed lines) together with numerical results (solid lines). We observe a good agreement between the analytical and numerical curves for weak electric field. The dots in the plot mark where an effective model up to order k_y^2 fails because the dispersion relation is dominated by k_y^4. This effect will be discussed in detail in Sec. 2.6.

Accounting for anisotropies, $\gamma_1 \neq \gamma_2$, in Ge we see that the SOI only weakly depends on the growth direction of the NW in agreement with Refs. [11, 52]. In particular, the maximum SOI is reached for $z \parallel [110]$ and the NW parallel to [001]. This is equivalent to the optimal direct Rashba SOI direction reported in Ref. [11]. Comparing this result for the SOI to the result with isotropic approximation for a square NW with side length of 22 nm at $B = 0.1\,\mathrm{T}$ we have a maximum SOI of $\alpha_{so} = 53.8\,\mathrm{meV\,nm}$ at $E = 1.6\,\mathrm{V\,\mu m^{-1}}$ [calculated numerically by diagonalizing H in Eq. (2.1)] instead of $\alpha_{so} = 38.3\,\mathrm{meV\,nm}$ at $E = 2.6\,\mathrm{V\,\mu m^{-1}}$. Hence, with the right choice of the NW growth direction an even larger SOI at lower electric field than shown by the analytical results before is possible. In contrast to the SOI, the effective g factor strongly depends on the growth direction and is highly sensitive to anisotropies as discussed in detail in Sec. 2.7.

The calculation of the correction to the g factor coming from the mixing term is inaccurate because it is a second-order term in the parity-mixing Hamiltonian [cf. Eq. (2.46)] and requires to account for many states to converge to the numerical solution. In the following section, therefore, we use a fully numerical approach to calculate the NW quantum levels at $k_y = 0$. From this solution, we obtain the effective g factor and then by treating k_y perturbatively, we compute the SOI and the effective masses of the low-energy states.

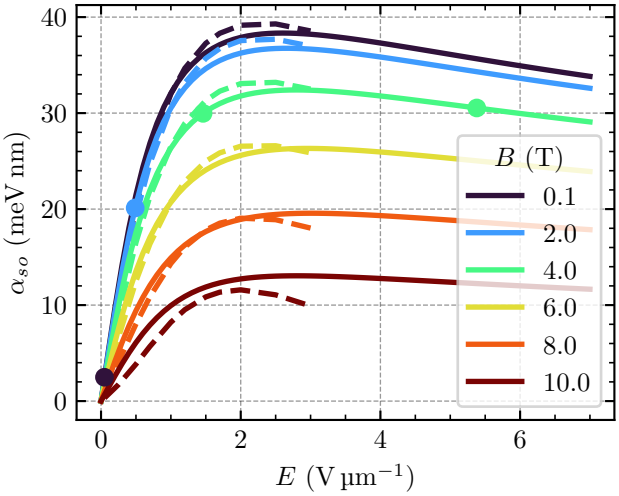

Figure 2.5: Effective SOI strength α_{so} of a Ge NW with square cross section, $L_x = L_z = 22\,\mathrm{nm}$, as a function of the electric field E for different values of the magnetic field. The solid lines are numerical solutions obtained with the discrete basis given in Eq. (2.58), while the dashed lines show the results from the semianalytical formulas in Eqs. (2.56) and (2.57). For weak electric field the analytical result compares to the numerics very well. The SOI decreases with increasing magnetic field due to orbital effects. The dots mark the points where the ground-state dispersion relation becomes flat and where one needs to include in the effective theory terms that are of higher order in momentum (see Sec. 2.6).

2.4 Effective g-factor and effective masses

In this section we present numerical results for the effective g factor and the effective mass. For the numerical calculations we use the discrete basis

$$f_{n_x,n_z}(x,z) = \frac{2\sin\left[n_x\left(\frac{x}{L_x}+\frac{1}{2}\right)\right]\sin\left[n_z\left(\frac{z}{L_z}+\frac{1}{2}\right)\right]}{\sqrt{L_x L_z}} \tag{2.58}$$

with $0 < n_x, n_z \leq 16$. This basis fulfills the HW boundary conditions in the x and z directions. We obtain the eigenvalues $E_{n,S}$ of the Hamiltonian in Eq. (2.1) with their corresponding eigenfunctions $\psi_{n,S}$, where n labels the states ascending with energy starting from the lowest eigenstate and S is their pseudospin. In the following we extract the parameters of an effective model describing the two states $\psi_{1,\uparrow}(E,B)$ and $\psi_{1,\downarrow}(E,B)$ that are lowest in energy. By second order perturbation theory, we obtain an effective model Hamiltonian up to order k_y^2,

$$H_{\mathrm{eff}} = \frac{\hbar^2}{2\bar{m}}k_y^2 - \beta\sigma_z k_y^2 + g_{\mathrm{eff}}\frac{\mu_B B}{2}\sigma_z + \alpha_{so}k_y\sigma_x, \tag{2.59}$$

with the average effective mass $1/\bar{m}$, the spin-dependent term β, the effective g factor g_{eff}, and the SOI strength α_{so}. Here β can be interpreted as a spin-dependent mass, which depends on magnetic field and vanishes at $B = 0$. Generally, there are further terms possible, such as a diagonal term linear in k_y or an off-diagonal term quadratic in k_y. However, these terms are zero in the isotropic LK Hamiltonian [70].

This effective model works well in different geometries; however in this section we restrict ourselves to the analysis of NWs with square cross section. We discuss alternative geometries in Sec. 2.5. The energy levels at $E = 1\,\mathrm{V\,\mu m^{-1}}$ are shown in Fig. 2.6 (solid lines). The dashed lines show the same spectrum without orbital effects. Excluding orbital effects, the dashed green and orange lines cross, while their solid pendants including orbital effects anti-cross. Thus, the effective g factor is largely reduced by orbital effects. The large difference between the energies calculated with and without orbital effects leads us to the conclusion that by neglecting orbital effects in Ge NWs, one tends to strongly overestimate the g factor. Note also that in contrast to Fig. 2.3, here the parity mixing term is fully accounted for. In this case, the parity mixing term leads to a splitting at $B = 0$ of the degenerate states with $n_x = 2$ and $n_z = 1$ and with $n_x = 1$ and $n_z = 2$ already in the weak electric field limit.

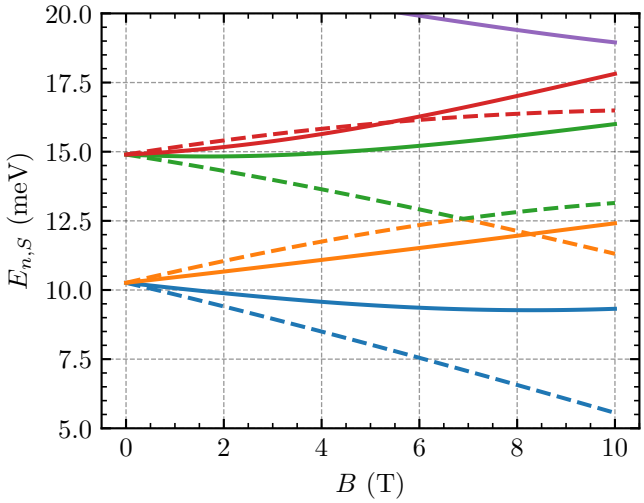

Figure 2.6: Energy levels of the Hamiltonian in Eq. (2.1) calculated numerically by using the discrete basis ($0 < n_x, n_z \leq 16$) defined in Eq. (2.58) with (solid lines) and without (dashed lines) orbital effects as a function of the magnetic field. We note that the energy spectrum is substantially modified if orbital effects are taken into account. We consider a square cross-section NW with $L_x = L_z = 22\,\mathrm{nm}$, $E = 1\,\mathrm{V\,\mu m^{-1}}$, and $\epsilon_s = 0$. Note that, in contrast to Fig. 2.3, here the parity-mixing term defined in Eq. (2.30) (without orbital effects) or in Eq. (2.46) (with orbital effects) is included.

More explicitly, we define here the effective g factor for a magnetic field B applied along the z direction as

$$g_{\mathrm{eff}} = \frac{E_{1,\uparrow} - E_{1,\downarrow}}{\mu_B B}. \tag{2.60}$$

In Fig. 2.7(a) we show the dependence of g_{eff} in a square-cross-section NW as a function of the electric field E applied along the z direction. The qualitative behavior is the same at each value of the magnetic field: First, the g factor decreases, it reaches a minimum, and then it grows again. The minimal value of the g factor depends on both electric and magnetic fields and it moves from $g_{\mathrm{eff}} = 6.6$ at $E = 1.6\,\mathrm{V\,\mu m^{-1}}$ for $B = 0.1\,\mathrm{T}$ to $g_{\mathrm{eff}} = 5.3$ at $E = 0.8\,\mathrm{V\,\mu m^{-1}}$ for $B = 10\,\mathrm{T}$. A similar effective g factor of a cylindrical Ge NW for weak B has been predicted in Ref. [63] and for strong magnetic field in Ref. [64].

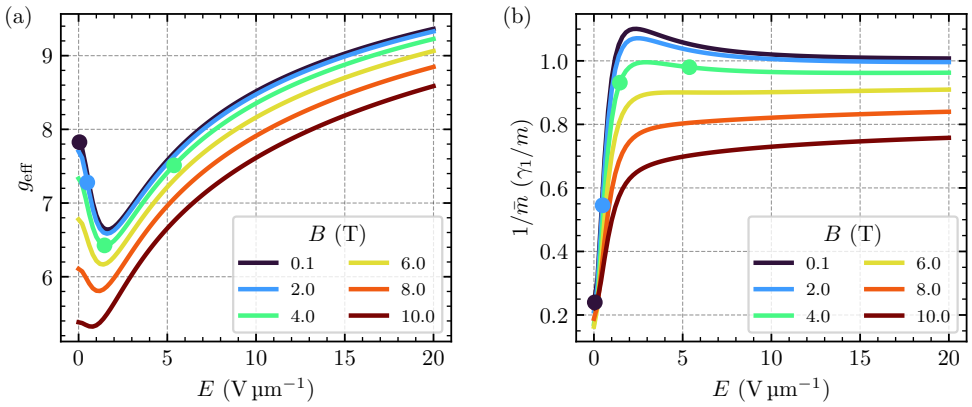

Figure 2.7: (a) Effective g factor $g_{\rm eff}$ from Eq. (2.60) and (b) average inverse effective mass $1/\bar{m}$ from Eq. (2.66) of a Ge NW with square cross section, $L_x = L_z = 22\,$nm, as a function of the electric field E at $k_y = 0$ for different values of the magnetic field B. The g factor is large even at the minimum ($g_{\rm eff} > 5$), but it decreases with increasing magnetic field. As described in Sec. 2.6, the minimum is preserved in a QD, resulting in a sweet spot where charge noise is suppressed. The averaged inverse effective mass $1/\bar{m}$ starts from a small value at weak electric fields and approaches a value close to the average HH-LH inverse m ass γ_1/m at large E. The dots mark the points where the ground-state dispersion relation becomes flat and where one needs to include in the effective theory terms that are of higher order in momentum (see Sec. 2.6).

We now analyze the effective mass of the NW, m_S. At finite values of the magnetic field, this parameter depends on the spin S and can be decomposed into the sum of two contributions

$$\frac{1}{m_S} = \frac{1}{m_S^u} + \frac{1}{m_S^p}. \tag{2.61}$$

The first unperturbed (u) contribution comes from projecting the part of the LK Hamiltonian [see Eq. (2.2)] quadratic in k_y,

$$H_{k_y^2} = \frac{\hbar^2}{2m}\begin{pmatrix} \gamma_+ & 0 & \sqrt{3}\gamma_s & 0 \\ 0 & \gamma_- & 0 & \sqrt{3}\gamma_s \\ \sqrt{3}\gamma_s & 0 & \gamma_- & 0 \\ 0 & \sqrt{3}\gamma_s & 0 & \gamma_+ \end{pmatrix} k_y^2, \tag{2.62}$$

onto the eigenbasis of $H(k_y = 0)$ where H is given in Eq. (2.1),

$$\frac{\hbar^2 k_y^2}{2m_S^u} = \langle \psi_{1,S} | H_{k_y^2} | \psi_{1,S} \rangle \,. \tag{2.63}$$

The second perturbative (p) term is a second-order correction coming from the term linear in k_y,

$$H_{k_y} = \frac{\hbar^2\sqrt{3}\gamma_s}{2m}\begin{pmatrix} \frac{\gamma_+}{\sqrt{3}\gamma_s}x & ik_z & (ik_x + x) & 0 \\ -ik_z & \frac{\gamma_-}{\sqrt{3}\gamma_s}x & 0 & (ik_x + x) \\ (-ik_x + x) & 0 & \frac{\gamma_-}{\sqrt{3}\gamma_s}x & -ik_z \\ 0 & (-ik_x + x) & ik_z & \frac{\gamma_+}{\sqrt{3}\gamma_s}x \end{pmatrix} k_y \tag{2.64}$$

(see e.g. Ref. [71]),

$$\frac{\hbar^2 k_y^2}{2m_S^p} = \sum_{n\geq 2, S'=\uparrow,\downarrow} \frac{\left|\langle \psi_{n,S'}|H_{k_y}|\psi_{1,S}\rangle\right|^2}{E_{1,S} - E_{n,S'}}. \tag{2.65}$$

At this point, we also define an average effective mass $\bar{m}$ and a spin-dependent term β as they appear in the effective model in Eq. (2.59):

$$\frac{1}{\bar{m}} := \frac{m_\downarrow + m_\uparrow}{2m_\downarrow m_\uparrow} = \frac{1}{2}\left(\frac{1}{m_\uparrow} + \frac{1}{m_\downarrow}\right), \tag{2.66}$$

$$\beta := -\hbar^2 \frac{m_\downarrow - m_\uparrow}{m_\downarrow m_\uparrow} = -\hbar^2 \left(\frac{1}{m_\uparrow} - \frac{1}{m_\downarrow}\right). \tag{2.67}$$

The average effective mass $1/\bar{m}$ is shown in Fig. 2.7(b) as a function of the electric field. Generally, when E is large, $1/\bar{m}$ approaches a constant value close to γ_1/m, the average HH-LH mass in the LK Hamiltonian. The exact large E limit of $1/\bar{m}$ depends on the magnetic field. Also note that when below $B < 6\,\mathrm{T}$, $1/\bar{m}$ has a maximum, while for $B > 6\,\mathrm{T}$, $1/\bar{m}$ increases monotonically.

We show the spin-dependent masslike term β as a function of the magnetic field in Fig. 2.8. This term is linear in B at low magnetic field and decreases with the electric field. At $B = 0$, $\beta = 0$ due to time-reversal symmetry. While generally this term is significant, at weak magnetic fields (or at strong electric fields), it can be justified to consider a simplified effective model with $\beta = 0$.

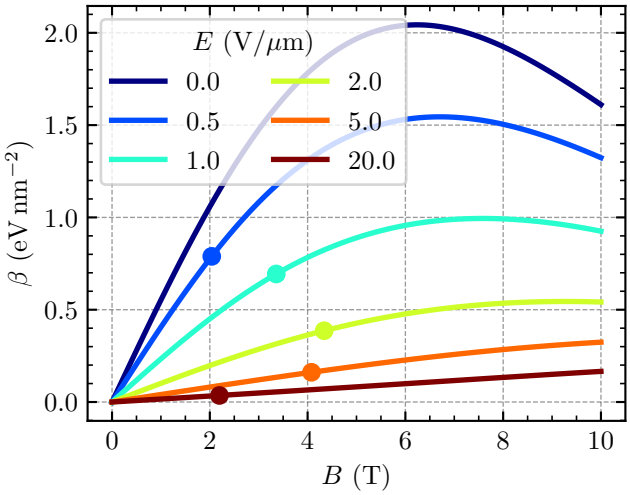

Figure 2.8: Spin-dependent masslike term β defined in Eq. (2.67) as a function of the magnetic field B at $k_y = 0$ for different values of the electric field. At $B = 0$, β is zero due to time-reversal symmetry and it increases linearly for small B. At large E, β increases very slowly. The dots mark the points where the ground state dispersion relation becomes flat and where one needs to include in the effective theory terms that are of higher order in momentum, see Sec. 2.6. Here we use $L_x = L_z = 22\,\mathrm{nm}$.

The effective model in Eq. (2.59) is valid when the subband gap is larger than the quantization energy along the y axis. The subband gap including orbital effects is smallest at large values of

the magnetic field (see Fig. 2.6) and at $E = 0$ (not plotted). However, in the system considered the gap remains larger than 1.9 meV, justifying the use of an effective 2×2 model for sufficiently long QDs. We note that the subband gap can be increased by reducing the side lengths $L_{x,z}$ or by including strain. Importantly, we also remark that orbital effects extend the validity of this effective model to large values of the magnetic field and that without them, the effective model can only be valid at weak B, far away from the crossing in Fig. 2.6.

2.5 Effect of the geometry and confinement details

In the following we compare the parameters of square NWs with side $L_x = L_z = L$, cylindrical NW with radius R, and two-dimensional heterostructures with an electrostatically defined one-dimensional channel [see Fig. 2.1(b)]. In the latter case, the electrostatic potential confining the NW in x direction is

$$U(x) = \frac{\hbar^2 \gamma_1}{2 m l_x^4} x^2 \tag{2.68}$$

and is parameterized by the harmonic length l_x. To describe this case, we use the first 16 eigenstates of the harmonic oscillator. For the NW with circular cross-section with radius R, we discretize the cross section in real space. To compare different cross sections we choose $l_x = L/\pi$ and $R = L/\sqrt{\pi}$, with L the side length of the square NW.

Furthermore, here we study the effect of strain. For the NW we consider strain induced in the Ge core by a Si shell of relative thickness $\gamma = (L_s - L)/L = 0.1$ [$\gamma = (R_s - R)/R = 0.1$ for cylindrical NW]. The strain in the NW is included by the BP Hamiltonian in Eq. (2.5). In contrast, in the two-dimensional heterostructure, the strain is controlled via the percentage of Si in the SiGe layers and it is aligned perpendicularly to the two-dimensional plane as explained in Sec. 2.2 [see in particular Eq. (2.6)]. A comparison between the effective parameters of the unstrained (solid lines) and strained (dashed lines) devices is shown in Figs. 2.9 and 2.10.

The g factors, shown in Fig. 2.9(a), are similar for both NW geometries at weak electric fields and only weakly depend on strain. In this case, the shape of the NW does not play a relevant role because the wave function is centered in the middle of the cross section, away from the edges. On the one hand, at strong electric fields the one-dimensional channel resembles a square cross-section NW because the wave function is compressed at the top of the Ge layer and the parabolic confinement in x becomes less relevant. On the other hand, the difference between circular and square cross-section becomes increasingly important when the wave function is compressed to the top of the NW.

Moreover, strain generally increases the g factor at weak electric field and moves its minimal value to stronger electric fields. At larger electric fields the g factor of the NWs with strain becomes smaller than without strain. Strain affects much more the one-dimensional channel compared to the NW and it increases the g factor at $E = 0$ by almost a factor of three. At strong electric field the values with and without strain are closer to each other, but the strained channel still has a larger g factor.

In addition, in all cases the SOI strength increases linearly with E at weak electric fields. However, at large E, the behavior of the SOI strength depends on the cross section and it either saturates or reaches a maximum before decreasing. These trends are shown in Fig. 2.9(b). Without strain the SOI for the square NW and the 1D channel reaches a maximum at around $E = 2\,\mathrm{V\,\mu m^{-1}} - 3\,\mathrm{V\,\mu m^{-1}}$, while the cylindrical NW increases monotonically in the whole range of E studied, from $E = 0$ to $E = 20\,\mathrm{V\,\mu m^{-1}}$. In general, strain decreases the SOI at weak electric field since the SOI is inversely proportional to the HH-LH gap, which increases with strain [12].

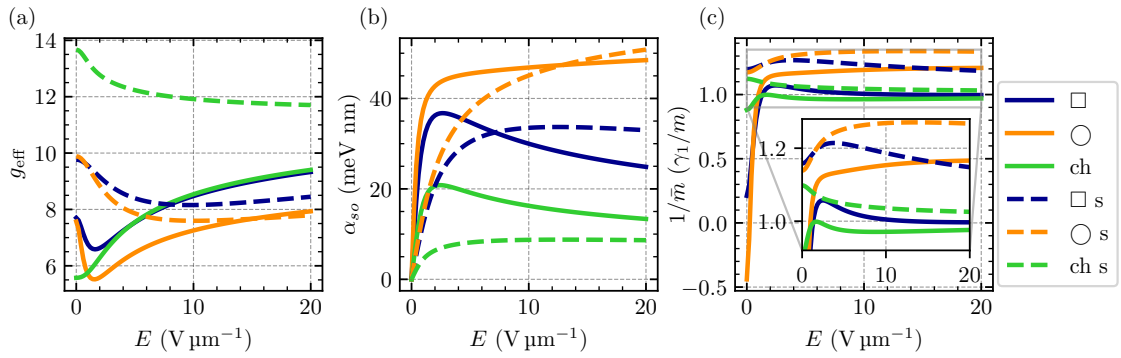

Figure 2.9: Comparison of the effective parameters of Ge NWs with different geometries with (dashed) and without (solid) strain, obtained by the numerical diagonalization of the Hamiltonian in Eq. (2.1), as described in the text. Here □ denotes a NW with a square cross section (blue) and ◯ a NW with a circular cross section (orange); ch denotes the one-dimensional gate-defined channel (green). With s we label strained devices ($|\varepsilon_s| = 0.62\,\%$ [51], $\varepsilon_s > 0$ for the NW, $\varepsilon_s < 0$ for the channel). (a) Effective g factor g_{eff}. In the NW, this quantity has a minimum that persists even in the presence of strain. (b) SOI strength α_{so}. The maximum value of α_{so} is reached at comparably weak electric field without strain. With strain a stronger electric field is required to reach the largest SOI. (c) Average effective mass $1/\bar{m}$. This quantity tends to converge to a value close to γ_1/m and in unstrained NWs with circular cross-section, it is negative at small E. Here $B = 2\,\text{T}$, $L = 22\,\text{nm}$, $R = L/\sqrt{\pi} \approx 12.4\,\text{nm}$, and $l_x = L/\pi \approx 7\,\text{nm}$.

At stronger electric fields, however, the situation changes for the NW devices. In fact, the SOI is larger in the strained NW because the HH-LH gap is decreased by strain (not shown here) and thus the negative effect of strain on the SOI can be overcome by applying stronger electric fields. The reduction of the SOI due to strain at weak electric field is also reported in Ref. [72].

Next, Fig. 2.9(c) shows the average effective mass $1/\bar{m}$ as a function of the electric field. In analogy to the analysis in Sec. 2.4, this quantity reaches a value close to γ_1/m at strong electric fields, which is slightly increased by strain. At low electric fields $E < 2\,\text{V}\,\mu\text{m}^{-1}$, the NWs however present small average masses. In particular, we observe that in NWs with circular cross section, the average mass is negative $1/m_\uparrow < 0$. The average mass remains negative at low electric field in a broad range of magnetic fields, from $B = 0$ to fields above $B = 10\,\text{T}$. However, even when the mass is negative, there are additional terms that are of higher order in k that ensure the positive curvature of the dispersion relation at large k, as discussed in Sec 2.6.2. Thus, even in these cases, it is possible to confine a QD in the NW with an electrostatic potential. Also, in strained devices, the average mass remains positive. In Appendix 2.B we highlight the differences in the dispersion relation of a NW with circular cross section and having a positive and negative average effective mass.

Finally, in Fig. 2.10 we show the spin-dependent mass term β. Regardless of the geometry and strain, β is linear in B at weak magnetic field. Although this term is typically small, at sufficiently low electric field, it is not negligible and it affects the g factor of an elongated QD created by gating the NW, as shown in the next section.

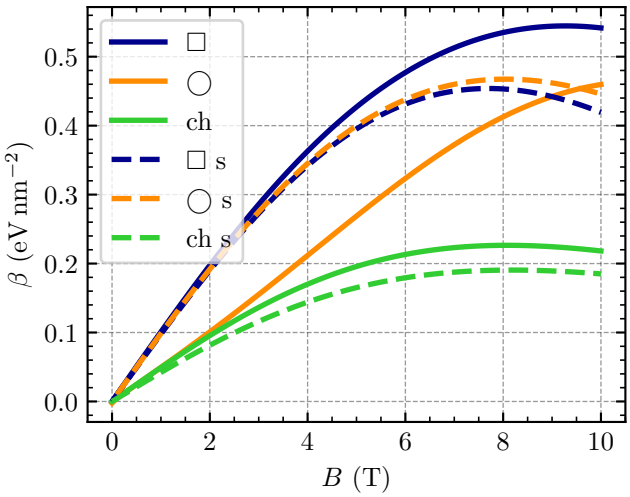

Figure 2.10: Comparison of the spin-dependent masslike term β in Ge NWs with different geometries with (dashed) and without (solid) strain as function of perpendicular magnetic field B in the z direction. These results are obtained by the numerical diagonalization of the Hamiltonian in Eq. (2.1). Here □ denotes the square cross section, ◯ the circular cross section, and ch the one-dimensional gate-defined channel. With s we label the lines with strain ($|\varepsilon_s| = 0.62\,\%$ [51], $\varepsilon_s > 0$ for the NW, $\varepsilon_s < 0$ for the channel). Time-reversal symmetry at $B = 0$ demands $\beta = 0$. At small B we observe a linear increase regardless of the geometry and strain. Here $E = 2\,\mathrm{V\,\mu m^{-1}}$, $L = 22\,\mathrm{nm}$, $R = L/\sqrt{\pi} \approx 12.4\,\mathrm{nm}$, and $l_x = L/\pi \approx 7\,\mathrm{nm}$.

2.6 Quantum dot physics

This section is dedicated to the physics of a QD in a NW. The dot is defined by an electrostatic confinement potential from gates as sketched in Fig. 2.1(a). In Sec. 2.6.1 we focus on the QD g factor and show how strain can be used to tune the position of its minimum such that it occurs at the same electric field where the SOI is maximal. These conditions provide an ideal working point in the parameter space, where the qubit can be driven fast, but at the same time the decoherence rate is diminished by a reduced sensitivity to charge noise [73, 74]. At this sweet spot, we predict ultrafast qubits at low power. In Sec. 2.6.2 we analyze the effective NW model in Eq. (2.59) for small k_y and show that this model works generally well, except at specific fine-tuned parameters where one needs to include corrections of higher order in momentum.

In the model given by Eq. (2.59), the eigenenergies expanded around $k_y = 0$ are

$$E_{\uparrow/\downarrow} = \pm\frac{E_Z}{2} + E^{(2)}_{\uparrow/\downarrow} k_y^2 + \mathcal{O}(k_y^4), \tag{2.69}$$

with Zeeman energy $E_Z = g_{\mathrm{eff}}\mu_B B$ [see Eq. (2.60)] and

$$E^{(2)}_{\uparrow/\downarrow} = \frac{\hbar^2}{2\tilde{m}} \mp \beta \pm \frac{\alpha_{so}^2}{E_Z}. \tag{2.70}$$

In inversion symmetric cross sections and at zero electric field, the SOI α_{so} is zero [71]. As the SOI increases with the electric field, the spectrum gradually splits into two separate parabolas with minima at a finite value of k_y; at $k_y = 0$, these bands are split by $E_Z = g_{\mathrm{eff}}\mu_B B$. We note that for

a certain combination of electric and magnetic fields, the mass of the ground state vanishes, i.e., $E_{\downarrow}^{(2)} = 0$. In particular, this occurs when

$$E_{\downarrow}^{(2)} = 0 \Rightarrow E_Z = \alpha_{so}^2 \frac{2\bar{m}}{\pm\hbar^2 + 2\beta\bar{m}} \tag{2.71}$$

$$\Leftrightarrow m_{\downarrow} = \frac{E_Z \hbar^2}{2\alpha_{so}^2}. \tag{2.72}$$

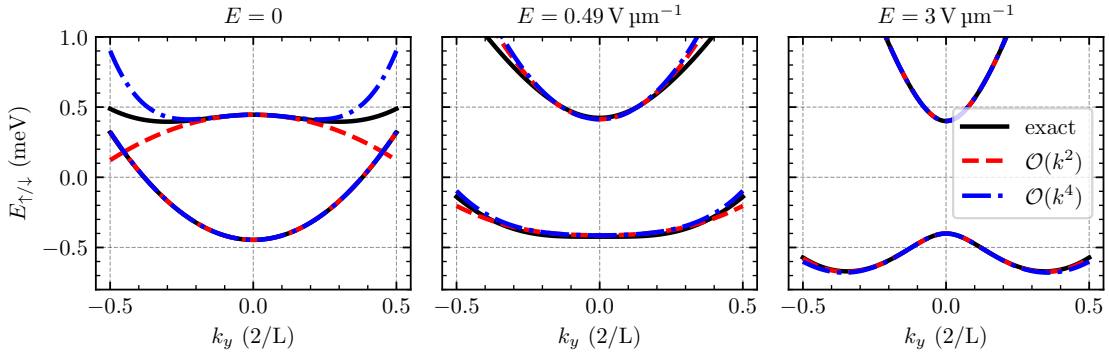

Figure 2.11: Dispersion relations of a NW with square cross section of side length $L = 22\,\mathrm{nm}$ at $B = 2\,\mathrm{T}$ for (a) $E = 0$, (b) $E = 0.49\,\mathrm{V\,\mu m^{-1}}$, and (c) $E = 3\,\mathrm{V\,\mu m^{-1}}$. The figures compare the exact numerical solution (black solid line) obtained by the diagonalization of the Hamiltonian in Eq. (2.1), the effective model quadratic in k_y (red dashed line) in Eq. (2.59), and the effective model quartic in k_y (blue dash-dotted line) discussed in Sec. 2.6.2. We observe that the ground-state dispersion is well described by both effective models around $k = 0$. Only when the condition from Eq. (2.72) is fulfilled as in (b), the $\mathcal{O}(k_y^2)$ model gives rise to a flat lowest-energy band and quartic corrections become more relevant.

In the vicinity of this point our model quadratic in k_y is not valid and would predict the appearance of a flat band. In this case, we extend our results to fourth order in k_y. The points where $E_{\downarrow}^{(2)} = 0$ are marked with dots in Figs. 2.5, 2.7, and 2.8 and the spectrum at one of these points is shown in Fig. 2.11(b). In this figure we also show the spectrum for different electric fields and compare our analytical theory in Eq. (2.59) with numerical results obtained by diagonalizing H in Eq. (2.1) using the basis in Eq. (2.58). We observe that in general the spectrum is well described by an effective Hamiltonian quadratic in k_y. When $E = 0$, this effective model fits the ground-state dispersion nicely; however, the dispersion of the first excited state is qualitatively correct only up to momenta $|0.3/L|$ and it requires additional higher-order corrections for larger k_y. Moreover, as anticipated, there are points, e.g., at $E = 0.49\,\mathrm{V\,\mu m^{-1}}$, where $E_{\downarrow}^{(2)} = 0$, and the $\mathcal{O}(k_y^2)$ model gives a relatively flat ground-state dispersion. In this case, also the exact ground-state dispersion is rather flat and can be well described by including terms proportional to k_y^4.

2.6.1 Qubit operation

Having shown the validity of the effective model in Eq. (2.59), we now use it to analyze a QD. In particular, we study the QD g factor, its sweet spot, and by including an ac electric field $E_y(t)$ applied along the NW, we calculate the frequency of Rabi oscillations induced by EDSR [75]. Here we consider parameters that are sufficiently far away from the vanishing effective mass condition

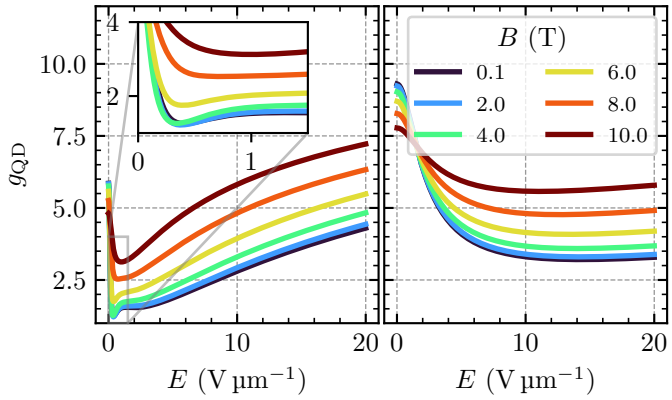

Figure 2.12: Effective g factor g_{QD} of a Ge NW QD according to Eq. (2.74) as a function of the electric field E at $k_z = 0$ for different values of the magnetic field B. The NW has a square cross section of side length $L = 22\,\mathrm{nm}$ and the QD confinement length is $l_y = 35\,\mathrm{nm}$. (a) The sweet spot is at very small electric fields, where the NW is unstrained, and (b) it is shifted to larger electric fields when strain is included. We consider here a strain tensor element $\varepsilon_s = 0.62\,\%$.

in Eq. (2.72). We consider an harmonic confinement potential $V_c = \frac{1}{2}\bar{m}\omega^2 y^2$ with the harmonic length $l_y = \sqrt{\hbar/(\bar{m}\omega)}$ along the NW. Following Ref. [52], we further introduce the external driving Hamiltonian $H_D(t) = -\hbar k_y \partial_t d_y(t)$ with the time-dependent position of the center of the QD $d_y(t)$. We restrict the motion of the QD to the y direction even if the ac field is not perfectly aligned to the NW since the QD is strongly confined in the directions perpendicular to the NW. This leads to the total NW Hamiltonian

$$H_{\mathrm{W}} = \frac{\hbar^2}{2\bar{m}}k_y^2 + \tilde{g}\frac{B}{2}\sigma_z + \alpha_{so}k_y\sigma_x + V_c + H_D(t), \tag{2.73}$$

where we introduce $\tilde{g} = \mu_B g_{\mathrm{eff}} - \beta_0 k_y^2$ with the NW g factor g_{eff}. Because at weak magnetic fields $\beta \propto B$, we also define the quantity $\beta_0 = \beta/B$ [cf. Figs. 2.8 and 2.10]. The spin-dependent transformation [29] $S = e^{-i\sigma_x y/l_{so}}$ removes the SOI via $S^\dagger(H_{\mathrm{eff}} + V_c)S$ where we use the spin-orbit length $l_{so} = \hbar^2/(\bar{m}\alpha_{so})$. When the confinement energy ω is much larger than the driving and the Zeeman energy, we obtain an effective QD Hamiltonian by projecting onto the harmonic-oscillator ground state at $B = E_y(t) = 0$,

$$H_{\mathrm{QD}} = \underbrace{\frac{B}{2}e^{-l_y^2/l_{so}^2}\left(\mu_B g_{\mathrm{eff}} - \frac{\beta_0}{2l_y^2}\right)}_{=:g_{\mathrm{QD}}\mu_B}\sigma_z + \frac{\hbar\partial_t d_y(t)}{l_{so}}\sigma_x. \tag{2.74}$$

We now discuss the parameters of the QD theory.

In Fig. 2.12, we show the effective renormalized QD g factor g_{QD} [22, 29, 76] for a QD in a NW with square cross section of side length $L_x = 22\,\mathrm{nm}$ and QD confinement length $l_y = 35\,\mathrm{nm}$. Without strain the QD g factor has a minimum at weak electric field [see Fig. 2.12(a)]. With strain, as shown in Fig. 2.12(b), the situation is drastically altered. First, in agreement with the analysis in Sec. 2.5, we observe that the QD g factor increases with strain. Furthermore, strain shifts the g factor sweet spot to larger electric fields. We find the minimal value $g_{\mathrm{QD}} = 3.2$ with strain at the static electric field in z direction $E_{\mathrm{sw}} = 14.3\,\mathrm{V\,\mu m^{-1}}$ instead of $g_{\mathrm{QD}} = 1.3$ at $E_{\mathrm{sw}} = 0.4\,\mathrm{V\,\mu m^{-1}}$ and at $B = 0.1\,\mathrm{T}$.

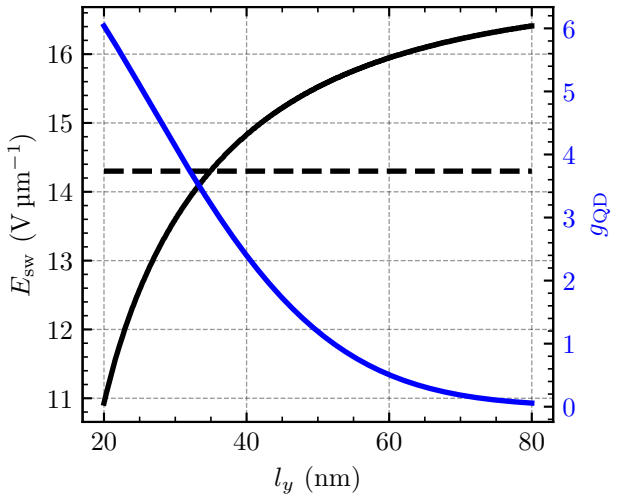

Figure 2.13: Position of the sweet spot $E_{\rm sw}$ (black solid line) of the effective g factor $g_{\rm QD}$ in a strained Ge NW QD as a function of the QD confinement length l_y. We consider here $B = 0.1\,\mathrm{T}$ and we calculated $g_{\rm QD}$ [see Eq. (2.74)] numerically by using the discrete basis defined in Eq. (2.58) for diagonalizing H defined in Eq. (2.1). The NW has a square cross section of side length $L = 22\,\mathrm{nm}$. The blue solid line shows the value of $g_{\rm QD}$ at the sweet spot and the horizontal black dashed line marks the electric field at which the SOI is maximal. By changing the size of the QD, l_y, we can tune the position of the sweet spot of $g_{\rm QD}$ to be at the same value of the electric field at which SOI also achieves its maximum strength.

Importantly, including strain the sweet spot of the g factor occurs exactly at the same value of the electric field that maximizes the SOI ($E = 14.3\,\mathrm{V\,\mu m^{-1}}$) [see Fig. 2.9(b)]. Also, we remark that because of the term β_0 in Eq. (2.74), one can tune the position of these sweet spots by adjusting the size of the QD via the harmonic length l_y. The dependence of $g_{\rm QD}$ on l_y is examined in detail in Fig. 2.13, where we show that at certain values of l_y, the minimal value of $g_{\rm QD}$ coincides with the optimal SOI. These working points are ideal for qubit manipulation because they maximize the speed of operation while reducing drastically the effect of charge noise [73, 74].

Moreover, when the harmonic drive is given by $E_y(t) = E_{ac}\sin(\omega_D t)$, we can calculate the Rabi frequency ω_R at the resonance

$$\omega_D = e^{-l_y^2/l_{so}^2}\left(\mu_B g - \frac{\beta_0}{l_y^2}\right)B \tag{2.75}$$

as [52]

$$\omega_R = \frac{l_y}{2l_{so}}\left(\frac{l_y}{l_E\gamma_1^{1/3}}\right)^3\frac{E_{ac}}{E}\omega_D. \tag{2.76}$$

At the g-factor sweet spot and at $B = 0.1\,\mathrm{T}$, we reach with the realistic driving field amplitude $E_{ac} = 0.02\,\mathrm{V\,\mu m^{-1}}$ the extremely large Rabi frequency $\omega_R = 3.7\,\mathrm{GHz}$ with a resonant driving frequency of $\omega_D = 4.5\,\mathrm{GHz}$. These results indicate that in the setups analyzed here, one can perform ultrafast qubit operations at low power.

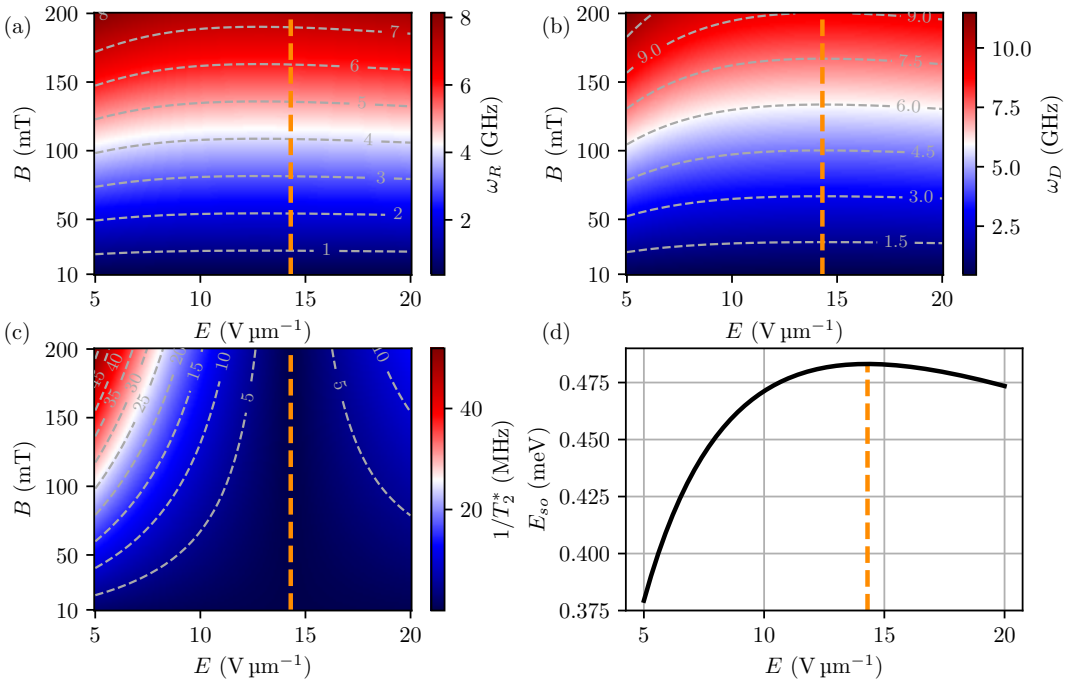

Figure 2.14: Qubit parameters of a Ge NW QD as a function of electric and magnetic field. The dashed vertical line marks $E = 14.3\,\mathrm{V\,\mu m^{-1}}$, where the minimum of g_{QD} and the maximum of E_{so} is located. (a) Rabi frequency ω_R according to Eq. (2.76) for $E_{ac} = 0.02\,\mathrm{V\,\mu m^{-1}}$. The Rabi frequency increases linearly with B due to the resonance driving frequency ω_D and is almost constant with E. (b) Resonance driving frequency ω_D according to Eq. (2.75). (c) Dephasing rate $1/T_2^*$ according to Eq. (2.77). Independently of the magnetic field, $1/T_2^*$ has a minimum at $E = 14.3\,\mathrm{V\,\mu m^{-1}}$. However, for stronger B the dephasing rate increases faster when the electric field is not exactly at the sweet spot. (d) The spin-orbit energy $E_{so} = \bar{m}\alpha_{so}/(2\hbar^2)$, as well as the QD g factor in Fig. 2.12, starts to depend on the magnetic field noticeably only at stronger B. We choose $L = 22\,\mathrm{nm}$, $l_y = 35\,\mathrm{nm}$, and $\sqrt{\langle \partial E^2 \rangle}/E = 10^{-3}$.

For a complete picture of the qubit, we estimate the dephasing rate when the QD is left in the idle state. For this aim we assume $1/f$-charge noise and small fluctuations δE of the electric field. This results in an approximate dephasing rate of [52, 71, 77, 78]

$$\frac{1}{T_2^*} = \mu_B B \sqrt{\langle \delta E^2 \rangle} \frac{\partial g_{\mathrm{QD}}}{\hbar \partial E} \sqrt{\frac{1}{2\pi} \log\left(\frac{g_{\mathrm{QD}} \mu_B B \sqrt{\langle \delta E^2 \rangle}}{\hbar \omega_{ir}} \right)}, \tag{2.77}$$

where we assume a cut-off frequency of $\omega_{ir} = 1\,\mathrm{Hz}$. At the sweet spot the qubit is protected against fluctuations of the g factor, but it is not protected against other sources of noise such as random fluctuations of l_y due to gate potential fluctuations or hyperfine noise, which could still be addressed by appropriately designing the QD [45, 71]. Moreover, in echo experiments the dephasing rate can be further reduced. For a detailed analysis of charge noise sources for hole spin qubits in quantum dots in diamond crystal structure materials such as Si and Ge, see Ref. [79]. A detailed analysis of all noise sources in Ge NWs is of interest but is beyond the scope of the present work.

In Fig. 2.14 we give an overview over the important parameters for qubit operations. Figs. 2.14(a) – 2.14(c) show the Rabi frequency ω_R, the resonance driving frequency ω_D, and the dephasing rate $1/T_2^*$ as a function of electric and magnetic field. The Rabi and resonance driving frequencies increase linearly with the magnetic field as we can see in Eqs. (2.75) and (2.76). For electric fields $E > 10\,\mathrm{V\,\mu m^{-1}}$ both frequencies stay almost constant as E increases. The dashed vertical lines in all plots mark $E = 14.3\,\mathrm{V\,\mu m^{-1}}$ where the decoherence rate has a minimum. Since we only account for charge noise due to g-factor fluctuations the decoherence rate is zero at the first-order minimum. With our very simple model for decoherence, we predict away from the sweet spot a large quality factor of 300 at $E = 8\,\mathrm{V\,\mu m^{-1}}$ and $B = 50\,\mathrm{mT}$ compared to 18 [19] or 45 [18] measured in a Ge hut-wire experiment. The figures show that for reasonable values of E_{ac} the qubit can be driven so fast that corrections beyond the rotating wave approximation will come into play. For more moderate driving power, still very fast Rabi rotations that do not invalidate the approximations are achievable. In Fig. 2.14(d) we present the spin-orbit energy $E_{so} = \bar{m}\alpha_{so}/(2\hbar^2)$ as a function of E since it depends only slightly on the magnetic field, similarly to the QD g factor in Fig. 2.12. The maximum spin-orbit energy coincides with the maximum coherence time of the qubit.

2.6.2 Beyond the harmonic approximation

In the following we discuss in more detail the case of $E_\downarrow^{(2)} = 0$. Including the term $H_4 = \left(\frac{A_+}{2} + \frac{A_-}{2}\sigma_z\right) k_y^4$, coming from fourth order perturbation theory in k_y, the eigenenergies modify as

$$E_{\uparrow/\downarrow} = \pm\frac{E_Z}{2} + \left(\hbar^2 A_\downarrow + \frac{\hbar^2\alpha_{so}^2}{2E_Z^2|m_\uparrow|}\right) k_y^4 + \mathcal{O}(k_y^6), \tag{2.78}$$

where we define $A_{\downarrow/\uparrow} = (A_+ \mp A_-)/2$. The Hamiltonian H_4 completely determines the spectrum when $E_\downarrow^{(2)} = 0$. The spectrum given by the effective model in Eq. (2.59) including the term H_4 is shown in Fig. 2.11 with blue lines. The values of the parameter $A_\uparrow$ and $A_\downarrow$ used in the figure are given in Tab. 2.1. For large k_y, the quartic Hamiltonian gives a better estimate for the ground-state dispersion compared to quadratic model in Eq. (2.59).

Table 2.1: Explicit values for $A_\uparrow$ and $A_\downarrow$ used in Fig. 2.11 calculated numerically in fourth-order perturbation theory.

	$E = 0$	$E = 0.49\,\mathrm{V\,\mu m^{-1}}$	$E = 3\,\mathrm{V\,\mu m^{-1}}$
$A_\uparrow$ [eVnm^4]	0.358	−8.19	−4.61
$A_\downarrow$ [eVnm^4]	183	55.3	−5.88

We point out that when the mass vanishes, there are many energy states that are close in energy and thus we envision that this regime could be interesting for simulations of strongly correlated matter, e.g., the Sachdev-Ye-Kitaev model [80–82]. We now estimate the number of states we can put into such a QD. To do so, we consider an harmonic QD confinement $V_c y^2 = \frac{1}{2}\bar{m}\omega^2 y^2$ with the confinement length $l_y = \sqrt{\hbar/(\bar{m}\omega)}$ along the NW. Then we solve the differential equation

$$(E_\downarrow^{(2)} k_y^2 + E_\downarrow^{(4)} k_y^4 + V_c y^2)\phi(k_y) = E\phi(k_y) \tag{2.79}$$

numerically and find its lowest eigenvalues. This procedure allows us to see how many states can coexist in the QD below a certain energy threshold $E_T = k_B T$ set by the temperature. In what

follows we focus on the number of states at $T = 1\,\mathrm{K}$. With a confinement length of $l_y = 186\,\mathrm{nm}$,[2] we obtain $V_c = 4.25 \times 10^{-7}\,\mathrm{meV\,nm^{-2}}$; we consider also a NW with side length $L = 15\,\mathrm{nm}$ and magnetic field $B = 2\,\mathrm{T}$, such that the condition for vanishing mass in Eq. (2.72) is fulfilled at $E = 0.72\,\mathrm{V\,\mu m^{-1}}$. With these parameters we have in total eleven single-hole states in the QD, in contrast to a QD with typical effective mass m/γ_1, where under the same conditions, one obtains three states below E_T. A detailed analysis of hole-hole interactions in these system is an interesting problem for future work, but it goes beyond the scope of the present paper.

2.7 Beyond the isotropic approximation

In this section we analyze the limits of the isotropic approximation used in the previous sections and commonly adopted in the literature [54, 63, 64, 72]. As we show in Sec. 2.4, at low magnetic fields only the effective g factor is significantly affected by orbital effects. Thus, we focus on the effective NW g factor and how it depends on the growth direction with and without orbital effects.

We use here the general anisotropic LK Hamiltonian

$$H_{\mathrm{LK}} = \frac{\hbar^2}{2m}\left[\gamma_k \boldsymbol{\pi}^2 - 2\gamma_2(\pi_{x'}^2 J_{x'}^2 + \pi_{y'}^2 J_{y'}^2 + \pi_{z'}^2 J_{z'}^2) - 4\gamma_3\left(\{\pi_{x'}, \pi_{y'}\}\{J_{x'}, J_{y'}\} + \mathrm{c.p.}\right)\right], \tag{2.80}$$

where the primed indices x', y', and z' denote the axes aligned to the main crystallographic axes [100], [010], and [001], respectively. Strain is included via the isotropic BP Hamiltonian introduced in Eq. (2.5) and neglecting corrections coming from different growth directions [51]. We consider the coordinate system specified in Fig. 2.1 including orbital effects via the Landau gauge $\boldsymbol{A} = (0, x, 0)B$. Since we are mainly interested in the orbital effects of the magnetic field, we consider at first $E = 0$. To account for different growth directions, we rotate the LK Hamiltonian and solve for the eigenvalues numerically as described in Sec. 2.4. For further information on the rotations see App. 2.C.

In Fig. 2.15 we show how the effective NW g factor g_{eff} depends on the growth direction of the NW. As in the previous sections, we consider a NW parallel to y and $\boldsymbol{B} \parallel z$ (see Fig. 2.1). In particular, we analyze the four cases shown at the top of Fig. 2.15: First, we consider three typical growth directions of a NW ($y \parallel [001]$, [110], and [111]) and, second, we consider a magnetic field aligned to a main crystallographic axis, i.e, $B \parallel [001] \parallel z$. We also rotate the coordinate system by an angle φ according to Tab. 2.2. More specifically, by varying φ in the first case, the magnetic field points along different crystallographic axes, and in the second case the growth direction of the NW changes (Note that to improve readability, in Tab. 2.2, Tab. 2.3, and App. 2.C, we choose a different coordinate system compared to here. In particular, the coordinate system in the main text is related to the one in the appendix by the replacements $x \to y$, $y \to z$, and $z \to x$).

The orange curve in Fig. 2.15 shows the g factor when the magnetic field $\boldsymbol{B} \parallel z$ is aligned to one of the main crystallographic axes, i.e., $\boldsymbol{B} \parallel [100], [010], [001]$, while the blue curve shows g_{eff} when the NW is aligned to these axes, i.e., $y \parallel [100], [010], [001]$. At the angles $\varphi = 0, \pi/2, \pi$, these two curves describe the same situation and thus the values of g_{eff} coincide. In analogy, the orange curve at $\varphi = \pi/4, 3\pi/4$ describes a NW grown along the [110] direction with a magnetic field aligned to a main crystallographic axis; this case is equivalently described by the green line at $\varphi = \pi/2$.

Moreover, the dotted black curve shows the values of the NW g factors in the isotropic approximation and is independent of the angle φ. In the other cases, however, we expect the g factor to

[2] We obtain this value from explicitly solving the Laplace equation for a three-gate setup with gate side length 200 nm , distance between the gates 100 nm, distance between the QD and the gates 120 nm, center gate voltage 50 mV, and side gate voltages 55 mV

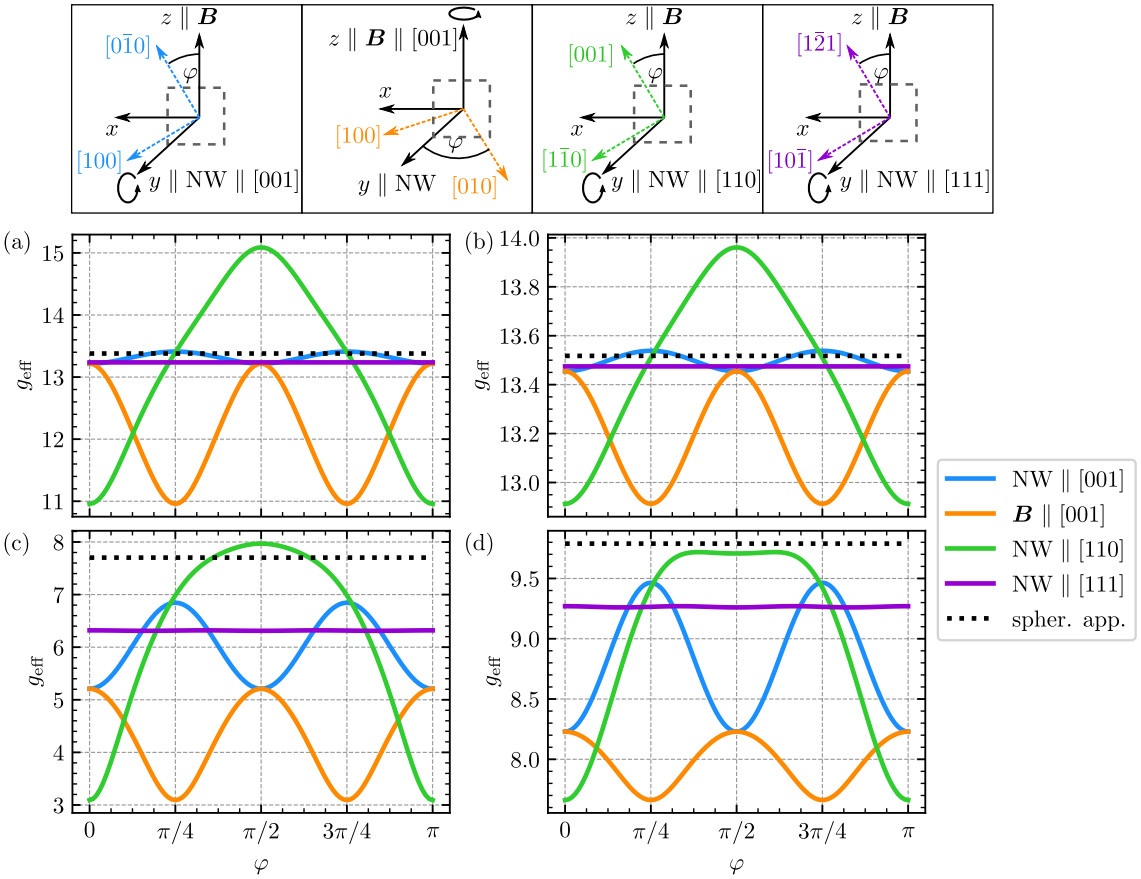

Figure 2.15: Effective g factor g_{eff} for different growth directions of the NW, obtained numerically from the diagonalization of the Hamiltonian given by Eq. (2.1) and the anisotropic LK Hamiltonian given by Eq. (2.80), using the discrete basis defined in Eq. (2.58). The four panles on top show the rotations of the coordinate system corresponding to the color code in the legend. In each case one axis is fixed and then we rotate by the angle φ around it. For the blue, green, and purple lines the NW axis (y) is fixed parallel to the crystallographic directions [001], [100], and [111], respectively. For the orange line, we fix $z \parallel [001]$. The dashed square indicates the NW cross section and how it is fixed with respect to the coordinate axes. (a) Without orbital effects, without strain; (b) without orbital effects, with strain; (c) with orbital effects, without strain; and (d) with orbital effects, with strain. The g factor depends on the growth direction and this dependence changes when orbital effects are included. This leads to the conclusion that the isotropic approximation is not well justified in Ge NWs in a general case without strain. In core/shell NWs with strain the isotropic approximation is better justified. We choose a NW with a square cross section with side length $L_x = L_z = 22\,\text{nm}$, $B = 0.1\,\text{T}$, $E = 0$, and strain tensor element $\varepsilon_s = 0.62\,\%$.

be an oscillating function of φ. These oscillations can have a rather large amplitude when $y \parallel [001]$ and $y \parallel [110]$. Without orbital effects [see Fig. 2.15(a)], g_{eff} varies at most of $\pm 20\,\%$ from the g factor obtained with the isotropic approximation and therefore this approximation is justified in this case.

To have a better understanding of the origin of these oscillations, we refer to App. 2.C, where

Table 2.2: For each line in Fig. 2.15 we fix one axis and then rotate around this axis as shown below. We use the coordinate system with the NW parallel to z and $\boldsymbol{B} \parallel x$.

Fixed axis	Rotation	Rotation
$z \parallel [001]$	$x \parallel -\sin(\varphi)[100] - \cos(\varphi)[010]$	$y \parallel \cos(\varphi)[100] - \sin(\varphi)[010]$
$x \parallel [001]$	$y \parallel \cos(\varphi)[100] - +\sin(\varphi)[010]$	$z \parallel \sin(\varphi)[100] + \cos(\varphi)[010]$
$z \parallel [110]$	$x \parallel \frac{-\sin(\varphi)}{\sqrt{2}}[100] + \frac{\sin(\varphi)}{\sqrt{2}}[010] + \cos(\varphi)[001]$	$y \parallel \frac{\cos(\varphi)}{\sqrt{2}}[100] - \frac{\cos(\varphi)}{\sqrt{2}}[010] + \sin(\varphi)[001]$
$z \parallel [111]$	$x \parallel \left(\frac{\cos(\varphi)}{\sqrt{6}} - \frac{\sin(\varphi)}{\sqrt{2}}\right)[100] - \sqrt{\frac{2}{3}}\cos(\varphi)[010] + \left(\frac{\cos(\varphi)}{\sqrt{6}} + \frac{\sin(\varphi)}{\sqrt{2}}\right)[001]$	$y \parallel \left(\frac{\cos(\varphi)}{\sqrt{2}} + \frac{\sin(\varphi)}{\sqrt{6}}\right)[100] - \sqrt{\frac{2}{3}}\sin(\varphi)[010] + \left(-\frac{\cos(\varphi)}{\sqrt{2}} + \frac{\sin(\varphi)}{\sqrt{6}}\right)[001]$

Table 2.3: Explicit crystallographic directions for certain rotation angles φ. We use the coordinate system with the NW parallel to z and $\boldsymbol{B} \parallel x$.

Direction	$\varphi = 0$	$\varphi = \pi/4$	$\varphi = \pi/2$	$\varphi = 3\pi/4$	$\varphi = \pi$
$z \parallel [001]$	$x \parallel [0\bar{1}0], y \parallel [100]$	$x \parallel [\bar{1}\bar{1}0], y \parallel [1\bar{1}0]$	$x \parallel [\bar{1}00], y \parallel [0\bar{1}0]$	$x \parallel [\bar{1}\bar{1}0], y \parallel [\bar{1}\bar{1}0]$	$x \parallel [010], y \parallel [\bar{1}00]$
$x \parallel [001]$	$y \parallel [100], z \parallel [010]$	$y \parallel [1\bar{1}0], z \parallel [110]$	$y \parallel [0\bar{1}0], z \parallel [100]$	$y \parallel [\bar{1}\bar{1}0], z \parallel [1\bar{1}0]$	$y \parallel [\bar{1}00], z \parallel [0\bar{1}0]$
$z \parallel [110]$	$x \parallel [001], y \parallel [1\bar{1}0]$		$x \parallel [\bar{1}10], y \parallel [001]$		$x \parallel [00\bar{1}], y \parallel [\bar{1}10]$
$z \parallel [111]$	$x \parallel [1\bar{2}1], y \parallel [10\bar{1}]$		$x \parallel [\bar{1}01], y \parallel [1\bar{2}1]$		$x \parallel [\bar{1}2\bar{1}], y \parallel [\bar{1}01]$

we report explicit expressions of the LK Hamiltonian in all the cases considered here (note the different coordinate system used in the Appendix). In particular, when the NW is parallel to [001], the LK Hamiltonian in Eq. (2.94) has a term proportional to $e^{\pm 4i\varphi}$ that modulates the amplitude of the coupling between spin $\pm\frac{3}{2}$ to spin $\mp\frac{1}{2}$. This modulation leads to a change of the HH-LH mixing with φ and thus to an oscillation of the g factor with a periodicity of $\pi/2$. The maximum LH contribution to the ground state is obtained at $\varphi = \pi/4$ where the g factor is minimal. In analogy, the orange curves corresponding to the case where $\boldsymbol{B} \parallel z \parallel [001]$ have a similar φ dependence, which can also be explained by a term proportional to $\cos(4\varphi)$. In contrast, when the NW is parallel to [110] (green curve) the φ-dependent coupling between spins $\pm\frac{3}{2}$ and $\mp\frac{1}{2}$ is proportional to $e^{\pm i\varphi}$ [see Eq. (2.95)], resulting in a π-periodic g_{eff}.

Interestingly, we note that the oscillations disappear when $y \parallel [111]$ (purple line). In this case, in fact, the rotation angle φ only changes the phase of the HH-LH matrix elements in the LK Hamiltonian, but it does not affect their amplitude [see Eq. (2.96)]. Consequently φ does not modify the g factor at $k_y = 0$.

We obtain a similar result with strain [cf. Fig. 2.15(b)]. The deviation from the g factor with isotropic approximation (dashed lines in Fig. 2.15) is less than 5 %. Hence, with strain the isotropic approximation is even more justified than in the unstrained case. This difference can be explained by the larger subband gap between the two lowest-energy states and the excited states with strain [11]. Interestingly, with and without strain, the g factor for the NW parallel to [110] is closest to the isotropic approximation for $\varphi = \pi/4, 3\pi/4$ corresponding to $\boldsymbol{B}$ being parallel to highly nonsymmetric directions.

Including orbital effects into our calculations changes drastically the picture. Without strain [cf. Fig. 2.15(c)], for specific angles the g factor can vary up to 60 % from the isotropic approximation.

This large variation occurs when $\boldsymbol{B} \parallel [001]$ with $\varphi = \pi/4$ and $\varphi = 3\pi/4$, where $x \parallel [110]$ and the NW is parallel to $[\bar{1}10]$ and where $x \parallel [1\bar{1}0]$ and the NW is parallel to $[110]$, respectively, and the NW is parallel to $[110]$ with $\varphi = 0$ where $\boldsymbol{B} \parallel [1\bar{1}0]$ and $x \parallel [00\bar{1}]$ and with $\varphi = \pi$ where $\boldsymbol{B} \parallel [\bar{1}10]$ and $x \parallel [001]$. With such a large deviation, the isotropic approximation is not well justified anymore to describe the g factor correctly. For the NW parallel to [111] the g factor oscillates now slightly with the angle between 6.31 and 6.32 due to an additional angle dependence in the orbital effect terms that couple spin $\pm\frac{3}{2}$ to spin $\mp\frac{1}{2}$ states [see Eq. (2.96)]. Because of the triangular symmetry of the crystal when the NW is parallel to [111], the periodicity is $\pi/3$.

Additionally including strain into our calculations generally increases the g-factor and brings it closer to the g factor with isotropic approximation. In this case, the maximum deviation from the g factor with isotropic approximation is around 20 %. These results show the profound impact of the magnetic orbital effects even at weak magnetic fields and they show how big the influence of strain can be.

In conclusion, our results show that without strain the isotropic approximation is justified only in special cases where the effective g factor depends only weakly on the rotation angle. With strain the results for the g factor deviate less form the result with isotropic approximation, and thus increasing the strain by using a thicker Si shell would render the Ge core even more isotropic.

2.8 Conclusion

We derived a low-energy effective one-dimensional model that describes the physics of confined hole systems when electric and magnetic fields are applied in one of the confined directions. We developed an analytic approach to quantify the spin-orbit interactions of this model and, assisted by numerical calculations, we investigate the dependence of SOI, g factor, and effective masses on the applied fields, on strain, and on the magnetic orbital effects. These effects are crucial to have a good description of the system.

In particular, by complementing the analytical approach with numerical calculations, we found that the g factor is strongly renormalized by orbital effects even at low magnetic fields. Moreover, the orbital effects introduce a strong dependence of the g factor on the material growth direction, which leads to a breakdown of the isotropic approximation typically employed for Ge.

We find excellent agreement between analytically and numerically computed SOIs in the weak electric field limit. At strong fields, our analytical theory captures the qualitative trend of the numerical results, but is quantitatively imprecise. We also find that the SOI decreases with increasing magnetic field. Our analysis enables a better understanding of approximately isotropic semiconductor NWs including orbital effects. Moreover, we show that a square cross section is not the best choice for optimizing the SOI and that the optimal NW cross section is rectangular with a width that depends on the electric field as $L_x \approx 2.74 l_E \gamma_1$. We also identify an extra term that can be interpreted as a spin-dependent effective mass.

The analysis of different NW geometries revealed that at low electric field circular and square cross sections are very similar, while in the strong field limit (typically reached for $E > 3\,\mathrm{V\,\mu m^{-1}}$) a gate defined one-dimensional channel is comparable to the square cross section. Furthermore, we analyze the influence of strain and observe that it increases the g factor and reduces the SOI at weak electric field.

We show that in a QD in qubit operation mode it is possible to tune the SOI maximum and the g-factor sweet spot to be at the same electric field by designing strain and confinement potential. At the sweet spot we predict Rabi frequencies in the gigahertz range at low power, enabling ultrafast gates. With this result it is possible to optimize electrically controlled qubits in Ge NW QDs and we believe a similar optimization is possible in other approximately isotropic semiconductor NWs.

The effective model (2.59) we present is valid for most of the relevant NW growth directions. We discussed the growth direction dependence of the g factor and show that orbital effects play an important role, even at low magnetic field, but that they can be counteracted by strain. Finally, we observed that the effective NW model can break down at certain electric and magnetic fields, resulting in a flat band over k. In these cases the physics is dominated by a k^4 term. This interesting working point could open up the possibility of investigating strongly correlated systems in QDs.

Acknowledgments. We would like to thank Christoph Kloeffel and Alice Descoeudres for usedul discussions and comments. This work was supported by the Swiss National Science Foundation and NCCR SPIN. M.B. achnowledges support form the Georg H. Endress Foundation. This project received funding for J. K. from the European Union's Horizon 2020 research and innovation program (ERC Starting Grant, Grant Agreement No. 757725).

2.A Wave functions with orbital effects

In this Appendix we provide some details on the wave functions in which orbital effects are included exactly. If we neglect the parity mixing term $H_{\text{mix}}^{k_y=0}$, the general solutions for the wavefunctions of $H_0 = H_{zz} + H_Z + H_E + H_{xy}^{k_y=0}$ with orbital effects are written as

$$\Psi_{\uparrow}^{\lambda}(x,z) = \begin{pmatrix} \phi_{n_z}^{\mathrm{H}}(z)\Psi_{\uparrow,\mathrm{H}}^{\lambda}(x) \\ 0 \\ \phi_{n_z}^{\mathrm{L}}(z)\Psi_{\uparrow,\mathrm{L}}^{\lambda}(x) \\ 0 \end{pmatrix}, \tag{2.81}$$

$$\Psi_{\downarrow}^{\lambda}(x,z) = \begin{pmatrix} 0 \\ \phi_{n_z}^{\mathrm{L}}(z)\Psi_{\downarrow,\mathrm{L}}^{\lambda}(x) \\ 0 \\ \phi_{n_z}^{\mathrm{H}}(z)\Psi_{\downarrow,\mathrm{H}}^{\lambda}(x) \end{pmatrix}, \tag{2.82}$$

where the z part $\phi_{n_z}^{\mathrm{H/L}}(z)$ is given by Eq. (2.19) and the spinor components of the in-plane contribution read

$$\Psi_{\uparrow,\mathrm{H}}^{\lambda}(x) = \psi_{\eta_-+2}^{\lambda}(L_x/2)c_{\uparrow}^{\lambda}(\eta_+)\psi_{\eta_+}^{\lambda}(x) - \psi_{\eta_++2}^{\lambda}(L_x/2)c_{\uparrow}^{\lambda}(\eta_-)\psi_{\eta_-}^{\lambda}(x), \tag{2.83}$$

$$\Psi_{\uparrow,\mathrm{L}}^{\lambda}(x) = \psi_{\eta_-+2}^{\lambda}(L_x/2)\psi_{\eta_++2}^{\lambda}(x) - \psi_{\eta_++2}^{\lambda}(L_x/2)\psi_{\eta_-+2}^{\lambda}(x), \tag{2.84}$$

$$\Psi_{\downarrow,\mathrm{L}}^{\lambda}(x) = \psi_{\chi_-+2}^{\lambda}(L_x/2)c_{\downarrow}^{\lambda}(\chi_+)\psi_{\chi_+}^{\lambda}(x) - \psi_{\chi_++2}^{\lambda}(L_x/2)c_{\downarrow}^{\lambda}(\chi_-)\psi_{\chi_-}^{\lambda}(x), \tag{2.85}$$

$$\Psi_{\downarrow,\mathrm{H}}^{\lambda}(x) = \psi_{\chi_-+2}^{\lambda}(L_x/2)\psi_{\chi_++2}^{\lambda}(x) - \psi_{\chi_++2}^{\lambda}(L_x/2)\psi_{\chi_-+2}^{\lambda}(x), \tag{2.86}$$

where $\eta_{\pm}$ are the two solutions of the quadratic equation

$$\frac{\varepsilon_z^{-1/2}(n_z)}{\hbar\omega_c} - \varepsilon + \gamma_-\left(\eta + \frac{5}{2}\right) = \frac{3\gamma_s^2(\eta+2)(\eta+1)\langle\phi_{n_z}^{\mathrm{H}}|\phi_{n_z}^{\mathrm{L}}\rangle^2}{\frac{\varepsilon_z^{3/2}(n_z)}{\hbar\omega_c} - \varepsilon + \gamma_+\left(\eta+\frac{1}{2}\right)} \tag{2.87}$$

and $\chi_\pm$ the solutions of

$$\frac{\varepsilon_z^{-3/2}(n_z)}{\hbar\omega_c} - \varepsilon + \gamma_+\left(\chi + \frac{5}{2}\right) = \frac{3\gamma_s^2(\chi+2)(\chi+1)\langle\phi^{\mathrm{H}}_{n_z}|\phi^{\mathrm{L}}_{n_z}\rangle^2}{\frac{\varepsilon_z^{1/2}(n_z)}{\hbar\omega_c} - \varepsilon + \gamma_-\left(\chi+\frac{1}{2}\right)}. \tag{2.88}$$

The constants are defined as

$$c^e_\uparrow(\eta) = \frac{(\gamma_1-\gamma_s)(\eta+5/2) - \varepsilon + \varepsilon_z^{-1/2}(n_z)/(\hbar\omega_c)}{\sqrt{3}\gamma_s\langle\phi^{\mathrm{H}}_{n_z}|\phi^{\mathrm{L}}_{n_z}\rangle(\eta+1)}, \tag{2.89}$$

$$c^o_\uparrow(\eta) = \frac{(\gamma_1-\gamma_s)(\eta+5/2) - \varepsilon + \varepsilon_z^{-1/2}(n_z)/(\hbar\omega_c)}{\sqrt{3}\gamma_s\langle\phi^{\mathrm{H}}_{n_z}|\phi^{\mathrm{L}}_{n_z}\rangle(\eta+2)}, \tag{2.90}$$

$$c^e_\downarrow(\chi) = \frac{(\gamma_1+\gamma_s)(\chi+5/2) - \varepsilon + \varepsilon_z^{-3/2}(n_z)/(\hbar\omega_c)}{\sqrt{3}\gamma_s\langle\phi^{\mathrm{H}}_{n_z}|\phi^{\mathrm{L}}_{n_z}\rangle(\chi+1)}, \tag{2.91}$$

$$c^o_\downarrow(\chi) = \frac{(\gamma_1+\gamma_s)(\chi+5/2) - \varepsilon + \varepsilon_z^{-3/2}(n_z)/(\hbar\omega_c)}{\sqrt{3}\gamma_s\langle\phi^{\mathrm{H}}_{n_z}|\phi^{\mathrm{L}}_{n_z}\rangle(\chi+2)}. \tag{2.92}$$

Imposing the hard-wall boundary conditions on $\Psi^\lambda_{\downarrow,\mathrm{H}}$ and $\Psi^\lambda_{\downarrow,\mathrm{L}}$ we calculate the eigenvalues ε numerically.

2.B Dispersion relation with negative average mass

In this Appendix we show a plot of the dispersion relation of a NW with circular cross section of radius $R = 22\,\mathrm{nm}/\sqrt{\pi}$. We choose the same parameters as in Fig. 2.9 in the main text and show the dispersion relation in Fig. 2.16(a) with negative average effective mass and in Fig. 2.16(b) with positive effective mass. Interestingly, we observe a crossing between the lowest two states close to $k_y = 1/(2R)$ at $E = 0$ which becomes an anticrossing for larger electric field due to the SOI. As already mentioned in the main text, terms higher order in k_y make sure that the dispersion relation has a positive curvature at large values of k_y even when $\bar{m} < 0$.

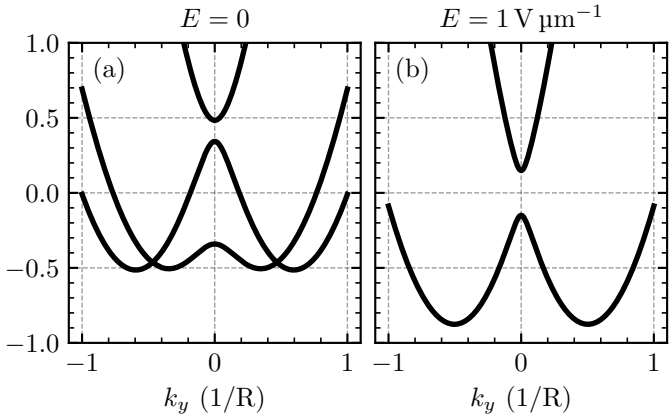

Figure 2.16: Dispersion relation of the lowest-energy states of a circular NW calculated numerically by diagonalizing the Hamiltonian in Eq. (2.1) as described in Sec 2.4 for (a) $E = 0$ and $\bar{m} < 0$ and (b) $E = 1\,\mathrm{V\,\mu m^{-1}}$ and $\bar{m} > 0$. Here $B = 2\,\mathrm{T}$ and $R = 22\,\mathrm{nm}/\sqrt{\pi}$.

2.C Rotations of the LK Hamiltonian

In the main text we consider the situations where the NW is parallel to y as well as $z \parallel \boldsymbol{B}$. In the following we switch to a different coordinate system in order to express the LK Hamiltonian where the spin quantization axis is aligned along the NW axis. This is a more convenient basis for the interpretation of the matrix elements of the LK Hamiltonian. To switch to the new coordinate system, we make the replacements $x \to y$, $y \to z$, and $z \to x$. Then the NW is parallel to the z axis and the magnetic field is parallel to the x axis.

For each of considered case we keep one coordinate axes fixed parallel to a certain crystallographic axis and rotate around this axis as specified in Tab. 2.2 and as illustrated at the top of Fig. 2.15. The rotations around the fixed main crystallographic axes are performed via standard Euler rotation matrices $\mathcal{R}$. Then, we only need to solve the following equations for the momenta k_j and spin-$\frac{3}{2}$ matrices J_j, $j = x, y, z$,

$$\begin{pmatrix} k_{x'} \\ k_{y'} \\ k_{z'} \end{pmatrix} = \mathcal{R} \begin{pmatrix} k_x \\ k_y \\ k_z \end{pmatrix}, \quad \begin{pmatrix} J_{x'} \\ J_{y'} \\ J_{z'} \end{pmatrix} = \mathcal{R} \begin{pmatrix} J_x \\ J_y \\ J_z \end{pmatrix} \tag{2.93}$$

and plug them into the LK Hamiltonian in Eq. (2.80). For certain angles φ we give the crystallographic directions to which the coordinate axes are parallel in Tab. 2.3.

The LK Hamiltonians for the different growth directions fixed along the z axis discussed in the main text are, given in the coordinate system with the NW parallel to z and $\boldsymbol{B} \parallel x$,

$$\begin{aligned} H_{\mathrm{LK}}^{z\parallel[001]} = \frac{\hbar^2}{2m} \Bigg[& \begin{pmatrix} (\gamma_1+\gamma_2)\pi_+\pi_- & 0 & M & 0 \\ 0 & (\gamma_1-\gamma_2)\pi_+\pi_- & 0 & M \\ M^* & 0 & (\gamma_1-\gamma_2)\pi_+\pi_- & 0 \\ 0 & M^* & 0 & (\gamma_1+\gamma_2)\pi_+\pi_- \end{pmatrix} \\ & + \begin{pmatrix} 0 & -2\sqrt{3}\gamma_3\pi_- & 0 & 0 \\ -2\sqrt{3}\gamma_3\pi_+ & 0 & 0 & 0 \\ 0 & 0 & 0 & 2\sqrt{3}\gamma_3\pi_- \\ 0 & 0 & 2\sqrt{3}\gamma_3\pi_+ & 0 \end{pmatrix} \pi_z \\ & + \begin{pmatrix} \gamma_1-2\gamma_2 & 0 & 0 & 0 \\ 0 & \gamma_1+2\gamma_2 & 0 & 0 \\ 0 & 0 & \gamma_1+2\gamma_2 & 0 \\ 0 & 0 & 0 & \gamma_1-2\gamma_2 \end{pmatrix} \pi_z^2 \Bigg], \end{aligned} \tag{2.94}$$

$$H_{\mathrm{LK}}^{z\|[110]} = \frac{\hbar^2}{2m}\left[\begin{pmatrix} N_+ & 0 & O & 0 \\ 0 & N_- & 0 & O \\ O^* & 0 & N_- & 0 \\ 0 & O^* & 0 & N_+ \end{pmatrix} + \begin{pmatrix} 0 & -P & 0 & 0 \\ -P^* & 0 & 0 & 0 \\ 0 & 0 & 0 & P \\ 0 & 0 & P^* & 0 \end{pmatrix}\pi_z \right.$$
$$\left. + \begin{pmatrix} \frac{1}{2}(2\gamma_1-\gamma_2-3\gamma_3) & 0 & \frac{\sqrt{3}}{2}e^{-2i\varphi}(\gamma_2-\gamma_3) & 0 \\ 0 & \frac{1}{2}(2\gamma_1+\gamma_2+3\gamma_3) & 0 & \frac{\sqrt{3}}{2}e^{-2i\varphi}(\gamma_2-\gamma_3) \\ \frac{\sqrt{3}}{2}e^{2i\varphi}(\gamma_2-\gamma_3) & 0 & \frac{1}{2}(2\gamma_1+\gamma_2+3\gamma_3) & 0 \\ 0 & \frac{\sqrt{3}}{2}e^{2i\varphi}(\gamma_2-\gamma_3) & 0 & \frac{1}{2}(2\gamma_1-\gamma_2-3\gamma_3) \end{pmatrix}\pi_z^2\right], \tag{2.95}$$

$$H_{\mathrm{LK}}^{z\|[111]} = \frac{\hbar^2}{2m}\left[\begin{pmatrix} (\gamma_1+\gamma_3)\pi_+\pi_- & \sqrt{\frac{2}{3}}e^{-3i\varphi}(\gamma_2-\gamma_3)\pi_+^2 & -\frac{\gamma_2+2\gamma_3}{\sqrt{3}}\pi_-^2 & 0 \\ \sqrt{\frac{2}{3}}e^{3i\varphi}(\gamma_2-\gamma_3)\pi_-^2 & (\gamma_1-\gamma_3)\pi_+\pi_- & 0 & -\frac{\gamma_2+2\gamma_3}{\sqrt{3}}\pi_-^2 \\ -\frac{\gamma_2+2\gamma_3}{\sqrt{3}}\pi_+^2 & 0 & (\gamma_1-\gamma_3)\pi_+\pi_- & -\sqrt{\frac{2}{3}}e^{-3i\varphi}(\gamma_2-\gamma_3)\pi_+^2 \\ 0 & -\frac{\gamma_2+2\gamma_3}{\sqrt{3}}\pi_+^2 & -\sqrt{\frac{2}{3}}e^{3i\varphi}(\gamma_2-\gamma_3)\pi_-^2 & (\gamma_1+\gamma_3)\pi_+\pi_- \end{pmatrix}\right.$$
$$+ \begin{pmatrix} 0 & -\frac{2}{\sqrt{3}}(2\gamma_2+\gamma_3)\pi_- & \sqrt{\frac{8}{3}}e^{-3i\varphi}(\gamma_2-\gamma_3)\pi_+ & 0 \\ -\frac{2}{\sqrt{3}}(2\gamma_2+\gamma_3)\pi_+ & 0 & 0 & \sqrt{\frac{8}{3}}e^{-3i\varphi}(\gamma_2-\gamma_3)\pi_+ \\ \sqrt{\frac{8}{3}}e^{3i\varphi}(\gamma_2-\gamma_3)\pi_- & 0 & 0 & \frac{2}{\sqrt{3}}(2\gamma_2+\gamma_3)\pi_- \\ 0 & \sqrt{\frac{8}{3}}e^{3i\varphi}(\gamma_2-\gamma_3)\pi_- & \frac{2}{\sqrt{3}}(2\gamma_2+\gamma_3)\pi_+ & 0 \end{pmatrix}\pi_z$$
$$\left. + \begin{pmatrix} \gamma_1-2\gamma_3 & 0 & 0 & 0 \\ 0 & \gamma_1+2\gamma_3 & 0 & 0 \\ 0 & 0 & \gamma_1+2\gamma_3 & 0 \\ 0 & 0 & 0 & \gamma_1-2\gamma_3 \end{pmatrix}\pi_z^2\right]. \tag{2.96}$$

with $\pi_\pm = \pi_x \pm i\pi_y$. The matrix elements are defined as

$$M = -\frac{\sqrt{3}}{2}\left(e^{-4i\varphi}(\gamma_2-\gamma_3)\pi_+^2 + (\gamma_2+\gamma_3)\pi_-^2\right), \tag{2.97}$$
$$N_\pm = \frac{1}{4}\left[\mp 3(\gamma_2-\gamma_3)(e^{-2i\varphi}\pi_+^2 + e^{2i\varphi}\pi_-^2) + (4\gamma_1 \pm \gamma_2 \pm 3\gamma_3)\pi_+\pi_-\right], \tag{2.98}$$
$$O = \frac{\sqrt{3}}{8}\left(3e^{-4i\varphi}(\gamma_3-\gamma_2)\pi_+^2 + 2e^{-2i\varphi}(\gamma_3-\gamma_2)\pi_+\pi_- - (3\gamma_2+5\gamma_3)\pi_-^2\right), \tag{2.99}$$
$$P = \sqrt{3}\left(e^{-2i\varphi}(\gamma_3-\gamma_2)\pi_+ + (\gamma_2+\gamma_3)\pi_-\right). \tag{2.100}$$

Looking at the $\pi_z = k_z = 0$ parts of the Hamiltonians explains the periodicity of the g factor under rotation by the angle φ around the labeled fixed axis. The off-diagonal matrix elements M [cf. Eq. (2.97)] of the Hamiltonian in Eq. (2.94) at $k_z = 0$ contain the exponential $\exp(-4i\varphi)$ and couple the spins $\pm\frac{3}{2}$ and $\mp\frac{1}{2}$. This explains the $\pi/2$ periodicity of the effective g factor for the NW parallel to [001]. Similarly, the Hamiltonian in Eq. (2.95) at $k_z = 0$ contains off-diagonal matrix elements O which have a term proportional to $\exp(-2i\varphi)$ [cf. Eq. (2.99)]. Also, these matrix elements couple spin $\pm\frac{3}{2}$ to spin $\mp\frac{1}{2}$ and thus explain the π periodicity of the g factor for the NW parallel to [110]. In contrast to that, the Hamiltonian in Eq. (2.96) at $k_z = 0$ contains a φ dependence only in the matrix elements coupling spin $\pm\frac{3}{2}$ and $\pm\frac{1}{2}$. Hence, only the phase of the HH-LH wave function is changed and not the amplitude leaving the g factor for the NW parallel to [111] unchanged.

The LK Hamiltonian with $x \parallel [001]$, again in the coordinate system with the NW parallel to z and $\boldsymbol{B} \parallel x$, reads

$$
\begin{aligned}
H_{\mathrm{LK}}^{x\parallel[001]} =& \frac{\hbar^2}{2m}\Bigg[\begin{pmatrix} Q_+ & \frac{i\sqrt{3}}{2}(\gamma_2-\gamma_3)\sin(4\varphi)\pi_y^2 & R & 0 \\ \frac{i\sqrt{3}}{2}(\gamma_3-\gamma_2)\sin(4\varphi)\pi_y^2 & Q_- & 0 & R \\ R^* & 0 & Q_- & \frac{i\sqrt{3}}{2}(\gamma_3-\gamma_2)\sin(4\varphi)\pi_y^2 \\ 0 & R^* & \frac{i\sqrt{3}}{2}(\gamma_2-\gamma_3)\sin(4\varphi)\pi_y^2 & Q_+ \end{pmatrix} \\
&+ \begin{pmatrix} \frac{3}{2}(\gamma_2-\gamma_3)\sin(4\varphi)\pi_y & S & \frac{\sqrt{3}}{2}(\gamma_2-\gamma_3)\sin(4\varphi)\pi_y & 0 \\ S^* & -\frac{3}{2}(\gamma_2-\gamma_3)\sin(4\varphi)\pi_y & 0 & \frac{\sqrt{3}}{2}(\gamma_2-\gamma_3)\sin(4\varphi)\pi_y \\ \frac{\sqrt{3}}{2}(\gamma_2-\gamma_3)\sin(4\varphi)\pi_y & 0 & -\frac{3}{2}(\gamma_2-\gamma_3)\sin(4\varphi)\pi_y & -S \\ 0 & \frac{\sqrt{3}}{2}(\gamma_2-\gamma_3)\sin(4\varphi)\pi_y & -S^* & \frac{3}{2}(\gamma_2-\gamma_3)\sin(4\varphi)\pi_y \end{pmatrix}\pi_z \\
&+ \begin{pmatrix} T_+ & -\frac{i\sqrt{3}}{2}(\gamma_2-\gamma_3)\sin(4\varphi) & \frac{\sqrt{3}}{2}(\gamma_2-\gamma_3)\sin^2(2\varphi) & 0 \\ \frac{i\sqrt{3}}{2}(\gamma_2-\gamma_3)\sin(4\varphi) & T_- & 0 & \frac{\sqrt{3}}{2}(\gamma_2-\gamma_3)\sin^2(2\varphi) \\ \frac{\sqrt{3}}{2}(\gamma_2-\gamma_3)\sin^2(2\varphi) & 0 & T_- & \frac{i\sqrt{3}}{2}(\gamma_2-\gamma_3)\sin(4\varphi) \\ 0 & \frac{\sqrt{3}}{2}(\gamma_2-\gamma_3)\sin^2(2\varphi) & -\frac{i\sqrt{3}}{2}(\gamma_2-\gamma_3)\sin(4\varphi) & T_+ \end{pmatrix}\pi_z^2\Bigg],
\end{aligned}
\tag{2.101}
$$

with the explicit matrix elements

$$Q_\pm = \frac{1}{4}\left[4(\gamma_1 \pm \gamma_2)\pi_x^2 + (4\gamma_1 \pm \gamma_2 \pm 3\gamma_3)\pi_y^2 \pm 3(\gamma_2-\gamma_3)\cos(4\varphi)\pi_y^2\right], \tag{2.102}$$

$$R = \frac{\sqrt{3}}{4}\left[-4\gamma_2\pi_x^2 + 8i\gamma_3\pi_x\pi_y + (3\gamma_2+\gamma_3)\pi_y^2 + (\gamma_2-\gamma_3)\cos(4\varphi)\pi_y^2\right], \tag{2.103}$$

$$S = i\sqrt{3}[2i\gamma_3\pi_x + (\gamma_2+\gamma_3)\pi_y - (\gamma_2-\gamma_3)\cos(4\varphi)\pi_y], \tag{2.104}$$

$$T_\pm = \frac{1}{4}\left[4\gamma_1 \mp 5\gamma_2 \mp 3\gamma_3 \mp 3(\gamma_2-\gamma_3)\cos(4\varphi)\right]. \tag{2.105}$$

The g factor for $\boldsymbol{B} \parallel [001]$ is again $\pi/2$ periodic, which is explained well by the matrix element R in Eq. (2.103), the only matrix element coupling spins $\pm\frac{3}{2}$ and $\mp\frac{1}{2}$ at $k_z = 0$. The matrix element R contains a term proportional to $\cos(4\varphi)$ leading to the $\pi/2$ periodicity.

References

[1] D. Loss and D. P. DiVincenzo, "Quantum computation with quantum dots", Phys. Rev. A **57**, 120 (1998).

[2] K. C. Nowack, F. H. L. Koppens, Y. V. Nazarov, and L. M. K. Vandersypen, "Coherent control of a single electron spin with electric fields", Science **318**, 1430 (2007).

[3] M. Pioro-Ladrière, Y. Tokura, T. Obata, T. Kubo, and S. Tarucha, "Micromagnets for coherent control of spin-charge qubit in lateral quantum dots", Appl. Phys. Lett. **90**, 024105 (2007).

[4] M. Pioro-Ladrière, T. Obata, Y. Tokura, Y.-S. Shin, T. Kubo, K. Yoshida, T. Taniyama, and S. Tarucha, "Electrically driven single-electron spin resonance in a slanting Zeeman field", Nat. Phys. **4**, 776 (2008).

[5] J. Yoneda, K. Takeda, T. Otsuka, T. Nakajima, M. R. Delbecq, G. Allison, T. Honda, T. Kodera, S. Oda, Y. Hoshi, N. Usami, K. M. Itoh, and S. Tarucha, "A quantum-dot spin qubit with coherence limited by charge noise and fidelity higher than 99.9%", Nat. Nanotechnol. **13**, 102 (2018).

[6] E. Kawakami, P. Scarlino, D. R. Ward, F. R. Braakman, D. E. Savage, M. G. Lagally, M. Friesen, S. N. Coppersmith, M. A. Eriksson, and L. M. K. Vandersypen, "Electrical control of a long-lived spin qubit in a Si/SiGe quantum dot", Nat. Nanotechnol. **9**, 666 (2014).

[7] M. Benito, X. Croot, C. Adelsberger, S. Putz, X. Mi, J. R. Petta, and G. Burkard, "Electric-field control and noise protection of the flopping-mode spin qubit", Phys. Rev. B **100**, 125430 (2019).

[8] X. Croot, X. Mi, S. Putz, M. Benito, F. Borjans, G. Burkard, and J. R. Petta, "Flopping-mode electric dipole spin resonance", Phys. Rev. Res. **2**, 012006(R) (2020).

[9] N. W. Hendrickx, W. I. L. Lawrie, M. Russ, F. van Riggelen, S. L. de Snoo, R. N. Schouten, A. Sammak, G. Scappucci, and M. Veldhorst, "A four-qubit germanium quantum processor", Nature **591**, 580 (2021).

[10] R. Maurand, X. Jehl, D. Kotekar-Patil, A. Corna, H. Bohuslavskyi, R. Laviéville, L. Hutin, S. Barraud, M. Vinet, M. Sanquer, and S. D. Franceschi, "A CMOS silicon spin qubit", Nat. Commun. **7**, 13575 (2016).

[11] C. Kloeffel, M. J. Rančić, and D. Loss, "Direct Rashba spin-orbit interaction in Si and Ge nanowires with different growth directions", Phys. Rev. B **97**, 235422 (2018).

[12] C. Kloeffel, M. Trif, and D. Loss, "Strong spin-orbit interaction and helical hole states in Ge/Si nanowires", Phys. Rev. B **84**, 195314 (2011).

[13] X.-J. Hao, T. Tu, G. Cao, C. Zhou, H.-O. Li, G.-C. Guo, W. Y. Fung, Z. Ji, G.-P. Guo, and W. Lu, "Strong and tunable spin-orbit coupling of one-dimensional holes in Ge/Si core/shell nanowires", Nano Lett. **10**, 2956 (2010).

[14] Y. Hu, F. Kuemmeth, C. M. Lieber, and C. M. Marcus, "Hole spin relaxation in Ge-Si core-shell nanowire qubits", Nat. Nanotechnol. **7**, 47 (2011).

[15] G. Scappucci, C. Kloeffel, F. A. Zwanenburg, D. Loss, M. Myronov, J.-J. Zhang, S. D. Franceschi, G. Katsaros, and M. Veldhorst, "The germanium quantum information route", Nat. Rev. Mater. **6**, 926 (2021).

[16] L. A. Terrazos, E. Marcellina, Z. Wang, S. N. Coppersmith, M. Friesen, A. R. Hamilton, X. Hu, B. Koiller, A. L. Saraiva, D. Culcer, and R. B. Capaz, "Theory of hole-spin qubits in strained germanium quantum dots", Phys. Rev. B **103**, 125201 (2021).

[17] F. N. M. Froning, L. C. Camenzind, O. A. H. van der Molen, A. Li, E. P. A. M. Bakkers, D. M. Zumbühl, and F. R. Braakman, "Ultrafast hole spin qubit with gate-tunable spin-orbit switch functionality", Nat. Nanotechnol. **16**, 308 (2021).

[18] K. Wang, G. Xu, F. Gao, H. Liu, R.-L. Ma, X. Zhang, Z. Wang, G. Cao, T. Wang, J.-J. Zhang, D. Culcer, X. Hu, H.-W. Jiang, H.-O. Li, G.-C. Guo, and G.-P. Guo, "Ultrafast coherent control of a hole spin qubit in a germanium quantum dot", Nat. Commun. **13**, 206 (2022).

[19] H. Watzinger, J. Kukučka, L. Vukušić, F. Gao, T. Wang, F. Schäffler, J.-J. Zhang, and G. Katsaros, "A germanium hole spin qubit", Nat. Commun. **9**, 3902 (2018).

[20] N. W. Hendrickx, D. P. Franke, A. Sammak, G. Scappucci, and M. Veldhorst, "Fast two-qubit logic with holes in germanium", Nature **577**, 487 (2020).

[21] N. W. Hendrickx, W. I. L. Lawrie, L. Petit, A. Sammak, G. Scappucci, and M. Veldhorst, "A single-hole spin qubit", Nat. Commun. **11**, 3478 (2020).

[22] F. N. M. Froning, M. J. Rančić, B. Hetényi, S. Bosco, M. K. Rehmann, A. Li, E. P. A. M. Bakkers, F. A. Zwanenburg, D. Loss, D. M. Zumbühl, and F. R. Braakman, "Strong spin-orbit interaction and g-factor renormalization of hole spins in Ge/Si nanowire quantum dots", Phys. Rev. Res. **3**, 013081 (2021).

[23] X. Hu, Y.-x. Liu, and F. Nori, "Strong coupling of a spin qubit to a superconducting stripline cavity", Phys. Rev. B **86**, 035314 (2012).

[24] M. Benito, X. Mi, J. M. Taylor, J. R. Petta, and G. Burkard, "Input-output theory for spin-photon coupling in Si double quantum dots", Phys. Rev. B **96**, 235434 (2017).

[25] X. Mi, M. Benito, S. Putz, D. M. Zajac, J. M. Taylor, G. Burkard, and J. R. Petta, "A coherent spin-photon interface in silicon", Nature **555**, 599 (2018).

[26] N. Samkharadze, G. Zheng, N. Kalhor, D. Brousse, A. Sammak, U. C. Mendes, A. Blais, G. Scappucci, and L. M. K. Vandersypen, "Strong spin-photon coupling in silicon", Science **359**, 1123 (2018).

[27] F. Borjans, X. G. Croot, X. Mi, M. J. Gullans, and J. R. Petta, "Resonant microwave-mediated interactions between distant electron spins", Nature **577**, 195 (2019).

[28] P. Harvey-Collard, J. Dijkema, G. Zheng, A. Sammak, G. Scappucci, and L. M. K. Vandersypen, "Circuit quantum electrodynamics with two remote electron spins", Phys. Rev. X **12**, 021026 (2022).

[29] M. Trif, V. N. Golovach, and D. Loss, "Spin dynamics in InAs nanowire quantum dots coupled to a transmission line", Phys. Rev. B **77**, 045434 (2008).

[30] C. Kloeffel, M. Trif, P. Stano, and D. Loss, "Circuit QED with hole-spin qubits in Ge/Si nanowire quantum dots", Phys. Rev. B **88**, 241405(R) (2013).

[31] S. E. Nigg, A. Fuhrer, and D. Loss, "Superconducting grid-bus surface code architecture for hole-spin qubits", Phys. Rev. Lett. **118**, 147701 (2017).

[32] D. Jirovec, A. Hofmann, A. Ballabio, P. M. Mutter, G. Tavani, M. Botifoll, A. Crippa, J. Kukucka, O. Sagi, F. Martins, J. Saez-Mollejo, I. Prieto, M. Borovkov, J. Arbiol, D. Chrastina, G. Isella, and G. Katsaros, "A singlet-triplet hole spin qubit in planar Ge", Nat. Mater. **20**, 1106 (2021).

[33] J. Fischer and D. Loss, "Hybridization and spin decoherence in heavy-hole quantum dots", Phys. Rev. Lett. **105**, 266603 (2010).

[34] F. Maier and D. Loss, "Effect of strain on hyperfine-induced hole-spin decoherence in quantum dots", Phys. Rev. B **85**, 195323 (2012).

[35] D. Klauser, W. A. Coish, and D. Loss, "Nuclear spin state narrowing via gate-controlled Rabi oscillations in a double quantum dot", Phys. Rev. B **73**, 205302 (2006).

[36] J. H. Prechtel, A. V. Kuhlmann, J. Houel, A. Ludwig, S. R. Valentin, A. D. Wieck, and R. J. Warburton, "Decoupling a hole spin qubit from the nuclear spins", Nat. Mater. **15**, 981 (2016).

[37] C. Testelin, F. Bernardot, B. Eble, and M. Chamarro, "Hole–spin dephasing time associated with hyperfine interaction in quantum dots", Phys. Rev. B **79**, 195440 (2009).

[38] J. Fischer, W. A. Coish, D. V. Bulaev, and D. Loss, "Spin decoherence of a heavy hole coupled to nuclear spins in a quantum dot", Phys. Rev. B **78**, 155329 (2008).

[39] W. M. Witzel and S. Das Sarma, "Quantum theory for electron spin decoherence induced by nuclear spin dynamics in semiconductor quantum computer architectures: spectral diffusion of localized electron spins in the nuclear solid-state environment", Phys. Rev. B **74**, 035322 (2006).

[40] W. Yao, R.-B. Liu, and L. J. Sham, "Theory of electron spin decoherence by interacting nuclear spins in a quantum dot", Phys. Rev. B **74**, 195301 (2006).

[41] Ł. Cywiński, W. M. Witzel, and S. Das Sarma, "Electron spin dephasing due to hyperfine interactions with a nuclear spin bath", Phys. Rev. Lett. **102**, 057601 (2009).

[42] A. V. Khaetskii, D. Loss, and L. Glazman, "Electron spin decoherence in quantum dots due to interaction with nuclei", Phys. Rev. Lett. **88**, 186802 (2002).

[43] W. A. Coish and D. Loss, "Hyperfine interaction in a quantum dot: Non-Markovian electron spin dynamics", Phys. Rev. B **70**, 195340 (2004).

[44] R. Hanson, L. P. Kouwenhoven, J. R. Petta, S. Tarucha, and L. M. K. Vandersypen, "Spins in few-electron quantum dots", Rev. Mod. Phys. **79**, 1217 (2007).

[45] S. Bosco and D. Loss, "Fully tunable hyperfine interactions of hole spin qubits in Si and Ge quantum dots", Phys. Rev. Lett. **127**, 190501 (2021).

[46] Y. Hu, H. O. H. Churchill, D. J. Reilly, J. Xiang, C. M. Lieber, and C. M. Marcus, "A Ge/Si heterostructure nanowire-based double quantum dot with integrated charge sensor", Nat. Nanotechnol. **2**, 622 (2007).

[47] K. Itoh, W. Hansen, E. Haller, J. Farmer, V. Ozhogin, A. Rudnev, and A. Tikhomirov, "High purity isotopically enriched ^{70}Ge and ^{74}Ge single crystals: isotope separation, growth, and properties", J. Mater. Res. **8**, 1341 (1993).

[48] K. M. Itoh and H. Watanabe, "Isotope engineering of silicon and diamond for quantum computing and sensing applications", MRS Commun. **4**, 143 (2014).

[49] D. V. Bulaev and D. Loss, "Spin relaxation and decoherence of holes in quantum dots", Phys. Rev. Lett. **95**, 076805 (2005).

[50] D. V. Bulaev and D. Loss, "Electric dipole spin resonance for heavy holes in quantum dots", Phys. Rev. Lett. **98**, 097202 (2007).

[51] C. Kloeffel, M. Trif, and D. Loss, "Acoustic phonons and strain in core/shell nanowires", Phys. Rev. B **90**, 115419 (2014).

[52] S. Bosco, M. Benito, C. Adelsberger, and D. Loss, "Squeezed hole spin qubits in Ge quantum dots with ultrafast gates at low power", Phys. Rev. B **104**, 115425 (2021).

[53] P. Philippopoulos, S. Chesi, D. Culcer, and W. A. Coish, "Pseudospin-electric coupling for holes beyond the envelope-function approximation", Phys. Rev. B **102**, 075310 (2020).

[54] V. P. Michal, B. Venitucci, and Y.-M. Niquet, "Longitudinal and transverse electric field manipulation of hole spin-orbit qubits in one-dimensional channels", Phys. Rev. B **103**, 045305 (2021).

[55] P. Stano, C.-H. Hsu, M. Serina, L. C. Camenzind, D. M. Zumbühl, and D. Loss, "g-factor of electrons in gate-defined quantum dots in a strong in-plane magnetic field", Phys. Rev. B **98**, 195314 (2018).

[56] P. Stano, C.-H. Hsu, L. C. Camenzind, L. Yu, D. Zumbühl, and D. Loss, "Orbital effects of a strong in-plane magnetic field on a gate-defined quantum dot", Phys. Rev. B **99**, 085308 (2019).

[57] Z. Wang, E. Marcellina, A. R. Hamilton, J. H. Cullen, S. Rogge, J. Salfi, and D. Culcer, "Optimal operation points for ultrafast, highly coherent Ge hole spin-orbit qubits", npj Quantum Inf. **7**, 54 (2021).

[58] J. M. Luttinger and W. Kohn, "Motion of electrons and holes in perturbed periodic fields", Phys. Rev. **97**, 869 (1955).

[59] J. M. Luttinger, "Quantum theory of cyclotron resonance in semiconductors: general theory", Phys. Rev. **102**, 1030 (1956).

[60] G. L. Bir and G. E. Pikus, *Symmetry and strain-induced effects in semiconductors* (Wiley, New York, 1974).

[61] P. Lawaetz, "Valence-band parameters in cubic semiconductors", Phys. Rev. B **4**, 3460 (1971).

[62] N. O. Lipari and A. Baldereschi, "Angular momentum theory and localized states in solids. Investigation of shallow acceptor states in semiconductors", Phys. Rev. Lett **25**, 1660 (1970).

[63] R. Li, "Low-energy subband wave-functions and effective g-factor of one-dimensional hole gas", J. Phys.: Condens. Mat. **33**, 355302 (2021).

[64] R. Li, "Searching strong 'spin'-orbit coupled one-dimensional hole gas in strong magnetic fields", J. Phys.: Condens. Mat. **34**, 075301 (2022).

[65] Y. A. Bychkov and E. I. Rashba, "Oscillatory effects and the magnetic susceptibility of carriers in inversion layers", J. Phys. C **17**, 6039 (1984).

[66] R. Winkler, D. Culcer, S. J. Papadakis, B. Habib, and M. Shayegan, "Spin orientation of holes in quantum wells", Semicond. Sci. Technol. **23**, 114017 (2008).

[67] R. Winkler, *Spin-orbit coupling effects in two-dimensional electron and hole systems* (Springer, Berlin, Oct. 10, 2003).

[68] J. Menéndez, R. Singh, and J. Drucker, "Theory of strain effects on the Raman spectrum of Si-Ge core-shell nanowires", Ann. Phys. **523**, 145 (2010).

[69] A. Sammak, D. Sabbagh, N. W. Hendrickx, M. Lodari, B. P. Wuetz, A. Tosato, L. Yeoh, M. Bollani, M. Virgilio, M. A. Schubert, P. Zaumseil, G. Capellini, M. Veldhorst, and G. Scappucci, "Shallow and undoped germanium quantum wells: a playground for spin and hybrid quantum technology", Adv. Funct. Mater. **29**, 1807613 (2019).

[70] B. Hetényi, C. Kloeffel, and D. Loss, "Exchange interaction of hole-spin qubits in double quantum dots in highly anisotropic semiconductors", Phys. Rev. Res. **2**, 033036 (2020).

[71] S. Bosco, B. Hetényi, and D. Loss, "Hole spin qubits in si FinFETs with fully tunable spin-orbit coupling and sweet spots for charge noise", PRX Quantum **2**, 010348 (2021).

[72] M. Milivojević, "Electrical control of the hole spin qubit in Si and Ge nanowire quantum dots", Phys. Rev. B **104**, 235304 (2021).

[73] D. Vion, A. Aassime, A.Cottet, P. Joyez, H. Pothier, C. Urbina, D. Esteve, and M. H. Devoret, "Manipulating the quantum state of an electrical circuit", Science **296**, 886 (2002).

[74] K. D. Petersson, J. R. Petta, H. Lu, and A. C. Gossard, "Quantum coherence in a one-electron semiconductor charge qubit", Phys. Rev. Lett. **105**, 246804 (2010).

[75] V. N. Golovach, M. Borhani, and D. Loss, "Electric-dipole-induced spin resonance in quantum dots", Phys. Rev. B **74**, 165319 (2006).

[76] O. Dmytruk and J. Klinovaja, "Suppression of the overlap between Majorana fermions by orbital magnetic effects in semiconducting-superconducting nanowires", Phys. Rev. B **97**, 155409 (2018).

[77] V. N. Golovach, A. Khaetskii, and D. Loss, "Phonon-induced decay of the electron spin in quantum dots", Phys. Rev. Lett. **93**, 016601 (2004).

[78] Y. Makhlin, G. Schön, and A. Shnirman, "Dissipative effects in Josephson qubits", Chem. Phys. **296**, 315 (2004).

[79] O. Malkoc, P. Stano, and D. Loss, "Charge-noise induced dephasing in silicon hole-spin qubits", Phys. Rev. Lett. **129**, 247701 (2022).

[80] S. Sachdev and J. Ye, "Gapless spin-fluid ground state in a random quantum Heisenberg magnet", Phys. Rev. Lett. **70**, 3339 (1993).

[81] S. Sachdev, "Bekenstein-Hawking entropy and strange metals", Phys. Rev. X **5**, 041025 (2015).

[82] A. Altland, D. Bagrets, and A. Kamenev, "Sachdev-Ye-Kitaev non-Fermi-liquid correlations in nanoscopic quantum transport", Phys. Rev. Lett. **123**, 226801 (2019).

CHAPTER 3

Enhanced orbital magnetic field effects in Ge hole nanowires

Adapted from:
Christoph Adelsberger, Stefano Bosco, Jelena Klinovaja, and Daniel Loss
"Enhanced orbital magnetic field effects in Ge hole nanowires",
Phys. Rev. B **106**, 235408 (2022)

Hole semiconductor nanowires (NW) are promising platforms to host spin qubits and Majorana bound states for topological qubits because of their strong spin-orbit interactions (SOI). The properties of these systems depend strongly on the design of the cross section and on strain, as well as on external electric and magnetic fields. In this paper, we analyze in detail the dependence of the SOI and g factors on the orbital magnetic field. We focus on magnetic fields aligned along the axis of the NW, where orbital effects are enhanced and result in a renormalization of the effective g factor up to 400 %, even at small values of magnetic field. We provide an exact analytical solution for holes in Ge NWs and we derive an effective low-energy model that enables us to investigate the effect of electric fields applied perpendicular to the NW. We also discuss in detail the role of strain, growth direction, and high-energy valence bands in different architectures, including Ge/Si core/shell NWs, gate-defined one-dimensional channels in planar Ge, and curved Ge quantum wells. By comparing NWs with different growth directions, we find that the isotropic approximation is well justified. Curved Ge quantum wells feature large effective g factors and SOI at low electric field, ideal for hosting Majorana bound states. In contrast, at strong electric field, these quantities are independent of the field, making hole spin qubits encoded in curved quantum wells to good approximation not susceptible to charge noise, and significantly boosting their coherence time.

3.1 Introduction

Semiconducting nanostructures based on holes are emerging as frontrunner candidates to process quantum information because of their large spin-orbit interaction (SOI) [1–6] that enables ultrafast and coherent manipulations of spin qubits [7–12], strong coupling to resonators [13–15], and is an essential ingredient to host exotic particles such as Majorana bound states (MBSs) [16, 17]. In hole nanostructures, the SOI is not only surprisingly strong, orders of magnitude larger than in electronic systems [1, 18, 19], but it is also highly tunable by external electromagnetic fields and it can be engineered by the confinement potential and by strain [20–28], resulting in sweet spots where the charge noise plaguing state-of-the-art spin qubits is strongly suppressed [29–31]. The qubit coherence is further enhanced by the weak hyperfine noise, another crucial issue for spin-based quantum information processing [32–37], that in hole spin qubits encoded in Si and Ge quantum dots (QDs) can be suppressed by isotopic purification [38, 39] or by an appropriate QD design [40–46].

In particular, the largest SOI arises in quasi-one-dimensional architectures, including Ge nanowires (NWs) [1, 9, 24, 47] and gate-defined squeezed QDs in planar heterostructures [25]. In these systems, experiments have shown a large proximity-induced superconductivity [48–50], making hole NWs promising candidates for topological quantum information processing based on MBSs [51–61]. A stable topological phase, however, also requires a large g factor, that allows to reach a sufficiently large Zeeman energy overcoming the induced superconducting gap even at the weak magnetic fields compatible with superconductors [17, 52, 59, 62, 63].

Orbital magnetic field effects play a crucial role in defining the property of hole nanostructures, yielding significant corrections of the g factor and of the effective mass in planar heterostructures [64, 65] as well as in NWs [28, 31, 66]. Orbital effects are also used to study the shape anisotropy in gate defined quantum dots [67]. In hole NWs, these effects are enhanced by magnetic fields that point along the direction of the NW, where we will show that they yield a renormalization of the g factor as large as 400%.

In this paper, we demonstrate the importance of orbital magnetic field effects in one-dimensional hole systems in Ge, see Fig. 3.1. We present an analytical solution, exactly including orbital effects, for low-energy holes in isotropic semiconductor NWs in the presence of a magnetic field parallel to the NW axis. This solution allows us to derive an effective low-energy model describing the effect of homogeneous and inhomogeneous electric fields perpendicular to the NW. Our model unravels the strong dependence of the g factor, SOI, and effective mass on external electromagnetic fields and on strain. We discuss the emergence of a spin-dependent mass term, that appears also at magnetic fields perpendicular to the NW axis [28].

Moreover, in Si/Ge core/shell NWs, strain is crucial to increase the subband gap between the lowest pair of energy states and the excited states [23, 24, 28]. We analyze its effect analytically and predict that strain enhances the g factor at the cost of weaker SOI. This effect is understood by introducing a strain-induced energy scale which in these systems favors a light hole (LH) ground state over mixed heavy hole (HH)-LH states.

We compare our analytical results for Ge NWs to numerical calculations of gate-defined one-dimensional channels in a planar heterostructure [25, 28] and curved Ge quantum wells (CQW) [31]. Gate-defined channels exhibit a smaller g factor and weaker SOI than in core/shell NWs, but with a similar qualitative behavior of the effective parameters against electric field and strain. In contrast, the response of the CQWs is strikingly different. In these architectures, the orbital magnetic field effects are extremely important because of their annular cross section, yielding large g factors and strong SOI at weak electric field, ideal to host MBSs. Moreover, we show that the g factor and the SOI remain constant in a wide range of strong electric fields, and thus CQWs are an ideal platform

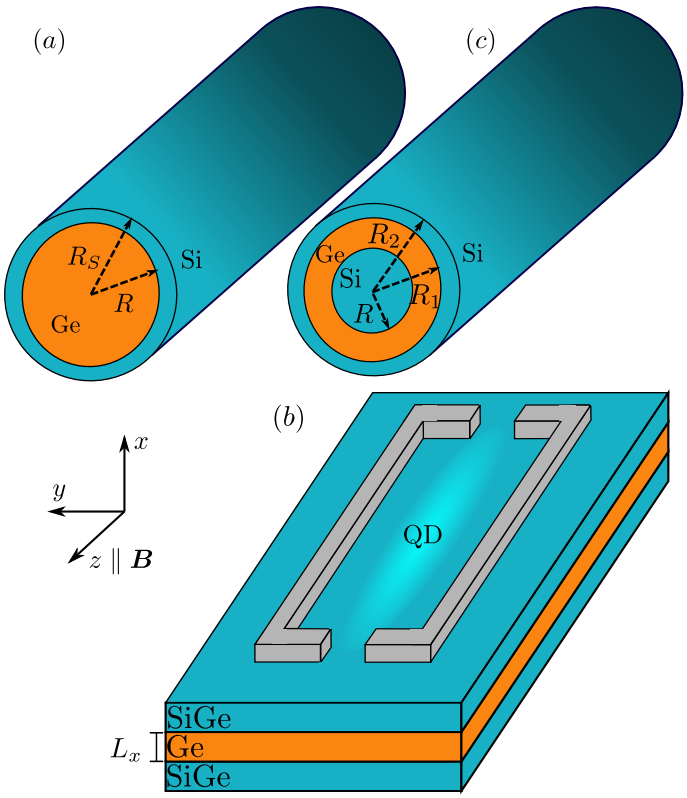

Figure 3.1: Sketches of the architectures analyzed. (a) Cylindrical NW with radius R extending along the z axis. The NW core (Ge) is covered by a shell (Si) that induces strain into the core. We denote by R_S the radius of the NW including the shell. (b) Sketch of a planar Ge/SiGe heterostructure with gate-defined one-dimensional channel. The Ge layer has width L_x and the channel is electrostatically defined by a harmonic confinement in the y direction with harmonic length l_y. (c) Sketch of a CQW: a NW with an annular cross section. The setup consists of a Si core of radius R covered by an inner Ge shell (radius R_1) that hosts the holes. Another Si layer (radius R_2) covers the Ge shell. Strain is induced into the Ge layer from the Si core and the outer Si shell. In all three cases we consider a magnetic field of strength $B = |\boldsymbol{B}|$ applied parallel to the z axis as indicated by the coordinate system.

to encode spin qubits, with a strongly suppressed susceptibility to charge noise, a crucial issue in core/shell NWs [18, 19].

Furthermore, we numerically analyze corrections to our model, focusing in particular on the influence of holes belonging to the spin-orbit split-off band (SOB) and on cubic anisotropies of the valence band, which are neglected in our analytical calculations. The SOB does not qualitatively alter our predictions and only changes the quantitative values of the parameters. Most notably, in narrow NWs, the SOB reduces the g factor significantly; the SOI is less affected by the SOB. Our analysis of anisotropies reveals that the isotropic approximation (IA) is well justified for the description of NWs grown along one of the main crystallographic axes, along the [110] (often used in experiments [68–70]), or along the [111] direction. This result further justifies the application of the IA in the rest of the paper.

This paper is organized as follows. In Sec. 3.2 we introduce the model used to describe low-energy holes in semiconductor NWs. Our analytical solution for a NW with magnetic field parallel to the NW taking orbital effects of the magnetic field exactly into account is derived and discussed in Sec. 3.3. We start with briefly showing the non-parabolic bulk dispersion relation in the presence of orbital effects and continue by adding hard-wall (HW) boundary conditions to model NWs with circular cross sections. Furthermore, we investigate the effective g factor, the direct Rashba SOI [22, 24], and the effective mass of the holes by considering an effective low-energy model to second order perturbation theory, also including homogeneous and inhomogeneous electric fields perpendicular to the NW. Moreover, we discuss how strain increases the g factor, the subband gap between ground state and excited states, and the effective mass, while it decreases the SOI and magnitude of the spin-dependent mass. In Sec. 3.4 we compare our results to numerically calculated effective parameters of a gate-defined one-dimensional channel defined in planar heterostructures. Likewise we study numerically holes in CQWs consisting of a Ge shell that hosts the holes around a Si core in Sec. 3.5. In Sec. 3.6 we extend our model for the NW by correcting terms and analyze its validity. In particular, we include the SOB and find that these states cause quantitative corrections to the effective parameters. Finally, we investigate the anisotropies in Ge/Si core/shell and CQWs. Conclusion and outlook are provided in Sec. 3.7. Details on the calculations are given in the Appendices.

3.2 Model of nanowire

In this section we present the theoretical model used in this paper. The general Hamiltonian modeling hole nanostructures in the presence of a magnetic field is given by

$$H = H_{\mathrm{LK}} + H_Z + H_{\mathrm{BP}} + V \ . \tag{3.1}$$

The Luttinger-Kohn (LK) Hamiltonian H_{LK} describes the mixing of HHs and LHs, and by including orbital magnetic field effects it is given by [24, 71–74]

$$\begin{aligned} H_{\mathrm{LK}} =& \frac{\hbar^2}{2m}\left[\gamma_k \pi^2 - 2\gamma_2(\pi_{x'}^2 J_{x'}^2 + \pi_{y'}^2 J_{y'}^2 + \pi_{z'}^2 J_{z'}^2)\right. \\ & \left. - 4\gamma_3\left(\{\pi_{x'}, \pi_{y'}\}\{J_{x'}, J_{y'}\} + \text{c.p.}\right)\right], \end{aligned} \tag{3.2}$$

where $\{A, B\} = (AB + BA)/2$, $\gamma_k = \gamma_1 + 5\gamma_2/2$, and "c.p." means cyclic permutations. The primed indices x', y', and z' denote the axes aligned to the main crystallographic axes [100], [010], and [001], respectively, and J_i [with $i = x', y', z'$] are the standard spin-3/2 operators. The HHs correspond to the spin component $\pm 3/2$ and the LHs to $\pm 1/2$ of J_z. The coefficients γ_1, γ_2, and γ_3 are the material-dependent Luttinger parameters [74] and m is the bare electron mass. Furthermore, the kinematic momentum operators in Eq. (3.2) include orbital effects of the magnetic field by the Peierls substitution [72]

$$\boldsymbol{\pi} = \boldsymbol{k} + \frac{e}{\hbar}\boldsymbol{A} \tag{3.3}$$

with canonical momenta $k_j = -i\hbar\partial_j$, positive elementary charge $e > 0$, and vector potential $\boldsymbol{A}$. The magnetic field $\boldsymbol{B}$ also splits the spin states by the Zeeman Hamiltonian

$$H_Z = 2\kappa\mu_B \boldsymbol{B}\cdot\boldsymbol{J} \ , \tag{3.4}$$

with $\kappa = 3.41$ in Ge. We neglect here the small anisotropic Zeeman energy $\propto J_i^3$ [24, 72]. In this paper we focus on magnetic fields aligned to the NW; a detailed analysis of perpendicular magnetic fields is provided in Ref. [28].

In Ge the Luttinger parameters $\gamma_1 = 13.35$, $\gamma_2 = 4.25$, and $\gamma_3 = 5.69$ [75] describe a relatively isotropic semiconductor with $(\gamma_3 - \gamma_2)/\gamma_1 \approx 0.1$, thus, we will often use the approximate isotropic Luttinger-Kohn (ILK) Hamiltonian

$$H_{\mathrm{ILK}} = \frac{\hbar^2}{2m}\left[\gamma_k \pi^2 - 2\gamma_s (\boldsymbol{k}\cdot\boldsymbol{J})^2\right] + H_{\mathrm{orb}}, \tag{3.5}$$

commonly adopted in literature [22, 24, 25, 73, 76, 77], with

$$\begin{aligned} H_{\mathrm{orb}} = \frac{\hbar e}{2m}\Bigg\{ & \gamma_k \left(\frac{e}{\hbar}\boldsymbol{A}^2 + 2\boldsymbol{k}\cdot\boldsymbol{A}\right) - \frac{2\gamma_s e}{\hbar}(\boldsymbol{A}\cdot\boldsymbol{J})^2 \\ & - 4\gamma_s \left[k_x A_x J_x^2 + (\{k_x, A_y\} + \{k_y, A_x\})\{J_x, J_y\} + \mathrm{c.p.}\right]\Bigg\}, \end{aligned} \tag{3.6}$$

where $\gamma_s = (\gamma_2 + \gamma_3)/2 = 4.97$. We stress that while our analysis here is restricted to Ge, our analytical results are valid more generally for holes in GaAs, InAs, or InSb, where the ILK is valid [74].

The quasi-one-dimensional system is defined by a confinement potential V that models the different NWs schematically depicted in Fig. 3.1. In this paper, we first consider a Ge/Si core/shell NW with cylindrical cross section [Fig. 3.1(a)]. The Ge NW of radius R is covered by a Si shell of thickness $R_S - R$, that produces a large strain on the Ge core. This strain is known to play a relevant role for the properties of the NW [23] and we include its effect by the Bir-Pikus (BP) Hamiltonian [78]. In this setup, the BP Hamiltonian is well-approximated by [24]

$$H_{\mathrm{BP}} = |b|\varepsilon_s J_{z'}^2. \tag{3.7}$$

The strain energy $|b|\varepsilon_s$, with $\varepsilon_s = \varepsilon_\perp - \varepsilon_{z'z'} > 0$, is typically positive [23] and it comprises the deformation potential $b = -2.5\,\mathrm{eV}$ [78] and the strain tensor elements $\varepsilon_\perp$ and $\varepsilon_{z'z'}$. Under the assumption of homogeneous strain in the core of the NW, these strain elements depend only on the relative shell thickness $\gamma = (R_S - R)/R$ [23, 79]. For the typical value $\gamma = 0.1$, one finds [23] $|b|\varepsilon_s = 15.5\,\mathrm{meV}$.

For the gate-defined one-dimensional channel in a planar Ge/SiGe heterostructure as depicted in Fig. 3.1(b), we consider a Ge layer with width L_x and confined in the y direction by a harmonic potential parametrized by the harmonic length l_y. This setup describes squeezed quantum dots in planar Ge [25, 28]. In this case, the strain due to the lattice mismatch between the Ge and SiGe layers results in the BP Hamiltonian [4, 30]

$$H_{\mathrm{BP}}^{\mathrm{ch}} = |b|\varepsilon_s J_x^2. \tag{3.8}$$

In contrast to the core/shell NW case [cf. Eq. (3.7)] the strain energy $|b|\varepsilon_s < 0$, and the strain favors a HH groundstate, with quantization axis perpendicular to the substrate. The strain energy can be engineered by the percentage of Si in the SiGe layers.

Moreover, we compare Ge/Si core/shell NWs to a CQW sketched in Fig. 3.1(c). The CQW consists of a Si core of radius R, a thin Ge shell of thickness $R_1 - R$ that hosts the holes, and an outer Si shell of thickness $R_2 - R_1$. In addition to the longitudinal strain typical of core/shell NWs [see Eq. (3.7)], the CQW is also subject to a radial strain that resembles the strain in planar heterostructures. Explicitly, the total BP Hamiltonian of CQWs is well-approximated by [31]

$$H_{\mathrm{BP}}^{\mathrm{CQW}} = |b|\left(\varepsilon_z J_z^2 - \varepsilon_r J_r^2\right) \tag{3.9}$$

where we define the radial spin-3/2 matrix as

$$J_r = \hat{\boldsymbol{e}}_{\boldsymbol{r}} \cdot \boldsymbol{J}, \tag{3.10}$$

with the unit vector in radial direction $\hat{\boldsymbol{e}}_{\boldsymbol{r}} = (\cos\theta, \sin\theta, 0)$. In Eq. (3.9) we approximate the longitudinal and radial strain energies as [31]

$$\varepsilon_z \approx \varepsilon_p \frac{R_1 - R}{R_1 + R} \left(1 - \frac{R_1 - R}{2(R_1 + R)} - \frac{(R_1 + R)^2}{2R_2^2}\right), \tag{3.11}$$

$$\varepsilon_r \approx \varepsilon_p \left(1 - \frac{R_1 - R}{R_1 + R}\right)^2, \tag{3.12}$$

respectively. We assume here $|b|\varepsilon_p \approx 140.8\,\mathrm{meV}$, a value which can be reduced by replacing the Si in the inner and outer shells by a $\mathrm{Si}_x\mathrm{Ge}_{1-x}$ alloy.

In order to study the validity of the ILK approximation in Eq. (3.5), we examine also the effect of the cubic anisotropies of the LK Hamiltonian in Eq. (3.2). In general, the behavior of the system depends on the growth direction of the NW. In this paper, we focus on a few important cases. Particularly relevant examples are NWs grown along the [001] axis, where the SOI is maximized or fully tunable [24, 29]. We also study NWs grown along the [110] crystallographic axis, consistent with several recent experiments [68–70]. Finally, we consider another relevant growth direction that is experimentally achievable [80–85], where the NW is grown along the $z \parallel [111]$ direction. The explicit form of the rotated LK Hamiltonian in these cases is reported in Ref. [28].

3.3 Analytical solution for Ge nanowires

In the following we utilize the ILK Hamiltonian from Eq. (3.5) to find an exact analytical description of low-energy holes in a Ge or a Ge/Si core/shell NW. Our approach fully accounts for orbital magnetic field effects that are typically neglected or included perturbatively [76, 77, 86, 87]. We find that, in Ge, these effects strongly renormalize the system response, and, thus, cannot be safely neglected even at weak magnetic fields. With the help of our analytical results, we analyze in detail the behavior of the system under the effect of both, electric and magnetic fields, and we include also strain in Ge/Si core/shell NWs.

To describe the analytical procedure, we begin with the analysis of the ILK Hamiltonian, cf. Eq. (3.5), in the bulk in Sec. 3.3.1. Therefore, we separate the ILK Hamiltonian into three parts according to their order in the momentum π_z [28]

$$H_{\mathrm{ILK}} = H_{xy} + H_{\mathrm{int}}\pi_z + H_{zz}\pi_z^2. \tag{3.13}$$

First, we present a simple approach where we derive the bulk solution for H_{xy} where the magnetic field is taken into account exactly since it is the starting point for the perturbation theory in π_z. However, in the bulk, we do not resort to perturbation theory but give an exact solution for the dispersion relation in Appendix 3.A. In Sec. 3.3.2, we proceed for a NW in analogy to the bulk by deriving an exact solution for H_{xy} including the orbital effects of the magnetic field exactly. This can be highly relevant because the effective g factor is considerably renormalized due to orbital effects even at weak magnetic field as discussed in Sec. 3.3.3. In the NW it is not as straightforward as in the bulk to find an exact solution for finite π_z. Thus, we develop an effective theory in perturbation theory in Sec. 3.3.4 and Sec. 3.3.5 following Ref. [24], where we discuss the effects of homogeneous and inhomogeneous electric fields. Finally, in Sec. 3.3.6 we discuss strain in Ge/Si core/shell NWs.

3.3.1 Bulk solution

For the following derivation of the bulk solution we assume a magnetic field along the z direction that we will identify with the NW axis in Sec. 3.3.2. The complete analytical solution of the bulk ILK Hamiltonian in this case is provided in Appendix 3.A, but the solution is rather complicated and not straightforwardly generalizable to NWs.

Instead, in this section we discuss a simpler approach, that will provide the starting point for our analysis of NWs. We restrict ourselves to the analysis of long wave length excitations, with a wave length $1/k_z$ much longer than the characteristic length defining the variation of the wave function in the x, y plane. In the bulk analysis, this condition means that $k_z l_B \ll 1$, where $l_B = \sqrt{\hbar/eB}$ is the magnetic length. At small values of k_z, the system is well described by the eigenstates of H_{xy}, and the k_z dependence can be studied by treating $H_{\rm int}$ and H_{zz} in perturbation theory.

To better study the magnetic orbital effects, we now neglect the Zeeman energy. To do so, we introduce the Landau ladder operator

$$a = \frac{\pi_x - i\pi_y}{\sqrt{2}} l_B, \tag{3.14}$$

obeying the canonical commutation relation $\left[a, a^\dagger\right] = 1$. In the spin basis (+3/2, −1/2, −3/2, +1/2), H_{xy} becomes

$$\frac{H_{xy}}{\hbar\omega_c} = \begin{pmatrix} \gamma_+ \left(a^\dagger a + \frac{1}{2}\right) & -\sqrt{3}\gamma_s a^2 \\ -\sqrt{3}\gamma_s \left(a^\dagger\right)^2 & \gamma_- \left(a^\dagger a + \frac{1}{2}\right) \end{pmatrix} \oplus \begin{pmatrix} \gamma_+ \left(a^\dagger a + \frac{1}{2}\right) & -\sqrt{3}\gamma_s \left(a^\dagger\right)^2 \\ -\sqrt{3}\gamma_s a^2 & \gamma_- \left(a^\dagger a + \frac{1}{2}\right) \end{pmatrix}, \tag{3.15}$$

where $\gamma_\pm = \gamma_1 \pm \gamma_s$ and the symbol "$\oplus$" refers to the direct sum of matrices. The energy is given here in units of $\hbar\omega_c$, with cyclotron frequency $\omega_c = eB/m$, and the lengths are in units of l_B. Focusing on the upper block ($\uparrow$) and solving the Schrödinger equation

$$\frac{1}{\sqrt{3}\gamma_s}\left[\gamma_+\left(a^\dagger a + \frac{1}{2}\right) - \varepsilon\right]\psi_{\rm HH} = a^2 \psi_{\rm LH}, \tag{3.16}$$

$$\frac{1}{\sqrt{3}\gamma_s}\left[\gamma_-\left(a^\dagger a + \frac{1}{2}\right) - \varepsilon\right]\psi_{\rm LH} = \left(a^\dagger\right)^2 \psi_{\rm HH}, \tag{3.17}$$

with the HH (LH) components of the wave function $\psi_{\rm HH(LH)}$ we find for the energy spectrum written in magnetic units

$$\varepsilon_\pm^\uparrow(\bar{n}) = \gamma_1\left(\bar{n} - \frac{1}{2}\right) \pm \sqrt{\gamma_1^2 + (1-2\bar{n})\gamma_1\gamma_s + \left[4\bar{n}(\bar{n}-1) + \frac{1}{4}\right]\gamma_s^2}, \tag{3.18}$$

where $\bar{n}$ is the eigenvalue of the number operator $a^\dagger a$. In the bulk solution, $\bar{n}$ is an integer because the wave function is required to vanish at infinity. In the absence of magnetic fields, time-reversal symmetry implies that for the energy spectrum of the lower block ($\downarrow$) is the same as for $\uparrow$.

Starting from these solutions for $\pi_z = 0$, we can proceed with a perturbation theory in π_z to find the dispersion relation for the different Landau level subbands. We will do such a perturbation theory in Secs. 3.3.4 and 3.3.5 for the NW. However, in the bulk case it is possible to derive an exact analytical solution that we provide in Appendix 3.A.

In Fig. 3.2 we compare the bulk dispersion relations of holes in Ge with and without orbital effects given in Appendix 3.A. The figure illustrates how the dispersion relation deviates from a

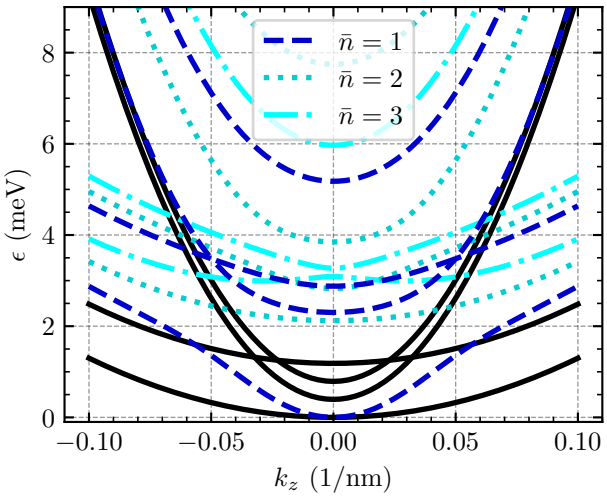

Figure 3.2: Comparison of the bulk dispersion relations of holes in Ge with (color lines) and without (black solid lines) orbital effects according to the analytical solution in Appendix 3.A. Eq. (3.18) gives the bulk energies of the upper block at $k_z = 0$ and $B = 0$. For the curves that include orbital effects, we consider $B = 1\,\mathrm{T}$ and we depict the dispersion relation for the lowest three $\bar{n}$ as indicated in the legend. Orbital effects modify the dispersion relation, yielding even a non-parabolic dispersion relation for the ground state. For the curves without orbital effects we choose $k_x = k_y = 0$.

parabolic spectrum (black lines) in the presence of orbital effects (color lines). Importantly, we stress that the orbital effects strongly renormalize the mass and even result in a non-parabolic dispersion of the ground state, as we can observe by comparing to the ground state without orbital magnetic fields (black lines).

3.3.2 Cylindrical nanowire with hard-wall confinement

In this subsection, we consider a cylindrical NW with radius R in a magnetic field $\boldsymbol{B} = (0, 0, B)$ in the z direction parallel to the NW, see Fig. 3.1(a). For now, we neglect the strain present in Ge/Si core/shell NWs and we will include it in Sec. 3.3.6. A convenient gauge in this case is the symmetric gauge $\boldsymbol{A} = (-y, x, 0)B/2$, which preserves the rotational invariance of the cross section. Thus the total angular momentum $I_z = s_z + L_z$, with effective spin s_z and orbital angular momentum L_z, is preserved too. Moreover, as $\boldsymbol{B} \parallel z$, the translational invariance along the NW is also preserved and $\pi_z = k_z$ is a good quantum number (QN). We assume a hard-wall (HW) confinement potential

$$V(r) = \begin{cases} 0, & r = \sqrt{x^2 + y^2} < R, \\ \infty, & \text{otherwise.} \end{cases} \tag{3.19}$$

Following the procedure described in Sec. 3.3.1, we find that at $k_z = 0$ the unnormalized wave function of the $\uparrow$ block of the Hamiltonian in Eq. (3.15) is given in the presence of the HW boundary

condition [see Eq. (3.19)] by

$$\Psi_m^{\uparrow} = \begin{pmatrix} \Psi_m^{+3/2} \\ \Psi_m^{-1/2} \end{pmatrix} = L^m_{\alpha_-^{\uparrow}}\left(\frac{R^2}{2}\right)\begin{pmatrix} \psi_{m,\alpha_+^{\uparrow}}(\boldsymbol{r}) \\ c_+^{\uparrow}\psi_{m-2,\alpha_+^{\uparrow}+2}(\boldsymbol{r}) \end{pmatrix} - L^m_{\alpha_+^{\uparrow}}\left(\frac{R^2}{2}\right)\begin{pmatrix} \psi_{m,\alpha_-^{\uparrow}}(\boldsymbol{r}) \\ c_-^{\uparrow}\psi_{m-2,\alpha_-^{\uparrow}+2}(\boldsymbol{r}) \end{pmatrix}, \quad (3.20)$$

where the first component of the spinor, $\Psi_m^{+3/2}$, corresponds to the HH spin $+3/2$ and the second, $\Psi_m^{-1/2}$, to the LH spin $-1/2$. Here, $L_\alpha^m(x)$ is the associated Laguerre function and

$$\psi_{m,\alpha}(\boldsymbol{r}) = i^m 2^{-\frac{m}{2}} e^{-im\varphi} e^{-\frac{r^2}{4}} r^m L_\alpha^m\left(\frac{r^2}{2}\right), \quad (3.21)$$

where $\boldsymbol{r}$ is given in polar coordinates with the radial coordinate r and the angle φ. A detailed derivation of this result is provided in Appendix 3.B. Note that all lengths are given in units of l_B. In analogy to the solution in Sec. 3.3.1, the spin QN is now substituted by a pseudo-spin that we denote by $\uparrow$ and $\downarrow$ referring to the two blocks of H_{xy} in Eq. (3.15). The additional QN m is an integer that is related to the total angular momentum QN I_z by $m = 2I_z + 1$. The coefficients $\alpha_\pm^{\uparrow}$ are given by

$$\begin{aligned} \alpha_\pm^{\uparrow} = \Bigg\{ & -\frac{3}{2}\gamma_1^2 + \gamma_1(\varepsilon - \frac{\kappa}{2}) + \gamma_s(6\gamma_s + \kappa) \\ & \pm \Bigg[\gamma_1^2\left(\gamma_1^2 - \frac{23}{4}\gamma_s^2 - 2\gamma_s\varepsilon\right) - \kappa(\gamma_1 - 2\gamma_s)\left[2\gamma_1^2 + 3\gamma_1\gamma_s - 2\gamma_s(\varepsilon + \gamma_s)\right] \\ & + \kappa^2(\gamma_1 + \gamma_s)(\gamma_1 - 2\gamma_s) + \gamma_s^2(7\gamma_s^2 + 8\gamma_s\varepsilon + 4\varepsilon^2)\Bigg]^{1/2}\Bigg\}/(\gamma_1^2 - 4\gamma_s^2), \end{aligned} \quad (3.22)$$

which are real numbers and depend on the Zeeman energy via κ. If $\alpha_\pm^s$, $s = \uparrow, \downarrow$, is an integer and $\kappa = 0$, we recover the bulk solution in Eq. (3.18). The coefficients $c_\pm^{\uparrow}$ are given by

$$c_\pm^{\uparrow} = \frac{(2\alpha_\pm^{\uparrow} + 1)(\gamma_1 + \gamma_s) + 3\kappa - 2\varepsilon}{2\sqrt{3}\gamma_s}. \quad (3.23)$$

Imposing the HW boundary conditions, which follow from Eq. (3.19), on the wave functions defined in Eq. (3.20), we find the implicit eigenvalue equation determining the energy $\varepsilon_m^s(n)$,

$$\frac{c_-^{\uparrow}}{c_+^{\uparrow}} = \frac{L^m_{\alpha_-^{\uparrow}}\left(\frac{R^2}{2}\right) L^{m-2}_{\alpha_+^{\uparrow}+2}\left(\frac{R^2}{2}\right)}{L^m_{\alpha_+^{\uparrow}}\left(\frac{R^2}{2}\right) L^{m-2}_{\alpha_-^{\uparrow}+2}\left(\frac{R^2}{2}\right)}. \quad (3.24)$$

Here we introduce an additional QN n to number the energies consecutively by their magnitude for each m. In analogy, for the $\downarrow$ block of H_{xy} in Eq. (3.15) describing the spin states $(-3/2, +1/2)$ we find the spinor

$$\Psi_m^{\downarrow} = \begin{pmatrix} \Psi_m^{-3/2} \\ \Psi_m^{+1/2} \end{pmatrix} = L^{-m}_{\alpha_-^{\downarrow}}\left(\frac{R^2}{2}\right)\begin{pmatrix} c_+^{\downarrow}\psi_{m-2,\alpha_+^{\downarrow}+2}(\boldsymbol{r}) \\ \psi_{m,\alpha_+^{\downarrow}}(\boldsymbol{r}) \end{pmatrix} - L^m_{\alpha_+^{\downarrow}}\left(\frac{R^2}{2}\right)\begin{pmatrix} c_-^{\downarrow}\psi_{m-2,\alpha_-^{\downarrow}+2}(\boldsymbol{r}) \\ \psi_{m,\alpha_-^{\downarrow}}(\boldsymbol{r}) \end{pmatrix}. \quad (3.25)$$

Together with the solution for the ↑ block this is the exact analytical solution for an isotropic semiconductor hole NW with circular cross section in a magnetic field parallel to the NW axis. The coefficients $\alpha_{\pm}^{\downarrow}$ and $c_{\pm}^{\downarrow}$ for the ↓ block are

$$\begin{aligned}\alpha_{\pm}^{\downarrow} =& \Bigg\{ -\frac{3}{2}\gamma_1^2 + \gamma_1(\varepsilon + \frac{\kappa}{2}) + \gamma_s(6\gamma_s - \kappa) \\ &\pm \left[\gamma_1^2\left(\gamma_1^2 - \frac{23}{4}\gamma_s^2 + 2\gamma_s\varepsilon\right) - \kappa(\gamma_1 - 2\gamma_s)\left[2\gamma_1^2 + 3\gamma_1\gamma_s + 2\gamma_s(\varepsilon - \gamma_s)\right]\right. \\ &\left. + \kappa^2(\gamma_1 + \gamma_s)(\gamma_1 - 2\gamma_s) + \gamma_s^2(7\gamma_s^2 - 8\gamma_s\varepsilon + 4\varepsilon^2)\right]^{1/2}\Bigg\}/(\gamma_1^2 - 4\gamma_s^2) \end{aligned} \tag{3.26}$$

and

$$c_{\pm}^{\downarrow} = \frac{(2\alpha_{\pm}^{\downarrow} + 1)(\gamma_1 - \gamma_s) + \kappa - 2\varepsilon}{2\sqrt{3}\gamma_s}. \tag{3.27}$$

The spinor in Eq. (3.25) immediately gives the dispersion relation similar to the one for the upper block in Eq. (3.24)

$$\frac{c_-^{\downarrow}}{c_+^{\downarrow}} = \frac{L_{\alpha_-^{\downarrow}+1}^{m-2}\left(\frac{R^2}{2}\right) L_{\alpha_+^{\downarrow}}^{m}\left(\frac{R^2}{2}\right)}{L_{\alpha_+^{\downarrow}+2}^{m-2}\left(\frac{R^2}{2}\right) L_{\alpha_-^{\downarrow}}^{m}\left(\frac{R^2}{2}\right)}. \tag{3.28}$$

The implicit Eqs. (3.24) and (3.28) are solved numerically, yielding the energies $\varepsilon_m^s(n)$. Note that the eigenstates depend on n via α.

3.3.3 Orbital corrections of the g factor

The analytical solution of H_{xy} [see Eq. (3.15)] obtained in the previous section includes exactly orbital and Zeeman effects and, thus, it allows us to directly derive the g factor of the NW. We demonstrate that the orbital magnetic fields lead to a correction of the g factor by 400 % and discuss the reason for this strong renormalization. Here, we focus on a rather large NW of radius $R = 20\,\mathrm{nm}$ where orbital effects are more pronounced.

Numerically solving Eq. (3.24) and Eq. (3.28), we directly calculate the g factor of the NW at $k_z = 0$. In Fig. 3.3(a) we present the energy spectrum of the NW as a function of the magnetic field given in units of the radius-dependent magnetic field $B_0 = \hbar/eR^2 = \Phi_0/\pi R^2 = 658.2\,\mathrm{T} \times \mathrm{nm}^2/\mathrm{R}^2$, which is one flux quantum $\Phi_0 = h/e$ through the cross section. We note that $B/B_0 = R^2/l_B^2$. By considering a NW of radius $R = 20\,\mathrm{nm}$, we obtain $B_0 = 1.65\,\mathrm{T}$.

For comparison we provide in Fig. 3.3(b) the spectrum for the same parameters without taking orbital effects into account ($\boldsymbol{A} = 0$). We calculate the spectrum by numerically diagonalizing the discretized version of the Hamiltonian in Eq. (3.1). In both plots, at weak magnetic fields, there is a large separation between the energies of the lowest two pairs of Kramers partners (orange and blue lines) and the states further above. Within the range up to $2\,B_0$ the ground state is close to the first excited state. However, only when orbital effects are taken into account, the first two pairs of former Kramers partners are coupled, resulting in an avoided crossing, which causes the orbital magnetic field induced reduction of the ground-state g factor.

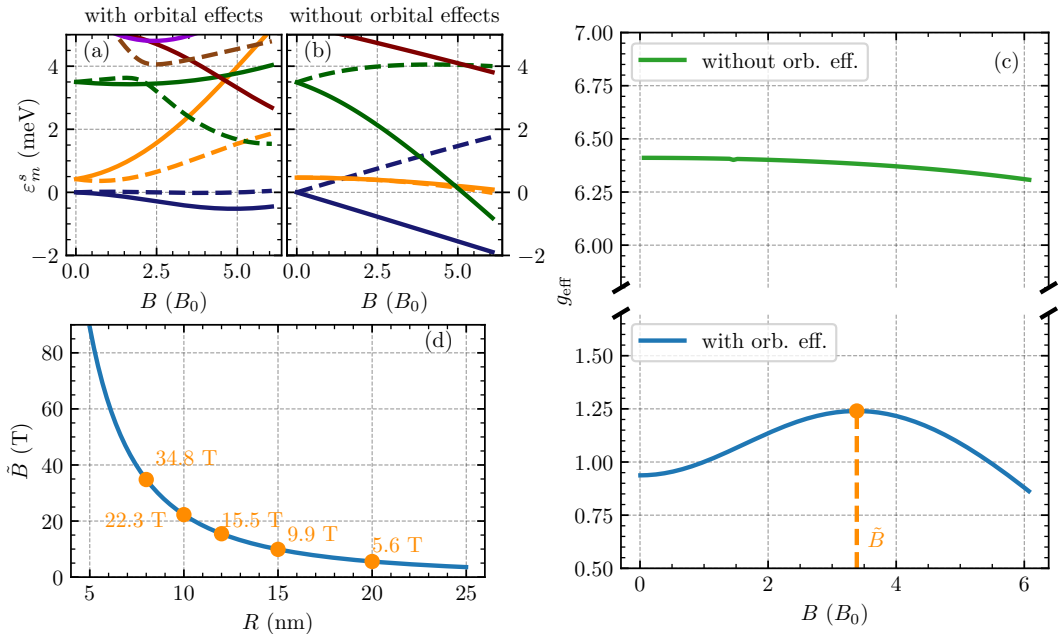

Figure 3.3: [(a),(b)] Energy spectrum of a Ge NW with circular cross section of radius $R = 20\,\text{nm}$ as a function of B in units of the radius-dependent magnetic field B_0 at $k_z = 0$. The colors indicate the Kramers partners. The solid (dashed) lines correspond to pseudospin $\uparrow$ ($\downarrow$) states. At $B = 0$ we observe Kramers degeneracy that is lifted by a finite magnetic field. (a) Energy spectrum calculated semi-analytically by numerically solving Eqs. (3.24) and (3.28), in which we include orbital effects. (b) Energy spectrum of the Hamiltonian H defined in Eq. (3.1) calculated by numerically diagonalizing the discretized version of the Hamiltonian in Eq. (3.1) neglecting orbital effects (lattice spacing 0.5 nm). The g factor is strongly renormalized due to orbital effects. (c) The effective g factor g_{eff} [see Eq. (3.29)] obtained numerically using the lowest two states (blue lines) of panels (a) and (b). The green line depicts the effective g factor without taking orbital effects into account, while the blue line does take them into account. The latter has a maximum at $\tilde{B} = 3.4\,B_0$. The effective g factor only depends on the ratio R^2/l_B^2 and is seen to be strongly reduced by orbital magnetic field effects. (d) The position $\tilde{B} = 3.4\,B_0$ of the maximum of the effective g factor from the panel (c) as a function of the radius R. For smaller radius the maximum is located at stronger magnetic field. The functional dependence $\tilde{B} \propto 1/R^2$ is indicated by the blue line.

From the energies in Figs. 3.3(a) and 3.3(b) we directly deduce the effective g factor as the difference between the $\downarrow$ and $\uparrow$ energies of the ground state Kramers partners

$$g_{\text{eff}} = \frac{\varepsilon_0^{\downarrow} - \varepsilon_2^{\uparrow}}{\mu_B B}. \tag{3.29}$$

Note that the QN m is different for the $\uparrow$ and $\downarrow$ ground states due to the operators a^2 and $(a^\dagger)^2$ in H_{xy} [see Eq. (3.15)]. In Fig. 3.3(c), we show the down-renormalization of the NW g factor by 400 % due to orbital effects. This large renormalization can be understood from the spectra shown in Figs. 3.3(a) and 3.3(b). At $B = 0$, the ground state Kramers pair (blue lines) is close to the first excited pairs (orange lines). At finite B, these pairs are coupled by orbital effects, yielding an

avoided crossing [cf. Fig. 3.3(a)] that strongly reduces the g factor. Note that for the calculation of the g factor without orbital effects we always take the difference between the dashed and solid blue line and ignore the crossing with higher energy Kramers partners (orange and green lines).

Interestingly, we observe a maximum of the effective g factor with orbital effects of $g_{\text{eff}} = 1.24$ at the magnetic field $B = \tilde{B} = 3.4\,B_0$, which decreases at larger values of R. This trend is illustrated in Fig. 3.3(d), where we show that $\tilde{B} \propto 1/R^2$. We also provide the values of $\tilde{B}$ for some specific radii and we conclude that the maximum of the g factor can be reached at realistic values of magnetic fields only in rather wide NWs.

3.3.4 Effective Hamiltonian

We use the exact solution of the Hamiltonian at $k_z = 0$ to construct a simple effective low-energy theory that models the dynamics of holes in NWs and long QDs. We treat the k_z-dependent terms, H_{zz} and H_{int}, of the full ILK Hamiltonian H_{ILK} in Eq. (3.13) as perturbation. Applying the definition of the Landau level operators a from Eq. (3.14), the interaction part H_{int} can be rewritten in the spin basis $(+3/2, -1/2, -3/2, +1/2)$ as

$$\frac{H_{\text{int}}}{\hbar\omega_c} = \sqrt{6}\gamma_s \begin{pmatrix} 0 & 0 & 0 & -a \\ 0 & 0 & a & 0 \\ 0 & a^\dagger & 0 & 0 \\ -a^\dagger & 0 & 0 & 0 \end{pmatrix} l_B. \tag{3.30}$$

Using Eqs. (3.20) and (3.25), we calculate the eigenfunctions of H_{xy} [see Eq. (3.15)] which we arrange in the four-dimensional spinors in the same spin basis

$$\varphi_m^\uparrow = \left(\Psi_m^{+3/2}, \Psi_m^{-1/2}, 0, 0\right), \tag{3.31}$$

$$\varphi_m^\downarrow = \left(0, 0, \Psi_m^{-3/2}, \Psi_m^{+1/2}\right). \tag{3.32}$$

In order to model the effects of external electric fields induced by the metallic gates, we consider a multipole expansion of the electrostatic potential. In particular, we consider a homogeneous electric field $\boldsymbol{E} = (E_x, E_y, 0)$ and a quadratic potential parametrized by a matrix δE_{ij}. Explicitly, we consider the electrostatic energy in the form

$$\begin{aligned} H_E &= eE_x r\cos\varphi + eE_y r\sin\varphi \\ &+ \frac{e}{2}(\delta E_{xx}\cos^2\varphi + \delta E_{yy}\sin^2\varphi + \delta E_{xy}\cos\varphi\sin\varphi)r^2. \end{aligned} \tag{3.33}$$

This potential accurately describes the electrostatic potential in several experimental setups comprising multiple gates [29]. As we are studying an isotropic NW with circular cross section, without loss of generality, we now fix the direction of the homogeneous field to the x direction ($E_y = 0$). The inhomogeneous term can be neglected in narrow NWs, while in thick NWs the inhomogeneous electric field becomes relevant and we include it in our analysis.

The low-energy holes are well described by an effective Hamiltonian comprising the three lowest Kramers partners. Explicitly, this Hilbert space is spanned by the six component basis $(\varphi_2^\uparrow, \varphi_1^\uparrow, \varphi_0^\uparrow, \varphi_0^\downarrow, \varphi_1^\downarrow, \varphi_2^\downarrow)$ consisting of the lowest six states in Fig. 3.3(a) (at $B = 0$). The states correspond to the solid-blue, solid-orange, solid-green, dashed-blue, dashed-orange, and dashed-green lines in Fig. 3.3 in the order as they appear in the basis. For all these states the QN is $n = 1$ and if

not stated otherwise we assume $n = 1$ in the following. States with larger n lie at higher energies and, thus, are neglected here. In this basis the effective Hamiltonian $H_{\mathrm{LK}}^{\mathrm{eff}}$ can be expressed as

$$H_{\mathrm{LK}}^{\mathrm{eff}} = \begin{pmatrix} \frac{\hbar^2 k_z^2}{2m_2^{\uparrow}} + \varepsilon_2^{\uparrow} + q_2^{\uparrow}\delta E_+ & id_1^{\uparrow}E_x & q^{\uparrow}\delta E_- & 0 & \alpha_1 k_z & 0 \\ -id_1^{\uparrow}E_x & \frac{\hbar^2 k_z^2}{2m_1^{\uparrow}} + \varepsilon_1^{\uparrow} + q_1^{\uparrow}\delta E_+ & id_2^{\uparrow}E_x & \alpha_2 k_z & 0 & 0 \\ q^{\uparrow}\delta E_-^* & -id_2^{\uparrow}E_x & \frac{\hbar^2 k_z^2}{2m_0^{\uparrow}} + \varepsilon_0^{\uparrow} + q_0^{\uparrow}\delta E_+ & 0 & 0 & 0 \\ 0 & \alpha_2 k_z & 0 & \frac{\hbar^2 k_z^2}{2m_0^{\downarrow}} + \varepsilon_0^{\downarrow} + q_0^{\downarrow}\delta E_+ & id_1^{\downarrow}E_x & q^{\downarrow}\delta E_- \\ \alpha_1 k_z & 0 & 0 & -id_1^{\downarrow}E_x & \frac{\hbar^2 k_z^2}{2m_1^{\downarrow}} + \varepsilon_1^{\downarrow} + q_1^{\downarrow}\delta E_+ & id_2^{\downarrow}E_x \\ 0 & 0 & 0 & q^{\downarrow}\delta E_-^* & -id_2^{\downarrow}E_x & \frac{\hbar^2 k_z^2}{2m_2^{\downarrow}} + \varepsilon_2^{\downarrow} + q_2^{\downarrow}\delta E_+ \end{pmatrix}, \tag{3.34}$$

where we defined

$$\delta E_+ = \delta E_{xx} + \delta E_{yy}, \tag{3.35}$$

$$\delta E_- = \delta E_{xx} - \delta E_{yy} - i\delta E_{xy}. \tag{3.36}$$

We note that the parameters $d_{1,2}^{\uparrow,\downarrow}$, $q^{\uparrow,\downarrow}$, $q_{0,1,2}^{\uparrow,\downarrow}$, and $\alpha_{1,2}$ are real and will be defined explicitly below. The energies

$$\varepsilon_m^s = \langle \varphi_m^s | H_{xy} + H_Z + V | \varphi_m^s \rangle \tag{3.37}$$

($s = \uparrow, \downarrow$) are obtained numerically from the implicit relations in Eqs. (3.24) and (3.28). The expressions for effective masses m_i^s ($i = 0, 1, 2$) consist of two contributions. The first one arises from H_{zz} as $\langle \varphi_i^s | H_{zz} | \varphi_j^s \rangle$, which simplifies to the matrix elements with $i = j$, since in our case there are only diagonal matrix entries. The second contribution of order k_z^2 arises from H_{int} in second-order perturbation theory and is also diagonal. The total effective mass is then given by [29]

$$\frac{\hbar^2}{2m_i^s} = \langle \varphi_i^s | H_{zz} | \varphi_i^s \rangle + \sum_{l,n} \frac{|\langle \varphi_i^s | H_{\mathrm{int}} | \varphi_l^s(n) \rangle|^2}{\varepsilon_i^s - \varepsilon_l^s(n)}. \tag{3.38}$$

The sum runs over all states outside the considered subspace. We observe strong couplings $\langle \varphi_i^s | H_{\mathrm{int}} | \varphi_l^s(n) \rangle$ to states with large n that lead to considerable perturbative contributions to the effective mass. Thus, to ensure the convergence of the perturbation theory numerically, we take into account states up to $n = 10$.

Next, we calculate the SOI terms that couple the $\uparrow$ and $\downarrow$ blocks as the following overlaps between HH and LH states:

$$\alpha_1 = \sqrt{6}\gamma_s \hbar\omega_c l_B \left(\left\langle \Psi_2^{-1/2} \middle| a \middle| \Psi_1^{-3/2} \right\rangle - \left\langle \Psi_2^{+3/2} \middle| a \middle| \Psi_1^{+1/2} \right\rangle \right), \tag{3.39}$$

$$\alpha_2 = \sqrt{6}\gamma_s \hbar\omega_c l_B \left(\left\langle \Psi_1^{-1/2} \middle| a \middle| \Psi_0^{-3/2} \right\rangle - \left\langle \Psi_1^{+3/2} \middle| a \middle| \Psi_0^{+1/2} \right\rangle \right). \tag{3.40}$$

The electric dipole moments, which result from the first term of Eq. (3.33), are given by

$$d_1^s = \frac{e}{2i} \left(\left\langle \Psi_2^{\pm 3/2} \middle| r \middle| \Psi_1^{\pm 3/2} \right\rangle + \left\langle \Psi_2^{\mp 1/2} \middle| r \middle| \Psi_1^{\mp 1/2} \right\rangle \right), \tag{3.41}$$

$$d_2^s = \frac{e}{2i} \left(\left\langle \Psi_1^{\pm 3/2} \middle| r \middle| \Psi_0^{\pm 3/2} \right\rangle + \left\langle \Psi_1^{\mp 1/2} \middle| r \middle| \Psi_0^{\mp 1/2} \right\rangle \right), \tag{3.42}$$

and the quadrupole moments from the second term are given by

$$q^s = \frac{e}{8}\left(\left\langle \Psi_2^{\pm 3/2}\middle| r^2 \middle|\Psi_0^{\pm 3/2}\right\rangle + \left\langle \Psi_2^{\mp 1/2}\middle| r^2 \middle|\Psi_0^{\mp 1/2}\right\rangle\right) \tag{3.43}$$

and

$$q_i^s = \frac{e}{4}\left(\left\langle \Psi_i^{\pm 3/2}\middle| r^2 \middle|\Psi_i^{\pm 3/2}\right\rangle + \left\langle \Psi_i^{\mp 1/2}\middle| r^2 \middle|\Psi_i^{\mp 1/2}\right\rangle\right) \tag{3.44}$$

$(i = 0, 1, 2)$.

For a discussion of the behavior of the effective parameters as a function of the magnetic field we refer to Appendix 3.C. In the next section, we construct an effective low-energy theory of the two lowest energy states by integrating out the states at higher energy.

3.3.5 2×2 wire Hamiltonian

To obtain a simple NW Hamiltonian describing the two states lowest in energy, we start with the Hamiltonian $H_{\mathrm{LK}}^{\mathrm{eff}}$ introduced in Eq. (3.34), resort to a second order perturbation theory, and project onto the low-energy 2×2 subspace. This procedure is well justified when the energy scale characterizing the holes in the z direction is much smaller than the subband gap $\varepsilon_0^{\downarrow} - \varepsilon_1^{\downarrow}$. Without strain and at weak B field, this condition puts a strong constraint on the possible confinement energy in the z direction because the subband energy gap is rather small, cf. Fig. 3.3(a). Larger values of the confinement along the NW can be achieved at stronger B fields or by considering strain, as we discuss in Sec. 3.3.6. We now focus on the effect of the electrostatic potential.

Homogeneous electric field limit

We first consider a homogeneous electric field E_x. Since we are interested in the ground-state $(\varphi_2^{\uparrow}, \varphi_0^{\downarrow})$, we can restrict ourselves to the analysis of the ground state pair and the pair of states $(\varphi_1^{\uparrow}, \varphi_1^{\downarrow})$ coupled to it via the SOI $\alpha_{1,2}$ and the dipole coupling d_1^s. The states $\varphi_0^{\uparrow}$ and $\varphi_2^{\downarrow}$ are decoupled from the ground state, and thus we assume that they have only a weak influence. We also introduce the following averages and differences of energies

$$\varepsilon_{\pm}^{\uparrow} = \frac{\varepsilon_1^{\uparrow} \pm \varepsilon_2^{\uparrow}}{2}, \tag{3.45}$$

$$\varepsilon_{\pm}^{\downarrow} = \frac{\varepsilon_1^{\downarrow} \pm \varepsilon_0^{\downarrow}}{2}. \tag{3.46}$$

Additionally, we define the angles

$$\tan\theta^s = \frac{\varepsilon_-^s + \Omega^s}{d_1^s E_x} \tag{3.47}$$

with $s = \uparrow, \downarrow$ and with the energies

$$\Omega^s = \sqrt{\left(d_1^s E_x\right)^2 + \left(\varepsilon_-^s\right)^2} \tag{3.48}$$

being dependent on the electric field E_x. Next, we rotate the $\uparrow$ and $\downarrow$ blocks by $\theta^{\uparrow}$ and $\theta^{\downarrow}$, respectively, as described in Appendix 3.D. Working with second-order perturbation theory and projecting the results onto the ground-state subspace $(\varphi_2^{\uparrow}, \varphi_0^{\downarrow})$, we obtain up to second order in k_z

$$H^{2\times 2} = \frac{\hbar^2}{2\bar{m}} k_z^2 + \frac{1}{2}\left(g_{\mathrm{eff}}\mu_B B + \frac{\hbar^2 k_z^2}{\delta m}\right)\sigma_z - \alpha_{so} k_z \sigma_y. \tag{3.49}$$

In some cases a cubic SOI term becomes relevant, which requires to extend the perturbation theory to third order [88]. The effective g factor is electric field dependent and is given by

$$\mu_B B g_{\text{eff}} = \varepsilon_+^{\downarrow} - \varepsilon_+^{\uparrow} - \Omega^{\downarrow} + \Omega^{\uparrow}. \tag{3.50}$$

Moreover, the direct Rashba SOI [22, 24] is given by

$$\begin{aligned} \alpha_{so} =& \alpha_1 \cos\left(\theta^{\downarrow}\right) \sin\left(\theta^{\uparrow}\right) - \alpha_2 \cos\left(\theta^{\uparrow}\right) \sin\left(\theta^{\downarrow}\right) && (3.51)\\ =& \frac{d_1^{\downarrow}\alpha_1\varepsilon_-^{\uparrow} - d_1^{\uparrow}\alpha_2\varepsilon_-^{\downarrow}}{\varepsilon_-^{\downarrow}\varepsilon_-^{\uparrow}} E_x + \mathcal{O}(E_x^3), && (3.52) \end{aligned}$$

and it is linear at weak electric field. We also introduce the average effective mass

$$\begin{aligned} \frac{1}{\bar{m}} =& \frac{m_1^{\uparrow} + m_2^{\uparrow} - (m_1^{\uparrow} - m_2^{\uparrow})\cos\left(2\theta^{\uparrow}\right)}{4m_1^{\uparrow}m_2^{\uparrow}} + \frac{m_0^{\downarrow} + m_1^{\downarrow} + (m_0^{\downarrow} - m_1^{\downarrow})\cos\left(2\theta^{\downarrow}\right)}{4m_0^{\downarrow}m_1^{\downarrow}} \\ & - \frac{m}{\hbar\omega_c l_B^2}\left(\frac{\left[\alpha_1 \sin\left(\theta^{\uparrow}\right)\sin\left(\theta^{\downarrow}\right) + \alpha_2 \cos\left(\theta^{\uparrow}\right)\cos\left(\theta^{\downarrow}\right)\right]^2}{\varepsilon_+^{\downarrow} - \varepsilon_+^{\uparrow} + \Omega^{\uparrow} + \Omega^{\downarrow}} \right. \\ & \left. + \frac{\left[\alpha_1 \cos\left(\theta^{\uparrow}\right)\cos\left(\theta^{\downarrow}\right) + \alpha_2 \sin\left(\theta^{\uparrow}\right)\sin\left(\theta^{\downarrow}\right)\right]^2}{\varepsilon_+^{\uparrow} - \varepsilon_+^{\downarrow} + \Omega^{\uparrow} + \Omega^{\downarrow}} \right), \end{aligned} \tag{3.53}$$

and the spin-dependent mass

$$\begin{aligned} \frac{1}{\delta m} =& \frac{m_1^{\uparrow} + m_2^{\uparrow} - (m_1^{\uparrow} - m_2^{\uparrow})\cos\left(2\theta^{\uparrow}\right)}{4m_1^{\uparrow}m_2^{\uparrow}} - \frac{m_0^{\downarrow} + m_1^{\downarrow} + (m_0^{\downarrow} - m_1^{\downarrow})\cos\left(2\theta^{\downarrow}\right)}{4m_0^{\downarrow}m_1^{\downarrow}} \\ & + \frac{m}{\hbar\omega_c l_B^2}\left(\frac{\left[\alpha_1 \cos\left(\theta^{\uparrow}\right)\cos\left(\theta^{\downarrow}\right) + \alpha_2 \sin\left(\theta^{\uparrow}\right)\sin\left(\theta^{\downarrow}\right)\right]^2}{\varepsilon_+^{\uparrow} - \varepsilon_+^{\downarrow} + \Omega^{\uparrow} + \Omega^{\downarrow}} \right. \\ & \left. - \frac{\left[\alpha_1 \sin\left(\theta^{\uparrow}\right)\sin\left(\theta^{\downarrow}\right) + \alpha_2 \cos\left(\theta^{\uparrow}\right)\cos\left(\theta^{\downarrow}\right)\right]^2}{\varepsilon_+^{\downarrow} - \varepsilon_+^{\uparrow} + \Omega^{\uparrow} + \Omega^{\downarrow}} \right). \end{aligned} \tag{3.54}$$

We note that both masses δm and $\bar{m}$ inherit an electric field dependence by the angles θ^s and energies Ω^s.

In Fig. 3.4(a), we study the effective g factor g_{eff} as a function of the electric field E_x for different values of the magnetic field B (solid lines). For a comparison we provide results from numerical calculations (dots) where we diagonalize the discretized version of the Hamiltonian in Eq. (3.1) including the homogeneous electric field given by Eq. (3.33). The comparison shows that the perturbation theory gives a good estimate for g_{eff} at weak electric field. At $E_x \approx 0.25\,\text{V}\,\mu\text{m}^{-1}$ ($E_x \approx 0.5\,\text{V}\,\mu\text{m}^{-1}$ and $B \geq 5\,\text{T}$) the perturbation theory starts to fail and predicts an unphysical increase of g_{eff}. The effective SOI [cf. Fig. 3.4(b)] α_{so} increases linearly at weak E_x according to Eq. (3.52) [illustrated by the dashed lines in Fig. 3.4(b)], and it saturates at stronger electric field ($E_x \gtrsim 0.5\,\text{V}\,\mu\text{m}^{-1}$). Due to orbital effects, we observe a decrease of α_{so} with increasing magnetic field. For the realization of MBSs in the Ge NW, a weak electric field is favorable because there the effective g factor is not so strongly suppressed, enabling to reach the topological phase [52, 54, 58, 89] at lower magnetic fields, away from the critical magnetic field of the superconductor. We note that, if the NW is in proximity to the thin bulk superconductor, there will be an additional renormalization of NW parameters, so-called metallization [90–95], which needs to be taken into account.

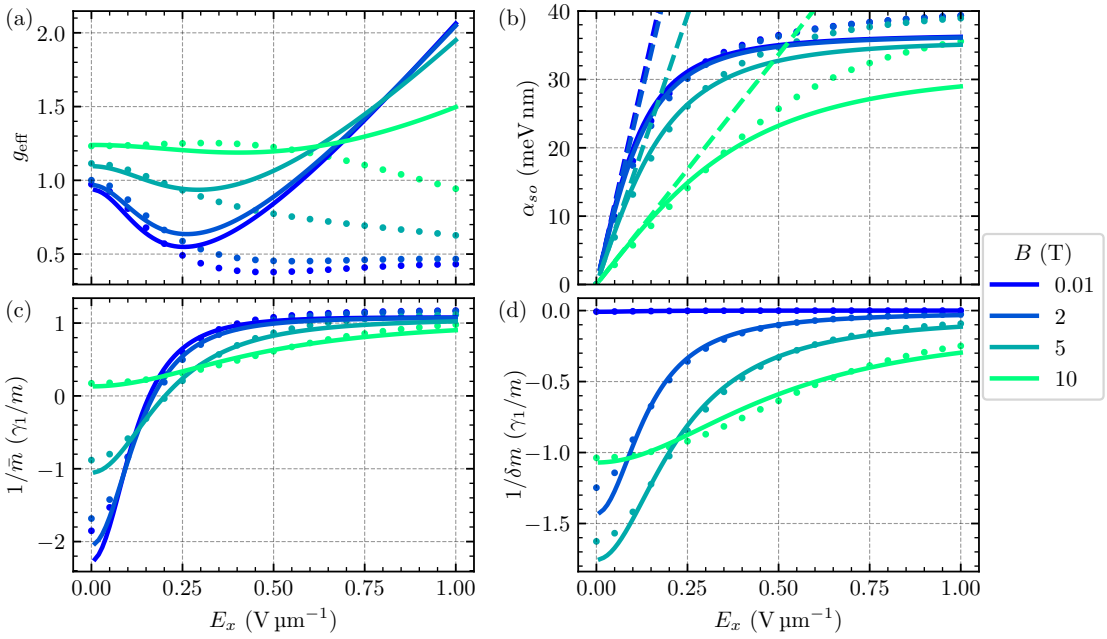

Figure 3.4: Effective parameters of the effective 2×2 model $H^{2\times2}$ (solid lines) as a function of the homogeneous electric field E_x for a Ge NW with radius $R = 15\,\text{nm}$. The dots show the same parameters calculated numerically with the Hamiltonian in Eq. (3.1) discretized in real space (lattice spacing 0.25 nm). (a) Effective g factor g_{eff} according to Eq. (3.50). At weak B, the results from perturbation theory are valid only at rather weak electric fields ($E_x < 0.25\,\text{V}\,\mu\text{m}^{-1}$) while at strong B, the perturbation theory can be extended to $E_x < 0.5\,\text{V}\,\mu\text{m}^{-1}$. At stronger electric field the perturbative g factor increases unphysically, while it should decrease and stay at a small value as the numerical results show. (b) The effective SOI coefficient α_{so} [cf. Eq. (3.51)] exhibits a linear behavior at weak electric field as provided by the expansion of Eq. (3.52). At stronger electric field α_{so} saturates and with increasing B it decreases due to orbital effects. (c) Inverse average effective mass $1/\bar{m}$ from Eq. (3.53) and (d) inverse spin-dependent mass $1/\delta m$ from Eq. (3.54). The average mass can take negative values at weak electric field and approaches the average HH-LH mass m/γ_1 at stronger E_x. The spin-dependent mass is zero at $B = 0$ due to time-reversal symmetry and decreases with E_x at $B \neq 0$. The electric field dependence of the mass terms and the SOI is captured well by the perturbation theory up to $E_x = 1\,\text{V}\,\mu\text{m}^{-1}$. However, α_{so} is underestimated for strong electric fields. The mass terms from numerical calculations deviate visibly from the perturbative result at $E_x = 0$ due to the limited number of states that can be taken into account for the calculation of the term coming from H_{int} in Eq. (3.38) in the numerics.

In addition, in Figs. 3.4(c) and 3.4(d), we present the inverse average effective mass $1/\bar{m}$ and spin-dependent mass $1/\delta m$, respectively. Interestingly, the inverse average mass is negative at weak electric field $E_x \lesssim 0.2\,\text{V}\,\mu\text{m}^{-1}$ and $B \lesssim 9\,\text{T}$. It approaches the average HH-LH mass γ_1/m at stronger electric fields. As expected from time-reversal symmetry at $B = 0$, the inverse spin-dependent mass term $1/\delta m = 0$ [28]. It is relevant only at weak electric fields and we observe that it vanishes at strong E_x. We find a simple formula for the inverse effective masses in the limit

$E_x \to 0$,

$$\lim_{E_x\to 0} \bar{m}^{-1} = \frac{m_0^{\downarrow}+m_2^{\uparrow}}{2m_0^{\downarrow}m_2^{\uparrow}} - \frac{m}{\hbar\omega_c l_B^2}\left(\frac{2\alpha_1^2}{\varepsilon_+^{\uparrow}-\varepsilon_+^{\downarrow}+\left|\varepsilon_-^{\uparrow}\right|+\left|\varepsilon_-^{\downarrow}\right|}+\frac{2\alpha_2^2}{-\varepsilon_+^{\uparrow}+\varepsilon_+^{\downarrow}+\left|\varepsilon_-^{\uparrow}\right|+\left|\varepsilon_-^{\downarrow}\right|}\right), \tag{3.55}$$

$$\lim_{E_x\to 0} \delta m^{-1} = \frac{m_0^{\downarrow}-m_2^{\uparrow}}{2m_0^{\downarrow}m_2^{\uparrow}} + \frac{m}{\hbar\omega_c l_B^2}\left(\frac{2\alpha_2^2}{-\varepsilon_+^{\uparrow}+\varepsilon_+^{\downarrow}+\left|\varepsilon_-^{\uparrow}\right|+\left|\varepsilon_-^{\downarrow}\right|}-\frac{2\alpha_1^2}{\varepsilon_+^{\uparrow}-\varepsilon_+^{\downarrow}+\left|\varepsilon_-^{\uparrow}\right|+\left|\varepsilon_-^{\downarrow}\right|}\right). \tag{3.56}$$

These formulas make manifest that the spin-dependent mass is dominated by the average mass of the states $\varphi_0^{\downarrow}$ and $\varphi_2^{\uparrow}$ $(m_0^{\downarrow} \pm m_2^{\uparrow})/2m_0^{\downarrow}m_2^{\uparrow}$, but it acquires a correction by the SOI coefficients $\alpha_{1,2}$. The results for the SOI and the mass terms from perturbation theory agree well with the numerical results in the displayed range of electric field; the SOI is underestimated at strong E_x by the perturbation theory.

Inhomogeneous electric field

In thick NWs, the approximation of a homogeneous electric field is not well-justified and there can be corrections arising from inhomogeneity of the electric field [29], captured by the Hamiltonian $H_{\mathrm{LK}}^{\mathrm{eff}}$ defined in Eq. (3.34). For simplicity we neglect the inhomogeneous electric field term δE_{xy} in Eq. (3.33) since the final results for the effective parameters only depend on the absolute value of the total inhomogeneous electric field. We find that the quadrupole moment terms can strongly renormalize the effective parameters, in particular, the g factor at weak E_x.

In analogy to the homogeneous electric field limit, we derive an effective Hamiltonian $H^{2\times 2}$ for the lowest two states in second order perturbation theory. We arrive at the same form of the effective 2×2 Hamiltonian as in Eq. (3.49). However, the effective masses and the SOI depend now also on the electric field gradient $\delta E_{\pm}$, see Fig. 3.5. The electric field dependence of the effective parameters is calculated perturbatively starting from the analytical result at $E_x = \delta E_{xx} = \delta E_{yy} = 0$. We analyze the same electric field range as in Fig. 3.4 and focus on weak inhomogeneous electric fields, where the qualitative dependence on E_x stays as for $\delta E_{xx} = \delta E_{yy} = 0$. The effect of the inhomogeneous electric field on the effective parameters displayed in Fig. 3.5 is strong at weak homogeneous electric field. The main effect is coming from the diagonal quadrupole moment terms q_i^s $(i = 0, 1, 2)$ which cause an enhancement of the subband gap between the lowest Kramers pair and the states higher in energy. This enhancement results in a significant renormalization of the g factor at $\delta E_{xx} = \delta E_{yy} = 10\,\mathrm{V\,\mu m^{-2}}$ where the off-diagonal quadrupole moment terms in the Hamiltonian in Eq. (3.34) vanish. The effective g factor and the masses tend closer to zero with increasing inhomogeneous electric field at $E_x = 0$. For the g factor this effect is overestimated by the effective model while it is underestimated for the mass terms as the comparison to the numerical results (dots) shows. As expected from Fig. 3.4(a) the effective model fails to predict the electric field dependence of the effective g factor at strong homogeneous electric field correctly. However, the effective model describes the SOI and the mass terms well.

3.3.6 Strain

In Ge/Si core/shell NWs, strain is a crucial feature required to increase the subband energy gap between the lowest Kramers pair and the excited states [23, 24, 28]. A large subband gap is required to define QDs because it ensures that the effective theory of $H^{2\times 2}$ defined in Eq. (3.49) is accurate even in short quantum dots with a large confinement potential along the z direction.

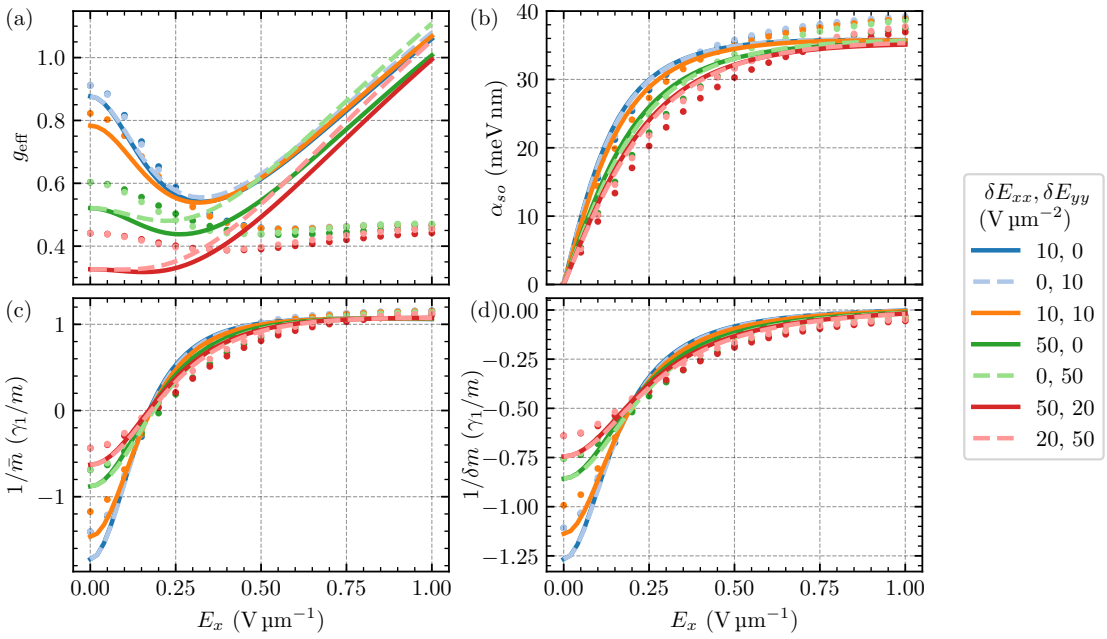

Figure 3.5: Effective parameters of the 2×2 model described by $H^{2\times2}$ in Eq. (3.49) for a circular Ge NW are shown here, including an inhomogeneous electric field δE_{xx} and δE_{yy} calculated perturbatively (solid and dashed lines) and numerically by diagonalizing the Hamiltonian in Eq. (3.1) including the inhomogeneous electric field term in Eq. (3.33) discretized in real space (dots) at $B = 2\,\text{T}$ as a function of the homogeneous electric field E_x. Here, we assume the radius $R = 15\,\text{nm}$ for the cross section of the NW and a lattice spacing of 0.25 nm for the numerical calculations. In general the effect of the electric field gradient is pronounced at weak E_x. At $E_x = 1\,\text{V}\,\mu\text{m}^{-1}$ the effective parameters are renormalized only slightly by the inhomogeneous field. The main reason for the renormalization of the parameters are the diagonal quadrupole moment terms q_i^s $(i = 0, 1, 2)$ and thus we observe a strong effect at $\delta E_{xx} = \delta E_{yy} = 10\,\text{V}\,\mu\text{m}^{-2}$ where the off-diagonal terms in the Hamiltonian in Eq. (3.34) vanish. (a) The effective g factor g_{eff} is reduced by the inhomogeneous field at weak E_x. The effective model overestimates the effect of the inhomogeneous field at weak E_x and becomes inaccurate at strong E_x in agreement with Fig. 3.4(a). (b) The effective SOI strength α_{so} decreases with increasing inhomogeneous field slightly. (c) The inverse average effective mass $1/\bar{m}$ moves closer to zero at $E_x = 0$ and still approaches a value close to γ_1/m at strong electric field. (d) The inverse spin-dependent mass $|1/\delta m|$ is reduced by the inhomogeneous electric field at $E_x = 0$ and approaches zero at strong E_x. The SOI and the mass terms are well described by the effective model as the comparison with the numerical result shows.

We describe the strain in Ge/Si core/shell NWs by the BP Hamiltonian H_{BP} [see Eq. (3.7)], which is $\propto J_z^2$. As a result, we can straightforwardly extend the analytical solution in Sec. 3.3.2 by including the effects of strain. Strain enters the solution by modifying the coefficients $c_\pm^s$ and $\alpha_\pm^s$ in Eqs. (3.23), (3.27), (3.22), and (3.26) to Eqs. (3.93), (3.94), (3.95), and (3.96) given in Appendix 3.B.

In the inset in Fig. 3.6(a), we show how the effective g factor, g_{eff}, changes for different values of strain. The strain energies in the range between $|b|\varepsilon_s = 3.7\,\text{meV}$ and $|b|\varepsilon_s = 40\,\text{meV}$ can be

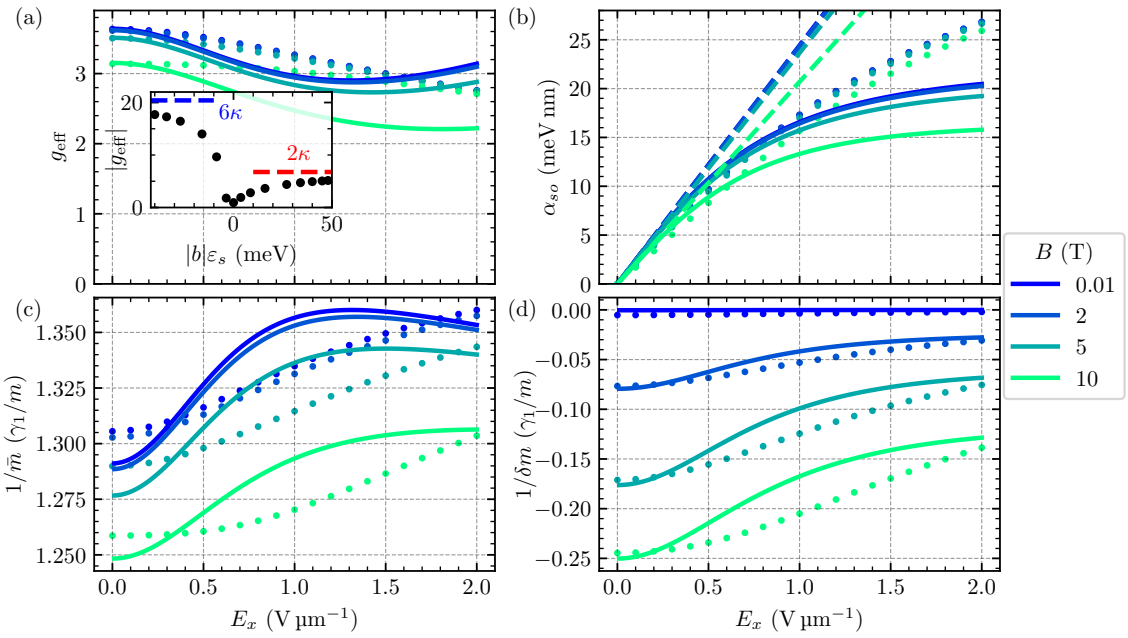

Figure 3.6: Effective parameters of the a strained core/shell NW of radius $R = 15\,\text{nm}$ according to the effective 2×2 model, $H^{2\times2}$ in Eq. (3.49) (solid lines), as a function of the electric field E_x for strain energy $|b|\varepsilon_s = 15.7\,\text{meV}$ (corresponds to $\gamma = 0.1$). Strain is included via the BP Hamiltonian H_{BP} defined in Eq. (3.7). The dots show the same quantities calculated numerically by diagonalizing the Hamiltonian in Eq. (3.1) discretized in real space (lattice spacing 0.25 nm) (a) The effective g factor [see Eq. (3.50)] is large at weak E_x and decreases throughout the whole depicted range. The perturbatively calculated g factor deviates from this behavior at strong electric field and increases after reaching a minimum as in Fig. 3.4(a). The inset in (a) shows g_{eff} calculated semi-analytically according to Eqs. (3.24), (3.28), and (3.29) as a function of the strain energy $|b|\varepsilon_s$ at $B = 0.01\,\text{T}$. The result is almost independent of the strength of the magnetic field. Strain increases g_{eff} independently of the sign of $|b|\varepsilon_s$. For $|b|\varepsilon_s \geq 0$, the ground state is LH and we approach the LH g factor 2κ for infinite strain energy (red-dashed line). For $|b|\varepsilon_s < 0$, the ground state becomes more and more HH-like and we obtain the HH g factor 6κ in the limit of infinite negative strain energy (blue-dashed line). (b) In comparison to the results obtained without strain [cf. Fig. 3.4(b)], α_{so} [cf. Eq. (3.51)] is strongly reduced. The SOI is underestimated by the perturbation theory at strong electric field. (c) With strain, $1/\bar{m}$ [cf. Eq. (3.53)] is positive also at weak E_x. The ground state is now more LH-like, which manifests in the fact that $1/\bar{m}$ is closer to the LH mass $(\gamma_1 + 2\gamma_s)/m$ than to the average HH-LH mass γ_1/m. (d) The spin-dependence of the effective mass [cf. Eq. (3.54)] becomes less relevant with strain even at strong B. Note that with strain one needs to use the definitions for $c^s_\pm$ and $\alpha^s_\pm$ given by Eqs. (3.93), (3.94), (3.95), and (3.96) in Appendix 3.B to calculate the effective parameters. The numerics and perturbation theory disagree at $E_x = 0$ due to the same reason given in the caption of Fig. 3.4. Numerics and perturbation theory show both that $1/\bar{m}$ is almost constant with the electric field for the chosen value of strain due to the enhanced subband gap.

realized by varying the relative shell thickness of the Si shell around the Ge core from $\gamma = 0.002$ to $\gamma = 0.4$ [23]. While negative values of $|b|\varepsilon_s$ are not reached in Ge/Si NWs, for completeness we include these cases in our analysis. Such negative strain energies can occur in Ge NWs where the outer shell comprises a material with a larger lattice constant than Ge. In this figure, we define the g factor at $B = 0.01\,\mathrm{T}$. We also remark that in the inset in Fig. 3.6(a) we plot the absolute value of g_{eff}. In fact, interestingly, strain can cause a change of sign of g_{eff}: with positive strain energy the ground state is a $\uparrow$-state and the first excited state is a $\downarrow$-state, while with negative strain energy the order is reversed. We note that a finite value of strain (positive or negative) tends to increase $|g_{\mathrm{eff}}|$. This enhancement of $|g_{\mathrm{eff}}|$ is caused by a reduced susceptibility of the NW to orbital effects. In fact, in Fig. 3.3, we relate the reduction of g to the avoided crossing between lowest and first Kramers pairs (blue and orange lines) induced by orbital effects. In the presence of strain, at $B = 0$ the subband gap between these states is increased, thus pushing the avoided crossing to larger values of B, and enhancing the effective g factor.

The enhanced g factor at small values of B is a noteworthy advantage to host MBSs and for spin qubit applications. However, we point out that a prerequisite for the formation of MBSs is proximity-induced superconductivity in the Ge NW, a requirement that strongly limits the possible thickness of the Si shell (and thus the values of strain). In experiments proximity-induced superconductivity was demonstrated at Si shell thicknesses between 1.5 nm and 3 nm [49, 96], corresponding to strain energies between $|b|\varepsilon_s = 15.7\,\mathrm{meV}$ and $|b|\varepsilon_s = 26.5\,\mathrm{meV}$ in a Ge NW with $R = 15\,\mathrm{nm}$. As shown in Fig. 3.6(a) these strain parameters are sufficient to significantly increase the g factor at weak electric field compared to the result without strain in Fig. 3.4(a).

At positive strain energies, the ground state is given by $\varphi_2^{\uparrow}$ with the Kramers partner $\varphi_0^{\downarrow}$, as in the case without strain. These states are almost exclusively LH at $E_x = 0$, and therefore, in the limit of infinite positive strain energy, $g_{\mathrm{eff}} \to 2\kappa$ [cf. red dashed line in the inset in Fig. 3.6(a)], corresponding to the pure LH g factor. At negative strain, the ground state becomes $\varphi_0^{\uparrow}$ with the Kramers partner $\varphi_2^{\downarrow}$ which becomes HH-like with increasing negative strain energy. At $|b|\varepsilon_s \to -\infty$ the ground state is purely HH and we obtain the HH g factor $g_{\mathrm{eff}} \to 6\kappa$ [cf. blue dashed line in the inset in Fig. 3.6(a)]. This trend is analogous to planar Ge heterostructures, see Sec. 3.4.

We now focus on a Ge/Si core/shell NW with $|b|\varepsilon_s = 15.7\,\mathrm{meV}$ ($\gamma = 0.1$). We follow the calculations presented in Appendix 3.D and we adapt the formulas from Sec. 3.3.5 to accommodate for strain, by considering the energies given by Eqs. (3.24) and (3.28) with the coefficients in Eqs. (3.93), (3.94), (3.95), and (3.96). The results are presented in Fig. 3.6. In comparison to the results obtained before without strain (cf. Fig. 3.4), the g factor is strongly enhanced at small values of E_x as expected from the inset in Fig. 3.6(a). Similar to the qualitative behavior of the g factor of unstrained NWs, the perturbatively calculated g_{eff} in the presence of strain deviates form the result from numerical calculations at strong electric field, compare Figs. 3.6(a) and 3.4(a). The SOI is strongly reduced by strain [cf. Fig. 3.6(b)]. The slope in the linear regime as well as the maximum value at stronger E_x is smaller than without strain because of the enhanced subband energy gap. The perturbation theory underestimates the SOI strength at strong electric field. Moreover, the strain regularizes the inverse average effective mass $1/\bar{m}$, which is approximately constant as a function of E_x and remains positive even at $E_x \to 0$, as shown in Fig. 3.6(c). The inverse mass $1/\bar{m}$ is enlarged by strain and it approaches the LH mass $(\gamma_1 + 2\gamma_s)/m$ [$(\gamma_1 + 2\gamma_s)/\gamma_1 = 1.74$]. As can be seen from Fig. 3.6(d), strain also reduces the spin-dependent mass term.

3.4 One-dimensional channel

In this section, we analyze how the details of the confinement affect the parameters of the effective model, $H^{2\times 2}$, introduced in Eq. (3.49). In particular we consider a one-dimensional channel defined

by gates in a planar Ge/SiGe heterostructure as shown in Fig. 3.1(b). The channel extends in the z direction. We consider a HW confinement, see Eq. (3.19), in x direction, perpendicular to the substrate, that models the interfaces between the Ge layer with width L_x and the SiGe layers. We consider an electrostatic gate creating a harmonic confinement potential in the y direction given by

$$U(y) = \frac{\hbar\gamma_1}{2ml_y^4} y^2. \tag{3.57}$$

The confinement potential is parametrized by the harmonic confinement length l_y. Here, we consider $l_y = L_x/\pi$ in order to have comparable confinement in x and y direction. The magnetic field is applied in the z direction, parallel to the channel. Strain is included via the BP Hamiltonian $H_{\mathrm{BP}}^{\mathrm{ch}}$ given in Eq. (3.8). For our calculations we choose realistic values for the strain energy compared to values typically measured in Ge/SiGe heterostructures ($|b|\varepsilon_s \approx 16\,\mathrm{meV}$) [97] and we also analyze the limit of weak strain.

In this architecture, we solve the problem by diagonalizing the Hamiltonian in Eq. (3.1) at $k_z = 0$ numerically directly including the electric field. For the numerical diagonalization of the LK Hamiltonian we use the first 20 eigenstates of the harmonic oscillator in y direction and the basis

$$f_{n_x}(x) = \frac{\sqrt{2}\sin\left[n_x\left(\frac{x}{L_x}+\frac{1}{2}\right)\right]}{\sqrt{L_x}} \tag{3.58}$$

with $0 < n_x \leq 20$ in x direction, fulfilling the HW boundary conditions.

In Fig. 3.7, we present the results of our analysis where we consider a magnetic field of $B = 2\,\mathrm{T}$ along the channel and a homogeneous electric field E_x perpendicular to the substrate. We compare the results for a channel of HW confinement length $L_x = 26.6\,\mathrm{nm}$ and harmonic confinement length $l_y = L_x/\pi = 8.5\,\mathrm{nm}$ (solid lines) for different values of the strain energy to a Ge/Si core/shell NW of radius $R = 15\,\mathrm{nm}$ and strain energy $|b|\varepsilon_s = 15.7\,\mathrm{meV}$ (dashed lines). With these choices for the confinement details, the areas of the cross sections in the two cases are comparable. We emphasize again that the sign of the strain energy in planar Ge is opposite to the strain in the NW, see Eqs. (3.7) and (3.8). Furthermore, we also make a comparison to a channel with a much smaller cross section with $L_x = 15\,\mathrm{nm}$ and $l_y = 15\,\mathrm{nm}/\pi = 4.8\,\mathrm{nm}$ (dot-dashed lines).

The one-dimensional channel geometry exhibits a few features that are different from those observed in the NW. In particular, as shown in Fig. 3.7, only the SOI and the g factor exhibit the same qualitative behavior in both the NW and channel geometry. In a channel with $|b|\varepsilon_s = -1.9\,\mathrm{meV}$, we also observe at weak electric field quantitatively similar values of α_{so} as in a NW with $|b|\varepsilon_s = 15.7\,\mathrm{meV}$. In Fig. 3.7(a), we show that g_{eff} is significantly smaller in the channel than in the NW and that it decreases with the amount of strain in the planar structure. In the channel with smaller cross section, the electric field dependence of g_{eff} is reduced.

In Figs. 3.7(c) and 3.7(d), we analyze the inverse average and spin-dependent masses, respectively. With increasing (negative) strain energy the inverse average mass $1/\bar{m}$ increases. Also the qualitative behavior changes and instead of having a maximum that occurs for $|b|\varepsilon_s = -1.9\,\mathrm{meV}$, at larger strain energies, $1/\bar{m}$ decreases monotonically with E_x. This trend is in contrast to the monotonic increase of the inverse averages mass in the Ge/Si NW. Interestingly, the inverse spin-dependent mass is positive in the channel, while it is negative for the NW with respect to the g factor. As in the NW geometry, also in the channel geometry the spin-dependent mass is most relevant at $E_x \to 0$ and for small values of strain, and it is negligible otherwise.

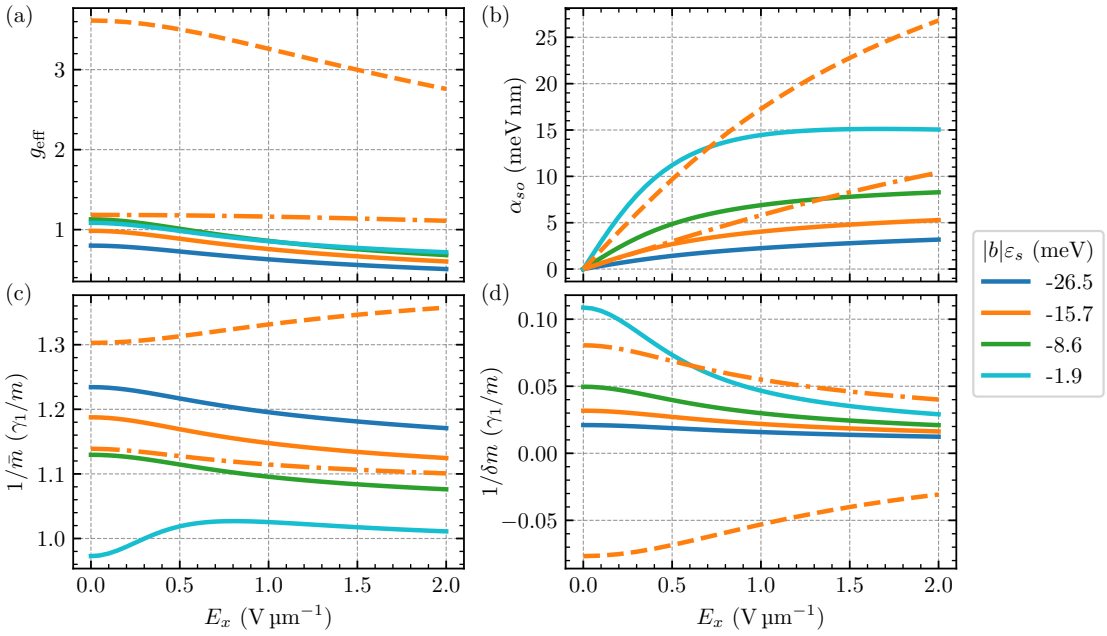

Figure 3.7: Effective parameters of a gate-defined one-dimensional channel in a Ge/SiGe heterostructure as a function of the electric field perpendicular to the heterostructure plane (E_x) with a magnetic field along the channel ($B = 2\,\text{T}$). The solid lines show the numerical results (calculated as described in the main text) for the channel with a HW confinement of length $L_x = 26.6\,\text{nm}$ in x direction and a harmonic confinement in y direction with harmonic confinement length $l_y = L_x/\pi = 8.5\,\text{nm}$ for different values of the strain energy $|b|\varepsilon_s$ indicated by the legend. The dash-dotted lines show the same for HW confinement length $L_x = 15\,\text{nm}$ for $|b|\varepsilon_s = -15.7\,\text{meV}$. The dashed lines show the results for a Ge/Si core/shell NW of Radius $R = 15\,\text{nm}$ with $|b|\varepsilon_s = 15.7\,\text{meV}$ calculated numerically by diagonalizing the Hamiltonian in Eq. (3.1) discretized in real space (lattice spacing 0.25 nm). Strain is included for the NW via the BP Hamiltonian H_{BP} from Eq. (3.7) and for the channel via the BP Hamiltonian $H_{\text{BP}}^{\text{ch}}$ from Eq. (3.8). The g factor and SOI of the channel exhibit the same qualitative behavior as the NW, while the mass terms are different in the two different geometries. (a) The effective g factor of the channel is much smaller than for the NW. A decrease of the channel cross section (dash-dotted line) leads to a weaker dependence on the external electric field and a slightly larger g factor. (b) The SOI of the channel with $L_x = 26.6\,\text{nm}$ and $|b|\varepsilon_s = -1.9\,\text{meV}$ is quantitatively in the same range as the SOI of the NW at weak electric field. With increasing strain in the channel, the SOI decreases. (c) While the NW exhibits an inverse average effective mass that increases, the same quantity decreases with E_x in the channel except for $|b|\varepsilon_s = -1.9\,\text{meV}$ where a maximum occurs at $E_x = 0.8\,\text{V}\,\mu\text{m}^{-1}$. Generally, $1/\bar{m}$ is smaller in the channel than in the NW. (d) The inverse spin-dependent mass has an opposite sign in the channel with respect to the NW.

3.5 Curved quantum well

In the following, we consider a CQW as sketched in Fig. 3.1(c). The confinement for the CQW is given by

$$V(r) = \begin{cases} \infty, & r = \sqrt{x^2 + y^2} < R, \\ 0, & R < r < R_1, \\ \infty, & r > R_1 \end{cases} \tag{3.59}$$

where the radii are defined as in Fig. 3.1(c). The strain induced into the Ge shell is modeled by the BP Hamiltonian $H_{\mathrm{BP}}^{\mathrm{CQW}}$ defined in Eq. (3.9), as discussed in Ref. [31]. The longitudinal and radial strain energies can be engineered individually by the radii of the inner and outer shell, R_1 and R_2, see Eqs. (3.11) and (3.12). Only the longitudinal strain energy $|b|\varepsilon_z$ depends on the thickness of the outer shell.

We now calculate the energy spectrum of the CQW as a function of the magnetic field by numerically diagonalizing the discretized version of the Hamiltonian in Eq. (3.1) where we account for the BP Hamiltonian $H_{\mathrm{BP}}^{\mathrm{CQW}}$ defined in Eq. (3.9) and the confinement introduced above. Orbital effects are crucial in the CQW as illustrated by Fig. 3.8 and discussed in Ref. [31]. A comparison between Fig. 3.8(a) [with orbital effects] and Fig. 3.8(b) [without orbital effects] clearly illustrates the strikingly different magnetic field dependence of the system properties when orbital effects are included. In particular, there is a number of level crossings when orbital magnetic field is accounted for. Only at weak magnetic field ($B < 1\,\mathrm{T}$), the levels in Fig. 3.8(a) do not cross, thus, in the following we focus on the regime of weak magnetic field.

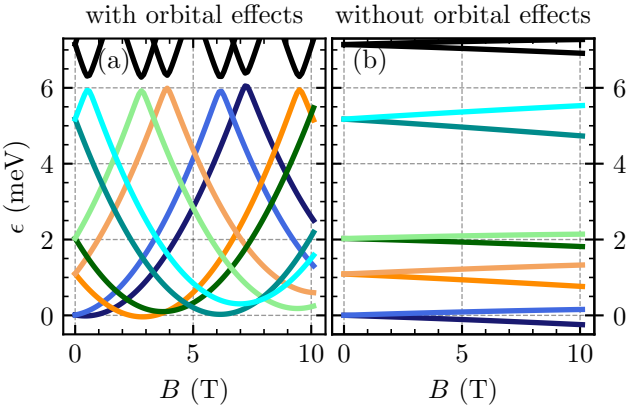

Figure 3.8: Energy spectrum of a CQW as a function of the magnetic field B at $k_z = 0$ calculated by numerically diagonalizing $H_{\mathrm{ILK}} + H_{\mathrm{BP}}^{\mathrm{CQW}} + H_Z + V$ (a) including orbital effects and (b) neglecting orbital effects. Orbital effects have a huge impact on the evolution of the energy states with the magnetic field. Only at weak $B < 1\,\mathrm{T}$ the levels in the panel (a) do not cross. The colors indicate Kramers partners. The inner core radius is given by $R = 15\,\mathrm{nm}$. The thin outer Ge shell is defined by $R_1 = 25\,\mathrm{nm}$ and $R_2 = 35\,\mathrm{nm}$. We use a lattice spacing of $0.5\,\mathrm{nm}$.

The states in the CQW are close in energy even with strain [31], thus, we cannot accurately include an electric field perturbatively. As a result, we include a homogeneous electric field perpendicular to the NW numerically. The results we obtain by this approach are presented in Fig. 3.9. We compare the effective g factor and the SOI strength for different radii R as well as with and

without including orbital effects. We consider a Ge shell of width $R_1 - R = 10\,\text{nm}$ and the outer Si shell $R_2 - R_1 = 10\,\text{nm}$. The strain energies for the different radii considered in Fig. 3.9 are provided in Table 3.1. With increasing core radius R the longitudinal strain component ε_z decreases quickly and becomes negligible at $R = 25\,\text{nm}$. In contrast, the radial strain component ε_r increases with the core radius.

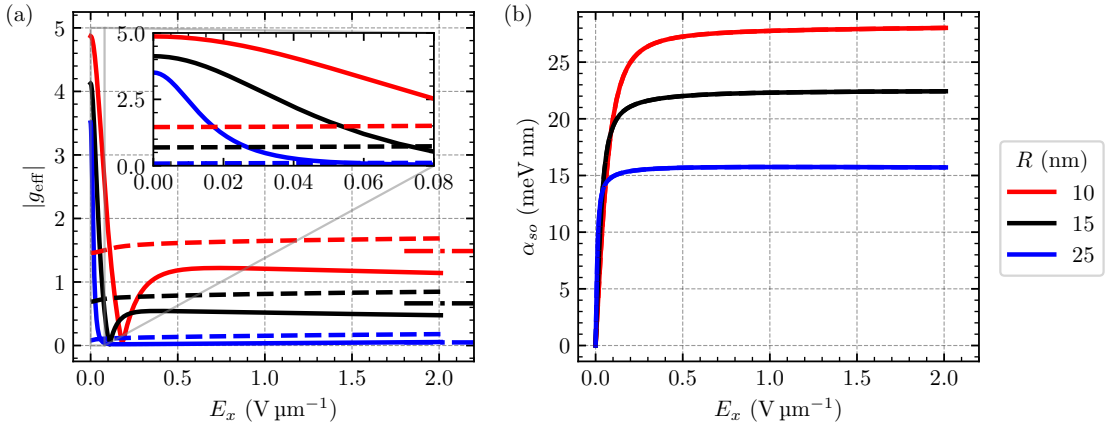

Figure 3.9: (a) Effective g factor g_{eff} and (b) SOI α_{so} of a CQW ($R_1 - R = 10\,\text{nm}$ and $R_2 - R_1 = 10\,\text{nm}$) as a function of the electric field E_x at $k_z = 0$ and $B = 0.1\,\text{T}$ calculated by numerically diagonalizing the Hamiltonian in Eq. (3.1) accounting for strain via $H_{\text{BP}}^{\text{CQW}}$ defined in Eq. (3.9) and the homogeneous electric field via $H_E = -eE_x x$. (a) The solid (dashed) lines correspond to the results calculated including (excluding) orbital effects. At weak $E_x \lesssim 0.05\,\text{V}\,\mu\text{m}^{-1}$, the lowest energy states are close and influence each other strongly. If E_x is increased, the subband gap between the ground state Kramers pair and the excited states also increases, resulting in a constant g factor. At moderate electric field, g_{eff} is smaller when orbital effects are taken into account. The dash-dotted lines in the right of the panel (a) correspond to g_{eff} obtained from Eq. (3.60), which is valid at strong E_x. (b) We find that α_{so} is the same with and without orbital effects. The SOI increases rapidly at weak E_x and then stays constant at a large value. We use a lattice spacing of 0.5 nm.

Table 3.1: Longitudinal ($|b|\varepsilon_z$) and radial ($|b|\varepsilon_r$) strain energy in the CQW according to Eq. (3.11) and Eq. (3.12), respectively, for the inner radii chosen for Fig. 3.9. The Ge shell thickness is fixed at $R_1 - R = 10\,\text{nm}$ and the outer shell radius is fixed at $R_2 - R_1 = 10\,\text{nm}$.

R (nm)	10	15	25
$\|b\|\varepsilon_z$ (meV)	15.6	7.8	0.65
$\|b\|\varepsilon_r$ (meV)	62.6	79.2	97.8

Importantly, a finite electric field causes an increase of the small subband gap between the ground state Kramers pair and the excited states shown in Fig. 3.8 [31]. Due to the small subband gap at weak electric field, the effective g factor in Fig. 3.9(a) changes rapidly. It becomes a rather constant function of the electric fields above a certain critical field. An almost electric-field-independent g_{eff} is a critical advantage for spin qubit applications because it strongly suppresses

the susceptibility to charge noise [98, 99], a key issue in hole NWs [18, 19]. We anticipate that the large g factor for $R = 10\,\mathrm{nm}$ can acquire significant corrections coming from the high energy holes, as we will discuss in Sec. 3.6. Despite the weak magnetic field of $B = 0.1\,\mathrm{T}$, the g factor is enhanced considerably at weak electric field ($E_x < 0.1\,\mathrm{V\,\mu m^{-1}}$) due to orbital effects. For small radius, the orbital effects reduce the g factor at strong electric field. The main reason for the g factor to decrease with increasing radius R is not the weaker confinement in the larger cross section but the larger value of radial strain (cf. Table 3.1).

Analytical calculations analogous to the ones in Ref. [31] predict that the g factor at strong electric fields is independent of orbital effects and reduces to

$$g_{\mathrm{eff}} = 6\kappa \frac{|b|\varepsilon_z}{|b|\varepsilon_z + 2|b|\varepsilon_r + \frac{2\hbar^2\pi^2\gamma_s}{m(R_1-R)^2}}. \tag{3.60}$$

We show the predicted value as dot-dashed lines on the right side of Fig. 3.9. The analytical formula provides a good estimation for the g factor for thin Ge shells and large values of $|b|\varepsilon_z$ but we observe that it also reasonably captures the g factor at rather small values of longitudinal strain and thick shells. In the latter cases, there are small variations of g_{eff} by orbital effects. These variations however do not change the slope of the curves and g_{eff} remains a rather flat function of E_x.

In contrast to the g factor, the SOI strength [cf. Fig. 3.9(b)] is not influenced by the orbital magnetic field at this value of the magnetic field for any of the chosen values of R. At weak electric field the SOI increases rapidly and then remains constant at a large value. This behavior is extremely advantageous for various spin qubit applications because it removes the need of fine-tuning the electric field to reach the maximal value of α_{so}. The SOI could still be switched off completely at $E_x = 0$. In contrast to the g factor, the SOI depends mainly on the radius and less on the strain energy. We note that even at weak electric field where the g factor remains sizable the SOI can also be large (at $E_x = 0.06\,\mathrm{V\,\mu m^{-1}}$ and $R = 10\,\mathrm{nm}$: $g_{\mathrm{eff}} = 3.3$ and $\alpha_{so} = 15\,\mathrm{meV\,nm}$), which makes this platform suitable to find Majorana bound states.

3.6 Corrections to the model

In this section, we resort to fully numerical calculations using a discretized model in real space to analyze the validity of the analytical results in the presence of additional effects including split-off holes and cubic anisotropies. We focus here on cylindrical Ge/Si core/shell NWs and on CQWs.

3.6.1 Spin-orbit split-off band

In the following we explore the effect of the spin-orbit SOB on the effective g factor, the SOI, and the effective mass of Ge NWs and CQWs. We calculate the effective parameters with a 6×6 LK Hamiltonian (cf. Appendix 3.E) taking into account the two LH, the two HH and the two split-off hole states. To study the effect of the SOB, here, we restrict our analysis to the isotropic 6×6 LK Hamiltonian ($\gamma_2 = \gamma_3 = \gamma_s$). The spin-orbit gap for Ge is $\Delta_{SO} = 296\,\mathrm{meV}$ [74]. However, despite this large gap, the SOB renormalizes the parameters of the effective model and causes a considerable quantitative change in the system. Note that the spin of the split-off holes is truly 1/2 while the LHs correspond to the $\pm 1/2$ eigenvalues of the spin-3/2 matrix J_z.

Ge nanowire

Our result from numerical calculations of the g factor of a Ge NW is presented in Fig. 3.10. Due to the SOB, the effective g factor at $E_x = 0$ depends on both R/l_B and $\Delta_{SO}/\hbar\omega_c$. By comparing

with Fig. 3.3(c), we observe that qualitatively the dependence of g_{eff} on B still resembles the one obtained for the 4×4 LK Hamiltonian but the SOB tends to reduce g_{eff}, especially in NWs with a small radius. With increasing radius the 4×4 LK Hamiltonian becomes more accurate because the confinement energy $\propto 1/R^2$ becomes smaller compared to Δ_{SO}, and the states in the SOB are well-separated from the low-energy HH-LH subspace. More precisely, in Table 3.2, we show the dependence of the position (at $B = \tilde{B}$) and value $[g_{\text{eff}}(B = \tilde{B})]$ of the maximum of g_{eff} for the five radii used in Fig. 3.10. At $R = 20\,\text{nm}$ the maximum value of g_{eff} deviates only 8% from the value of 1.24 obtained without accounting for the SOB, thus justifying the analysis in Sec. 3.3.

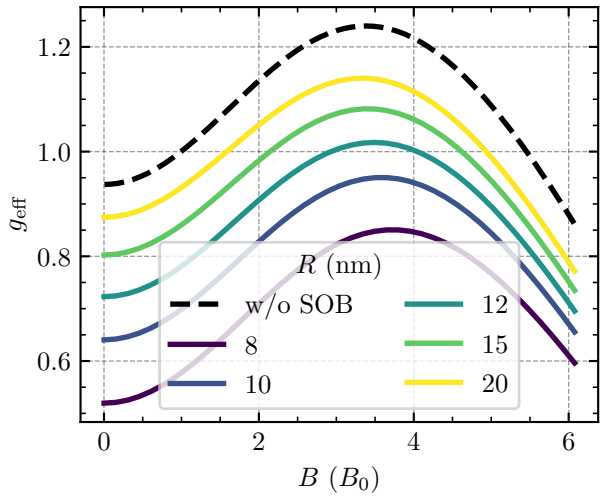

Figure 3.10: Effective g factor g_{eff} of a Ge NW with circular cross section as a function of the magnetic field (in units of $B_0 = 658.2\,\text{T} \times \text{nm}^2/\text{R}^2$) calculated numerically using the 6×6 LK Hamiltonian $H^{6\times6}$ (given in Appendix 3.E), which takes into account the spin-orbit SOB. For comparison we provide g_{eff} without the spin-orbit SOB (dashed line) calculated semi-analytically according to Eqs. (3.24), (3.28), and (3.29). The spin-orbit SOB causes a decrease of g_{eff} that is larger at small R. We use a lattice spacing of 0.5 nm.

Table 3.2: The position ($\tilde{B}$) and value ($g_{\text{eff,max}}$) of the maximum of the effective g factor in Ge NWs with circular cross section for different radii obtained numerically to include the SOB.

Radius R (nm)	8	10	12	15	20
$\tilde{B}$ (T)	39.1	24.0	16.0	9.8	5.5
$g_{\text{eff,max}}$	0.85	0.95	1.02	1.08	1.14

We study the effect of an electric field by numerically diagonalizing the discretized version of the Hamiltonian in Eq. (3.1) and show the results in Fig. 3.11. We compare numerical results obtained numerically by including the SOB with the results obtained from the 4×4 ILK Hamiltonian H_{ILK} [cf. Eq. (3.5)]. The holes in the SOB are more effective at small values of R. Thus, to emphasize their effect, here, we present the results of a simulation of a NW of a small radius $R = 8\,\text{nm}$. The SOB does not alter the qualitative behavior of the effective parameters, however, these states can renormalize the values quantitatively. In particular, in Fig. 3.10(a) and (b), we show that g_{eff} is

reduced by the SOB also at finite E_x and that the effective SOI α_{so} is only weakly renormalized even in narrow NWs, respectively. The effective masses also acquire corrections because of the SOB, which are more pronounced at small values of E_x, see Figs. 3.11(c) and (d). At stronger electric fields, the influence of the SOB on both mass terms becomes negligible.

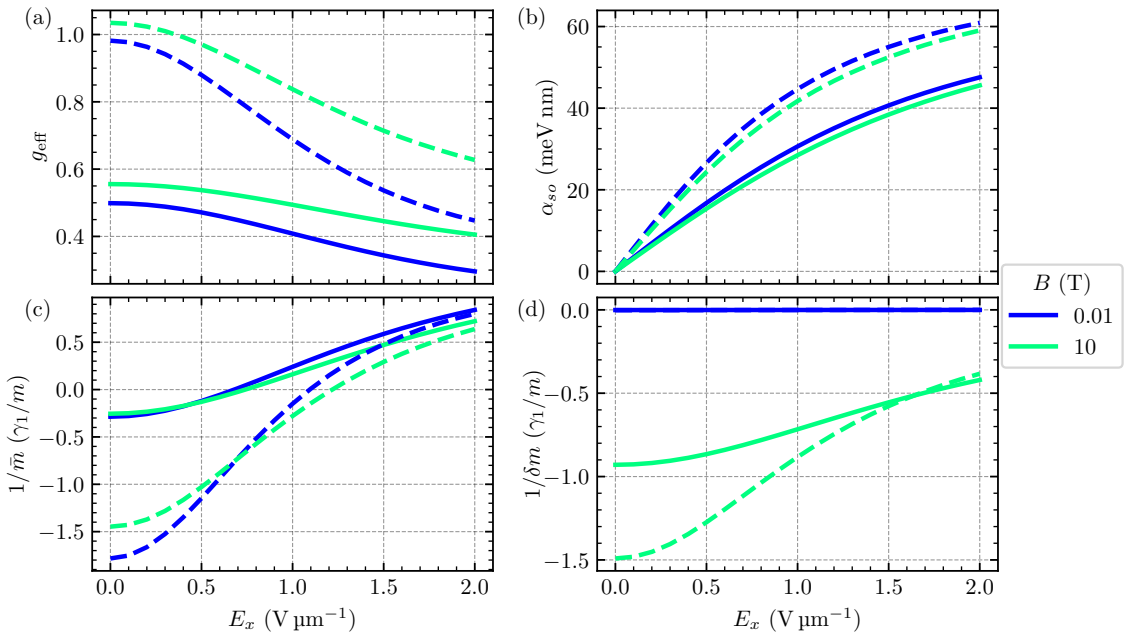

Figure 3.11: Effective parameters of a Ge NW with circular cross section as a function of the electric field E_x calculated numerically with the 6×6 LK Hamiltonian $H^{6\times6}$ (given in Appendix 3.E), which takes into account the spin-orbit SOB (solid lines). For comparison we provide the result without the spin-orbit SOB (dashed lines). We choose a relatively small radius $R = 8\,\text{nm}$ since the influence of the SOB is stronger for stronger confinement. (a) As we already know from Fig. 3.10, the effective g factor is reduced when the SOB is included. However, the qualitative E_x dependence stays the same. (b) The spin-orbit SOB reduces α_{so} only slightly. The correction is smallest at weak electric field. (c) At weak E_x, $|1/\bar{m}|$ is reduced due to the influence of the SOB. In addition, with the SOB, the average mass is negative at weak and positive at strong electric fields. (d) The SOB influences $|1/\delta m|$ only slightly towards a smaller value. As for the average mass the correction is largest at weak E_x. For all effective parameters, the difference between $B = 0.1\,\text{T}$ and $B = 10\,\text{T}$ is small in agreement with the results presented in Fig. 3.6. We use a lattice spacing of 0.16 nm.

Our findings confirm that, in most cases, the SOB only causes a quantitative correction to the 4×4 LK Hamiltonian defined for a Ge NW. This correction is rather small in wide NWs but it can be significant in narrow NWs and should be included in these cases to have an accurate description of the system.

Curved quantum well

The effect of the SOB on the g factor and the SOI strength of CQWs is shown by Fig. 3.12. In order to account for strain, in our numerical calculations, we resort to the 6×6 BP Hamiltonian given in

Appendix 3.E, see Eq. (3.106). Again, we compare the results obtained with the 4×4 Hamiltonian neglecting the SOB (solid lines) to the results where the SOB is accounted for (dashed lines). In analogy to Ge/Si core/shell NWs, in CQWs, the effects of the SOB are strongest in NWs with small radii, resulting in a renormalization of g_{eff} by up to 20% at $R = 10\,\text{nm}$ and $E_x = 1.0\,\text{V}\,\mu\text{m}^{-1}$. This correction is comparable to what we observe in the Ge NW of radius $R = 8\,\text{nm}$ [cf. Fig. 3.11(a)]. For weaker confinement and larger R the renormalization due to SOB becomes negligible. The SOB affects the SOI [cf. Fig. 3.12(b)] in a similar way.

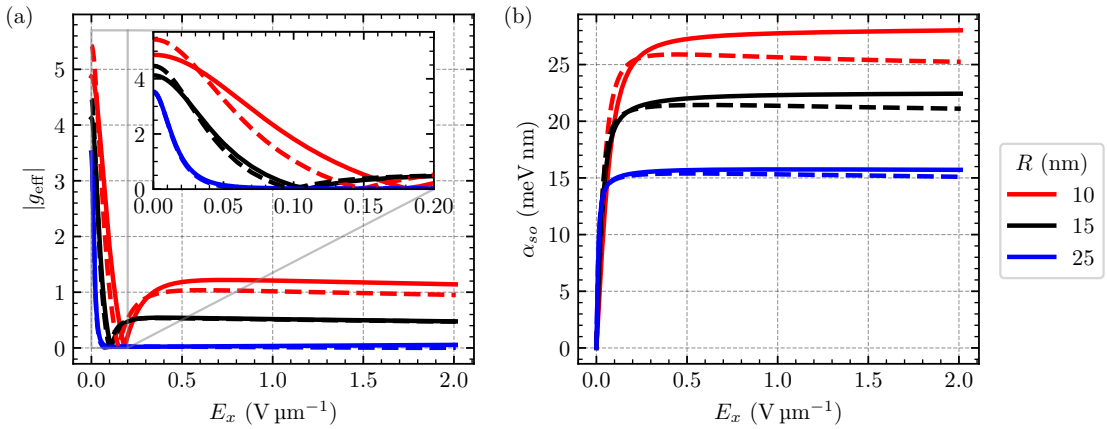

Figure 3.12: Numerically calculated (a) effective g factor g_{eff} and (b) SOI strength α_{so} of a CQW with $R_1 - R = 10\,\text{nm}$ and $R_2 - R_1 = 10\,\text{nm}$ [cf. Fig. 3.1(c)] as a function of the electric field E_x at $k_z = 0$ and $B = 0.1\,\text{T}$. The dashed lines depict the results calculated with the 6×6 LK Hamiltonian $H^{6\times6}$ given in Appendix 3.E, which includes the spin-orbit SOB. The solid lines correspond to the results obtained without including the SOB. Only for strong confinement ($R = 10\,\text{nm}$) the split-off holes renormalize both the g factor and the SOI strength. For weaker confinement the influence of the split-off holes is negligible. We use a lattice spacing of 0.5 nm.

3.6.2 Cubic Luttinger-Kohn anisotropies

In this subsection, we discuss the effects of anisotropy on the effective parameters of a Ge/Si core/shell NW and of a CQW. In addition, we investigate the validity of the ILK Hamiltonian H_{ILK} defined in Eq. (3.5). Here, we calculate the effective parameters numerically by using the general LK Hamiltonian H_{LK} provided in Eq. (3.2).We focus on rather wide NWs, thus, we neglect the SOB. If we include the cubic anisotropies of the LK Hamiltonian, the growth direction of the NW becomes relevant [24, 29]. Here, we consider the three situations introduced in Sec. 3.2, where the NW is grown along $z \parallel [001]$, $z \parallel [110]$, and $z \parallel [111]$, and compare these cases to the results obtained from the ILK Hamiltonian.

Ge/Si core/shell nanowire

In Fig. 3.13, we show g_{eff} at $E_x = 0$ in a Ge/Si core/shell NW as a function of the magnetic field applied parallel to the NW axis. Comparing to the result obtained within the ILK approximation (black-dashed line), we observe that the anisotropies reduce the g factor, especially, when the z axis is not aligned to a main crystallographic axis. In fact, when $z \parallel [001]$, the g factor agrees well with the ILK but, at $z \parallel [110]$ or $z \parallel [111]$, g_{eff} is significantly smaller. For a more anisotropic

material such as Si, we expect a larger difference between different growth directions but we do not analyze this case here.

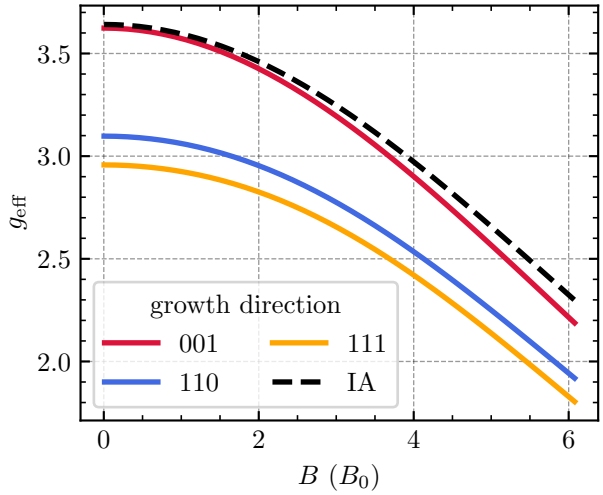

Figure 3.13: Effective g factor g_{eff} of a strained Ge/Si core/shell NW with circular cross section as a function of B (in units of $B_0 = 658.2\,\text{T} \times \text{nm}^2/\text{R}^2$) calculated numerically for different growth directions. Here, we fix strain to $|b|\varepsilon_s = 15.7\,\text{meV}$. For comparison, we also provide the result obtained from the ILK Hamiltonian (black dashed line). The [001] NW growth direction matches the isotropic result well. The growth directions [110] and [111] exhibit the same qualitative behavior of the g factor as the isotropic result. However, quantitatively for these growth directions g_{eff} is smaller. We use a lattice spacing of 0.5 nm.

In the following, we include a homogeneous electric field perpendicular to the NW axis and diagonalize the Hamiltonian in Eq. (3.1) disrectized in real space. As we account for anisotropies, the effective parameters depend on the direction of the electric field. In Fig. 3.14 we compare the results for the effective parameters of NWs of the three growth directions [001], [110], and [111] and an isotropic NW as a function of the direction of the electric field. We plot the results at $B = 2\,\text{T}$ and at a rather strong electric field, $E = 2\,\text{V}\,\mu\text{m}^{-1}$, where we expect a large effect of the anisotropies. However, for all three growth directions the parameters only weakly depend on the direction of the electric field, suggesting that the IA is a good approximation to describe Ge NWs even at strong electric fields. The effective g factors for the [110] and [111] growth directions deviate quantitatively from the result obtained with the isotropic LK Hamiltonian. For the NW grown parallel to the [110] direction the SOI depends on the direction of the electric field with a maximum of $\alpha_{so} = 31.2\,\text{meV nm}$ at $\boldsymbol{E} \parallel [\bar{1}10]$ ($\varphi = \pi/2$). The effective mass terms are well described by the IA. As expected from Sec. 3.3.6, the inverse average effective mass is positive because we are analyzing a strained Ge NW. In addition, it is larger than the average HH-LH mass γ_1/m. We find that $1/\delta m$ is small and negative, in agreement with the isotropic results shown in Fig. 3.6(d).

In summary, the ILK Hamiltonian H_{ILK} is well suited to describe the behavior of Ge/Si core/shell NWs grown along the [001], [110], or [111] direction. A more detailed analysis taking in to account anisotropies only gives quantitative corrections.

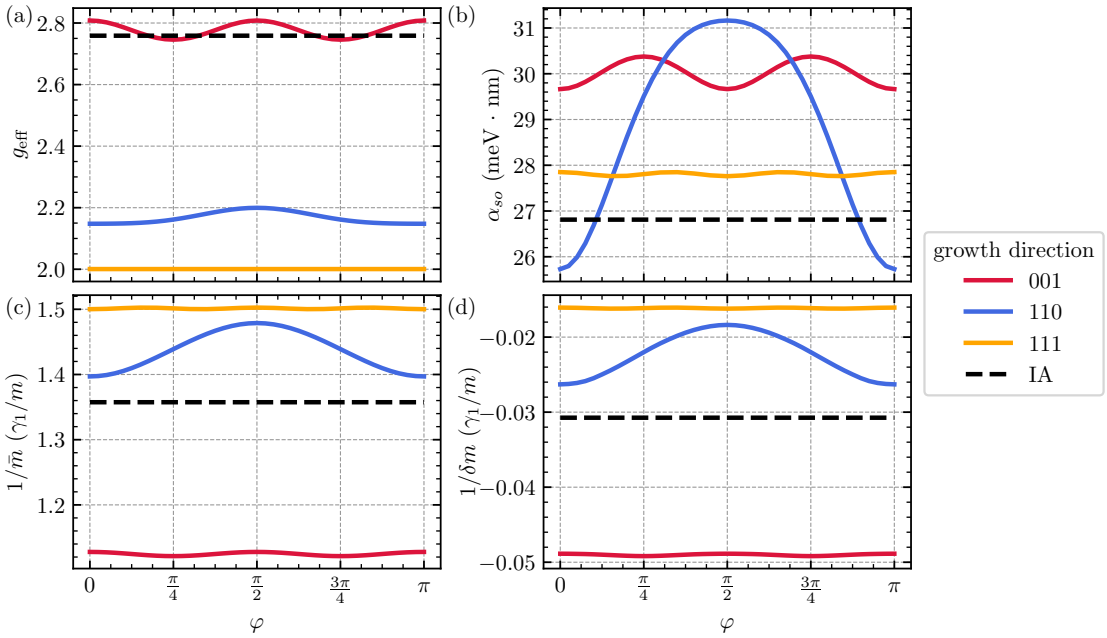

Figure 3.14: Effective parameters of a strained Ge/Si core/shell NW with circular cross section of radius $R = 15\,\text{nm}$ as a function of the electric field direction represented by the angle φ calculated numerically ($B = 2\,\text{T}$, $E = 2\,\text{V}\,\mu\text{m}^{-1}$, and $|b|\varepsilon_s = 15.7\,\text{meV}$) by diagonalizing the discretized version of the Hamiltonian in Eq. (3.1). The NW growth direction is fixed to $z \parallel [110]$ with $\boldsymbol{E} \perp z$. For $\varphi = 0$, $\boldsymbol{E} \parallel [001]$, whereas, for $\varphi = \pi/2$, $\boldsymbol{E} \parallel [\bar{1}10]$, and, for $\varphi = \pi$, $\boldsymbol{E} \parallel [00\bar{1}]$. Except for the SOI for the [110] growth direction the parameters depend only weakly on the growth direction of the NW. (a) Regardless of the growth direction of the NW the g factor is to a good approximation independent of the electric field direction. Quantitatively the IA gives a good estimate for the g factor of a NW grown along one of the main crystallographic axes. For the growth directions [110] and [111] the g factor is smaller than expected from the IA. (b) Only for the [110] growth direction the SOI depends on the direction of the electric field significantly and we find a maximum at $\boldsymbol{E} \parallel [\bar{1}10]$. The IA gives a good estimate for the average SOI. [(c),(d)] The effective mass terms depend only slightly on the direction of the electric field and agree on average well with the results from the isotropic LK Hamiltonian. As expected at strong electric field the spin-dependent mass term approaches zero.

Curved quantum well

Finally, in Fig. 3.15, we analyze the effect of anisotropies on the properties of the CQW. As in Fig. 3.14, we rotate the electric field around the z direction keeping it perpendicular to the NW. Here, we fix the strength of the electric field to $E = 0.5\,\text{V}\,\mu\text{m}^{-1}$ and consider the three growth directions introduced in Sec. 3.2. We observe that the g factor and the SOI strength obtained by the ILK Hamiltonian H_{ILK} are between the values estimated by using the anisotropic LK Hamiltonian. Similarly to the core/shell NW, the effective g factor of the CQW is to good approximation independent of the angle φ of the electric field for the $z \parallel [001]$ and $z \parallel [111]$ growth directions. The dependence on φ is more pronounced at $z \parallel [110]$. For this growth direction and

for $\boldsymbol{E} \parallel x \parallel [1\bar{1}0]$, the g factor is maximal and has a value of 0.87. Moreover, in $z \parallel [111]$-CQWs, the SOI oscillates between $\alpha_{so} = 17.5\,\text{meV nm}$ and $\alpha_{so} = 21.5\,\text{meV nm}$ with a $\pi/3$ periodicity, as expected from Ref. [28]. In contrast, in the $z \parallel [001]$-CQWs the periodicity is $\pi/2$ and it is π in $z \parallel [110]$-CQWs. We also point out that in analogy to core/shell NWs [see Fig. 3.14], the amplitudes of the oscillations of g_{eff} and α_{so} increase at larger values of the electric field (not show here).

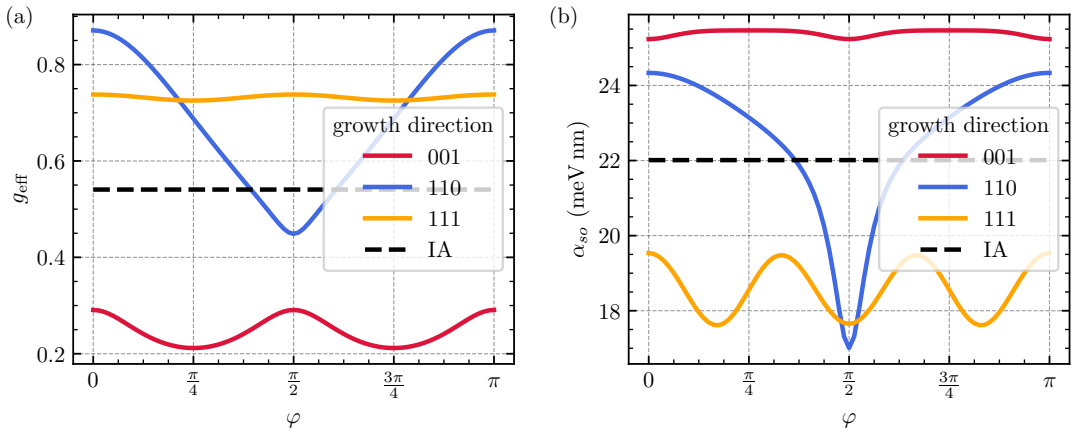

Figure 3.15: Numerically calculated (a) effective g factor g_{eff} and (b) SOI α_{so} of a CQW with $R = 15\,\text{nm}$, $R_1 = 25\,\text{nm}$, and $R_2 = 35\,\text{nm}$ [see Fig. 3.1(c)] as a function of the angle φ that determines the direction of the electric field. We consider the three growth directions indicated by the legend and compare the results to the effective parameters calculated applying the isotropic approximation (IA) of the ILK Hamiltonian H_{ILK}. The g factor and the SOI strength in the isotropic case lie in between the values obtained for the different growth directions in the anisotropic case. The g factor is smallest for the [001] growth direction and largest for [110] if, in addition, $\boldsymbol{E} \parallel x$. For the [110] growth direction, the g factor strongly depends on the direction of the electric field and shows a π periodicity. In contrast, for [111], the g factor is almost constant. Also for the NW grown along [001], the oscillations are small. The SOI is largest for the [001] growth direction. Interestingly, the SOI is almost constant for the bent shell grown along [001]. For [111], it oscillates with periodicity $\pi/3$. Similarly to the g factor, the SOI for [110] strongly depends on the direction of the electric field. Here, we choose $E = 0.5\,\text{V}\,\mu\text{m}^{-1}$ and $B = 0.1\,\text{T}$. We use a lattice spacing of 0.5 nm.

From these results, we conclude that the ILK Hamiltonian in CQWs provides a reasonable qualitative approximation but a more detailed analysis of the LK anisotropies is required to have a good quantitative description of the system, especially in CQWs grown along the [110] direction, where the effect of the cubic anisotropies is enhanced.

3.7 Conclusions

We presented a low-energy effective model that describes holes confined in a NW with a magnetic field parallel to the NW axis and in a perpendicular electric field. We discussed the bulk solution for holes in isotropic semiconductors, where we include the orbital effects of the magnetic field exactly, as well as we extend this result to NWs, providing an analytical solution for holes in

isotropic semiconductor NWs. These effects are found to be essential to accurately describe the properties of the NW.

In particular, we observe a strong renormalization of the effective g factor due to orbital effects even at small values of the external magnetic field. By using a second-order perturbation theory, we also analyze the effects of homogeneous and inhomogeneous electric fields. The homogeneous electric field decreases the effective g factor but enables a strong SOI. The average effective mass changes sign and the spin-dependent mass vanishes with increasing electric field. The inhomogeneous electric field has a strong effect at weak electric field where it leads to a decrease of the g factor. We also include strain in the system, which enhances the subband gap, thus, yielding a reduced HH-LH coupling. This effect increases the g factor but decreases the SOI.

We study also the low-energy physics of holes confined in a gate-defined one-dimensional channel and we predict a similar behavior of the g factor and SOI as in a Ge NW but with some qualitative differences in the average and spin-dependent effective mass, which are in this case only weakly dependent on the electric field. We also examine holes in a CQW, where we predict a g factor independent of the electric field in a wide range of parameters. This feature is relevant for spin qubits in quantum dots because it reduces the susceptibility to charge noise, a major decoherence channel in current devices. Orbital effects are also found to be extremely important in CQW, yielding an enhanced g factor at weak electric fields.

We predict that the spin-orbit split-off band causes a small quantitative correction of the effective parameters in Ge NWs. For particularly thin NWs and CQWs, this effect becomes more relevant, however, the qualitative behavior remains unchanged. By a comparison of our results form calculations with the IA to results where anisotropies are taken into account we find a good agreement justifying the application of the IA.

Acknowledgments. We thank Monica Benito and Christoph Kloeffel for useful discussions and comments. This work is supported by the Swiss National Science Foundation (SNSF) and NCCR SPIN (grant number 51NF40-180604).

3.A Bulk dispersion relation

In this Appendix, we show how to calculate the bulk dispersion relation for holes including orbital effects. We consider the LK Hamiltonian in Eq. (3.2). In the symmetric gauge $\boldsymbol{A} = (-y, x, 0)B/2$, using the Landau ladder operators from Eq. (3.14), the Hamiltonian explicitly reads in the spin basis $(+3/2, +1/2, -1/2, -3/2)$,

$$\frac{H_{\mathrm{LK}}}{\hbar\omega_c} = \begin{pmatrix} \frac{\gamma_-^z k_z^2}{2} + \gamma_+\left(a^\dagger a + \frac{1}{2}\right) & -\sqrt{6}\gamma_s a k_z & -\sqrt{3}\gamma_s a^2 & 0 \\ -\sqrt{6}\gamma_s a^\dagger k_z & \frac{\gamma_+^z k_z^2}{2} + \gamma_-\left(a^\dagger a + \frac{1}{2}\right) & 0 & -\sqrt{3}\gamma_s a^2 \\ -\sqrt{3}\gamma_s \left(a^\dagger\right)^2 & 0 & \frac{\gamma_+^z k_z^2}{2} + \gamma_-\left(a^\dagger a + \frac{1}{2}\right) & \sqrt{6}\gamma_s a k_z \\ 0 & -\sqrt{3}\gamma_s \left(a^\dagger\right)^2 & \sqrt{6}\gamma_s a^\dagger k_z & \frac{\gamma_-^z k_z^2}{2} + \gamma_+\left(a^\dagger a + \frac{1}{2}\right) \end{pmatrix}, \tag{3.61}$$

where $\gamma_\pm^z = (\gamma_1 - 2\gamma_s)/2$. Adding the Zeeman Hamiltonian from Eq. (3.4) leads to the Schrödinger equation

$$O_1(N, k_z^2)\varphi_1 = \sqrt{2}ak_z\varphi_2 + a^2\varphi_3, \tag{3.62}$$

$$O_2(N, k_z^2)\varphi_2 = \sqrt{2}a^\dagger k_z\varphi_1 + a^2\varphi_4, \tag{3.63}$$

$$O_3(N, k_z^2)\varphi_3 = -\sqrt{2}ak_z\varphi_4 + \left(a^\dagger\right)^2\varphi_1, \tag{3.64}$$

$$O_4(N, k_z^2)\varphi_4 = -\sqrt{2}a^\dagger k_z\varphi_3 + \left(a^\dagger\right)^2\varphi_2, \tag{3.65}$$

with energies normalized by $\hbar\omega_c$, lengths normalized by l_B, and the components of the wave function φ_i, $i = 1, 2, 3, 4$. The operators $O_i = O_i(N, k_z^2)$ are the diagonal entries of the Hamiltonian in Eq. (3.61) plus the Zeeman term minus the energy eigenvalue ε, explicitly given by

$$O_1 = \frac{1}{\sqrt{3}\gamma_s}\left(\frac{\gamma_-^z}{2}k_z^2 + \gamma_+\left(N+\frac{1}{2}\right) - \varepsilon + \frac{3\kappa}{2}\right), \tag{3.66}$$

$$O_2 = \frac{1}{\sqrt{3}\gamma_s}\left(\frac{\gamma_+^z}{2}k_z^2 + \gamma_-\left(N+\frac{1}{2}\right) - \varepsilon + \frac{\kappa}{2}\right), \tag{3.67}$$

$$O_3 = \frac{1}{\sqrt{3}\gamma_s}\left(\frac{\gamma_+^z}{2}k_z^2 + \gamma_-\left(N+\frac{1}{2}\right) - \varepsilon - \frac{\kappa}{2}\right), \tag{3.68}$$

$$O_4 = \frac{1}{\sqrt{3}\gamma_s}\left(\frac{\gamma_-^z}{2}k_z^2 + \gamma_+\left(N+\frac{1}{2}\right) - \varepsilon - \frac{3\kappa}{2}\right), \tag{3.69}$$

where we define the number operator $N = a^\dagger a$. In the following we will make use of the relation $a^\dagger a = aa^\dagger - 1$, which implies $a^m O_i(N, k_z^2) = O_i(N+m, k_z^2)a^m$ and $\left(a^\dagger\right)^m O_i(N, k_z^2) = O_i(N-m, k_z^2)\left(a^\dagger\right)^m$, $m \in \mathbb{N}$. Multiplying Eq. (3.63) by $\left(a^\dagger\right)^2$ and Eq. (3.64) by a^2 from the left side yields

$$\left(2k_z^2 a^\dagger a + \left(a^\dagger\right)^2 a^2\right)\varphi_4 = -\sqrt{2}a^\dagger k_z O_3(N, k_z^2)\varphi_3 + \left(a^\dagger\right)^2 O_2(N, k_z^2)\varphi_2, \tag{3.70}$$

$$\left(2k_z^2 aa^\dagger + a^2\left(a^\dagger\right)^2\right)\varphi_1 = \sqrt{2}ak_z O_2(N, k_z^2)\varphi_2 + a^2 O_3(N, k_z^2)\varphi_3, \tag{3.71}$$

respectively. Since the left side of these equations contains only the operators k_z^2 and combinations of a and $a^\dagger$, it can be rewritten in terms of N, and thus, this part of the equations commutes with $O_i(N, k_z^2)$. Thus, applying $O_4(N, k_z^2)$ to Eq. (3.70) and $O_1(N, k_z^2)$ to Eq. (3.71) results in

$$a^\dagger A(N+2, k_z^2)\varphi_2 = \sqrt{2}k_z B(N+1, k_z^2)\varphi_3, \tag{3.72}$$

$$\sqrt{2}k_z C(N-1, k_z^2)\varphi_2 = -aD(N-2, k_z^2)\varphi_3, \tag{3.73}$$

with

$$A(N, k_z^2) = N(N + 2k_z^2 - 1) - O_4(N, k_z^2)O_2(N-2, k_z^2), \tag{3.74}$$

$$B(N, k_z^2) = N(N + 2k_z^2 - 1) - O_4(N, k_z^2)O_3(N-1, k_z^2), \tag{3.75}$$

$$C(N, k_z^2) = N^2 + 3N + 2 + 2k_z^2(N+1) - O_1(N, k_z^2)O_2(N+1, k_z^2), \tag{3.76}$$

$$D(N, k_z^2) = N^2 + 3N + 2 + 2k_z^2(N+1) - O_1(N, k_z^2)O_3(N+2, k_z^2). \tag{3.77}$$

Acting with $\sqrt{2}k_z C(N-2, k_z^2)$ on Eq. (3.72) finally results in the implicit dispersion relation

$$2k_z^2 C(\bar{n}-2, k_z^2)B(\bar{n}+1) + \bar{n}A(\bar{n}+1, k_z^2)D(\bar{n}-2, k_z^2) = 0 \tag{3.78}$$

with $\bar{n}$ being the integer eigenvalue of N, i.e., $N\varphi_3 = \bar{n}\varphi_3$. We can solve this equation for the energies ε, which yields the bulk dispersion relation depicted in Fig. 3.2.

We also discuss the bulk solution excluding orbital effects. In this case, we only need to diagonalize the ILK Hamiltonian given in Eq. (3.5) where $H_{\text{orb}} = 0$ and $\boldsymbol{\pi} = \boldsymbol{k}$, which can easily be done by applying the unitary transformation

$$U = e^{i\theta J_y}e^{i\varphi J_z}. \tag{3.79}$$

We then obtain the diagonal matrix

$$UH_{\mathrm{LK}}U^{\dagger} = \frac{\hbar^2}{2m}\left(\gamma_k - 2\gamma_s J_z^2\right)k^2, \tag{3.80}$$

which yields two degenerate states with parabolic dispersion relation ($k = |\boldsymbol{k}|$). The rotation angles depend only on the direction of $\boldsymbol{k}$ and are given by

$$\theta = \arccos\left(\frac{k_z}{k}\right) \in [0, \pi), \tag{3.81}$$

$$\varphi = \operatorname{arctan2}\left(k_y, k_x\right) \in (-\pi, \pi], \tag{3.82}$$

with

$$\operatorname{arctan2}(y,x) = \begin{cases} 2\arctan\left(\frac{y}{x+\sqrt{x^2+y^2}}\right) & \text{if } \ x > 0 \| \ y \neq 0, \\ \pi & \text{if } x < 0 \ \wedge \ y = 0, \\ \text{undefined} & \text{if } x = 0 \ \wedge \ y = 0. \end{cases} \tag{3.83}$$

At $k_x = k_y = 0$ the angle φ is undefined but, in this case, the Hamiltonian is diagonalized directly by the rotation $e^{i\varphi J_z}$. The bulk dispersion relation without orbital effects is shown by the black solid lines in Fig. 3.2.

3.B Derivation of the analytical solution for a cylindrical nanowire

This Appendix provides the derivations for the exact analytical solution of an isotropic semiconductor hole NW with circular cross section in a magnetic field parallel to the NW. As a starting point, we consider the Hamiltonian for the perpendicular directions H_{xy} defined in Eq. (3.15) with creation and annihilation operators in polar coordinates defined as

$$a^{\dagger}a = \frac{1}{2}\left(-\partial_r^2 - \frac{1}{r}\partial_r - \frac{1}{r^2}\partial_\varphi^2 + \frac{r^2}{4} - i\partial_\varphi - 1\right), \tag{3.84}$$

$$a^{\dagger} = \frac{-ie^{i\varphi}}{\sqrt{2}}\left(\partial_r + \frac{i}{r}\partial_\varphi - \frac{r}{2}\right), \tag{3.85}$$

$$a = \frac{-ie^{-i\varphi}}{\sqrt{2}}\left(\partial_r - \frac{i}{r}\partial_\varphi + \frac{r}{2}\right). \tag{3.86}$$

Also we consider now the Zeeman Hamiltonian H_Z from Eq. (3.4). The eigenstates of the upper block ($\uparrow$) of H_{xy} are eigenfunctions of $a^{\dagger}a$. We find the general eigenfunction of $a^{\dagger}a$ in Eq. (3.84) by identifying the equation

$$a^{\dagger}a\left[e^{-im\varphi}r^m e^{-r^2/4}g(\boldsymbol{r})\right] = 0 \tag{3.87}$$

as the Laguerre differential equation with $m \in \mathbb{Z}$. The eigenvalues of $a^{\dagger}a$ are $\alpha \in \mathbb{R}$. We remark that in Sec. 3.3.1 for the bulk solution, the eigenvalues are $\alpha \to n \in \mathbb{N}$ because the bulk solutions are required to decay to zero at infinity. Here, in contrast, we have different boundary conditions, allowing for real valued α. Most generally, the eigenfunction to the eigenvalue α is

$$\psi_{m,\alpha}(\boldsymbol{r}) = 2^{-\frac{m}{2}}e^{-im\varphi}e^{-\frac{r^2}{4}}r^m\left[i^m L_\alpha^m\left(\frac{r^2}{2}\right) + \frac{(-i)^m}{\alpha!}U\left(-\alpha, m+1, \frac{r^2}{2}\right)\right], \tag{3.88}$$

where $L_a^b(x)$ is the associated Laguerre function and $U(a,b,x)$ is the confluent hyper-geometric function of the second kind. The effect of the creation and annihilation operators on this eigenfunction is given by

$$a^\dagger \psi_{m,\alpha}(\mathbf{r}) = (1+\alpha)\psi_{m-1,\alpha+1}(\mathbf{r}), \tag{3.89}$$
$$a\psi_{m,\alpha}(\mathbf{r}) = \psi_{m+1,\alpha-1}(\mathbf{r}). \tag{3.90}$$

The general eigenstate of the ↑ block of H_{xy} in Eq. (3.15) is of the form $(\psi_{m,\alpha}(\mathbf{r}),$ $c^\uparrow\psi_{m-2,\alpha+2}(\mathbf{r}))$, which we can insert into the Schrödinger equation given by the ↑ block of H_{xy} in Eq. (3.15), arriving at

$$\frac{1}{\sqrt{3}\gamma_s}\left[(\gamma_1+\gamma_s)\left(\alpha+\frac{1}{2}\right)-\varepsilon_{+3/2}\right]\psi_{m,\alpha}(\boldsymbol{r}) = c^\uparrow\psi_{m,\alpha}(\boldsymbol{r}), \tag{3.91}$$
$$\frac{c^\uparrow}{\sqrt{3}\gamma_s}\left[(\gamma_1-\gamma_s)\left(\alpha+\frac{5}{2}\right)-\varepsilon_{-1/2}\right]\psi_{m-2,\alpha+2}(\boldsymbol{r}) = (\alpha+1)(\alpha+2)\psi_{m-2,\alpha+2}(\boldsymbol{r}), \tag{3.92}$$

with the energies $\varepsilon_{+3/2} = \varepsilon - 3\kappa/2$ and $\varepsilon_{-1/2} = \varepsilon + \kappa/2$ redefined to include the Zeeman energy. The coefficients are given in the main text by Eqs. (3.22) and (3.23).

By imposing HW boundary conditions, following from Eq. (3.19), and by requiring each element of the spinor to vanish at $r = R$, we arrive at the expression for the wave function given in Eq. (3.20). For the lower block (↓) of H_{xy} in Eq. (3.15) describing the spin states $(-3/2, +1/2)$ we proceed analogously with a similar ansatz $\left(\psi_{m,\alpha}(\mathbf{r}), c^\downarrow\psi_{m-2,\alpha+2}(\mathbf{r})\right)$ as for the upper block (↑). We obtain in this case the coefficients given by Eqs. (3.26) and (3.27). With the ansatz for the ↓ block, we arrive at the spinor given in Eq. (3.25).

It is possible to include strain into our analytical calculations because of the simple form of the BP Hamiltonian H_{BP} defined in Eq. (3.7). Since $H_{\mathrm{BP}} \propto J_{z'}^2$ does not change the Schrödinger in Eqs. (3.91) and (3.92) qualitatively the calculation of the eigenstates is analogous. The solution keeps the same form, however, the coefficients $c_\pm^s$ and $\alpha_\pm^s$ are modified as

$$c_\pm^\uparrow = \frac{(2\alpha_\pm^\uparrow+1)(\gamma_1+\gamma_s)+3\kappa-2\varepsilon}{2\sqrt{3}\gamma_s} + \frac{9|b|\varepsilon_s}{4\sqrt{3}\gamma_s\hbar\omega_c}, \tag{3.93}$$
$$c_\pm^\downarrow = \frac{(2\alpha_\pm^\downarrow+1)(\gamma_1-\gamma_s)+\kappa-2\varepsilon}{2\sqrt{3}\gamma_s} + \frac{|b|\varepsilon_s}{4\sqrt{3}\gamma_s\hbar\omega_c}, \tag{3.94}$$
$$\begin{aligned}\alpha_\pm^\uparrow =& \frac{-6\gamma_1^2+24\gamma_s^2+4\gamma_1\varepsilon-2\gamma_1\kappa+4\gamma_s\kappa+(-5\gamma_1+4\gamma_s)\frac{|b|\varepsilon_s}{\hbar\omega_c}}{4(\gamma_1^2-4\gamma_s^2)} \\ &+\Bigg\{4\gamma_1^4-23\gamma_1^2\gamma_s^2+28\gamma_s^4-8\gamma_1^2\gamma_s\varepsilon+32\gamma_s^3\varepsilon+16\gamma_s^2\varepsilon^2 \\ &-4(\gamma_1-2\gamma_s)\left[2\gamma_1^2+3\gamma_1\gamma_s-2\gamma_s(\gamma_s+\varepsilon)\right]\kappa+4(\gamma_1-2\gamma_s)(\gamma_1+\gamma_s)\kappa^2 \\ &-2\left\{4\gamma_1^3+2\gamma_s^2\left[10(\gamma_s+\varepsilon)+\kappa\right]-\gamma_1^2(5\gamma_s+4\kappa)+\gamma_1\gamma_s\left[-4(4\gamma_s+\varepsilon)+7\kappa\right]\right\}\frac{|b|\varepsilon_s}{\hbar\omega_c} \\ &+\left(4\gamma_1^2+10\gamma_1\gamma_s+13\gamma_s^2\right)\left(\frac{|b|\varepsilon_s}{\hbar\omega_c}\right)^2\Bigg\}^{1/2} / \left[2(\gamma_1^2-4\gamma_s^2)\right],\end{aligned} \tag{3.95}$$

$$\alpha_{\pm}^{\downarrow} = \frac{-6\gamma_1^2 + 24\gamma_s^2 + 4\gamma_1\varepsilon + 2\gamma_1\kappa - 4\gamma_s\kappa + (-5\gamma_1 + 4\gamma_s)\frac{|b|\varepsilon_s}{\hbar\omega_c}}{4(\gamma_1^2 - 4\gamma_s^2)}$$
$$+ \Bigg\{ 4\gamma_1^4 - 23\gamma_1^2\gamma_s^2 + 28\gamma_s^4 + 8\gamma_1^2\gamma_s\varepsilon + 32\gamma_s^3\varepsilon + 16\gamma_s^2\varepsilon^2$$
$$- 4(\gamma_1 - 2\gamma_s)\left[2\gamma_1^2 + 3\gamma_1\gamma_s + 2\gamma_s(-\gamma_s + \varepsilon)\right]\kappa + 4(\gamma_1 - 2\gamma_s)(\gamma_1 + \gamma_s)\kappa^2$$
$$+ 2\left\{4\gamma_1^3 + 2\gamma_s^2\left[10(\gamma_s - \varepsilon) + \kappa\right] - \gamma_1^2(5\gamma_s + 4\kappa) + \gamma_1\gamma_s\left[4(-4\gamma_s + \varepsilon) + 7\kappa\right]\right\}\frac{|b|\varepsilon_s}{\hbar\omega_c}$$
$$+ \left(4\gamma_1^2 - 10\gamma_1\gamma_s + 13\gamma_s^2\right)\left(\frac{|b|\varepsilon_s}{\hbar\omega_c}\right)^2 \Bigg\}^{1/2} / \left[2(\gamma_1^2 - 4\gamma_s^2)\right]. \tag{3.96}$$

For $b = 0$ the coefficients coincide with the ones given in the main text by Eqs. (3.22), (3.23), (3.26), and (3.27).

3.C Effective parameters

The Hamiltonian $H_{\mathrm{LK}}^{\mathrm{eff}}$ introduced in Eq. (3.34) in Sec. 3.3.4 depends on several effective parameters that are defined in the main text. In this Appendix we show the dependence of these parameters (cf. Fig. 3.16) on the magnetic field. These parameters enter the calculations for the 2×2 NW Hamiltonian in Sec. 3.3.5.

The inverse effective masses $1/m_i^s$ are shown in Fig. 3.16(a). The ground state at $B = 0$ is almost exclusively of LH nature. Therefore, we would expect the inverse ground state masses to be $1/m_2^{\uparrow} = 1/m_0^{\downarrow} = \gamma_1 + 2\gamma_s = 23.3/m$ at $B = 0$, see Eq. (3.38). However, the corrections from second-order perturbation theory are large, yielding a larger mass. The states higher in energy are a mixture of HH and LH, and therefore, their masses are larger. Also, these values are considerably corrected by second-order perturbation theory. The mass $m_2^{\downarrow}$ decreases strongly above $B = 5\,\mathrm{T}$, a trend that can be explained by the anticrossing of states in the spectrum in Fig. 3.3(a). There is a clear avoided crossing between the green-dashed and the brown-dashed lines.

In Fig. 3.16(b), we plot the absolute value of the two SOI parameters α_1 and α_2 obtained from Eq. (3.39) and Eq. (3.40) as a function of the magnetic field B. Both parameters exhibit a linear dependence on the magnetic field for weak fields. Moreover, α_2 has a linear behavior in the whole range of B shown, while α_1 reaches a maximum at $B = 9.5\,\mathrm{T}$. At $B = 0$ both couplings are $\alpha_{1/2}(B = 0) \approx 2.5\,\hbar^2/(mR)$; at larger values of B, α_1 increases with the magnetic field while α_2 decreases.

The behaviors of the absolute values of the dipole and the quadrupole moments in a NW of radius $R = 15\,\mathrm{nm}$ are analyzed in Figs. 3.16(c) and 3.16(d), respectively. The dipole moment $|d_1^{\downarrow}|$ has a minimum at $B = 8.5\,\mathrm{T}$ and $|d_1^{\uparrow}|$ increases throughout the whole magnetic field range; moreover $|d_2^{\uparrow}|$ decreases linearly and $|d_2^{\downarrow}|$ has a maximum at $B = 6.7\,\mathrm{T}$ where it reaches $4.2\,\mathrm{meV\,\mu m\,V^{-1}}$. The strong magnetic field dependence of $|d_2^{\downarrow}|$ results from the already discussed anticrossing in the spectrum in Fig. 3.3(a).

The quadrupole moment $|q^{\uparrow}|$ strongly increases with the magnetic field while $|q^{\downarrow}|$ only weakly depends on B, exhibiting a minimum at $B = 4.7\,\mathrm{T}$. In general, there are terms originating from the quadrupole moments also in the diagonal part of $H_{\mathrm{LK}}^{\mathrm{eff}}$ given by Eq. (3.34). However, they are negligible compared to the contributions form H_{xy}, H_Z, and the mass terms, and we do not consider them here. As can be seen from the Hamiltonian $H_{\mathrm{LK}}^{\mathrm{eff}}$ [see Eq. (3.34)], the homogeneous field couples states from equal subspaces with neighboring m, while the field gradient couples the zero magnetic field ground states to the second excited states of equal subspaces. We note that

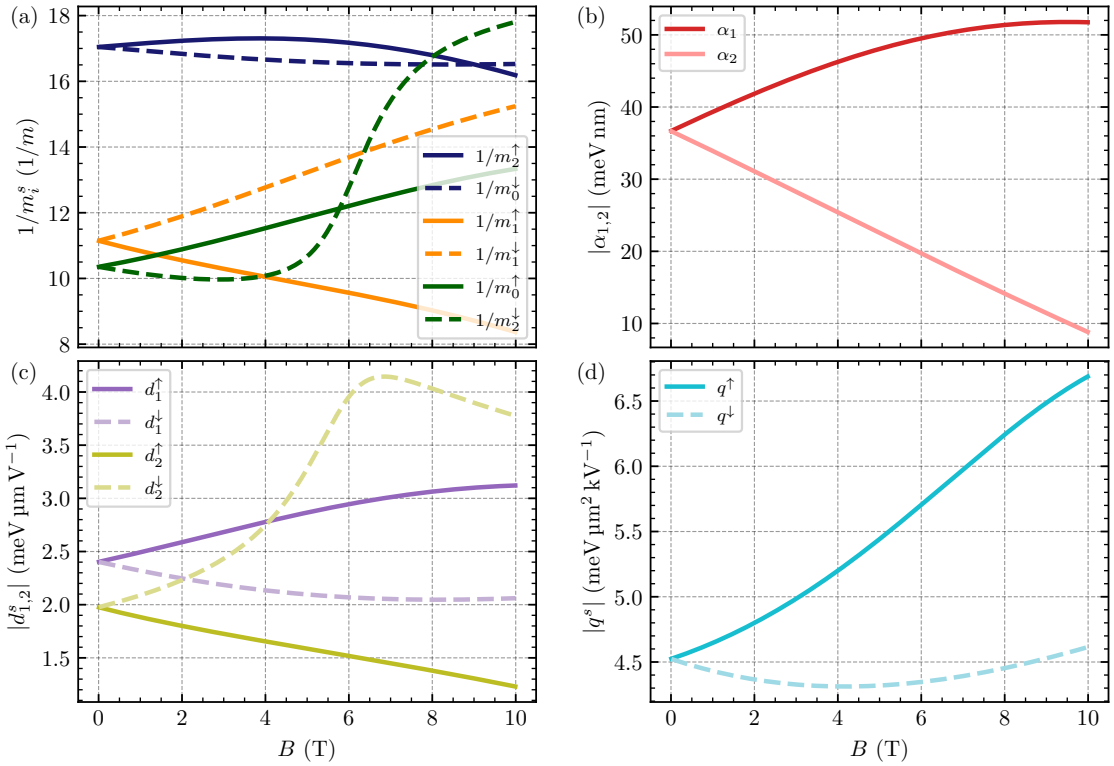

Figure 3.16: Effective parameters of a Ge NW with circular cross section of radius $R = 15\,\text{nm}$ as a function of B calculated semi-analytically at $E_x = E_y = \delta E = 0$. The solid lines in (a), (c), and (d) correspond to states from the $\uparrow$ subspace and the dashed ones to the $\downarrow$ subspace. (a) The effective masses $1/m_i^s$ are calculated by using Eq. (3.38). The masses of the lowest two energy states, $m_2^\uparrow$ and $m_0^\downarrow$ (blue) depend only weakly on B compared to the masses of the next higher in energy states, $m_1^\uparrow$ and $m_1^\downarrow$ (orange) or $m_0^\uparrow$ and $m_2^\downarrow$ (green). The mass $m_2^\downarrow$ (green dashed) varies strongly with B due to the anti-crossing in the spectrum [cf. Fig. 3.3(a)]. The colors of the lines are the same as for the corresponding states in Fig. 3.3(a). (b) The SOI term $|\alpha_1|$ [cf. Eq. (3.39)] increases with B and reaches a maximum at $B = 9.5\,\text{T}$, while $|\alpha_2|$ [cf. Eq. (3.40)] decreases linearly. (c) The dipole moments $|d_{1,2}^{\text{U,D}}|$ are given by Eqs. (3.41) and (3.42). For our choice of parameters, $|d_1^\uparrow|$ (violet solid) increases monotonically with B, $|d_1^\downarrow|$ (violet dashed) has a minimum, $|d_2^\uparrow|$ (green solid) decreases monotonically, and $|d_2^\downarrow|$ (green dashed) exhibits a distinctive maximum [cf. the anti-crossing in Fig. 3.3(a)]. (d) The quadruple moments q^s are given by Eq. (3.43). The quadrupole moment $|q^\uparrow|$ increases monotonically and $|q^\downarrow|$ increases after reaching a minimum at $B = 4.7\,\text{T}$. Note that in panels (b), (c), and (d) we present absolute values.

the matrix elements for the dipole moments $d_{1,2}^s$ are imaginary numbers whereas the quadrupole moments q^s are real numbers.

3.D Effective model

In this Appendix, we give more details on the calculations for the effective 2×2 model Hamiltonian $H^{2\times2}$ from Sec. 3.3.4. The definitions introduced in Eqs. (3.45)–(3.48) allow us to write the 4×4-matrix $H^{4\times4}$ spanned by the four component basis $(\varphi_2^{\uparrow},\varphi_1^{\uparrow},\varphi_0^{\downarrow},\varphi_1^{\downarrow})$ as

$$H^{4\times4}=\begin{pmatrix} \varepsilon_+^{\uparrow}+\Omega^{\uparrow}\cos\left(2\theta^{\uparrow}\right)+\frac{\hbar^2k_z^2}{2m_2^{\uparrow}} & i\Omega^{\uparrow}\sin\left(2\theta^{\uparrow}\right) & 0 & \alpha_1k_z \\ -i\Omega^{\uparrow}\sin\left(2\theta^{\uparrow}\right) & \varepsilon_+^{\uparrow}-\Omega^{\uparrow}\cos\left(2\theta^{\uparrow}\right)+\frac{\hbar^2k_z^2}{2m_1^{\uparrow}} & \alpha_2k_z & 0 \\ 0 & \alpha_2k_z & \varepsilon_+^{\downarrow}+\Omega^{\downarrow}\cos\left(2\theta^{\downarrow}\right)+\frac{\hbar^2k_z^2}{2m_0^{\downarrow}} & i\Omega^{\downarrow}\sin\left(2\theta^{\downarrow}\right) \\ \alpha_1k_z & 0 & -i\Omega^{\downarrow}\sin\left(2\theta^{\downarrow}\right) & \varepsilon_+^{\downarrow}-\Omega^{\downarrow}\cos\left(2\theta^{\downarrow}\right)+\frac{\hbar^2k_z^2}{2m_1^{\downarrow}} \end{pmatrix}. \tag{3.97}$$

In order to treat the electric field exactly, we diagonalize the block in the upper left and the lower right of this matrix at $k_z=0$ via the unitary transformation $U^{-1}H^{4\times4}U$ where

$$U=\begin{pmatrix} \cos\left(\theta^{\uparrow}\right) & -i\sin\left(\theta^{\uparrow}\right) & 0 & 0 \\ -i\sin\left(\theta^{\uparrow}\right) & \cos\left(\theta^{\uparrow}\right) & 0 & 0 \\ 0 & 0 & \cos\left(\theta^{\downarrow}\right) & -i\sin\left(\theta^{\downarrow}\right) \\ 0 & 0 & -i\sin\left(\theta^{\downarrow}\right) & \cos\left(\theta^{\downarrow}\right) \end{pmatrix}. \tag{3.98}$$

We use the resulting matrix and perform a second-order perturbation theory with respect to the ground state subspace $(\varphi_2^{\uparrow},\varphi_0^{\downarrow})$ and we project the results onto this subspace, yielding the effective 2×2 model in Eq. (3.49).

3.E Six-band Luttinger-Kohn model

In addition to the four HH and LH states considered in the Hamiltonian H defined in Eq. (3.1), we include in our calculations also the SOB. In this case, we use the following Hamiltonian [71, 72, 74, 100]:

$$H^{6\times6}=\begin{pmatrix} P+Q & S & R & 0 & -\frac{1}{\sqrt{2}}S & -\sqrt{2}R \\ S^* & P-Q & 0 & R & \sqrt{2}Q & \sqrt{\frac{3}{2}}S \\ R^* & 0 & P-Q & -S & \sqrt{\frac{3}{2}}S^* & -\sqrt{2}Q \\ 0 & R^* & -S^* & P+Q & \sqrt{2}R^* & -\frac{1}{\sqrt{2}}S^* \\ -\frac{1}{\sqrt{2}}S^* & \sqrt{2}Q & \sqrt{\frac{3}{2}}S & \sqrt{2}R & P+\Delta_{SO} & 0 \\ -\sqrt{2}R^* & \sqrt{\frac{3}{2}}S^* & -\sqrt{2}Q & -\frac{1}{\sqrt{2}}S & 0 & P+\Delta_{SO} \end{pmatrix}, \tag{3.99}$$

where the matrix entries are defined as

$$P = \frac{\hbar^2}{2m}\gamma_1 \boldsymbol{k}^2, \tag{3.100}$$

$$Q = \frac{\hbar^2}{2m}\gamma_2(k_x^2 + k_y^2 - 2k_z^2), \tag{3.101}$$

$$S = -\frac{\hbar^2}{2m}2\sqrt{3}\gamma_3 k_z k_-, \tag{3.102}$$

$$R = -\frac{\hbar^2}{2m}\frac{\sqrt{3}}{2}\left[(\gamma_2+\gamma_3)k_-^2 + (\gamma_2-\gamma_3)k_+^2\right], \tag{3.103}$$

with $k_\pm = k_\mp^* = k_x \pm ik_y$. The spin-orbit gap for Ge is $\Delta_{SO} = 296\,\text{meV}$. Including the SOB, the Zeeman Hamiltonian H_Z from Eq. (3.4) becomes [74]

$$H_Z^{6\times6} = \kappa\mu_B \begin{pmatrix} 3B_z & \sqrt{3}B_- & 0 & 0 & -\sqrt{\frac{3}{2}}B_- & 0 \\ \sqrt{3}B_+ & B_z & B_- & 0 & \sqrt{2}B_z & -\frac{1}{\sqrt{2}}B_- \\ 0 & B_+ & -B_z & \sqrt{3}B_- & \frac{1}{\sqrt{2}}B_+ & \sqrt{2}B_z \\ 0 & 0 & \sqrt{3}B_+ & -3B_z & 0 & \sqrt{\frac{3}{2}}B_+ \\ -\sqrt{\frac{3}{2}}B_+ & \sqrt{2}B_z & \frac{1}{\sqrt{2}}B_- & 0 & B_z & B_- \\ 0 & -\frac{1}{\sqrt{2}}B_+ & \sqrt{2}B_z & \sqrt{\frac{3}{2}}B_- & B_+ & -B_z \end{pmatrix}, \tag{3.104}$$

where we define $B_\pm = B_x \pm iB_y$.

The BP Hamiltonian including the SOB in the Ge/Si core/shell NW is given by

$$H_{\text{BP}}^{6\times6} = |b|\varepsilon_s \begin{pmatrix} \frac{9}{4} & 0 & 0 & 0 & 0 & 0 \\ 0 & \frac{1}{4} & 0 & 0 & \sqrt{2} & 0 \\ 0 & 0 & \frac{1}{4} & 0 & 0 & -\sqrt{2} \\ 0 & 0 & 0 & \frac{9}{4} & 0 & 0 \\ 0 & \sqrt{2} & 0 & 0 & \frac{5}{4} & 0 \\ 0 & 0 & -\sqrt{2} & 0 & 0 & \frac{5}{4} \end{pmatrix}, \tag{3.105}$$

while in a CQW it is given by [31]

$$\frac{H_{\text{BP}}^{6\times6,\text{CQW}}}{|b|} = \begin{pmatrix} \frac{9}{8}(\varepsilon_r+2\varepsilon_z) & 0 & -\frac{\sqrt{3}}{2}e^{-2i\theta}\varepsilon_r & 0 & 0 & \sqrt{\frac{3}{2}}e^{-2i\theta}\varepsilon_r \\ 0 & \frac{1}{8}(\varepsilon_r+2\varepsilon_z) & 0 & -\frac{\sqrt{3}}{2}e^{-2i\theta}\varepsilon_r & \frac{\varepsilon_r+2\varepsilon_z}{\sqrt{2}} & 0 \\ -\frac{\sqrt{3}}{2}e^{2i\theta}\varepsilon_r & 0 & \frac{1}{8}(\varepsilon_r+2\varepsilon_z) & 0 & 0 & -\frac{\varepsilon_r+2\varepsilon_z}{\sqrt{2}} \\ 0 & -\frac{\sqrt{3}}{2}e^{2i\theta}\varepsilon_r & 0 & \frac{9}{8}(\varepsilon_r+2\varepsilon_z) & -\sqrt{\frac{3}{2}}e^{2i\theta}\varepsilon_r & 0 \\ 0 & \frac{\varepsilon_r+2\varepsilon_z}{\sqrt{2}} & 0 & -\sqrt{\frac{3}{2}}e^{-2i\theta}\varepsilon_r & \frac{5}{8}(\varepsilon_r+2\varepsilon_z) & 0 \\ \sqrt{\frac{3}{2}}e^{2i\theta}\varepsilon_r & 0 & -\frac{\varepsilon_r+2\varepsilon_z}{\sqrt{2}} & 0 & 0 & \frac{5}{8}(\varepsilon_r+2\varepsilon_z) \end{pmatrix}. \tag{3.106}$$

Here, we introduce the polar coordinate angle θ (cf. Sec. 3.5) and the strain energies are defined in Eqs. (3.11) and (3.12).

References

[1] F. N. M. Froning, M. J. Rančić, B. Hetényi, S. Bosco, M. K. Rehmann, A. Li, E. P. A. M. Bakkers, F. A. Zwanenburg, D. Loss, D. M. Zumbühl, and F. R. Braakman, "Strong spin-orbit interaction and g-factor renormalization of hole spins in Ge/Si nanowire quantum dots", Phys. Rev. Res. **3**, 013081 (2021).

[2] X.-J. Hao, T. Tu, G. Cao, C. Zhou, H.-O. Li, G.-C. Guo, W. Y. Fung, Z. Ji, G.-P. Guo, and W. Lu, "Strong and tunable spin-orbit coupling of one-dimensional holes in Ge/Si core/shell nanowires", Nano Lett. **10**, 2956 (2010).

[3] Y. Hu, F. Kuemmeth, C. M. Lieber, and C. M. Marcus, "Hole spin relaxation in Ge-Si core-shell nanowire qubits", Nat. Nanotechnol. **7**, 47 (2011).

[4] L. A. Terrazos, E. Marcellina, Z. Wang, S. N. Coppersmith, M. Friesen, A. R. Hamilton, X. Hu, B. Koiller, A. L. Saraiva, D. Culcer, and R. B. Capaz, "Theory of hole-spin qubits in strained germanium quantum dots", Phys. Rev. B **103**, 125201 (2021).

[5] G. Scappucci, C. Kloeffel, F. A. Zwanenburg, D. Loss, M. Myronov, J.-J. Zhang, S. D. Franceschi, G. Katsaros, and M. Veldhorst, "The germanium quantum information route", Nat. Rev. Mater. **6**, 926 (2021).

[6] H. Liu, T. Zhang, K. Wang, F. Gao, G. Xu, X. Zhang, S.-X. Li, G. Cao, T. Wang, J. Zhang, X. Hu, H.-O. Li, and G.-P. Guo, "Gate-tunable spin-orbit coupling in a germanium hole double quantum dot", Phys. Rev. Appl. **17**, 044052 (2022).

[7] N. W. Hendrickx, D. P. Franke, A. Sammak, G. Scappucci, and M. Veldhorst, "Fast two-qubit logic with holes in germanium", Nature **577**, 487 (2020).

[8] N. W. Hendrickx, W. I. L. Lawrie, M. Russ, F. van Riggelen, S. L. de Snoo, R. N. Schouten, A. Sammak, G. Scappucci, and M. Veldhorst, "A four-qubit germanium quantum processor", Nature **591**, 580 (2021).

[9] H. Watzinger, J. Kukučka, L. Vukušić, F. Gao, T. Wang, F. Schäffler, J.-J. Zhang, and G. Katsaros, "A germanium hole spin qubit", Nat. Commun. **9**, 3902 (2018).

[10] D. Jirovec, A. Hofmann, A. Ballabio, P. M. Mutter, G. Tavani, M. Botifoll, A. Crippa, J. Kukucka, O. Sagi, F. Martins, J. Saez-Mollejo, I. Prieto, M. Borovkov, J. Arbiol, D. Chrastina, G. Isella, and G. Katsaros, "A singlet-triplet hole spin qubit in planar Ge", Nat. Mater. **20**, 1106 (2021).

[11] S. Geyer, L. C. Camenzind, L. Czornomaz, V. Deshpande, A. Fuhrer, R. J. Warburton, D. M. Zumbühl, and A. V. Kuhlmann, "Self-aligned gates for scalable silicon quantum computing", Appl. Phys. Lett. **118**, 104004 (2021).

[12] J. H. Qvist and J. Danon, "Probing details of spin-orbit coupling through Pauli spin blockade", Phys. Rev. B **106**, 235312 (2022).

[13] C. Kloeffel, M. Trif, P. Stano, and D. Loss, "Circuit QED with hole-spin qubits in Ge/Si nanowire quantum dots", Phys. Rev. B **88**, 241405(R) (2013).

[14] S. Bosco, P. Scarlino, J. Klinovaja, and D. Loss, "Fully tunable longitudinal spin-photon interactions in Si and Ge quantum dots", Phys. Rev. Lett. **129**, 066801 (2022).

[15] V. P. Michal, J. C. Abadillo-Uriel, S. Zihlmann, R. Maurand, Y.-M. Niquet, and M. Filippone, "Tunable hole spin-photon interaction based on g-matrix modulation", Phys. Rev. B **107**, l041303 (2023).

[16] A. Y. Kitaev, "Unpaired Majorana fermions in quantum wires", Phys. Usp. **44**, 131 (2001).

[17] J. Klinovaja and D. Loss, "Composite Majorana fermion wave functions in nanowires", Phys. Rev. B **86**, 085408 (2012).

[18] F. N. M. Froning, L. C. Camenzind, O. A. H. van der Molen, A. Li, E. P. A. M. Bakkers, D. M. Zumbühl, and F. R. Braakman, "Ultrafast hole spin qubit with gate-tunable spin-orbit switch functionality", Nat. Nanotechnol. **16**, 308 (2021).

[19] K. Wang, G. Xu, F. Gao, H. Liu, R.-L. Ma, X. Zhang, Z. Wang, G. Cao, T. Wang, J.-J. Zhang, D. Culcer, X. Hu, H.-W. Jiang, H.-O. Li, G.-C. Guo, and G.-P. Guo, "Ultrafast coherent control of a hole spin qubit in a germanium quantum dot", Nat. Commun. **13**, 206 (2022).

[20] D. V. Bulaev and D. Loss, "Spin relaxation and decoherence of holes in quantum dots", Phys. Rev. Lett. **95**, 076805 (2005).

[21] D. V. Bulaev and D. Loss, "Electric dipole spin resonance for heavy holes in quantum dots", Phys. Rev. Lett. **98**, 097202 (2007).

[22] C. Kloeffel, M. Trif, and D. Loss, "Strong spin-orbit interaction and helical hole states in Ge/Si nanowires", Phys. Rev. B **84**, 195314 (2011).

[23] C. Kloeffel, M. Trif, and D. Loss, "Acoustic phonons and strain in core/shell nanowires", Phys. Rev. B **90**, 115419 (2014).

[24] C. Kloeffel, M. J. Rančić, and D. Loss, "Direct Rashba spin-orbit interaction in Si and Ge nanowires with different growth directions", Phys. Rev. B **97**, 235422 (2018).

[25] S. Bosco, M. Benito, C. Adelsberger, and D. Loss, "Squeezed hole spin qubits in Ge quantum dots with ultrafast gates at low power", Phys. Rev. B **104**, 115425 (2021).

[26] P. Philippopoulos, S. Chesi, D. Culcer, and W. A. Coish, "Pseudospin-electric coupling for holes beyond the envelope-function approximation", Phys. Rev. B **102**, 075310 (2020).

[27] Y. Hu, H. O. H. Churchill, D. J. Reilly, J. Xiang, C. M. Lieber, and C. M. Marcus, "A Ge/Si heterostructure nanowire-based double quantum dot with integrated charge sensor", Nat. Nanotechnol. **2**, 622 (2007).

[28] C. Adelsberger, M. Benito, S. Bosco, J. Klinovaja, and D. Loss, "Hole-spin qubits in Ge nanowire quantum dots: interplay of orbital magnetic field, strain, and growth direction", Phys. Rev. B **105**, 075308 (2022).

[29] S. Bosco, B. Hetényi, and D. Loss, "Hole spin qubits in si FinFETs with fully tunable spin-orbit coupling and sweet spots for charge noise", PRX Quantum **2**, 010348 (2021).

[30] Z. Wang, E. Marcellina, A. R. Hamilton, J. H. Cullen, S. Rogge, J. Salfi, and D. Culcer, "Optimal operation points for ultrafast, highly coherent Ge hole spin-orbit qubits", npj Quantum Inf. **7**, 54 (2021).

[31] S. Bosco and D. Loss, "Hole spin qubits in thin curved quantum wells", Phys. Rev. Appl. **18**, 044038 (2022).

[32] W. M. Witzel and S. Das Sarma, "Quantum theory for electron spin decoherence induced by nuclear spin dynamics in semiconductor quantum computer architectures: spectral diffusion of localized electron spins in the nuclear solid-state environment", Phys. Rev. B **74**, 035322 (2006).

[33] W. Yao, R.-B. Liu, and L. J. Sham, "Theory of electron spin decoherence by interacting nuclear spins in a quantum dot", Phys. Rev. B **74**, 195301 (2006).

[34] Ł. Cywiński, W. M. Witzel, and S. Das Sarma, "Electron spin dephasing due to hyperfine interactions with a nuclear spin bath", Phys. Rev. Lett. **102**, 057601 (2009).

[35] A. V. Khaetskii, D. Loss, and L. Glazman, "Electron spin decoherence in quantum dots due to interaction with nuclei", Phys. Rev. Lett. **88**, 186802 (2002).

[36] W. A. Coish and D. Loss, "Hyperfine interaction in a quantum dot: Non-Markovian electron spin dynamics", Phys. Rev. B **70**, 195340 (2004).

[37] R. Hanson, L. P. Kouwenhoven, J. R. Petta, S. Tarucha, and L. M. K. Vandersypen, "Spins in few-electron quantum dots", Rev. Mod. Phys. **79**, 1217 (2007).

[38] K. Itoh, W. Hansen, E. Haller, J. Farmer, V. Ozhogin, A. Rudnev, and A. Tikhomirov, "High purity isotopically enriched ^{70}Ge and ^{74}Ge single crystals: isotope separation, growth, and properties", J. Mater. Res. **8**, 1341 (1993).

[39] K. M. Itoh and H. Watanabe, "Isotope engineering of silicon and diamond for quantum computing and sensing applications", MRS Commun. **4**, 143 (2014).

[40] J. Fischer and D. Loss, "Hybridization and spin decoherence in heavy-hole quantum dots", Phys. Rev. Lett. **105**, 266603 (2010).

[41] F. Maier and D. Loss, "Effect of strain on hyperfine-induced hole-spin decoherence in quantum dots", Phys. Rev. B **85**, 195323 (2012).

[42] D. Klauser, W. A. Coish, and D. Loss, "Nuclear spin state narrowing via gate-controlled Rabi oscillations in a double quantum dot", Phys. Rev. B **73**, 205302 (2006).

[43] J. H. Prechtel, A. V. Kuhlmann, J. Houel, A. Ludwig, S. R. Valentin, A. D. Wieck, and R. J. Warburton, "Decoupling a hole spin qubit from the nuclear spins", Nat. Mater. **15**, 981 (2016).

[44] C. Testelin, F. Bernardot, B. Eble, and M. Chamarro, "Hole–spin dephasing time associated with hyperfine interaction in quantum dots", Phys. Rev. B **79**, 195440 (2009).

[45] J. Fischer, W. A. Coish, D. V. Bulaev, and D. Loss, "Spin decoherence of a heavy hole coupled to nuclear spins in a quantum dot", Phys. Rev. B **78**, 155329 (2008).

[46] S. Bosco and D. Loss, "Fully tunable hyperfine interactions of hole spin qubits in Si and Ge quantum dots", Phys. Rev. Lett. **127**, 190501 (2021).

[47] M. Milivojević, "Electrical control of the hole spin qubit in Si and Ge nanowire quantum dots", Phys. Rev. B **104**, 235304 (2021).

[48] Y.-J. Doh, J. A. van Dam, A. L. Roest, E. P. A. M. Bakkers, L. P. Kouwenhoven, and S. D. Franceschi, "Tunable supercurrent through semiconductor nanowires", Science **309**, 272 (2005).

[49] J. Xiang, A. Vidan, M. Tinkham, R. M. Westervelt, and C. M. Lieber, "Ge/Si nanowire mesoscopic Josephson junctions", Nat. Nanotechnol. **1**, 208 (2006).

[50] J. Hajer, M. Kessel, C. Brüne, M. P. Stehno, H. Buhmann, and L. W. Molenkamp, "Proximity-induced superconductivity in CdTe-HgTe core-shell nanowires", Nano Lett. **19**, 4078 (2019).

[51] J. Alicea, "New directions in the pursuit of Majorana fermions in solid state systems", Rep. Prog. Phys. **75**, 076501 (2012).

[52] F. Maier, J. Klinovaja, and D. Loss, "Majorana fermions in Ge/Si hole nanowires", Phys. Rev. B **90**, 195421 (2014).

[53] S. M. Albrecht, A. P. Higginbotham, M. Madsen, F. Kuemmeth, T. S. Jespersen, J. Nygård, P. Krogstrup, and C. M. Marcus, "Exponential protection of zero modes in Majorana islands", Nature **531**, 206 (2016).

[54] R. M. Lutchyn, J. D. Sau, and S. Das Sarma, "Majorana fermions and a topological phase transition in semiconductor-superconductor heterostructures", Phys. Rev. Lett. **105**, 077001 (2010).

[55] R. M. Lutchyn, E. P. A. M. Bakkers, L. P. Kouwenhoven, P. Krogstrup, C. M. Marcus, and Y. Oreg, "Majorana zero modes in superconductor-semiconductor heterostructures", Nat. Rev. Mater. **3**, 52 (2018).

[56] V. Mourik, K. Zuo, S. M. Frolov, S. R. Plissard, E. P. A. M. Bakkers, and L. P. Kouwenhoven, "Signatures of Majorana fermions in hybrid superconductor-semiconductor nanowire devices", Science **336**, 1003 (2012).

[57] J. D. Sau, S. Tewari, R. M. Lutchyn, T. D. Stanescu, and S. Das Sarma, "Non-Abelian quantum order in spin-orbit-coupled semiconductors: search for topological Majorana particles in solid-state systems", Phys. Rev. B **82**, 214509 (2010).

[58] Y. Oreg, G. Refael, and F. von Oppen, "Helical liquids and Majorana bound states in quantum wires", Phys. Rev. Lett. **105**, 177002 (2010).

[59] J. Alicea, Y. Oreg, G. Refael, F. von Oppen, and M. P. A. Fisher, "Non-Abelian statistics and topological quantum information processing in 1D wire networks", Nat. Phys. **7**, 412 (2011).

[60] L. Mao, M. Gong, E. Dumitrescu, S. Tewari, and C. Zhang, "Hole-doped semiconductor nanowire on top of an *s*-wave superconductor: a new and experimentally accessible system for Majorana fermions", Phys. Rev. Lett. **108**, 177001 (2012).

[61] S. Gangadharaiah, B. Braunecker, P. Simon, and D. Loss, "Majorana edge states in interacting one-dimensional systems", Phys. Rev. Lett. **107**, 036801 (2011).

[62] K. Laubscher and J. Klinovaja, "Majorana bound states in semiconducting nanostructures", J. Appl. Phys. **130**, 081101 (2021).

[63] O. Dmytruk and J. Klinovaja, "Suppression of the overlap between Majorana fermions by orbital magnetic effects in semiconducting-superconducting nanowires", Phys. Rev. B **97**, 155409 (2018).

[64] P. Stano, C.-H. Hsu, M. Serina, L. C. Camenzind, D. M. Zumbühl, and D. Loss, "*g*-factor of electrons in gate-defined quantum dots in a strong in-plane magnetic field", Phys. Rev. B **98**, 195314 (2018).

[65] P. Stano, C.-H. Hsu, L. C. Camenzind, L. Yu, D. Zumbühl, and D. Loss, "Orbital effects of a strong in-plane magnetic field on a gate-defined quantum dot", Phys. Rev. B **99**, 085308 (2019).

[66] H. F. Legg, D. Loss, and J. Klinovaja, "Majorana bound states in topological insulators without a vortex", Phys. Rev. B **104**, 165405 (2021).

[67] L. C. Camenzind, S. Svab, P. Stano, L. Yu, J. D. Zimmerman, A. C. Gossard, D. Loss, and D. M. Zumbühl, "Isotropic and anisotropic *g*-factor corrections in GaAs quantum dots", Phys. Rev. Lett. **127**, 057701 (2021).

[68] B. Voisin, R. Maurand, S. Barraud, M. Vinet, X. Jehl, M. Sanquer, J. Renard, and S. D. Franceschi, "Electrical control of *g*-factor in a few-hole silicon nanowire MOSFET", Nano Lett. **16**, 88 (2015).

[69] R. Maurand, X. Jehl, D. Kotekar-Patil, A. Corna, H. Bohuslavskyi, R. Laviéville, L. Hutin, S. Barraud, M. Vinet, M. Sanquer, and S. D. Franceschi, "A CMOS silicon spin qubit", Nat. Commun. **7**, 13575 (2016).

[70] S. Barraud, R. Coquand, M. Casse, M. Koyama, J.-M. Hartmann, V. Maffini-Alvaro, C. Comboroure, C. Vizioz, F. Aussenac, O. Faynot, and T. Poiroux, "Performance of omega-shaped-gate silicon nanowire MOSFET with diameter down to 8 nm", IEEE Electron Device Lett. **33**, 1526 (2012).

[71] J. M. Luttinger and W. Kohn, "Motion of electrons and holes in perturbed periodic fields", Phys. Rev. **97**, 869 (1955).

[72] J. M. Luttinger, "Quantum theory of cyclotron resonance in semiconductors: general theory", Phys. Rev. **102**, 1030 (1956).

[73] N. O. Lipari and A. Baldereschi, "Angular momentum theory and localized states in solids. Investigation of shallow acceptor states in semiconductors", Phys. Rev. Lett **25**, 1660 (1970).

[74] R. Winkler, *Spin-orbit coupling effects in two-dimensional electron and hole systems* (Springer, Berlin, Oct. 10, 2003).

[75] P. Lawaetz, "Valence-band parameters in cubic semiconductors", Phys. Rev. B **4**, 3460 (1971).

[76] R. Li, "Low-energy subband wave-functions and effective g-factor of one-dimensional hole gas", J. Phys.: Condens. Mat. **33**, 355302 (2021).

[77] R. Li, "Searching strong 'spin'-orbit coupled one-dimensional hole gas in strong magnetic fields", J. Phys.: Condens. Mat. **34**, 075301 (2022).

[78] G. L. Bir and G. E. Pikus, *Symmetry and strain-induced effects in semiconductors* (Wiley, New York, 1974).

[79] J. Menéndez, R. Singh, and J. Drucker, "Theory of strain effects on the Raman spectrum of Si-Ge core-shell nanowires", Ann. Phys. **523**, 145 (2010).

[80] P. McIntyre and A. F. i Morral, "Semiconductor nanowires: to grow or not to grow?", Mater. Today Nano **9**, 100058 (2020).

[81] S. Conesa-Boj, A. Li, S. Koelling, M. Brauns, J. Ridderbos, T. T. Nguyen, M. A. Verheijen, P. M. Koenraad, F. A. Zwanenburg, and E. P. A. M. Bakkers, "Boosting hole mobility in coherently strained [110]-oriented Ge-Si core-shell nanowires", Nano Lett. **17**, 2259 (2017).

[82] L. Pei, H. Zhao, W. Tan, H. Yu, Y. Chen, J. Wang, C. Fan, J. Chen, and Q.-F. Zhang, "Low temperature growth of single crystalline germanium nanowires", Mater. Res. Bul. **45**, 153 (2010).

[83] Y. Xiang, I. Zardo, L. Y. Cao, T. Garma, M. Heiß, J. R. Morante, J. Arbiol, M. L. Brongersma, and A. F. i Morral, "Spatially resolved Raman spectroscopy on indium-catalyzed core-shell germanium nanowires: size effects", Nanotech. **21**, 105703 (2010).

[84] H. Adhikari, A. F. Marshall, C. E. D. Chidsey, and P. C. McIntyre, "Germanium nanowire epitaxy: shape and orientation control", Nano Lett. **6**, 318 (2006).

[85] H. Jagannathan, M. Deal, Y. Nishi, J. Woodruff, C. Chidsey, and P. C. McIntyre, "Nature of germanium nanowire heteroepitaxy on silicon substrates", J. Appl. Phys. **100**, 024318 (2006).

[86] K. C. Nowack, F. H. L. Koppens, Y. V. Nazarov, and L. M. K. Vandersypen, "Coherent control of a single electron spin with electric fields", Science **318**, 1430 (2007).

[87] J. H. Qvist and J. Danon, "Anisotropic g-tensors in hole quantum dots: role of transverse confinement direction", Phys. Rev. B **105**, 075303 (2022).

[88] B. Hetényi, S. Bosco, and D. Loss, "Anomalous zero-field splitting for hole spin qubits in Si and Ge quantum dots", Phys. Rev. Lett. **129**, 116805 (2022).

[89] J. Alicea, "Majorana fermions in a tunable semiconductor device", Phys. Rev. B **81**, 125318 (2010).

[90] C. Reeg, D. Loss, and J. Klinovaja, "Finite-size effects in a nanowire strongly coupled to a thin superconducting shell", Phys. Rev. B **96**, 125426 (2017).

[91] C. Reeg, D. Loss, and J. Klinovaja, "Metallization of a Rashba wire by a superconducting layer in the strong-proximity regime", Phys. Rev. B **97**, 165425 (2018).

[92] C. Reeg, D. Loss, and J. Klinovaja, "Proximity effect in a two-dimensional electron gas coupled to a thin superconducting layer", Beilstein J. Nanotechnol. **9**, 1263 (2018).

[93] B. D. Woods, S. Das Sarma, and T. D. Stanescu, "Electronic structure of full-shell InAs/Al hybrid semiconductor-superconductor nanowires: spin-orbit coupling and topological phase space", Phys. Rev. B **99**, 161118(R) (2019).

[94] G. W. Winkler, A. E. Antipov, B. van Heck, A. A. Soluyanov, L. I. Glazman, M. Wimmer, and R. M. Lutchyn, "Unified numerical approach to topological semiconductor-superconductor heterostructures", Phys. Rev. B **99**, 245408 (2019).

[95] T. Kiendl, F. von Oppen, and P. W. Brouwer, "Proximity-induced gap in nanowires with a thin superconducting shell", Phys. Rev. B **100**, 035426 (2019).

[96] M. Sistani, J. Delaforce, R. B. G. Kramer, N. Roch, M. A. Luong, M. I. den Hertog, E. Robin, J. Smoliner, J. Yao, C. M. Lieber, C. Naud, A. Lugstein, and O. Buisson, "Highly transparent contacts to the 1D hole gas in ultrascaled Ge/Si core/shell nanowires", ACS Nano **13**, 14145 (2019).

[97] A. Sammak, D. Sabbagh, N. W. Hendrickx, M. Lodari, B. P. Wuetz, A. Tosato, L. Yeoh, M. Bollani, M. Virgilio, M. A. Schubert, P. Zaumseil, G. Capellini, M. Veldhorst, and G. Scappucci, "Shallow and undoped germanium quantum wells: a playground for spin and hybrid quantum technology", Adv. Funct. Mater. **29**, 1807613 (2019).

[98] D. Vion, A. Aassime, A.Cottet, P. Joyez, H. Pothier, C. Urbina, D. Esteve, and M. H. Devoret, "Manipulating the quantum state of an electrical circuit", Science **296**, 886 (2002).

[99] K. D. Petersson, J. R. Petta, H. Lu, and A. C. Gossard, "Quantum coherence in a one-electron semiconductor charge qubit", Phys. Rev. Lett. **105**, 246804 (2010).

[100] D. Ahn, S. J. Yoon, S. L. Chuang, and C.-S. Chang, "Theory of optical gain in strained-layer quantum wells within the 6×6 Luttinger-Kohn model", J. Appl. Phys. **78**, 2489 (1995).

CHAPTER 4

Microscopic analysis of proximity-induced superconductivity and metallization effects in superconductor-germanium hole nanowires

Adapted from:
Christoph Adelsberger, Henry F. Legg, Daniel Loss, and Jelena Klinovaja
"Microscopic analysis of proximity-induced superconductivity and metallization effects in superconductor-germanium hole nanowires",
Phys. Rev. B **108**, 155433 (2023)

Low-dimensional germanium hole devices are promising systems with many potential applications such as hole spin qubits, Andreev spin qubits, and Josephson junctions, and can serve as a basis for the realization of topological superconductivity. This vast array of potential uses for Ge largely stems from the exceptionally strong and controllable spin-orbit interaction (SOI), ultralong mean free paths, long coherence times, and compatibility with complementary metal-oxide-semiconductor (CMOS) technology. However, when brought into proximity with a superconductor (SC), metallization normally diminishes many useful properties of a semiconductor, for instance, typically reducing the g factor and SOI energy, as well as renormalizing the effective mass. In this paper, we consider metallization of a Ge nanowire (NW) in proximity to a SC, explicitly taking into account the three-dimensional (3D) geometry of the NW. We find that proximitized Ge exhibits a unique phenomenology of metallization effects, where the 3D cross section plays a crucial role. For instance, in contrast to expectations, we find that SOI can be enhanced by strong coupling to the superconductor. We also show that the thickness of the NW plays a critical role in determining both the size of the proximity-induced pairing potential and metallization effects, since the coupling between the NW and SC strongly depends on the distance of the NW wave function from the interface with the SC. In the absence of electrostatic effects, we find that a sizable gap

opens only in thin NWs ($d \lesssim 3\,\mathrm{nm}$). In thicker NWs, the wave function must be pushed closer to the SC by electrostatic effects in order to achieve a sizable proximity gap such that the required electrostatic field strength can simultaneously induce a strong SOI. The unique and sometimes beneficial nature of metallization effects in SC-Ge NW devices evinces them as ideal platforms for future applications in quantum information processing.

4.1 Introduction

Hole gases in Ge heterostructures are one of the most promising platforms for applications in quantum information processing [1]. The compatibility of Ge with Si complementary metal-oxide-semiconductor (CMOS) technology is important to achieve the scalability that is required for the building blocks of any future quantum computer [2]. In addition, however, holes in Ge have many favorable properties, such as the possibility to grow ultraclean substrates with a mean free path up to 30 µm [3–6], the long spin coherence times due to weak hyperfine noise suppressed by appropriate quantum dot design [7–13] or isotopic purification [14, 15], the strong and tunable spin-orbit interaction (SOI) [16–22], and the tunable g factor [23–26]. These properties have already enabled the realization of high-quality spin qubits [27] with which electrically controlled single- [28–31] and two-qubit [32] gates, as well as singlet-triplet encoding [33] and a four-qubit processor [34], have been demonstrated.

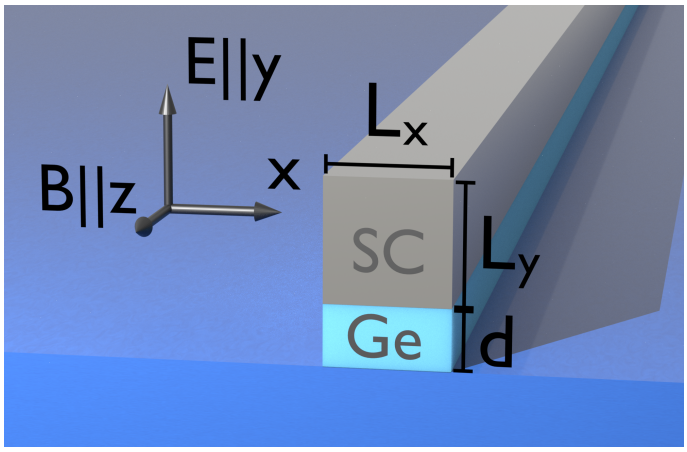

Figure 4.1: Sketch of a rectangular Ge NW in proximity to a superconductor (SC). The SC cross section is defined by $L_x = L_y = 10\,\text{nm}$ and the Ge NW cross section by the width $L_x = 10\,\text{nm}$ and height d, which is not fixed and will be used as a parameter in what follows. We assume an infinitely long system in the z direction. A magnetic field B is applied along the NW axis in the z direction, and an electric field E is applied in the perpendicular y direction.

In the last few years, there has been considerable progress in fabricating hybrid devices that couple Ge to superconductors (SCs) such as aluminum [35–43] (see Fig. 4.1). Hybrid SC-Ge devices substantially increase the possible applications of Ge, for instance, enabling electrically controllable Josephson junctions [35, 44–46], allowing for long-range coupling of spin qubits [47–50], providing the basis for Andreev spin qubits [51–54], and as a platform to realize topological superconductivity with associated Majorana bound states (MBSs) [55–64].

The coupling of a superconductor to a semiconductor, however, not only results in a proximity-induced superconducting pairing potential [65, 66] but has additional consequences due to metallization of the semiconductor by the SC [67]. Such effects, e.g., the renormalization of the effective mass, the g factor, and the spin-orbit energy, have been widely studied in platforms expected to achieve MBSs [67–78]. The most extensively investigated platform to achieve topological superconductivity is semiconducting nanowires (NWs) with strong Rashba SOI, such as InAs and InSb [79]. In such systems, it has been predicted that the opening of a proximity-induced gap in the NW also results in a reduction of the SOI energy and the g factor [67, 68]. When the SC strongly

couples to the semiconductor, metallization effects can make it difficult to find a regime capable of hosting MBSs because this simultaneously requires strong SOI, a large Zeeman energy, and a sizable proximity-induced pairing potential. Due to the unique phenomenology of holes in Ge, it was not yet clear what the consequences of metallization effects are in Ge and what limitations metallization places on the potential applications of Ge based platforms.

In this paper, we numerically investigate the metallization of holes in three-dimensional (3D) Ge NWs that have been brought into proximity with a 3D SC. Importantly, the wave function is nonuniformly distributed throughout the NW cross section. As a result, we find the thickness of the Ge NW plays a crucial role in both the size of the induced proximity gap and the consequences of metallization effects. In the absence of electrostatic fields, we show that only when the NW is very flat ($d \lesssim 3\,\mathrm{nm}$), such that the wave functions of states in the NW are close to the SC, can a sizable proximity-induced gap be achieved. However, for thicker NWs, electrostatic fields, e.g., due to gating or interface effects, can push the wave functions close to the Ge-SC interface, increasing the proximity-induced gap and with important separate consequences for the SOI strength. In particular, we will demonstrate that it is possible to enhance the SOI and the proximity-induced gap at the same time by tuning with an external electric field. Furthermore, using thicker NWs has the advantage that one can reach the optimal side length ratio for maximal SOI that depends on the electric field [25, 80] and that the g factor is larger than in flat NWs. The mechanism behind the strong SOI is the direct Rashba SOI typically present in one-dimensional (1D) hole systems [16, 17, 25, 26]. Our results show that metallization effects in SC-Ge hole hybrid devices have a unique phenomenology and are often either benign or even beneficial in nature. Our findings suggest that although metallization effects can have important consequences for SC-Ge devices, such hybrid systems remain a promising avenue for future quantum information processing applications.

The focus of this work lies in analyzing effective models for proximity-induced superconductivity and metallization in Ge hole NWs. These models facilitate the understanding of the qualitative behavior of the parameters and their mutual dependences, including the proximity-induced superconducting order parameter, the NW g factor, and the strength of the SOI. However, certain factors lie outside the scope of our study, such as the electrostatic potential resulting from band bending at the interface between the SC and the semiconductor, charges originating from impurities, or disorder. A comprehensive analysis of additional electrostatic effects, e.g., due to precise work function differences of atoms at the interface, necessitates computationally intensive *ab-initio* calculations such as density functional theory [81], which exceeds the boundaries of our current work. Although all the aforementioned phenomena are anticipated to lead to quantitative adjustments in our results, the qualitative behavior that we present here is expected to remain unchanged. In particular, the band bending at the interface, typically addressed in numerical Schrödinger-Poisson calculations [70, 71, 73, 74], gives rise to an accumulation or repulsion of charges at the interface. Accounting for these effects is expected to modify the strength of the external electric field required to confine the hole wave function at the interface, as discussed in Sec. 4.5; the outcome, however, would remain the same.

This paper is structured as follows. In Sec. 4.2, we introduce our theoretical model of a Ge hole NW coupled to a SC. In Sec. 4.3, we analyze the influence of the NW-SC coupling on the Fermi wave vector of the NW states. We show that the chemical potential of the SC with respect to the chemical potential of the NW decides whether the NW Fermi wave vector is increased or decreased with increasing coupling. We decide for the case where the Fermi wave vector of the NW is decreased with increasing coupling as the most relevant one. In Sec. 4.4, we investigate the consequences of changing the thickness of the NW. Our results show that without electrostatic fields, only thin NWs couple strongly to the SC, which can be explained by the distance of the wave function in the NW from the SC-Ge interface. In thick NWs, however, the wave function can

be localized close to the SC by an external electric field, as we show in Sec. 4.5. As a consequence, the spin-orbit energy and the induced gap can simultaneously increase with increasing electric field. A discussion of the coupling mechanism between NW and SC is given in Sec. 4.6. Finally, in Sec. 4.7, we conclude and give an outlook of implications for Ge-based superconducting devices.

4.2 Model

In this section, we introduce the model that we employ to describe a Ge NW that is coupled to a SC placed on top of the NW, with both NW and SC extending infinitely along the z direction (see Fig. 4.1). We model the cross section of the system by a finite 2D lattice in real space. The momentum $\hbar k$ along the z axis is a good quantum number since we assume translational invariance in this direction and periodic boundary conditions. The discrete model for the NW coupled to a SC is then

$$H(k) = H_w(k) + H_s(k) + H_c(k), \tag{4.1}$$

where $H_w(k)$ is the Hamiltonian for the hole NW, $H_s(k)$ is the Hamiltonian for the SC, and $H_c(k)$ is the Hamiltonian describing the tunnel coupling between the NW and the SC at the interface.

To describe the heavy hole (HH) and light hole (LH) nature of the Ge NW, we use the isotropic Luttinger-Kohn Hamiltonian,

$$H_{\mathrm{LK}} = -\frac{\hbar^2}{2m_e}\left[\gamma_k k^2 - 2\gamma_s(\boldsymbol{k}\cdot\boldsymbol{J})^2\right], \tag{4.2}$$

as commonly utilized in the literature to describe the states in Ge [16, 17, 80, 82–84]; here, $\gamma_k = \gamma_1 + 5\gamma_s/2$, $\gamma_s = (\gamma_2 + \gamma_3)/2 = 4.97$, and J_i [with $i = x, y, z$] are the standard spin-3/2 operators. In reality, the holes in Ge are not spin-3/2 particles, but their total angular momentum is $j = l + s = 3/2$, where l is the orbital angular momentum that is $l = 1$ for a p-type orbital and $s = 1/2$ is the spin. The coefficients $\gamma_1 = 13.35$, $\gamma_2 = 4.25$, and $\gamma_3 = 5.69$ are the material-dependent Luttinger parameters [85] and m_e is the free electron mass. Note the global negative sign in Eq. (4.2) for holes.

To lift the Kramers degeneracy, we add a small Zeeman field in the z direction that enters via the Zeeman Hamiltonian

$$H_Z = 2\kappa\mu_B B J_z, \tag{4.3}$$

with magnetic field strength B and $\kappa = 3.41$ in Ge [86]. Here we neglect the small anisotropic Zeeman energy $\propto J_i^3$ [16, 87] and effects of orbital magnetic fields [88–92] since we consider only very weak magnetic fields applied parallel to the NW. Furthermore, we include a homogeneous electric field in the y direction via the Hamiltonian

$$H_E = -eEy, \tag{4.4}$$

where E is the strength of the electric field in the y direction.

On the 2D square lattice that models the cross section of the NW, the NW Hamiltonian becomes

$$\begin{aligned} H_{w,k} = -\sum_{n=1,m=1}^{L_x/a,d/a} & \boldsymbol{c}^{\dagger}_{n,m,k}\Big[H_{\mathrm{LK}}^{k_z^2}k^2 + \frac{2}{a^2}\left(H_{\mathrm{LK}}^{k_x^2} + H_{\mathrm{LK}}^{k_y^2}\right) \\ & + H_Z + eEam - \mu_w\Big]\boldsymbol{c}_{n,m,k} \\ & + \Big[\boldsymbol{c}^{\dagger}_{n+1,m,k}\left(\frac{i}{2a}H_{\mathrm{LK}}^{k_xk_z}k - \frac{1}{a^2}H_{\mathrm{LK}}^{k_x^2}\right)\boldsymbol{c}_{n,m,k} \\ & + \boldsymbol{c}^{\dagger}_{n,m+1,k}\left(\frac{i}{2a}H_{\mathrm{LK}}^{k_yk_z}k - \frac{1}{a^2}H_{\mathrm{LK}}^{k_y^2}\right)\boldsymbol{c}_{n,m,k} \\ & - \boldsymbol{c}^{\dagger}_{n+1,m+1,k}\frac{1}{4a^2}H_{\mathrm{LK}}^{k_xk_y}\boldsymbol{c}_{n,m,k} + \mathrm{H.c.}\Big], \end{aligned} \tag{4.5}$$

with

$$H_{\mathrm{LK}}^{k_x^2} = \frac{\hbar^2}{m_e}\begin{pmatrix} \frac{\gamma_1+\gamma_s}{2} & 0 & -\frac{\sqrt{3}\gamma_s}{2} & 0 \\ 0 & \frac{\gamma_1-\gamma_s}{2} & 0 & -\frac{\sqrt{3}\gamma_s}{2} \\ -\frac{\sqrt{3}\gamma_s}{2} & 0 & \frac{\gamma_1-\gamma_s}{2} & 0 \\ 0 & -\frac{\sqrt{3}\gamma_s}{2} & 0 & \frac{\gamma_1+\gamma_s}{2} \end{pmatrix}, \tag{4.6}$$

$$H_{\mathrm{LK}}^{k_y^2} = \frac{\hbar^2}{m_e}\begin{pmatrix} \frac{\gamma_1+\gamma_s}{2} & 0 & \frac{\sqrt{3}\gamma_s}{2} & 0 \\ 0 & \frac{\gamma_1-\gamma_s}{2} & 0 & \frac{\sqrt{3}\gamma_s}{2} \\ \frac{\sqrt{3}\gamma_s}{2} & 0 & \frac{\gamma_1-\gamma_s}{2} & 0 \\ 0 & \frac{\sqrt{3}\gamma_s}{2} & 0 & \frac{\gamma_1+\gamma_s}{2} \end{pmatrix}, \tag{4.7}$$

$$H_{\mathrm{LK}}^{k_z^2} = \frac{\hbar^2}{m_e}\begin{pmatrix} \frac{\gamma_1-2\gamma_s}{2} & 0 & 0 & 0 \\ 0 & \frac{\gamma_1+2\gamma_s}{2} & 0 & 0 \\ 0 & 0 & \frac{\gamma_1+2\gamma_s}{2} & 0 \\ 0 & 0 & 0 & \frac{\gamma_1-2\gamma_s}{2} \end{pmatrix}, \tag{4.8}$$

$$H_{\mathrm{LK}}^{k_xk_y} = \frac{\hbar^2}{m_e}\begin{pmatrix} 0 & 0 & i\sqrt{3}\gamma_s & 0 \\ 0 & 0 & 0 & i\sqrt{3}\gamma_s \\ -i\sqrt{3}\gamma_s & 0 & 0 & 0 \\ 0 & -i\sqrt{3}\gamma_s & 0 & 0 \end{pmatrix}, \tag{4.9}$$

$$H_{\mathrm{LK}}^{k_xk_z} = \frac{\hbar^2}{m_e}\begin{pmatrix} 0 & -\sqrt{3}\gamma_s & 0 & 0 \\ -\sqrt{3}\gamma_s & 0 & 0 & 0 \\ 0 & 0 & 0 & \sqrt{3}\gamma_s \\ 0 & 0 & \sqrt{3}\gamma_s & 0 \end{pmatrix}, \tag{4.10}$$

$$H_{\mathrm{LK}}^{k_y k_z} = \frac{\hbar^2}{m_e}\begin{pmatrix} 0 & i\sqrt{3}\gamma_s & 0 & 0 \\ -i\sqrt{3}\gamma_s & 0 & 0 & 0 \\ 0 & 0 & 0 & -i\sqrt{3}\gamma_s \\ 0 & 0 & i\sqrt{3}\gamma_s & 0 \end{pmatrix}. \tag{4.11}$$

We define the four-dimensional vectors $\boldsymbol{c}^\dagger_{n,m,k} = \left(c^\dagger_{+\frac{3}{2}}, c^\dagger_{+\frac{1}{2}}, c^\dagger_{-\frac{1}{2}}, c^\dagger_{-\frac{3}{2}}\right)_{n,m,k}$, where $c^\dagger_{\pm\frac{3}{2}(\frac{1}{2})}$ describes the creation of a hole with total J_z angular momentum $\pm\frac{3}{2}(\frac{1}{2})$. The sum runs over all sites of the lattice (n, m) where the indices n and m run over the x and y coordinates, respectively. We measure the chemical potential μ_w from the Rashba crossing point at $k = 0$. For the calculations we choose the lattice spacing $a = 0.1\,\mathrm{nm}$.

The discretized Hamiltonian for the conventional s-wave superconductor is given by

$$\begin{aligned} H_{s,k} = &\sum_{n=1,m=1,\sigma=\uparrow,\downarrow}^{L_x/a,L_y/a} b^\dagger_{n,m,k,\sigma}\left[\frac{\hbar^2}{2m_s}\left(k^2+\frac{2}{a^2}\right)\right. \\ &\left. + \frac{g_s\mu_B}{2}B\sigma_z - \mu_s\right] b_{n,m,k,\sigma} \\ &- \frac{\hbar^2}{2m_s}\left(\sum_{\substack{m=1,\sigma=\uparrow,\downarrow \\ \langle n',n\rangle}}^{L_y/a} b^\dagger_{n',m,k,\sigma}\frac{1}{a^2}b_{n,m,k,\sigma}\right. \\ &\left. + \sum_{\substack{n=1,\sigma=\uparrow,\downarrow \\ \langle m',m\rangle}}^{L_x/a} b^\dagger_{n,m',k,\sigma}\frac{1}{a^2}b_{n,m,k,\sigma}\right) \\ &+ \sum_{n=1,m=1}^{L_x/a,L_y/a}\left(\Delta_0 b^\dagger_{n,m,k,\uparrow}b^\dagger_{n,m,-k,\downarrow}\right. \\ &\left. + \Delta_0^* b_{n,m,-k,\downarrow}b_{n,m,k,\uparrow}\right), \end{aligned} \tag{4.12}$$

where $b^\dagger_{n,m,k,\sigma}(b_{n,m,k,\sigma})$ creates an electron (hole) with spin $\sigma =\uparrow,\downarrow$ in the superconductor. The effective mass of the superconductor is m_s and, in addition, we take the superconducting pairing potential as $\Delta_0 = 0.2\,\mathrm{meV}$. The expression $\langle n', n\rangle$ ($\langle m', m\rangle$) describes a sum over neighboring sites in the $x(y)$ direction. We measure the chemical potential of the SC, μ_s, from the bottom of the lowest subband and we choose the effective mass $m_s = 0.95m_e$. This results in the hopping amplitude $t_s = \frac{\hbar^2}{2m_s a^2} \approx 4\,\mathrm{eV}$ and Fermi velocity $v_{F,s} = \partial_k\mathcal{E}(k)|_{k=k_F}/\hbar \approx 1.27\times10^6\,\mathrm{m\,s^{-1}}$ for $\mu_s = 8.75\,\mathrm{eV}$, where $\mathcal{E}(k) = (t_s/a^2)[1-\cos(ka)] - \mu_s$ is the dispersion relation.

Since the SC Hamiltonian is given in a spin basis and the NW Hamiltonian in a total angular momentum basis, we cannot couple them without first applying a basis transformation. In the following, for simplicity of presentation, we utilize the Hamiltonian H_M of a simple metal that is the same as Eq. (4.12) with no pairing potential, $\Delta_0 = 0$. The total J_z angular momentum basis states $P^{-1}|\psi\rangle = (|+3/2\rangle, |+1/2\rangle, |-1/2\rangle, |-3/2\rangle)$ of the NW are given in terms of the orbital

angular momentum and spin $|\psi\rangle = |l_z, s_z\rangle$ by [93]

$$\begin{aligned}
|+3/2\rangle &= |+1,\uparrow\rangle\,, \\
|+1/2\rangle &= \frac{1}{\sqrt{3}}\left(|+1,\downarrow\rangle + \sqrt{2}\,|0,\uparrow\rangle\right), \\
|-1/2\rangle &= \frac{1}{\sqrt{3}}\left(|-1,\uparrow\rangle + \sqrt{2}\,|0,\downarrow\rangle\right), \\
|-3/2\rangle &= |-1,\downarrow\rangle\,.
\end{aligned} \tag{4.13}$$

Note that the two spin-orbit split-off states ($J = 1/2$) are neglected here. The unitary matrix

$$P = P^{-1} = \begin{pmatrix} 1 & 0 & 0 & 0 \\ 0 & \frac{1}{\sqrt{2}} & \frac{1}{\sqrt{2}} & 0 \\ 0 & \frac{1}{\sqrt{2}} & -\frac{1}{\sqrt{2}} & 0 \\ 0 & 0 & 0 & 1 \end{pmatrix} \tag{4.14}$$

transforms the total angular momentum basis such that we can write the coupling between one site of the metal $H_{M,i}$ to one site of the NW $H_{w,i}$ as the matrix

$$\begin{pmatrix} P^{-1}H_{w,i}P & H_t \\ H_t^T & H_{M,i} \end{pmatrix}, \tag{4.15}$$

where the basis of this matrix is $(|\psi\rangle\,, |\uparrow\rangle\,, |\downarrow\rangle)$ and the coupling matrix is

$$H_t = \begin{pmatrix} t_{\mathrm{HH}} & t_{\mathrm{LH}} & 0 & 0 \\ 0 & 0 & t_{\mathrm{LH}} & t_{\mathrm{HH}} \end{pmatrix}^T, \tag{4.16}$$

with the LH (HH) coupling amplitudes t_{LH} (t_{HH}). This is a simplified model for the coupling between a semiconductor NW and a metal, but sufficient to capture the qualitative physics of metallization effects in Ge. We further simplify this by assuming HH and LH coupling amplitudes, i.e., $t = t_{\mathrm{HH}} = t_{\mathrm{LH}}$. For an analysis of the situation where $t_{\mathrm{LH}} \neq 0$ and $t_{\mathrm{HH}} = 0$, see Sec. 4.6. In general, the coupling amplitudes are different and depend on k [94, 95], which is neglected here. Furthermore, in an experiment, the Ge NW would be covered by a shell that induces strain into the NW and changes the tunnel barrier between SC and Ge. Another possible realization would be a gate-defined 1D channel in a planar Ge/SiGe heterostructure [26]. However, we expect only quantitative changes of our results due to these details.

Note that the coupling t between the SC and the Ge NW is a phenomenological parameter in our model, which is not an experimental observable. However, in the following we present the proximity-induced superconducting order parameter and the NW g factor and SOI as a function of t. In an experiment the proximity-induced gap can be measured which then relates to a certain value of our model parameter t. This then allows us to predict the g factor and SOI for the measured superconducting gap size.

4.3 Chemical potential of the superconductor

Before we discuss proximity-induced superconductivity in Ge NWs, we first analyze the dependence of the average Fermi wave vector in the NW, $\bar{k}_F = (k_F^1 + k_F^2)/2$, on the chemical potential of the SC,

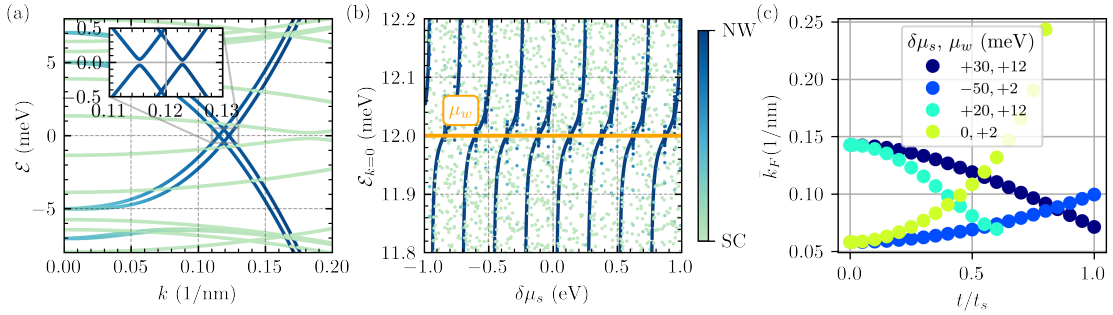

Figure 4.2: (a) Dispersion relation of the SC-Ge hole NW for $t = 0.5t_s$, where the color bar to the right of (b) shows the weight of the wave function in the NW and SC for (a) and (b). The gap opening in the NW band is shown in the inset in (a). Due to finite SOI for nonzero SC-NW coupling t, there are two Fermi momenta. The chemical potential of the SC is fixed to $\mu_s = 8.77\,\text{eV}$. In order to achieve coupling between the NW and SC states, they have to fulfill certain selection rules given by the confinement and the related quantum numbers [67, 68]. This is the reason why most of the SC subband states cross the NW subbands without hybridization, so without gap opening. (b) Energies of the SC-Ge hole NW states at $k = 0$ as a function of the shift of the chemical potential of the SC, $\delta\mu_s$, measured from $\mu_s = 8.75\,\text{eV}$ for $t = 0.1t_s$. Here, we set $\Delta_0 = 0$ and consider a metal instead of a SC. The energies of the NW states depend strongly on $\delta\mu_s$. For roughly half of the $\delta\mu_s$ values, the energy of the NW states at $k = 0$ increases compared to the chemical potential of the uncoupled NW, $\mu_w = 12\,\text{meV}$ (indicated by the orange line). For the other half of the $\delta\mu_s$ values, the energy of the NW states at $k = 0$ decreases. (c) As a consequence of the observed energy behavior, the average Fermi wave vector $\bar{k}_F$ can either increase or decrease with t, depending on the value of $\delta\mu_s$. For instance, the decrease in energy for $\delta\mu_s = 30\,\text{meV}$ (dark blue) causes the initial Fermi wave vector to decrease with increasing coupling t to the SC. For $\delta\mu_s = -50\,\text{meV}$ (light blue), the average Fermi wave vector increases with growing coupling to the SC. For $\delta\mu_s = 0$ (green) and $\delta\mu_s = 20\,\text{meV}$ (cyan), the NW state at $k = 0$ is very close in energy to a SC state that couples to the NW. At this resonance, $\bar{k}_F$ changes very strongly with t. If not stated differently, the parameters used are $\mu_w = 12\,\text{meV}$, $\mu_s = 8.75\,\text{eV}$, $d = 2\,\text{nm}$, $L_x = L_y = 10\,\text{nm}$, $a = 0.1\,\text{nm}$, $\Delta_0 = 0.2\,\text{meV}$, $E = 0$, and $B = 0.01\,\text{T}$.

μ_s, where $k_F^{1,2}$ are the two Fermi momenta in the presence of SOI [see Fig. 4.2(a)]. In the uncoupled case, we can connect the Fermi wave vector to the charge carrier density $n = e(k_F^1 + k_F^2)/\pi$ in the NW with the positive elementary charge e for holes. In general, the sizes of the induced gaps at the two different Fermi wave vectors are not equal. In the following, we refer to the Fermi wave vector k_F denoted, without further index, as the one at which the gap is smaller. In the following, we study the shift of the energy of the state at $k = 0$ and $\bar{k}_F$ of the NW on the chemical potential of the SC. However, in reality, it is challenging to control the chemical potential of the SC, but the thickness of the SC is under control. The same resonances as shown in Fig. 4.2(b) can be observed as a function of the thickness of the SC [67], which is obvious because the level spacing of the SC depends on the chemical potential via the Fermi velocity as well as on the thickness of the SC.

For Fig. 4.2(b), we set $\Delta_0 = 0$ and assume that the NW is coupled to a normal metal. We fix the chemical potential of the NW to $\mu_w = 12\,\text{meV}$ and sweep the chemical potential of the metal around $\mu_s = 8.75\,\text{eV}$. In Fig. 4.2(b), we show the energies of the NW and the metal states at $k = 0$. The energies of the NW states (dark-blue dots) show resonances at certain values of $\delta\mu_s$ every time the lowest NW state at $k = 0$ couples to a metal state that lies at the same energy.

Note that only certain metal states couple to the NW because they need to fulfill selection rules that are given by the quantum numbers related to the confinement [67, 68]. The periodicity of the resonances is set by the level spacing of the metal, $\pi\hbar v_{F,s}/L_y \approx 263\,\mathrm{meV}$.

From previous investigations of metallization effects in semiconductors [67, 68], we expect that coupling to the SC causes an increase of the Fermi wave vector of the NW states. This behavior is, indeed, found in a large parameter regime of our numerical study [see Fig. 4.2(b)]. However, within our model, shifting the chemical potential of the SC, μ_s, we find cases where $\bar{k}_F$ of the NW decreases. Whether $\bar{k}_F$ increases or decreases depends on whether $\delta\mu_s$ lies on the left or the right side of a resonance in Fig. 4.2(b). We show $\bar{k}_F$ as a function of the coupling t between SC and NW for different values of $\delta\mu_s$ in Fig. 4.2(c) to illustrate this behavior. The chemical potential of the NW, μ_w, takes two different values for the curves in Fig. 4.2(c). However, this is not the reason for the different behaviors. In the case where $\bar{k}_F$ decreases with increasing t, we need to set μ_w to a larger value at $t = 0$ to avoid a rapid depletion of the NW. For increasing $\bar{k}_F$, this is not necessary and we start at $t = 0$ with a smaller value for μ_w. The cyan line ends at $t = 0.6$, because at stronger coupling, the Fermi wave vector is no longer well defined as the energy of the state at $k = 0$ becomes comparable to the size of the superconducting gap.

In the following, we will focus on the situation where the average Fermi wave vector $\bar{k}_F$ decreases with increasing coupling to the SC. However, the coupling itself also causes a shift of chemical potentials in the NW and the SC and thus, as we will see below, a stronger SC-NW hybridization can occur as the coupling is increased. Furthermore, we choose μ_s such that it is away from the resonances. Calculations closer to a resonance show qualitatively the same, but quantitatively stronger effects. In order to hit such a resonance in an experiment, fine tuning of the SC thickness would be required, which is difficult in practice (but not impossible, e.g., in the case of epitaxial growth of the SC on top of the NW). For the situation where $\bar{k}_F$ increases with t, we observe the same effects, which is not shown here. The only noteworthy difference is that the proximity-induced superconducting order parameter does not converge to a constant value as quickly as in the case of decreasing $\bar{k}_F$. In fact, a convergence sets in only for $t > t_s$ which, however, is an unrealistic regime.

4.4 Nanowire thickness

In this section, we study how certain parameters, namely, the average Fermi wave vector $\bar{k}_F$, the induced superconducting gap Δ, the g factor, and the spin-orbit energy E_{so}, of the proximitized NW depend on the thickness d of the NW. Throughout, we keep the dimensions of the SC to $L_x = L_y = 10\,\mathrm{nm}$ and the width of the NW $L_x = 10\,\mathrm{nm}$ (see Fig. 4.1). We show the results in Fig. 4.3. As discussed in Sec. 4.3, we set the chemical potentials of the NW and the SC such that the average Fermi wave vector shrinks with increasing t. This is reflected by the results shown in Fig. 4.3(a) for all values of considered NW thicknesses d.

In Fig. 4.3(b), we show that with increasing coupling t, a superconducting gap Δ is induced in the NW and this gap increases with t until it reaches a maximum that depends on the thickness of the NW. The induced gap is largest for $d = 2\,\mathrm{nm}$, where it reaches $\Delta = 0.24\,\Delta_0$. When $d \geq 4\,\mathrm{nm}$, the gap is rather small because the NW wave function is localized in the center of the NW cross section far away from the interface coupled to the SC. Note that in Sec. 4.5, we will discuss a way to also reach a sizable gap in thicker NWs. As we expect, the size of the gap (crosses) shows the same functional behavior as the weight Ξ_{k_F} of the NW state in the SC at k_F (pluses) [see inset in Fig. 4.2(a)]. For $d = 4\,\mathrm{nm}, 5\,\mathrm{nm}$, and $6\,\mathrm{nm}$, the induced gap has peaks for certain values of the coupling t, which can be traced back to the strong hybridization of the NW state with a SC state it is coupled to at a resonance, as discussed in Sec. 4.3. However, for the induced gap,

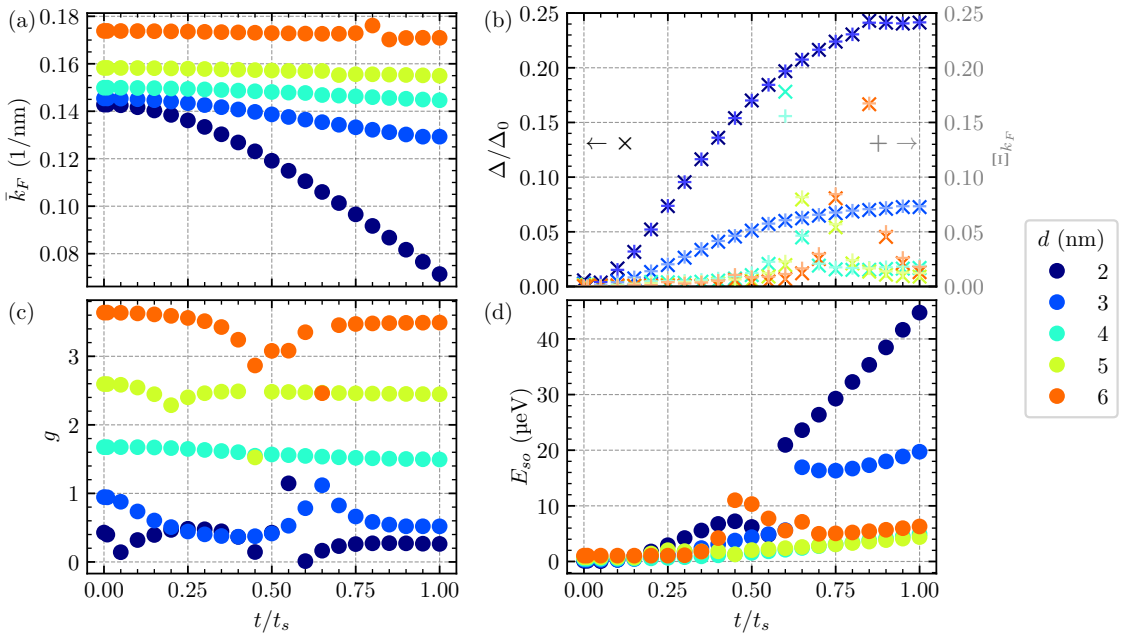

Figure 4.3: (a) Average Fermi wave vector $\bar{k}_F$, (b) proximity-induced superconducting gap (crosses, left axis) and the weight Ξ_{k_F} of the NW state in the SC at k_F (pluses, right axis), (c) NW g factor, and (d) spin-orbit energy as a function of the coupling t between SC and NW, and for various heights d of the Ge NW. The chemical potential of the SC is chosen such that $\bar{k}_F$ decreases with increasing coupling. The effect is strongest for a thin NW. As expected, the weight Ξ_{k_F} of the NW state in the SC shows the same functional behavior as the ratio of the induced superconducting gap and the parent SC pairing potential, Δ/Δ_0. The gap increases with the coupling and is largest for a thin NW. Only for a thin NW is the NW wave function main weight close to the SC-NW interface and the proximity effect can be sizable. The g factor is smallest for a thin NW ($d = 2$ nm), where the 2D physics dominates. It decreases slightly with increasing coupling. Due to the coupling between NW and SC, the NW wave function gains more weight at the interface breaking the inversion symmetry, which is similar to the response of the wave function to an external electric field. This symmetry breaking gives rise to a weak SOI that increases with the coupling t. At certain values of t, we observe deviations of the induced gap, g factor, and spin-orbit energy from the general t dependence. This is always the case close to a resonance, as discussed in Sec. 4.3. However, the g factor and the spin-orbit energy are more sensitive to resonances at $k = 0$, while the induced gap is more sensitive to resonances at $k = k_F$. Unless stated otherwise, the parameters are the same as in Fig. 4.2.

resonances at $k = k_F$ are more relevant than resonances at $k = 0$. By further increasing t, the SC and the NW states move away from each other in energy and the Δ profile returns to the general behavior. The same interpretation holds for the peaks and dips of the g factor [see Fig. 4.3(c)] and the spin-orbit energy E_{so} [see Fig. 4.3(d)]. The states in the Ge NW are mixed HH-LH states and thus the superconductivity has support from both types of holes.

The Ge hole NW g factor at $k = 0$ depends only slightly on t. In general, it decreases as the coupling becomes stronger. The g factor is largest ($g \approx 3.6$) for a thick NW ($d = 6\,\text{nm}$), where

the NW is governed by strong HH-LH mixing [16, 26], whereas for $d = 2\,\mathrm{nm}$, the lowest-energy eigenstates are almost purely of an HH nature, resulting in a small in-plane g factor ($g < 1$) [1].

Without coupling between the NW and the SC, the spin-orbit energy is zero in the NW since there is no electric field [17]. As the coupling increases, the NW wave function is pushed closer towards the NW-SC interface and thereby gets squeezed. This breaks the inversion symmetry similar to an external electric field that pushes the wave function towards the SC. Thus, a finite spin-orbit energy E_{so} develops, as shown in Fig. 4.3(d). The spin-orbit energy is larger for thinner NWs since there the coupling to the SC has the strongest effect due to the proximity of the wave functions of states in the NW to the SC. The spin-orbit energy is determined by the energy difference between the maximum of the negatively curved Rashba band and the spin-orbit crossing point at $k = 0$ of the hole NW.

4.5 Electric field

As discussed in Sec. 4.4, only in very thin NWs is it possible to induce a sizable superconducting gap since the wave function in the NW needs to be close to the NW-SC interface. However, there are several reasons for using thicker NWs. For instance, the g factor increases with the thickness d, as shown in Fig. 4.3(c). Also, with thicker NWs, it is possible to achieve the side length ratio of the NW that maximizes the SOI for a certain value of the electric field [25].

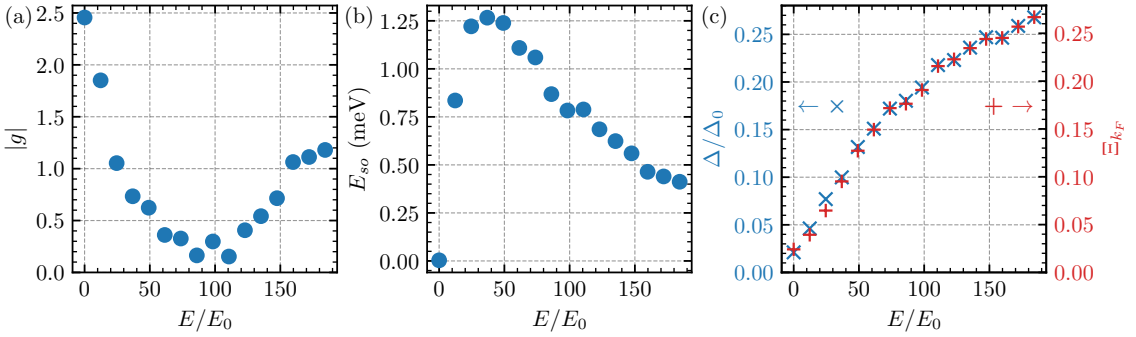

Figure 4.4: Dependence on the electric field E: (a) g factor, (b) spin-orbit energy E_{so}, and (c) proximity-induced gap Δ (blue crosses), as well as the weight Ξ_{k_F} of the NW state in the SC at k_F (red pluses) as a function of E applied in the y direction for $t = 0.8\,t_s$. The electric field is in units of $E_0 = \frac{\hbar^2\gamma_1}{2med^3} \approx 4\,\mathrm{V\,\mu m^{-1}}$ for $d = 5\,\mathrm{nm}$. The electric field has basically three effects: It squeezes the wave function in the NW, which reduces the g factor [see (a)], induces a strong SOI [see (b)], and pushes the wave function within the NW cross section close to the interface with the SC which enhances the leakage of the wave function into the SC and thereby the proximity-induced gap [see (c)]. Thus, it is possible to have strong SOI and a large proximity-induced gap simultaneously. Finding the best parameters for a sizable g factor, SOI, and superconducting proximity gap requires some optimization. Panel (a) shows the absolute value of the g factor. At $E \approx 80\,E_0$, the g factor changes sign. At strong electric field ($E \gtrsim 150\,E_0$), it is dominated by the SC g factor since the wave function at $k = 0$ has a weight of almost 70 % in the SC. The position of the maximum of the spin-orbit energy is approximately reached at $|eUE/\Delta_{sb}| \sim 1$ [16]. If not stated otherwise, the parameters are the same as in Fig. 4.2 and $d = 5\,\mathrm{nm}$.

Apart from reducing thickness, there is another way to move the wave function closer to the interface, namely, an external electric field in the y direction. In Fig. 4.4, we set the NW-

SC coupling to $t = 0.8\,t_s$, as well as $d = 5\,\mathrm{nm}$, and plot the g factor, SOI, and proximity-induced gap as a function of the external electric field E. We give the electric field in units of $E_0 = \frac{\hbar^2\gamma_1}{2med^3} \approx 4\,\mathrm{V\,\mu m^{-1}}$ for $d = 5\,\mathrm{nm}$. Note that $E/E_0 = d^3/l_E^3$ with the electric length $l_E = (\hbar^2\gamma_1/2meE)^{1/3}$, where m/γ_1 is the average HH-LH mass. Typically, the mass of the hole NW ground state converges to the average HH-LH mass for strong electric field [25]. Since the external electric field shifts the NW bands in energy and we want to focus on the lowest-energy NW state, we compensate for this effect by adjusting the chemical potential μ_w. As a function of the electric field, the g factor is first reduced until it changes sign at $E \approx 80\,E_0$ [see Fig. 4.4(a)]. The small increase for the g factor at $E \approx 100\,E_0$, followed by another dip, is associated with a resonance (see discussion in Sec. 4.3). Since we show the absolute value, the g factor increases for stronger electric fields. It reaches a value close to one, which is set by the SC g factor because at strong electric field ($E \gtrsim 150\,E_0$), the wave function at $k = 0$ has a weight of almost 70 % in the SC.

The spin-orbit energy, on the other hand, is small in the absence of an electric field [see Fig. 4.3(d)] and reaches a maximum at $E \approx 37\,E_0$, after which it is gradually reduced with further increasing the electric field [see Fig. 4.4(b)]. This is the typical behavior of the SOI in hole NWs, which is referred to as the direct Rashba SOI [16, 17, 25, 26]. This very strong type of SOI originates in the HH-LH mixing in 1D hole systems in combination with the breaking of inversion symmetry. The position of the maximal spin-orbit energy is approximately reached when $|eUE/\Delta_{sb}|$ becomes of the order of one [16], where Δ_{sb} is the subband gap in the NW and $U = 0.15d/2$. Interestingly, the proximity-induced gap increases with the electric field and reaches a value above $\Delta = 0.25\,\Delta_0$, which is comparable to the situation of the flat NW ($d = 2\,\mathrm{nm}$) in Fig. 4.3(b). Again, the induced gap shows the same dependence on E as the weight of the NW wave function in the SC, Ξ_{k_F} [see Fig. 4.4(c)].

The SOI behaves as expected from former studies [16, 25]. However, in a standard Rashba NW, the spin-orbit energy decreases as the proximity-induced gap increases [67]. Here, we find that this is not necessarily true for holes in Ge since an appropriate external electric field can cause strong SOI and a sizable superconducting gap in a Ge NW at the same time. Also relevant for the search of MBSs, where in addition to strong SOI and a proximity-induced gap a large Zeeman gap is required, it is important to avoid regimes of strongly reduced g factor. As shown in Fig. 4.4, it is possible to achieve a large SOI and reasonably large induced gap for realistic field strengths, while the g factor remains relatively small; however, it can also be optimized by adjusting the field strength. Furthermore, the coexistence of a large gap and strong SOI by itself is promising for proposals that achieve MBSs in Ge without any requirement for a large Zeeman energy or with reduced requirements on the Zeeman energy [61, 62, 96].

In order to get a better understanding for the observed behavior in Fig. 4.4, we plot in Fig. 4.5 the wave function of the NW state at $k = k_F$ (by k_F, we denote the Fermi wavevector at which the proximity-induced gap is smallest) for different values of the electric field. We choose $E = 0$ [see Fig. 4.5(a)], the electric field where the spin-orbit energy is maximal $E \approx 37\,E_0$ [see Fig. 4.5(b)], and the maximum considered electric field $E \approx 184\,E_0$ [see Fig. 4.5(c)]. In the absence of an external electric field for $d = 5\,\mathrm{nm}$, the coupling to the SC is not sufficient to push the NW wave function towards the interface with the SC. Thus, the wave function mostly remains in the center of the NW cross section, resulting in a rather weak SOI [see Fig. 4.4(b)] and small proximity-induced gap [see Fig. 4.4(c)]. At $E \approx 37\,E_0$, the wave function is squeezed in the y direction, which causes a drop in the g factor. At the same time, the wave function is pushed towards the NW-SC interface, breaking the symmetry. The proximity of the wave function to the SC allows for a stronger leakage of the NW wave function into the SC, resulting in an enhanced proximity-induced superconducting gap in the NW. At $E \approx 184\,E_0$, the wave function is further pushed towards the

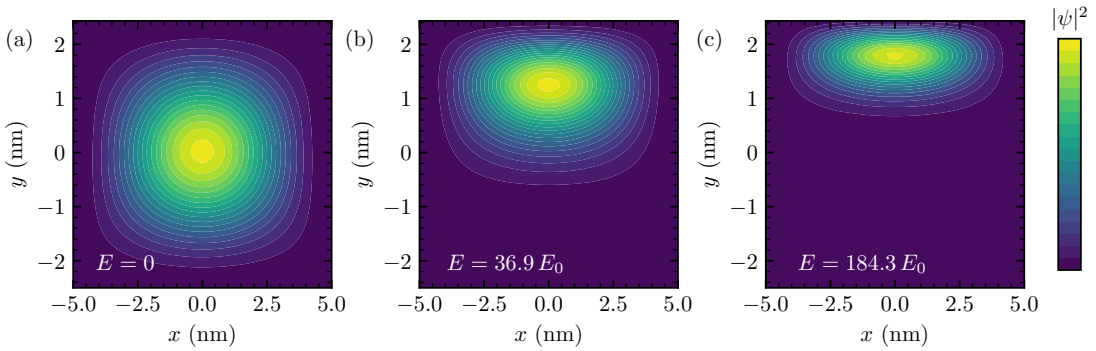

Figure 4.5: Wave function in the NW for NW-SC coupling $t = 0.8\,t_s$ at (a) $E = 0$, (b) $E = 36.9\,E_0$, and (c) $E = 184.3\,E_0$ at $k = k_F$. The superconductor is located on top of the NW. Without the electric field, the wave function is located in the center of the NW and the coupling to the SC is not sufficient to shift it towards the SC. For $E = 36.9\,E_0$, where we observe the maximum SOI in Fig. 4.4(b), the wave function is squeezed and pushed towards the NW-SC interface. This explains the gap opening and reduction of the g factor shown in Fig. 4.4. Further increasing the electric field to $E = 184.3\,E_0$ further pushes the wave function to the top and enhances the squeezing, resulting in a larger proximity-induced gap [see Fig. 4.4(c)]. If not stated differently, the parameters are the same as in Fig. 4.2 and $d = 5\,\mathrm{nm}$.

SC and the coupling, along with the induced gap, is increased. Also, the wave function is squeezed very strongly, which is why we would expect an even smaller g factor. However, the NW state now hybridizes strongly with the SC states, resulting in a g factor of the order of one.

For a Ge-based NW setup that is promising for the formation of Majorana bound states, we identify the following electric field regimes as optimal: Between $E \approx 25\,E_0$ and $E \approx 60\,E_0$, the g factor is between 0.3 and 1.1. At the same time, the spin-orbit energy reaches its maximum within this electric field range and the gap starts to open with values between $\Delta = 0.08\,\Delta_0$ and $\Delta = 0.15\,\Delta_0$. The regime $E \gtrapprox 120E_0$ is also promising. We find decent values of the spin-orbit energy E_{so} simultaneously with a gap around $\Delta = 0.25\,\Delta_0$, and with g factors larger than one, largely due to the finite g factor of the SC.

For the topological phase transition, if the chemical potential is tuned to the crossing point of the spin-orbit split subbands in the NW, it is required that the Zeeman gap becomes larger than the proximity-induced superconducting gap $\Delta_Z = \frac{1}{2} g \mu_B B > \Delta$ [58, 97, 98]. Taking as an example the values we get at $E = 160\,E_0$, where $E_{so} = 460\,\mu\mathrm{eV}$, $g = 1.06$, and $\Delta = 0.25\,\Delta_0 = 50\,\mu\mathrm{eV}$, a magnetic field of $B \sim 2\,\mathrm{T}$ is necessary to fulfill the topological condition. Thus, despite the very small g factor, it is within the realms of possibility to reach the topological phase in a Ge NW system since the critical field parallel to, e.g., thin Al films can be as large as $B_c = 5\,\mathrm{T}$ [99]. Note that this is just a rough estimate since an externally applied magnetic field influences the effective g factor in the Ge NW [26] and the induced superconducting gap will be suppressed. However, a detailed analysis taking these effects into account also predicts the topological phase to be possibly within reach [64].

We mention here that for a more symmetric NW cross section as in a cylindrical NW, the state is quasidegenerate, which spoils the potential formation of MBSs. However, due to static strain coming from a shell around the NW or from the contact to the SC, which is neglected in this work, a substantial subband gap emerges, lifting this quasidegeneracy [17, 25, 100].

In addition to the external electric field considered here, the band bending at the interface

between the SC and semiconductor is expected to create an electrostatic potential in a realistic device. We neglect these effects in this work because the electrostatics would only renormalize the electric field strength required to localize holes close to the interface. Therefore, the qualitative effect of simultaneously enhanced proximity-induced superconductivity and SOI can be expected to remain unaltered.

4.6 Coupling only to light holes in the nanowire

In this section, we analyze the case where $t_{\mathrm{LH}} \neq 0$ and $t_{\mathrm{HH}} = 0$ [see Eq. (4.16)] as an extreme case of $t_{\mathrm{LH}} \neq t_{\mathrm{HH}}$. In Fig. 4.6, we show the same plots as in Fig. 4.3, but with $t_{\mathrm{HH}} = 0$. In general, we observe the same qualitative behavior with and without coupling to the HHs. Interestingly, the proximity-induced gap Δ can be larger for $t_{\mathrm{HH}} = 0$ than for $t_{\mathrm{HH}} \neq 0$ [see Fig. 4.6(b)]. However, still the induced gap is rather small for $d \geq 4\,\mathrm{nm}$. Another interesting difference from Fig. 4.3 can be seen in Fig. 4.6(d). The spin-orbit energy, which is induced by coupling to the SC, is much smaller for $d = 2\,\mathrm{nm}$ and $d = 3\,\mathrm{nm}$ in the absence of the coupling to the HHs.

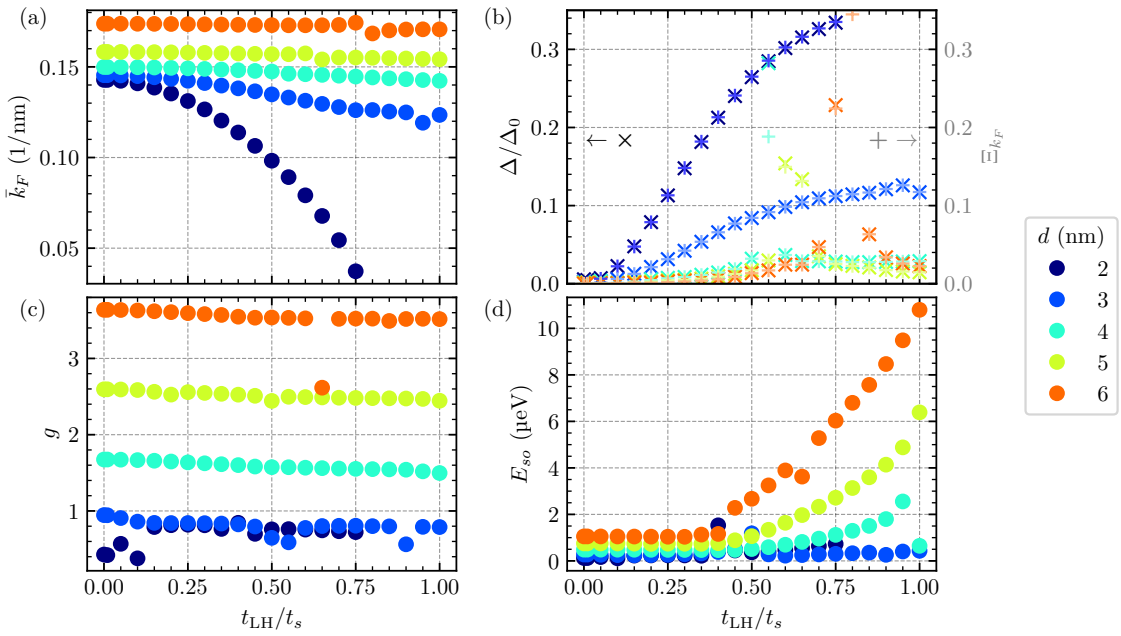

Figure 4.6: Same figure as Fig. 4.3, but the SC is coupled only to the LHs in the NW ($t_{\mathrm{HH}} = 0$). Qualitatively, there is no difference from Fig. 4.3. The proximity-induced gap is larger when the SC couples only to the LHs [see (b)]. The spin-orbit energy in (d) is strongly reduced without coupling to the HHs in the thin NWs ($d = 2\,\mathrm{nm}$ and $d = 3\,\mathrm{nm}$). In (a), the Fermi wave vector is not well defined for $t_{\mathrm{LH}} > 0.75\,t_s$, similarly to the cyan line in Fig. 4.2(c).

Also in the case without coupling to the HHs, we analyze the effect of an electric field that pushes the NW wave function towards the interface with the SC. In Fig. 4.7, we show the same data as in Fig. 4.4, but without coupling to the HHs. Again, we find a similar qualitative behavior as before. For $t_{\mathrm{HH}} = 0$, the g factor minimum is 0.8 and, for $E \gtrsim 50\,E_0$, it stays close to a value of $g \sim 1$ [see Fig. 4.7(a)]. The g factor does not drop to zero since the HHs remain uncoupled

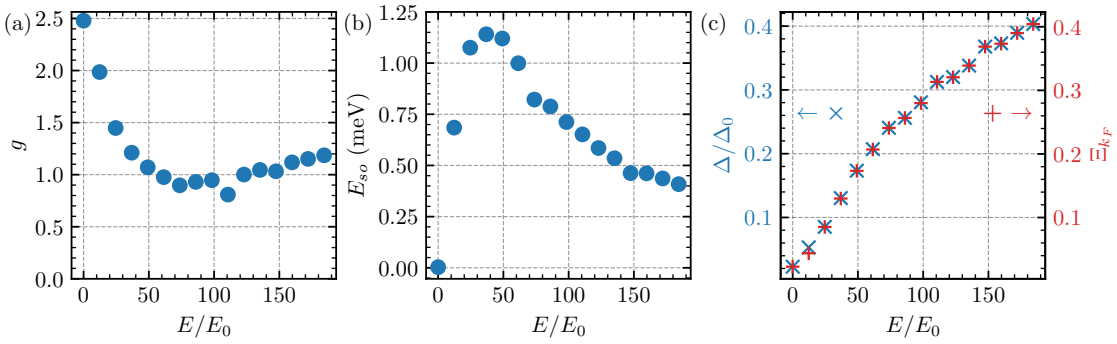

Figure 4.7: Same figure as Fig. 4.4, but the SC is coupled only to the LHs in the NW ($t_{\mathrm{HH}} = 0$, $t_{\mathrm{LH}} = 0.8\,t_s$). The qualitative behavior is similar to Fig. 4.4. (a) The g factor never drops to a value as low as with coupling also to HHs. For $E > 50\,E_0$, the g factor stays at a value of around one. (b) The spin-orbit energy is almost identical to the one in Fig. 4.4, but the maximum is slightly lower at $E_{so} = 1.1\,\mathrm{meV}$ instead of $E_{so} = 1.3\,\mathrm{meV}$. (c) The proximity-induced gap reaches $\Delta = 0.40\,\Delta_0$ at $E \approx 184\,E_0$, which is significantly larger than the maximum of $\Delta = 0.27\,\Delta_0$ in Fig. 4.4.

from the SC and the g factor does not change sign. For $E = 0$, the g factor is $g = 2.5$ regardless of the SC coupling to HHs. For $t_{\mathrm{HH}} = 0$, the spin-orbit energy E_{so} reaches only a slightly smaller value than the previous maximum, which again occurs close to $E = 37\,E_0$ [see Fig. 4.7(b)]. For $t_{\mathrm{HH}} = 0.8\,t_s$, the maximum spin-orbit energy is $E_{so} = 1.3\,\mathrm{meV}$, while it is $E_{so} = 1.1\,\mathrm{meV}$ for $t_{\mathrm{HH}} = 0$. The proximity-induced gap, on the other hand, is larger for $t_{\mathrm{HH}} = 0$ [see Fig. 4.7(c)]. At $E = 184\,E_0$, the gap is $\Delta = 0.40\,\Delta_0$ instead of $\Delta = 0.27\,\Delta_0$ for the previous case of $t_{\mathrm{HH}} = 0.8\,t_s$.

There are no crucial qualitative differences between the situations with $t_{\mathrm{HH}} = 0$ and $t_{\mathrm{HH}} \neq 0$ that would contradict our main message of simultaneously large spin-orbit energy and proximity-induced gap. In a realistic experiment, we expect $t_{\mathrm{HH}} \neq t_{\mathrm{LH}}$ and $t_{\mathrm{HH}} \neq 0$, which should result in a situation between the two that was discussed in this paper. Again, in such a realistic situation, we will likely find a regime where the g factor, the SOI, and the proximity-induced gap are just large enough to achieve the topological phase transition.

4.7 Conclusion

We have numerically investigated the coupling between a Ge NW and a SC that were both modeled as 3D systems. We showed that the average Fermi wave vector depends on the coupling to the SC and can increase or decrease with increasing coupling depending on the chemical potential of the SC with respect to the chemical potential of the NW.

We found that effects of the coupling between the NW and the SC strongly depend on the thickness of the NW. When no electric field is applied, only for thin NWs does the coupling result in a sizable proximity-induced gap in the NW. This observation can be explained by the distance of the NW wave function to the SC. Only if the wave function is close to the SC does it strongly couple. We showed that the g factor is largest for thicker NWs where, in the absence of an electric field, the proximity-induced gap remains negligibly small, even for large hopping between SC and NW sites at the interface. Since the induced gap depends on the distance of the NW wave function to the SC, the gap can be increased by pushing the wave function closer towards the SC by an

external electric field. We demonstrated that it is possible to achieve a large spin-orbit energy simultaneously with a sizable proximity-induced gap for a certain range of the electric field.

There, however, exists an electric field regime where the g factor drops to almost zero, which spoils the applicability of the Ge hole NW coupled to a SC for the formation of Majorana bound states. Still, some optimization allows for a regime where the g factor, spin-orbit energy, and proximity-induced gap are just large enough to achieve a topological phase transition. A rough estimate tells us that in the most optimal scenario, the topological phase can be reached with a magnetic field $B \sim 2\,\mathrm{T}$, which is below the critical field of thin Al films. A different type of coupling where the SC does not couple equally to HHs and LHs does not change the qualitative results. Coupling only to LHs even can have a positive effect on the g factor of the proximitized NW.

Our results indicate that there is a unique phenomenology of metallization effects in Ge. Most importantly, it is possible to find scenarios where the spin-orbit energy and the induced superconducting gap are sizable. This is encouraging for many potential applications of hybrid Ge-SC devices in quantum information processing, e.g., Andreev spin qubits. It is also promising for the realization of topological superconductivity in Ge-based systems, especially for protocols where no Zeeman energy is required [62, 96] since then no trade-off is necessary in order to optimize the g factor.

Acknowledgments. We thank Stefano Bosco and Dominik Zumbühl for useful discussions. This work is supported by the Swiss National Science Foundation (SNSF) and NCCR SPIN (Grant No. 51NF40-180604). This project has received funding from the European Union's Horizon 2020 research and innovation programme under Grant Agreement No 862046. H.F.L. acknowledges support from the Georg H. Endress Foundation.

References

[1] G. Scappucci, C. Kloeffel, F. A. Zwanenburg, D. Loss, M. Myronov, J.-J. Zhang, S. D. Franceschi, G. Katsaros, and M. Veldhorst, "The germanium quantum information route", Nat. Rev. Mater. **6**, 926 (2021).

[2] M. Veldhorst, H. G. J. Eenink, C. H. Yang, and A. S. Dzurak, "Silicon CMOS architecture for a spin-based quantum computer", Nat Commun. **8**, 1766 (2017).

[3] M. Myronov, J. Kycia, P. Waldron, W. Jiang, P. Barrios, A. Bogan, P. Coleridge, and S. Studenikin, "Holes outperform electrons in group IV semiconductor materials", Small Sci. **3**, 2200094 (2023).

[4] L. E. A. Stehouwer, A. Tosato, D. D. Esposti, D. Costa, M. Veldhorst, A. Sammak, and G. Scappucci, "Germanium wafers for strained quantum wells with low disorder", Appl. Phys. Lett. **123**, 092101 (2023).

[5] A. Sammak, D. Sabbagh, N. W. Hendrickx, M. Lodari, B. P. Wuetz, A. Tosato, L. Yeoh, M. Bollani, M. Virgilio, M. A. Schubert, P. Zaumseil, G. Capellini, M. Veldhorst, and G. Scappucci, "Shallow and undoped germanium quantum wells: a playground for spin and hybrid quantum technology", Adv. Funct. Mater. **29**, 1807613 (2019).

[6] Y. Kamata, "High-k/Ge MOSFETs for future nanoelectronics", Mater. Today **11**, 30 (2008).

[7] J. Fischer and D. Loss, "Hybridization and spin decoherence in heavy-hole quantum dots", Phys. Rev. Lett. **105**, 266603 (2010).

[8] F. Maier and D. Loss, "Effect of strain on hyperfine-induced hole-spin decoherence in quantum dots", Phys. Rev. B **85**, 195323 (2012).

[9] D. Klauser, W. A. Coish, and D. Loss, "Nuclear spin state narrowing via gate-controlled Rabi oscillations in a double quantum dot", Phys. Rev. B **73**, 205302 (2006).

[10] J. H. Prechtel, A. V. Kuhlmann, J. Houel, A. Ludwig, S. R. Valentin, A. D. Wieck, and R. J. Warburton, "Decoupling a hole spin qubit from the nuclear spins", Nat. Mater. **15**, 981 (2016).

[11] C. Testelin, F. Bernardot, B. Eble, and M. Chamarro, "Hole–spin dephasing time associated with hyperfine interaction in quantum dots", Phys. Rev. B **79**, 195440 (2009).

[12] J. Fischer, W. A. Coish, D. V. Bulaev, and D. Loss, "Spin decoherence of a heavy hole coupled to nuclear spins in a quantum dot", Phys. Rev. B **78**, 155329 (2008).

[13] S. Bosco and D. Loss, "Fully tunable hyperfine interactions of hole spin qubits in Si and Ge quantum dots", Phys. Rev. Lett. **127**, 190501 (2021).

[14] K. Itoh, W. Hansen, E. Haller, J. Farmer, V. Ozhogin, A. Rudnev, and A. Tikhomirov, "High purity isotopically enriched ^{70}Ge and ^{74}Ge single crystals: isotope separation, growth, and properties", J. Mater. Res. **8**, 1341 (1993).

[15] K. M. Itoh and H. Watanabe, "Isotope engineering of silicon and diamond for quantum computing and sensing applications", MRS Commun. **4**, 143 (2014).

[16] C. Kloeffel, M. J. Rančić, and D. Loss, "Direct Rashba spin-orbit interaction in Si and Ge nanowires with different growth directions", Phys. Rev. B **97**, 235422 (2018).

[17] C. Kloeffel, M. Trif, and D. Loss, "Strong spin-orbit interaction and helical hole states in Ge/Si nanowires", Phys. Rev. B **84**, 195314 (2011).

[18] X.-J. Hao, T. Tu, G. Cao, C. Zhou, H.-O. Li, G.-C. Guo, W. Y. Fung, Z. Ji, G.-P. Guo, and W. Lu, "Strong and tunable spin-orbit coupling of one-dimensional holes in Ge/Si core/shell nanowires", Nano Lett. **10**, 2956 (2010).

[19] Y. Hu, F. Kuemmeth, C. M. Lieber, and C. M. Marcus, "Hole spin relaxation in Ge-Si core-shell nanowire qubits", Nat. Nanotechnol. **7**, 47 (2011).

[20] L. A. Terrazos, E. Marcellina, Z. Wang, S. N. Coppersmith, M. Friesen, A. R. Hamilton, X. Hu, B. Koiller, A. L. Saraiva, D. Culcer, and R. B. Capaz, "Theory of hole-spin qubits in strained germanium quantum dots", Phys. Rev. B **103**, 125201 (2021).

[21] F. N. M. Froning, L. C. Camenzind, O. A. H. van der Molen, A. Li, E. P. A. M. Bakkers, D. M. Zumbühl, and F. R. Braakman, "Ultrafast hole spin qubit with gate-tunable spin-orbit switch functionality", Nat. Nanotechnol. **16**, 308 (2021).

[22] H. Liu, T. Zhang, K. Wang, F. Gao, G. Xu, X. Zhang, S.-X. Li, G. Cao, T. Wang, J. Zhang, X. Hu, H.-O. Li, and G.-P. Guo, "Gate-tunable spin-orbit coupling in a germanium hole double quantum dot", Phys. Rev. Appl. **17**, 044052 (2022).

[23] F. Maier, C. Kloeffel, and D. Loss, "Tunable g factor and phonon-mediated hole spin relaxation in Ge/Si nanowire quantum dots", Phys. Rev. B **87**, 161305(R) (2013).

[24] S. Bosco, P. Scarlino, J. Klinovaja, and D. Loss, "Fully tunable longitudinal spin-photon interactions in Si and Ge quantum dots", Phys. Rev. Lett. **129**, 066801 (2022).

[25] C. Adelsberger, M. Benito, S. Bosco, J. Klinovaja, and D. Loss, "Hole-spin qubits in Ge nanowire quantum dots: interplay of orbital magnetic field, strain, and growth direction", Phys. Rev. B **105**, 075308 (2022).

[26] C. Adelsberger, S. Bosco, J. Klinovaja, and D. Loss, "Enhanced orbital magnetic field effects in Ge hole nanowires", Phys. Rev. B **106**, 235408 (2022).

[27] D. Loss and D. P. DiVincenzo, "Quantum computation with quantum dots", Phys. Rev. A **57**, 120 (1998).

[28] K. Wang, G. Xu, F. Gao, H. Liu, R.-L. Ma, X. Zhang, Z. Wang, G. Cao, T. Wang, J.-J. Zhang, D. Culcer, X. Hu, H.-W. Jiang, H.-O. Li, G.-C. Guo, and G.-P. Guo, "Ultrafast coherent control of a hole spin qubit in a germanium quantum dot", Nat. Commun. **13**, 206 (2022).

[29] H. Watzinger, J. Kukučka, L. Vukušić, F. Gao, T. Wang, F. Schäffler, J.-J. Zhang, and G. Katsaros, "A germanium hole spin qubit", Nat. Commun. **9**, 3902 (2018).

[30] N. W. Hendrickx, W. I. L. Lawrie, L. Petit, A. Sammak, G. Scappucci, and M. Veldhorst, "A single-hole spin qubit", Nat. Commun. **11**, 3478 (2020).

[31] F. N. M. Froning, M. J. Rančić, B. Hetényi, S. Bosco, M. K. Rehmann, A. Li, E. P. A. M. Bakkers, F. A. Zwanenburg, D. Loss, D. M. Zumbühl, and F. R. Braakman, "Strong spin-orbit interaction and g-factor renormalization of hole spins in Ge/Si nanowire quantum dots", Phys. Rev. Res. **3**, 013081 (2021).

[32] N. W. Hendrickx, D. P. Franke, A. Sammak, G. Scappucci, and M. Veldhorst, "Fast two-qubit logic with holes in germanium", Nature **577**, 487 (2020).

[33] D. Jirovec, A. Hofmann, A. Ballabio, P. M. Mutter, G. Tavani, M. Botifoll, A. Crippa, J. Kukucka, O. Sagi, F. Martins, J. Saez-Mollejo, I. Prieto, M. Borovkov, J. Arbiol, D. Chrastina, G. Isella, and G. Katsaros, "A singlet-triplet hole spin qubit in planar Ge", Nat. Mater. **20**, 1106 (2021).

[34] N. W. Hendrickx, W. I. L. Lawrie, M. Russ, F. van Riggelen, S. L. de Snoo, R. N. Schouten, A. Sammak, G. Scappucci, and M. Veldhorst, "A four-qubit germanium quantum processor", Nature **591**, 580 (2021).

[35] J. Xiang, A. Vidan, M. Tinkham, R. M. Westervelt, and C. M. Lieber, "Ge/Si nanowire mesoscopic Josephson junctions", Nat. Nanotechnol. **1**, 208 (2006).

[36] N. W. Hendrickx, D. P. Franke, A. Sammak, M. Kouwenhoven, D. Sabbagh, L. Yeoh, R. Li, M. L. V. Tagliaferri, M. Virgilio, G. Capellini, G. Scappucci, and M. Veldhorst, "Gate-controlled quantum dots and superconductivity in planar germanium", Nat. Commun. **9**, 2835 (2018).

[37] J. Ridderbos, M. Brauns, J. Shen, F. K. de Vries, A. Li, E. P. A. M. Bakkers, A. Brinkman, and F. A. Zwanenburg, "Josephson effect in a few-hole quantum dot", Adv. Mater **30**, 1802257 (2018).

[38] N. W. Hendrickx, M. L. V. Tagliaferri, M. Kouwenhoven, R. Li, D. P. Franke, A. Sammak, A. Brinkman, G. Scappucci, and M. Veldhorst, "Ballistic supercurrent discretization and micrometer-long Josephson coupling in germanium", Phys. Rev. B **99**, 075435 (2019).

[39] F. Vigneau, R. Mizokuchi, D. C. Zanuz, X. Huang, S. Tan, R. Maurand, S. Frolov, A. Sammak, G. Scappucci, F. Lefloch, and S. D. Franceschi, "Germanium quantum-well Josephson field-effect transistors and interferometers", Nano Lett. **19**, 1023 (2019).

[40] J. Ridderbos, M. Brauns, F. K. de Vries, J. Shen, A. Li, S. Kölling, M. A. Verheijen, A. Brinkman, W. G. van der Wiel, E. P. A. M. Bakkers, and F. A. Zwanenburg, "Hard superconducting gap and diffusion-induced superconductors in Ge-Si nanowires", Nano Lett. **20**, 122 (2020).

[41] K. Aggarwal, A. Hofmann, D. Jirovec, I. Prieto, A. Sammak, M. Botifoll, S. Martí-Sánchez, M. Veldhorst, J. Arbiol, G. Scappucci, J. Danon, and G. Katsaros, "Enhancement of proximity-induced superconductivity in a planar Ge hole gas", Phys. Rev. Res. **3**, L022005 (2021).

[42] A. Tosato, V. Levajac, J.-Y. Wang, C. J. Boor, F. Borsoi, M. Botifoll, C. N. Borja, S. Martí-Sánchez, J. Arbiol, A. Sammak, M. Veldhorst, and G. Scappucci, "Hard superconducting gap in germanium", Commun. Mater. **4**, 23 (2023).

[43] E. Zhuo, Z. Lyu, X. Sun, A. Li, B. Li, Z. Ji, J. Fan, E. Bakkers, X. Han, X. Song, F. Qu, G. Liu, J. Shen, and L. Lu, "Hole-type superconducting gatemon qubit based on Ge/Si core/shell nanowires", npj Quantum Inf. **9**, 51 (2023).

[44] J. Ridderbos, M. Brauns, A. Li, E. P. A. M. Bakkers, A. Brinkman, W. G. van der Wiel, and F. A. Zwanenburg, "Multiple Andreev reflections and Shapiro steps in a Ge-Si nanowire Josephson junction", Phys. Rev. Mater. **3**, 084803 (2019).

[45] L. Casparis, M. R. Connolly, M. Kjaergaard, N. J. Pearson, A. Kringhøj, T. W. Larsen, F. Kuemmeth, T. Wang, C. Thomas, S. Gronin, G. C. Gardner, M. J. Manfra, C. M. Marcus, and K. D. Petersson, "Superconducting gatemon qubit based on a proximitized two-dimensional electron gas", Nat. Nanotechnol. **13**, 915 (2018).

[46] T. W. Larsen, M. E. Gershenson, L. Casparis, A. Kringhøj, N. J. Pearson, R. P. G. McNeil, F. Kuemmeth, P. Krogstrup, K. D. Petersson, and C. M. Marcus, "Parity-protected superconductor-semiconductor qubit", Phys. Rev. Lett. **125**, 056801 (2020).

[47] K. D. Petersson, L. W. McFaul, M. D. Schroer, M. Jung, J. M. Taylor, A. A. Houck, and J. R. Petta, "Circuit quantum electrodynamics with a spin qubit", Nature **490**, 380 (2012).

[48] M. Leijnse and K. Flensberg, "Coupling spin qubits via superconductors", Phys. Rev. Lett. **111**, 060501 (2013).

[49] T. W. Larsen, K. D. Petersson, F. Kuemmeth, T. S. Jespersen, P. Krogstrup, J. Nygård, and C. M. Marcus, "Semiconductor-nanowire-based superconducting qubit", Phys. Rev. Lett. **115**, 127001 (2015).

[50] G. Burkard, M. J. Gullans, X. Mi, and J. R. Petta, "Superconductor-semiconductor hybrid-circuit quantum electrodynamics", Nat. Rev. Phys. **2**, 129 (2020).

[51] E. J. H. Lee, X. Jiang, M. Houzet, R. Aguado, C. M. Lieber, and S. D. Franceschi, "Spin-resolved Andreev levels and parity crossings in hybrid superconductor-semiconductor nanostructures", Nat. Nanotechnol. **9**, 79 (2014).

[52] S. Park and A. L. Yeyati, "Andreev spin qubits in multichannel Rashba nanowires", Phys. Rev. B **96**, 125416 (2017).

[53] M. Hays, V. Fatemi, D. Bouman, J. Cerrillo, S. Diamond, K. Serniak, T. Connolly, P. Krogstrup, J. Nygård, A. L. Yeyati, A. Geresdi, and M. H. Devoret, "Coherent manipulation of an Andreev spin qubit", Science **373**, 430 (2021).

[54] M. Spethmann, X.-P. Zhang, J. Klinovaja, and D. Loss, "Coupled superconducting spin qubits with spin-orbit interaction", Phys. Rev. B **106**, 115411 (2022).

[55] A. Y. Kitaev, "Unpaired Majorana fermions in quantum wires", Phys. Usp. **44**, 131 (2001).

[56] D. A. Ivanov, "Non-Abelian statistics of half-quantum vortices in p-wave superconductors", Phys. Rev. Lett. **86**, 268 (2001).

[57] C. Nayak, S. H. Simon, A. Stern, M. Freedman, and S. Das Sarma, "Non-Abelian anyons and topological quantum computation", Rev. Mod. Phys. **80**, 1083 (2008).

[58] F. Maier, J. Klinovaja, and D. Loss, "Majorana fermions in Ge/Si hole nanowires", Phys. Rev. B **90**, 195421 (2014).

[59] F. Pientka, A. Keselman, E. Berg, A. Yacoby, A. Stern, and B. I. Halperin, "Topological superconductivity in a planar Josephson junction", Phys. Rev. X **7**, 021032 (2017).

[60] R. M. Lutchyn, E. P. A. M. Bakkers, L. P. Kouwenhoven, P. Krogstrup, C. M. Marcus, and Y. Oreg, "Majorana zero modes in superconductor-semiconductor heterostructures", Nat. Rev. Mater. **3**, 52 (2018).

[61] M. Luethi, K. Laubscher, S. Bosco, D. Loss, and J. Klinovaja, "Planar Josephson junctions in germanium: effect of cubic spin-orbit interaction", Phys. Rev. B **107**, 035435 (2023).

[62] M. Luethi, H. F. Legg, K. Laubscher, D. Loss, and J. Klinovaja, "Majorana bound states in germanium Josephson junctions via phase control", (2023), arXiv:2304.12689 [cond-mat.mes-hall].

[63] B. D. Woods, M. A. Eriksson, R. Joynt, and M. Friesen, "Spin-orbit enhancement in Si/SiGe heterostructures with oscillating Ge concentration", Phys. Rev. B **107**, 035418 (2023).

[64] K. Laubscher, J. D. Sau, and S. Das Sarma, "Majorana zero modes in gate-defined germanium hole nanowires", (2023), arXiv:2305.14313 [cond-mat.mes-hall].

[65] W. S. Cole, S. Das Sarma, and T. D. Stanescu, "Effects of large induced superconducting gap on semiconductor Majorana nanowires", Phys. Rev. B **92**, 174511 (2015).

[66] T. D. Stanescu and S. Das Sarma, "Proximity-induced low-energy renormalization in hybrid semiconductor-superconductor Majorana structures", Phys. Rev. B **96**, 014510 (2017).

[67] C. Reeg, D. Loss, and J. Klinovaja, "Metallization of a Rashba wire by a superconducting layer in the strong-proximity regime", Phys. Rev. B **97**, 165425 (2018).

[68] C. Reeg, D. Loss, and J. Klinovaja, "Finite-size effects in a nanowire strongly coupled to a thin superconducting shell", Phys. Rev. B **96**, 125426 (2017).

[69] C. Reeg and D. L. Maslov, "Transport signatures of topological superconductivity in a proximity-coupled nanowire", Phys. Rev. B **95**, 205439 (2017).

[70] A. E. Antipov, A. Bargerbos, G. W. Winkler, B. Bauer, E. Rossi, and R. M. Lutchyn, "Effects of gate-induced electric fields on semiconductor Majorana nanowires", Phys. Rev. X **8**, 031041 (2018).

[71] A. E. G. Mikkelsen, P. Kotetes, P. Krogstrup, and K. Flensberg, "Hybridization at superconductor-semiconductor interfaces", Phys. Rev. X **8**, 031040 (2018).

[72] M. W. A. de Moor, J. D. S. Bommer, D. Xu, G. W. Winkler, A. E. Antipov, A. Bargerbos, G. Wang, N. van Loo, R. L. M. O. het Veld, S. Gazibegovic, D. Car, J. A. Logan, M. Pendharkar, J. S. Lee, E. P. A. M. Bakkers, C. J. Palmstrøm, R. M. Lutchyn, L. P. Kouwenhoven, and H. Zhang, "Electric field tunable superconductor-semiconductor coupling in Majorana nanowires", New J. Phys. **20**, 103049 (2018).

[73] B. D. Woods, T. D. Stanescu, and S. Das Sarma, "Effective theory approach to the Schrödinger-Poisson problem in semiconductor Majorana devices", Phys. Rev. B **98**, 035428 (2018).

[74] G. W. Winkler, A. E. Antipov, B. van Heck, A. A. Soluyanov, L. I. Glazman, M. Wimmer, and R. M. Lutchyn, "Unified numerical approach to topological semiconductor-superconductor heterostructures", Phys. Rev. B **99**, 245408 (2019).

[75] O. A. Awoga, J. Cayao, and A. M. Black-Schaffer, "Supercurrent detection of topologically trivial zero-energy states in nanowire junctions", Phys. Rev. Lett. **123**, 117001 (2019).

[76] S. Vaitiekėnas, G. W. Winkler, B. van Heck, T. Karzig, M.-T. Deng, K. Flensberg, L. I. Glazman, C. Nayak, P. Krogstrup, R. M. Lutchyn, and C. M. Marcus, "Flux-induced topological superconductivity in full-shell nanowires", Science **367**, eaav3392 (2020).

[77] M. Aghaee, A. Akkala, Z. Alam, R. Ali, A. A. Ramirez, M. Andrzejczuk, A. E. Antipov, P. Aseev, M. Astafev, B. Bauer, J. Becker, S. Boddapati, F. Boekhout, J. Bommer, T. Bosma, L. Bourdet, S. Boutin, P. Caroff, L. Casparis, M. Cassidy, S. Chatoor, A. W. Christensen, N. Clay, W. S. Cole, F. Corsetti, A. Cui, P. Dalampiras, A. Dokania, G. de Lange, M. de Moor, J. C. E. Saldaña, S. Fallahi, Z. H. Fathabad, J. Gamble, G. Gardner, D. Govender, F. Griggio, R. Grigoryan, S. Gronin, J. Gukelberger, E. B. Hansen, S. Heedt, J. H. Zamorano, S. Ho, U. L. Holgaard, H. Ingerslev, L. Johansson, J. Jones, R. Kallaher, F. Karimi, T. Karzig, C. King, M. E. Kloster, C. Knapp, D. Kocon, J. Koski, P. Kostamo, P. Krogstrup, M. Kumar, T. Laeven, T. Larsen, K. Li, T. Lindemann, J. Love, R. Lutchyn, M. H. Madsen, M. Manfra, S. Markussen, E. Martinez, R. McNeil, E. Memisevic, T. Morgan, A. Mullally, C. Nayak, J. Nielsen, W. H. P. Nielsen, B. Nijholt, A. Nurmohamed, E. O'Farrell, K. Otani, S. Pauka, K. Petersson, L. Petit, D. I. Pikulin, F. Preiss, M. Quintero-Perez, M. Rajpalke, K. Rasmussen, D. Razmadze, O. Reentila, D. Reilly, R. Rouse, I. Sadovskyy, L. Sainiemi, S. Schreppler, V. Sidorkin, A. Singh, S. Singh, S. Sinha, P. Sohr, T. Stankevič, L. Stek, H. Suominen, J. Suter, V. Svidenko, S. Teicher, M. Temuerhan, N. Thiyagarajah, R. Tholapi, M. Thomas, E. Toomey, S. Upadhyay, I. Urban, S. Vaitiekėnas, K. V. Hoogdalem, D. V. Woerkom, D. V. Viazmitinov, D. Vogel, S. Waddy, J. Watson, J. Weston, G. W. Winkler, C. K. Yang, S. Yau, D. Yi, E. Yucelen, A. Webster, R. Zeisel, and R. Z. and, "InAs-Al hybrid devices passing the topological gap protocol", Phys. Rev. B **107**, 245423 (2023).

[78] H. F. Legg, D. Loss, and J. Klinovaja, "Metallization and proximity superconductivity in topological insulator nanowires", Phys. Rev. B **105**, 155413 (2022).

[79] K. Laubscher and J. Klinovaja, "Majorana bound states in semiconducting nanostructures", J. Appl. Phys. **130**, 081101 (2021).

[80] S. Bosco, M. Benito, C. Adelsberger, and D. Loss, "Squeezed hole spin qubits in Ge quantum dots with ultrafast gates at low power", Phys. Rev. B **104**, 115425 (2021).

[81] P. Rüßmann and S. Blügel, "Proximity induced superconductivity in a topological insulator", (2022), arXiv:2208.14289 [cond-mat.mes-hall].

[82] N. O. Lipari and A. Baldereschi, "Angular momentum theory and localized states in solids. Investigation of shallow acceptor states in semiconductors", Phys. Rev. Lett **25**, 1660 (1970).

[83] R. Li, "Low-energy subband wave-functions and effective g-factor of one-dimensional hole gas", J. Phys.: Condens. Mat. **33**, 355302 (2021).

[84] R. Li, "Searching strong 'spin'-orbit coupled one-dimensional hole gas in strong magnetic fields", J. Phys.: Condens. Mat. **34**, 075301 (2022).

[85] R. Winkler, *Spin-orbit coupling effects in two-dimensional electron and hole systems* (Springer, Berlin, Oct. 10, 2003).

[86] P. Lawaetz, "Valence-band parameters in cubic semiconductors", Phys. Rev. B **4**, 3460 (1971).

[87] J. M. Luttinger, "Quantum theory of cyclotron resonance in semiconductors: general theory", Phys. Rev. **102**, 1030 (1956).

[88] J. S. Lim, L. Serra, R. López, and R. Aguado, "Magnetic-field instability of Majorana modes in multiband semiconductor wires", Phys. Rev. B **86**, 121103 (2012).

[89] J. Osca and L. Serra, "Majorana states and magnetic orbital motion in planar hybrid nanowires", Phys. Rev. B **91**, 235417 (2015).

[90] B. Nijholt and A. R. Akhmerov, "Orbital effect of magnetic field on the Majorana phase diagram", Phys. Rev. B **93**, 235434 (2016).

[91] O. Dmytruk and J. Klinovaja, "Suppression of the overlap between Majorana fermions by orbital magnetic effects in semiconducting-superconducting nanowires", Phys. Rev. B **97**, 155409 (2018).

[92] P. Wójcik and M. P. Nowak, "Durability of the superconducting gap in Majorana nanowires under orbital effects of a magnetic field", Phys. Rev. B **97**, 235445 (2018).

[93] P. Y. Yu and M. Cardona, *Fundamentals of semiconductors: physics and materials properties, Physics and materials properties* (Springer, Berlin, Heidelberg, 2010).

[94] D. Futterer, M. Governale, U. Zülicke, and J. König, "Band-mixing-mediated Andreev reflection of semiconductor holes", Phys. Rev. B **84**, 104526 (2011).

[95] A. G. Moghaddam, T. Kernreiter, M. Governale, and U. Zülicke, "Exporting superconductivity across the gap: proximity effect for semiconductor valence-band states due to contact with a simple-metal superconductor", Phys. Rev. B **89**, 184507 (2014).

[96] O. Lesser, Y. Oreg, and A. Stern, "One-dimensional topological superconductivity based entirely on phase control", Phys. Rev. B **106**, L241405 (2022).

[97] R. M. Lutchyn, J. D. Sau, and S. Das Sarma, "Majorana fermions and a topological phase transition in semiconductor-superconductor heterostructures", Phys. Rev. Lett. **105**, 077001 (2010).

[98] Y. Oreg, G. Refael, and F. von Oppen, "Helical liquids and Majorana bound states in quantum wires", Phys. Rev. Lett. **105**, 177002 (2010).

[99] R. Meservey and P. M. Tedrow, "Properties of very thin aluminum films", J. Appl. Phys. **42**, 51 (1971).

[100] C. Kloeffel, M. Trif, and D. Loss, "Acoustic phonons and strain in core/shell nanowires", Phys. Rev. B **90**, 115419 (2014).

CHAPTER 5

Valley-free silicon fins by shear strain

Adapted from:
Christoph Adelsberger, Stefano Bosco, Jelena Klinovaja, and Daniel Loss
"Valley-free silicon fins by shear strain",
arXiv:2308.13448 (2023)

Electron spins confined in silicon quantum dots are promising architectures for large-scale quantum computers. However, the degeneracy of the conduction band of bulk silicon introduces additional levels dangerously close to the window of computational energies, where the quantum information can leak. The energy of the valley states -typically 0.1 meV- depends on hardly controllable atomistic disorder and still constitutes a fundamental limit to the scalability of these architectures. In this work, we introduce designs of CMOS-compatible silicon fin field-effect transistors that enhance the energy gap to non-computational states by more than one order of magnitude. Our devices comprise realistic silicon-germanium nanostructures with a large shear strain, where troublesome valley degrees of freedom are completely removed. The energy of non-computational states is therefore not affected by unavoidable atomistic disorder and can further be tuned in-situ by applied electric fields. Our design ideas are directly applicable to a variety of setups and will offer a blueprint towards silicon-based large-scale quantum processors.

5.1 Introduction

Spins in silicon and germanium quantum dots (QDs) are the workhorse of modern semiconductor-based quantum technology [1–12]. The most advanced platforms to date utilize planar heterostructures comprising planar Si and SiGe alloys, where the quantum information is carried by single electrons confined in the Si layer [9–13]. In these systems, long spin coherence is enabled by the weak spin-orbit interaction of the conduction band and by removing the unwanted nuclear spin isotopes of Si [14]. Electron spin resonance was harnessed to selectively control individual qubits [15–17] and tunable exchange interactions mediate fast, high-fidelity two-qubit gates [8, 18–23]. The versatility of these architectures permitted remote coupling of distant qubits via microwave cavities [24–26] and spin shuttling [27–30], as well as entanglement of three spin states [31]. Readout and two-qubit gate fidelities exceeding the error correction threshold [13, 32–34] and the recent demonstration of a six-qubit quantum processor [9] also constitute promising steps toward large-scale quantum processors.

However, further progress in electron spin qubits in silicon is currently hindered by the valley degeneracy of the conduction band of silicon. In planar Si/SiGe heterostructures tensile in-plane strain partially lifts the six-fold degeneracy of bulk silicon, pushing four valleys to higher energy; the groundstate remains two-fold degenerate [35–37]. The residual valleys introduce troublesome additional levels in the vicinity of the computational energies where the quantum information is processed. These states open the system to decoherence and relaxation channels and constitute a critical source of leakage [38–45]. The residual valley degeneracy can be lifted by strong electric fields, but the induced energy gap is relatively small $10\,\mu\text{eV} - 100\,\mu\text{eV}$ and dangerously close to the typical qubit energies $\sim 10\,\mu\text{eV}$. Because it strongly depends on atomistic details of the Si/SiGe interface, reliably and reproducibly control this gap is an open challenge [46–52]. Moreover, in hot qubits, valley states can be thermally excited hindering the scalability of quantum processors [53]. Larger valley splittings are reached by periodically altering the concentration of Ge in the well [54, 55]. In MOS structures splittings $\sim 0.5\,\text{meV}$ are reached by tightly confined electrons at the interfaces between Si and SiO_2, but the splittings largely depend on interface disorder [53, 56–58].

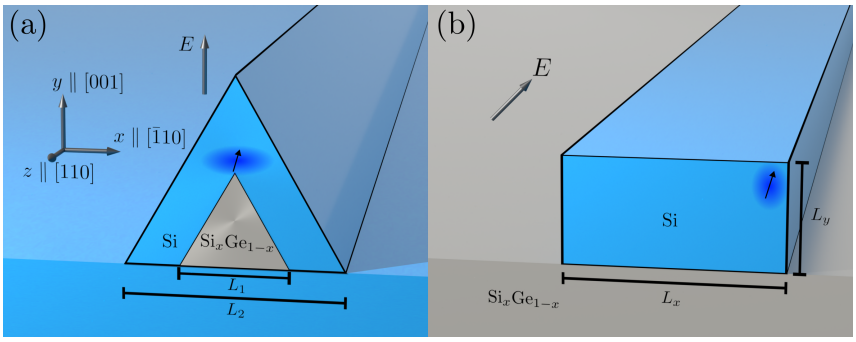

Figure 5.1: Design of valley-free fins in Si/Si_xGe_{1-x} heterostructures. (a) Equilateral triangular fin with inner and outer side lengths L_1 and L_2, respectively. The electron wavefunction is localized above the top of the Si_xGe_{1-x} fin by uniaxial strain and the electric field $\boldsymbol{E}$. The fin is assumed to be grown on a Si substrate, but the results are similar for a Ge substrate. (b) Rectangular Si slab with side lengths L_x and L_y on a Si_xGe_{1-x} substrate. The electrons are confined at the corners of the Si slab by an electric field $\boldsymbol{E}$ in the x-y plane. The blue dots show the position of the QD hosting the spin qubit in the respective figure. We assume infinitely long systems in z direction. The coordinate system in (a) shows the crystallographic growth directions for both geometries.

In this work, we propose alternative Si/SiGe nanostructures that completely lift the valley degeneracy and thus provide ideal platforms for future spin-based quantum processors. In our designs the electrons are confined in quasi one-dimensional Si fins, see Fig. 5.1, where, in contrast to planar heterostructures, the SiGe induces a large *shear* strain. By detailed simulations based on continuum elasticity theory and microscopic $\boldsymbol{k}\cdot\boldsymbol{p}$ theory, we show that our engineered strain profile enables a non-degenerate groundstate split from the excited states by energies $\sim 1\,\mathrm{meV} - 10\,\mathrm{meV}$, two to three orders of magnitude larger than in current devices. Importantly, this energy gap remains large for realistic values of applied electric fields and is independent of atomistic disorder at the interfaces, rendering our design robust in a wide variety of different fins.

5.2 Theoretical model

The conduction band of bulk Si has six degenerate minima in the first Brillouin zone, which are located at a distance $\pm k_0/2\pi = \pm 0.15/a$ from the X points. Here $a = 5.43\,\text{Å}$ is the lattice constant of Si [59]. Its low-energy electronic states are described by the microscopic two-band $\boldsymbol{k}\cdot\boldsymbol{p}$ Hamiltonian [60, 61]

$$H = \frac{\hbar^2}{2m_t}(k_{t_1}^2 + k_{t_2}^2) + \frac{\hbar^2}{2m_l}k_l^2 + \Xi_u\varepsilon_{ll} + e\boldsymbol{E}\cdot\boldsymbol{r} + V(\boldsymbol{r}) + \frac{\hbar^2}{m_l}k_0 k_l \tau_x - \left(\frac{\hbar^2}{M}k_{t_1}k_{t_2} - 2\Xi_{u'}\varepsilon_{t_1 t_2}\right)\tau_z \ , \tag{5.1}$$

where l is the longitudinal direction and t_1 and t_2 are the two transversal directions.

This Hamiltonian is based on a small-momentum expansion of the band structure around the X points and the Pauli matrices τ_i, with $i = x, y, z$, refer to the two valleys in the vicinity to the same X point. Because there are three inequivalent X-points, the six valleys are described by three independent copies of Eq. (5.1). The spin degree of freedom is not included in H. The transversal and longitudinal masses of Si are $m_t = 0.19\,m_e$ and $m_l = 0.91\,m_e$, respectively, with m_e being the free electron mass; $M \approx \left(m_t^{-1} - m_e^{-1}\right)^{-1}$ is the band-coupling mass [60, 62].

Because the lattice constant of Ge is $a_{\mathrm{Ge}} = 5.66\,\text{Å}$ [59], the Si is strained in Si and Ge heterostructures. The uniaxial strain ε_{ll} and the shear strain $\varepsilon_{t_1 t_2}$ modify the electron energy depending on the deformation potentials $\Xi_u = 9\,\mathrm{eV}$ [63, 64] and $\Xi_{u'} = 7\,\mathrm{eV}$ [60, 65], respectively. In the nanostructures sketched in Fig. 5.1, we simulate the elements of the strain tensor $\underline{\boldsymbol{\varepsilon}}$ by finite-element methods (FEM) based on continuum elasticity theory [66–69]. More details on the simulation of the strain in our setups is provided in App. 5.A. We assume that the lattice constant of an alloy of $\mathrm{Si}_x\mathrm{Ge}_{1-x}$ varies linearly from a to a_{Ge}, and thus we use the relation

$$\underline{\boldsymbol{\varepsilon}}_{\mathrm{Si/Si}_x\mathrm{Ge}_{1-x}} = (1-x)\underline{\boldsymbol{\varepsilon}}_{\mathrm{Si/Ge}} \ , \tag{5.2}$$

interpolating linearly from the minimal strain at $1-x=0$ to the maximal strain at $1-x=1$ [70, 71].

Eq. (5.1) also includes the homogeneous electric field $\boldsymbol{E}$ resulting in the electrostatic potential $-e\boldsymbol{E}\cdot\boldsymbol{r}$, with $e > 0$ being the electron charge and $\boldsymbol{r} = (x, y, z)$, and the confinement potential $V(\boldsymbol{r})$ accounting for the cross section of the fin. We model the sharp interface between Si and a $\mathrm{Si}_x\mathrm{Ge}_{1-x}$ alloy by using the step-like potential function

$$V(\boldsymbol{r}) = \begin{cases} 0 & \text{for } \boldsymbol{r} \in R_{\mathrm{Si}}, \\ (1-x)\,500\,\mathrm{meV} & \text{for } \boldsymbol{r} \in R_{\mathrm{SiGe}}, \end{cases} \ , \tag{5.3}$$

where R_{Si} (R_{SiGe}) indicates the region in the cross section occupied by Si (SiGe). In analogy to Eq. (5.2), we also assume that $V(\boldsymbol{r})$ decreases linearly from the maximal value of 500 meV (the band gap difference between Si and Ge) as the concentration of Si x in the alloy increases.

Because Si has an anisotropic dispersion relation, we emphasize that electrons lying in the three different pairs of valley states generally experience a different confinement potential. To account for this effect, we fix the z direction to be aligned to the fin and the y direction to be perpendicular to the substrate, see Fig. 5.1. We also restrict ourselves to the analysis of Si [001], with fins that are aligned to the [110] crystallographic axis, i.e. $y \parallel [001]$ and $z \parallel [110]$. This is the standard orientation of current devices [1, 2, 4, 72].

5.3 Shear-strain-induced lifting of the valley degeneracy

The Hamiltonian H in Eq. (5.1) allows us to accurately analyze the physics of the conduction band electrons in the fins shown in Fig. 5.1. We discretize H in real space for different cross sections with lattice spacings a_x, a_y and we find the dispersion relation of the lowest energy states. Importantly, we include the inhomogeneous strain tensor $\underline{\boldsymbol{\varepsilon}}$ simulated by FEM with COMSOL Multiphysics® [73], see the App. 5.A for more details.

The effect of uniaxial and shear strain in our fins is illustrated in Fig. 5.2(a), where we show the projection of the three-dimensional (3D) bulk valleys in Si onto the one-dimensional (1D) Brillouin zone (BZ) along $z \parallel [110]$, see Fig. 5.1. Along z, the four bulk Si valleys belonging to the xz-plane (purple ellipses) are projected onto $\pm\sqrt{2}k_0$ close to the X points and the two valleys along the $y \parallel [001]$ axis (turquoise circles) are projected onto the Γ point ($k_z = 0$). When $\underline{\boldsymbol{\varepsilon}} = 0$ (dashed gray lines) all the valleys are close in energy up to a small contribution caused by the anisotropic confinement. In analogy to planar heterostructures [61, 63, 69, 74] at finite values $\underline{\boldsymbol{\varepsilon}}$ (blue solid lines) uniaxial strain lifts the degeneracy of the valleys at the X points by several tens of meV.

However, the inherent shear strain in our fin devices results in the lifting of the remaining two valleys. A zoom into the dispersion relation in the vicinity of the Γ point, highlighting the shear-strain-induced valley splitting Δ is shown in Fig. 5.2(b). We focus here on the triangular fin sketched in Fig. 5.1(a), however, the results discussed are valid also for rectangular fins. We note that without Ge $\varepsilon_{xy} = 0$ and the lowest two energy states (dashed gray line) are degenerate [56, 75], see Eq. (5.1). The $\mathrm{Si}_x\mathrm{Ge}_{1-x}$ induces a finite ε_{xy} in the Si shell which lifts the valley degeneracy. More details on the simulated strain profile in our fins are provided in Fig. 5.3 and in App. 5.A. Considering a moderate Ge concentration of $1 - x = 0.3$, we estimate the valley splitting $\Delta = 0.65\,\mathrm{meV}$ for $E_y = 1\,\mathrm{V\,\mu m^{-1}}$ pointing along [001], significantly larger than what is obtained in planar heterostructures [38–45]. By increasing the Ge amount to $1 - x = 0.5$ the shear strain ε_{xy} increases [see Eq. (5.2)] and consequently a larger value of $\Delta = 2.35\,\mathrm{meV}$ is reached.

Because the electron is localized at the top of the Si fin, the substrate does not affect the values of Δ. We also emphasize that in striking contrast to the valley splitting arising in planar heterostructures, our Δ arises from shear strain and therefore is reproducible and robust against atomistic disorder at the Si/SiGe interfaces [36, 76]. We confirm this robustness with additional simulations shown in App. 5.B.

5.4 Electric-field-dependence of valley splitting

In planar Si/SiGe structures, the valley splitting Δ strongly depends on the applied electric field E. We show that in our fins, Δ can also be tuned in-situ by E, however at large enough concentrations of Ge in the $\mathrm{Si}_x\mathrm{Ge}_{1-x}$ alloy, Δ remains large and in the meV range.

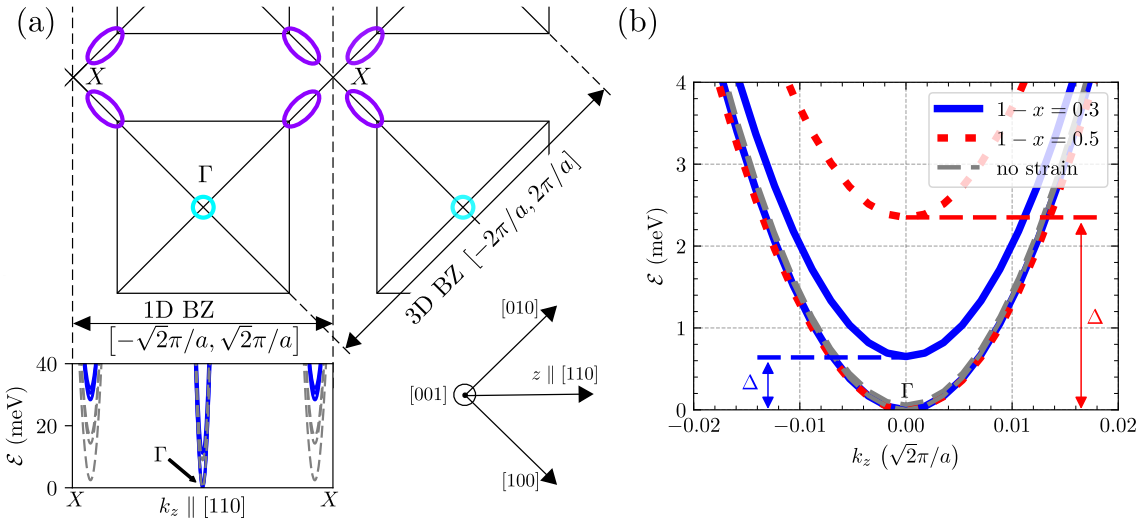

Figure 5.2: Band dispersion of electrons confined in our strained Si fins. (a) Projection of the six valleys of the 3D Brillouin zone (BZ) of bulk Si onto the 1D BZ with momentum $k_z \parallel [110]$. The purple ellipses indicate the four valleys in the xz-plane, while the turquoise circles indicate the two valleys near the X points in the out-of-plane direction y. At the bottom, we show the dispersion relation $\varepsilon(k_z)$ of the triangular Si fin sketched in Fig. 5.1(a). Without strain (dashed gray lines) all the six valleys in the fin are close in energy. Including a moderate strain induced by a Si_xGe_{1-x} alloy with $x = 0.7$ (solid blue lines), we observe that (i) uniaxial strain ε_{ll} pushes the four valleys in the xz-plane (purple ellipses) several tens of meV away and (ii) shear strain $\varepsilon_{t_1t_2}$ induces a gap in the remaining two valleys in the y direction (turquoise circles). (b) Zoom into the dispersion relation around the 1D Γ point at $k_z = 0$. When $\varepsilon_{t_1t_2} = 0$, the two valleys are quasi-degenerate. The degeneracy is lifted by the shear strain induced by the Si_xGe_{1-x}. The resulting energy gap (i.e. valley splitting) $\Delta \sim 1\,\text{meV}$ increases with decreasing concentration of Si x, as shown by the blue and red lines obtained for $x = 0.7$ and $x = 0.5$, respectively. The dispersion relation is qualitatively similar for the strained Si fin in Fig. 5.1(b). In the simulation we used $L_1 = 9.5\,\text{nm}$, $L_2 = 19\,\text{nm}$, $E_y = 1\,\text{V}\,\mu\text{m}^{-1}$ (pointing along [001]), $a_x = 0.32\,\text{nm}$, and $a_y = 0.28\,\text{nm}$.

The dependence of Δ on E and $1-x$ is analyzed in Fig. 5.3(a,e). In the triangular fin sketched in Fig. 5.1(a) a positive electric field E tends to decrease Δ. This trend can be understood by observing that E shifts the electron wavefunction towards the upper tip of the Si shell [see Fig. 5.3(b-d)], where shear strain decreases, see Fig. 5.3(j). A detailed explanation of the FEM simulation is provided in App. 5.A. In contrast, as the concentration of Ge increases, the strain also increases, resulting in $\Delta \gtrsim 15\,\text{meV}$ for a wide range of E.

We emphasize that because Δ depends on shear strain our results are robust against variations in the shape of the cross section. This robustness is verified in App. 5.C, where we simulate a rounded fin in a half-circular cross section, and we find similar values of Δ.

Large values of Δ also emerge for a wide range of parameters in the rectangular Si fins on a SiGe substrate sketched in Fig. 5.1(b). Similar Si nanostructures of comparable size are current state-of-the-art for spin qubits [4, 72, 79, 80] and can be adapted to our proposal by replacing the oxide substrate by SiGe. In this device, we observe in Fig. 5.3(e-i) a non-trivial interplay of $1-x$ and E, that we relate to the position of the wavefunction in the cross section. Note that in this case, we study the effect of an electric field E pushing the electron wavefunction toward the

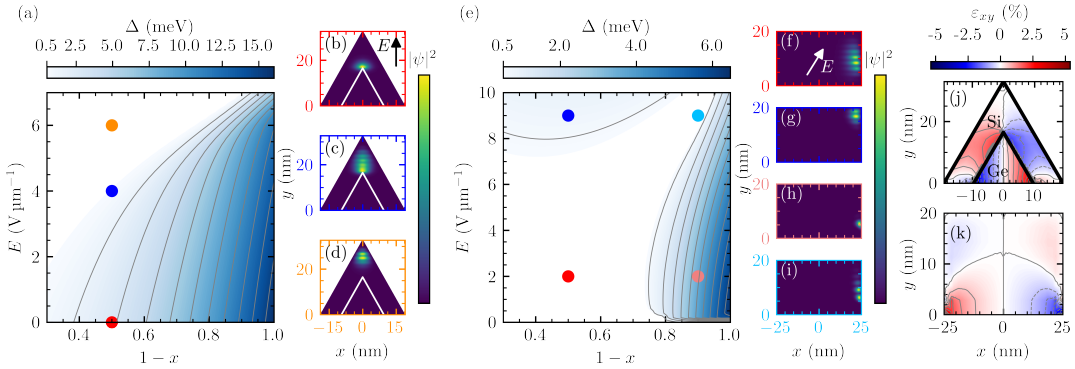

Figure 5.3: Valley splitting Δ in our Si/Si$_x$Ge$_{1-x}$ fins. (a) Δ against the Ge concentration $1-x$ and electric field E (applied along the y direction) in the triangular fin sketched in Fig. 5.1(a). For a wide range of experimentally relevant parameters $\Delta \gtrsim 0.5\,\text{meV}$, substantially larger than in planar heterostructures; Δ is maximized when shear strain increases, i.e. at $1-x=1$, and at small values of E. (b-d) Probability densities $|\psi|^2$ of the electron wavefunction at $1-x=0.5$ for (b) $E=0$, (c) $E=4\,\text{V}\,\mu\text{m}^{-1}$, and (d) $E=6\,\text{V}\,\mu\text{m}^{-1}$. These parameters are marked in (a). The inhogomeneous uniaxial strain localizes the electron at the top of the fin. At $E=0$ the electron lies at the Si/SiGe interface, where shear strain is maximal, and resulting in the largest Δ. Increasing the electric field the electron is pushed towards the tip of the Si shell, where shear strain is weaker and Δ decreases. In the simulation we used $L_1=9.5\,\text{nm}$ and $L_2=19\,\text{nm}$, as in Fig. 5.2. (e) Δ, and (f-i) $|\psi|^2$ in the rectangular fin sketched in Fig. 5.1(b). Note the different directions of E in the two setups indicated by the arrows in panels (b) and (f). Here shear strain is larger at the left and right sides of the cross section. At $1-x<0.75$ and for small E the electron is localized at the bottom of the cross section (not shown). (f) At $1-x=0.5$ and $E=2\,\text{V}\,\mu\text{m}^{-1}$, the electron is weakly localized at the right of the fin, resulting in $\Delta<0.5\,\text{meV}$. (g) At $1-x=0.5$ and $E=9\,\text{V}\,\mu\text{m}^{-1}$, the electron is pushed towards the upper-right corner of the fin, where shear strain is larger and the valley splitting increases to $\Delta>0.5\,\text{meV}$. (h) At $1-x=0.9$ and $E=2\,\text{V}\,\mu\text{m}^{-1}$, the larger concentration of Ge enhances locally the strain at the bottom corner of the rectangle where the electron is localized causing large Δ. However, in this case the necessary level of control of the position the QD is challenging to reach and the electron risks to leak into the substrate. (i) At $1-x=0.9$ and $E=9\,\text{V}\,\mu\text{m}^{-1}$, the large values of E in a strongly strained device cause the electron wavefunction to spread out across the side. Then the situation is similar to panel (f) and $\Delta<0.5\,\text{meV}$. We used $L_x=50\,\text{nm}$, $L_y=20\,\text{nm}$, $a_x=0.28\,\text{nm}$, and $a_y=0.34\,\text{nm}$. (j,k) Shear strain ε_{xy} simulated with the FEM for the two devices for pure Ge instead of SiGe. The other shear strain components are zero for an infinitely long system in z direction. (j) ε_{xy} is large above the tip of the inner Ge fin and becomes weaker towards the tip of the Si shell. (k) Large ε_{xy} is found close to the interfaces at the bottom of the Si slab. We used $a_{\text{Si}}=5.43\,\text{Å}$, $a_{\text{Ge}}=5.652\,\text{Å}$ [59], $C_{11}^{\text{Si}}=168\,\text{GPa}$, $C_{12}^{\text{Si}}=65.0\,\text{GPa}$, $C_{44}^{\text{Si}}=80.4\,\text{GPa}$ [77], $C_{11}^{\text{Ge}}=131\,\text{GPa}$, $C_{12}^{\text{Ge}}=49.2\,\text{GPa}$, and $C_{44}^{\text{Ge}}=68.2\,\text{GPa}$ [78].

upper right corner of the fin; because of symmetry the results are equivalent if the electric field pushes the electron towards the upper left corner. In particular, ε_{xy} is maximal at the left and right bottom sides of the fin, see Fig. 5.3(k), and thus Δ is large when the electron is localized close to these areas. We should emphasize, however, that when it is too close to the interface the electron risks to leak into the substrate. The QD is also easier to electrostatically control when it

is localized at one of the upper corners.

For low concentrations of Ge ($1 - x \lesssim 0.7$) electrons are localized at the upper corner of the cross section by a strong field E, and thus Δ increases with increasing E. For weak electric fields the wavefunction is spread over the right side and Δ is small because ε_{xy} averages to zero over the extension of the wavefunction. At larger values of $1 - x \gtrsim 0.7$, the inhomogeneous uniaxial strain localizes the electrons close to the edges already at small fields E, thus resulting in large values of Δ. In this case, Δ is only weakly dependent on E, and it decreases with increasing E because the electrons are pushed away from the substrate where strain is maximal and the shear strain is averaged out over the extension of the wavefunction.

The large valley splitting due to shear strain has important consequences for spin qubits realized in gate-defined QDs in Si fins. The spin qubit lifetime in planar Si/SiGe heterostructures is strongly limited at spin-valley relaxation hot spots where the qubit Zeeman and valley splittings become comparable [41, 49, 50, 56, 81]. These hot spots are naturally avoided in our devices because of the large difference between the typically small qubit Zeeman splitting of $\sim 10\,\mu\text{eV}$ and the valley splitting of $\sim 1\,\text{meV} - 10\,\text{meV}$ we predict.

5.5 Conclusion

In this work we show that shear strain substantially enhances the valley splitting in Si/SiGe heterostructures. In realistic Si fins we predict valley splitting gaps $\sim 1\,\text{meV} - 10\,\text{meV}$, orders of magnitude larger than in current devices. We show that the amplitude of the gap can be engineered by varying the composition of the $\text{Si}_x\text{Ge}_{1-x}$ alloy and is controllable in-situ by electric fields. Importantly, due to the large valley splitting spin-valley relaxation hot spots, which are a problem for spin qubits in planar Si/SiGe heterostructures, are avoided naturally in our proposed Si fins. Our designs are also robust against variations of the fin shape and, in contrast to planar systems, are not affected by atomistic disorder. By removing a critical issue of current electron spin qubits in Si, our devices will push these architectures towards new coherence standards and pave the way towards large-scale semiconductor-based quantum processors.

Acknowledgments. We thank Dominik Zumbühl for giving access to the license for COMSOL Multiphysics® and Andreas V. Kuhlmann for useful comments. This work is supported by the Swiss National Science Foundation (SNSF) and NCCR SPIN (Grant No. 51NF40-180604).

5.A Pseudomorphic strain

We consider strained Si/SiGe devices. Because of the mismatch of lattice constant between the materials, a force develops at their interfaces, resulting in a displacement field $\boldsymbol{u}(\boldsymbol{r})$ for the atoms. Consequently, in equilibrium the lattice constants of the two materials match at the interface; this is referred to as the pseudomorphic condition.

In linear elasticity theory [68] the change of lengths in a deformed body is given by the strain tensor

$$\varepsilon_{ij} = \frac{1}{2}\left(\frac{\partial u_i}{\partial x_j} + \frac{\partial u_j}{\partial x_i}\right) . \tag{5.4}$$

The strain tensor elements ε_{ij} are related to the stress tensor elements σ_{ij} by the material-dependent elastic stiffness tensor C_{ijkl}:

$$\sigma_{ij} = C_{ijkl}\varepsilon_{kl} , \tag{5.5}$$

implying Einstein summation. In the presence of a force f_j that deforms the body, the stress tensor satisfies the equilibrium condition

$$\frac{\partial \sigma_{ij}}{\partial x_i} = -f_j \ . \tag{5.6}$$

Therefore, we calculate ε_{ij} in the presence of a given force f_j^0 by solving the partial differential equation

$$\frac{\partial [C_{ijkl}\varepsilon_{kl}]}{\partial x_i} = -f_j^0 \ . \tag{5.7}$$

Our system comprising two materials with different lattice constants $a_i(\boldsymbol{r})$ and two different elastic stiffness tensors $C_{ijkl}(\boldsymbol{r})$ can be simulated by linear elasticity theory by introducing the equivalent body force [82]

$$f_i^0 = \frac{\partial}{\partial x_j}\left[C_{ijkl}(\boldsymbol{r})\varepsilon_{kl}^0(\boldsymbol{r})\right] \ , \tag{5.8}$$

where the strain from the lattice constant mismatch is given by

$$\varepsilon_{kk}^0(\boldsymbol{r}) = \frac{a_k^{(\mathrm{ref})} - a_k(\boldsymbol{r})}{a_k(\boldsymbol{r})} \ . \tag{5.9}$$

Here, $a_k^{(\mathrm{ref})}$ is a reference lattice constant that can be chosen to be the lattice constant of one of the two materials without loss of generality. The elastic stiffness tensor in Eq. (5.8) for crystals with cubic symmetry can be written as [67, 82]

$$\underline{\boldsymbol{C}} = \begin{pmatrix} C_{11} & C_{12} & C_{12} & 0 & 0 & 0 \\ C_{12} & C_{11} & C_{12} & 0 & 0 & 0 \\ C_{12} & C_{12} & C_{11} & 0 & 0 & 0 \\ 0 & 0 & 0 & C_{44} & 0 & 0 \\ 0 & 0 & 0 & 0 & C_{44} & 0 \\ 0 & 0 & 0 & 0 & 0 & C_{44} \end{pmatrix} \ , \tag{5.10}$$

where we use the Voigt notation. For our simulations the tensor is rotated such that it agrees with the [110] growth direction of the fin considered in our system. For the finite-element method (FEM) simulations we assume free boundary conditions at the outer boundaries of the devices.

To calculate the effect of strain due to lattice mismatch, we simulate the strain tensor elements ε_{ij} in our devices by solving the differential equation in Eq. (5.8) numerically. In particular, we use the FEM implemented in COMSOL Multiphysics® [73]. For the lifting of the valley degeneracy, we pay particular attention to the shear strain component ε_{xy} which is the main source of the large valley gap Δ in our fins.

In the main text, we show the simulated strain tensor component ε_{xy} in the cross sections of the two devices analyzed in the main text. The finite value of shear strain above the tip of the inner Ge fin and at the sides and the upper corners of the Si slab explain the large values for Δ shown in the main text.

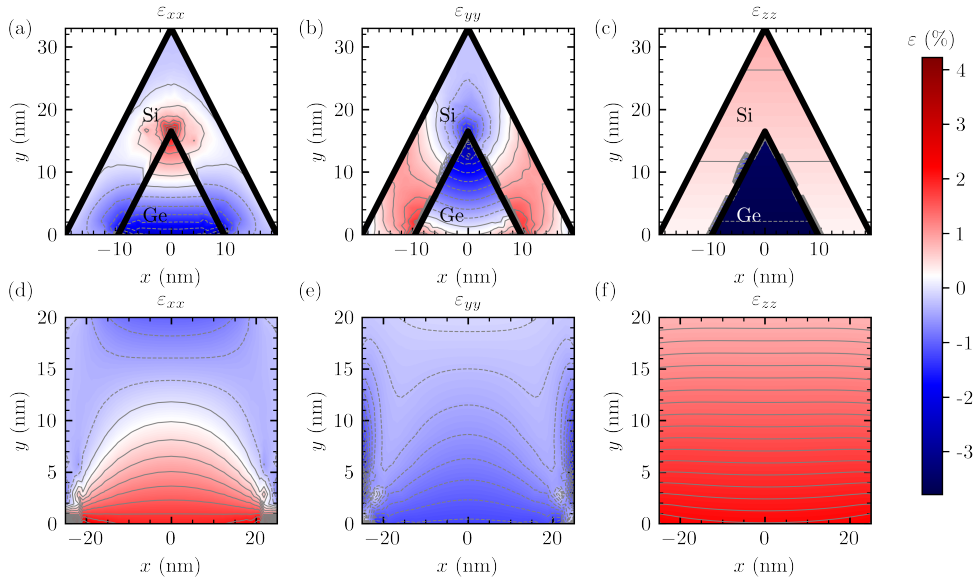

Figure 5.4: Uniaxial strain ε_{xx}, ε_{yy}, and ε_{zz} simulated with the FEM in the devices analyzed in the main text. Here we consider pure Ge; in Si_xGe_{1-x} alloys $\varepsilon_{xy} \to (1-x)\varepsilon_{xy}$ is rescaled linearly by the concentration of Ge. (a-c) Triangular fin. ε_{xx} and ε_{yy} counteract each other above the tip of the Ge fin because they have opposite sign. However, the electron wavefunction is localized above the tip of the Ge fin since $|\varepsilon_{yy}| > |\varepsilon_{xx}|$ and $\varepsilon_{yy} < 0$. (d-f) Rectangular fin. Both, ε_{xx} and ε_{yy}, have negative sign at the left and right sides of the Si slab. Thus, the wavefunction is localized at these sides. Note that the deviation from perfect symmetry in the plots comes from numerical inaccuracies. We used $a_{\mathrm{Si}} = 5.43\,\text{Å}$, $a_{\mathrm{Ge}} = 5.652\,\text{Å}$ [59], $C_{11}^{\mathrm{Si}} = 168\,\mathrm{GPa}$, $C_{12}^{\mathrm{Si}} = 65.0\,\mathrm{GPa}$, $C_{44}^{\mathrm{Si}} = 80.4\,\mathrm{GPa}$ [77], $C_{11}^{\mathrm{Ge}} = 131\,\mathrm{GPa}$, $C_{12}^{\mathrm{Ge}} = 49.2\,\mathrm{GPa}$, and $C_{44}^{\mathrm{Ge}} = 68.2\,\mathrm{GPa}$ [78].

In Fig. 5.4 we show the uniaxial strain components ε_{xx}, ε_{yy}, and ε_{zz} for both devices. In the triangular fin the components ε_{xx} and ε_{yy} have opposite sign at the region of interest above the tip of the Ge fin [see Fig. 5.4(a,b)]. Since $|\varepsilon_{yy}| > |\varepsilon_{xx}|$ and ε_{yy} has negative sign the electron wavefunction is localized above the tip of the Ge fin. The components ε_{xx} and ε_{yy} are both negative at the left and right side of the Si slab, localizing the wavefunction there [see Fig. 5.4(d,e)]. The ε_{zz} component is irrelevant for the localization of the electron [see Fig. 5.4(c,f)].

5.B Atomistic disorder at the Si/SiGe interfaces

In the main text, we analyze triangular and rectangular Si/SiGe fin structures and we argue that in contrast to planar heterostructures, in our fins atomistic disorder does not affect the valley splitting Δ. Here we show the results of a simulation including atomic steps at the interfaces of the two materials, as shown in Fig. 5.5(a). This disorder is known to strongly affect the planar structures [46–52] however we find that, as expected, it does not affect our fins.

In particular, we diagonalize the Hamiltonian in the main text discretized on the lattice shown in Fig. 5.5(a) with values of strain simulated in the triangular fin device without interface steps. The results are shown in Fig. 5.5(b) and comparing with the results in the main text we observe perfect agreement, thus corroborating our claim. This result can be understood because in contrast to planar heterostructures, the electron is localized away from the interface steps as discussed in the

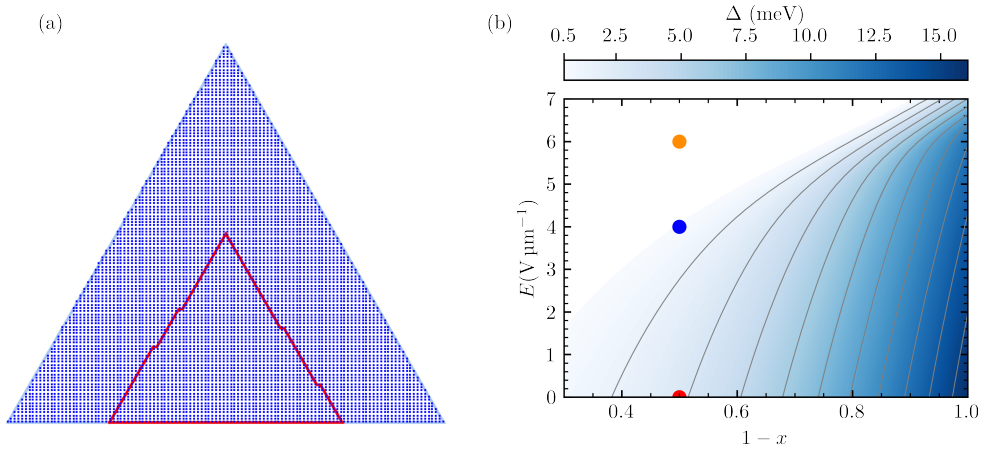

Figure 5.5: Atomistic disorder in our Si/SiGe fins. (a) Plot of the cross section of the triangular fin shown in Fig. 5.1(a) including disorder at the Si/SiGe interfaces. The blue dots depict the discrete lattice points used for the numerical diagonalization of the Hamiltonian in the main text and the red lines mark the interface between the inner SiGe fin and the outer Si shell including atomic size steps at random positions. (b) Valley splitting Δ plotted against the Ge concentration $1-x$ and electric field E (pointing along y direction) in the triangular fin. The result is exactly the same as for the triangular fin without interface steps. This is not surprising since the electron wavefunction is located far away from the interface steps.

main text. Moreover, the large valley splitting remains upon smoothening the interface between the Ge fin and the Si shell as we will discuss in the following section.

5.C Semicylindrical Si/SiGe device

In the main text we argue that Si/SiGe fins with different shapes have a similar valley splitting Δ and thus our results are largely independent of the fin shape. We support these claims here by simulating a semicircular fin, see Fig. 5.6. This fin comprises a Ge semicircle on top of a Si substrate with a Si outer shell, where the electron is localized. This fin resembles the triangular fin discussed in the main text [see Fig. 5.1(a)] if the triangle has a round tip.

Following the same procedure as before, we simulate first the strain tensor. In Figs. 5.6(a-d) we show the uniaxial and shear strain components. We observe a qualitatively similar trend as in the triangular fin, see main text.

The local shear strain explains the trend of the valley splitting Δ simulated in Fig. 5.6(f). At small concentration of Ge, with $1-x \lesssim 0.6$, the valley splitting decreases with increasing E. At higher values of $1-x$, where strain is larger, we observe a more interesting dependence of Δ on E. This dependence can be understood by looking at the localization of the electron at $1-x=0.8$ for different values of E, see Fig. 5.6(g-h). At $E=0$, the wavefunction is localized at one of the lower corners of the fin, where ε_{xy} is finite, thus resulting in a significant value of Δ. As the electric field increases, the electron is pushed towards the tip of the fin, and in particular at $E=4\,\mathrm{V\,\mu m^{-1}}$, the electron is localized at the bottom of the tip, where ε_{xy} is the largest, and thus resulting in a large value of Δ. As E is further increased the electron moves toward the topmost part of the fin, and Δ decreases due to the weaker shear strain [see Fig. 5.6(d)]. This trend is consistent with the

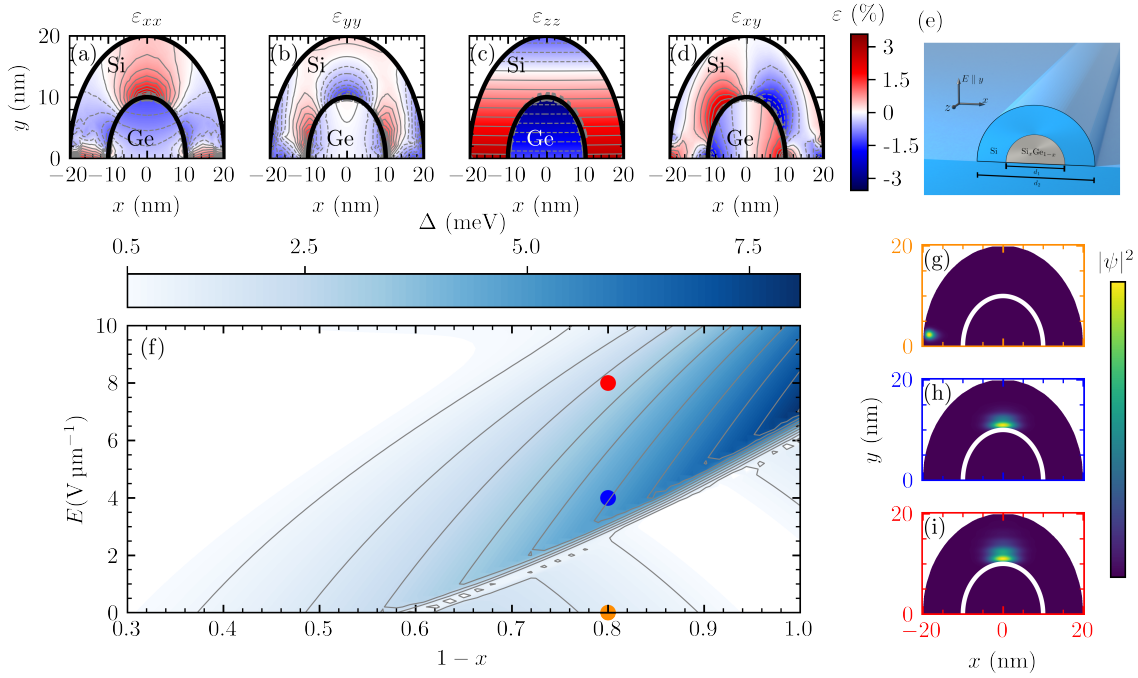

Figure 5.6: Simulation of a semicircular Si/SiGe fin. Uniaxial (a-c) and shear (d) strain components of the strain tensor simulated with the FEM. Large shear strain appears at the interface between Si and SiGe and decreases towards the surface. The material parameters are the same as in Fig. 5.4. (e) Sketch of the semicircular fin with inner diameter d_1 and outer diameter d_2. The electric field E points along the y direction. (f) Valley splitting Δ against the Ge concentration $1-x$ and the electric field E. (g-i) Probability densities $|\psi|^2$ of the electrons at $1-x=0.8$ and (g) $E=0$, (h) $E=4\,\mathrm{V\,\mu m^{-1}}$, and (i) $E=8\,\mathrm{V\,\mu m^{-1}}$. These points are marked in (f). In analogy to the triangular fin analyzed in the main text, we obtain $\Delta>0.5\,\mathrm{meV}$ for a wide experimentally-relevant range of parameters. This result proves that the sharp tip of the fin shown in Fig. 5.1(a) is not required to enable a large valley splitting. (g) Interestingly, for a large Ge concentration ($1-x\gtrsim 0.6$) and strong strain, the electron is localized at the bottom of the device, close to the surface. This effect is caused by the uniaxial strain as shown in (a,b). (h, i) An electric field E pushes the electron to the top of the device. Note that for smaller Ge concentration $1-x$, the electron is localized at the top even at $E=0$; this also occurs for triangular fins. We used $d_1=20\,\mathrm{nm}$, $d_2=40\,\mathrm{nm}$, $a_x=0.34\,\mathrm{nm}$, and $a_y=0.17\,\mathrm{nm}$. We chose the size of the system such that the Si and Si/Ge parts of the cross section cover the same areas as their counterparts in the triangular fin device in the main text.

simulation of the triangular fin discussed in the main text. Consequently, we conclude that large values of Δ in Si/SiGe fins can be reached independently of the sharpness of the tip of the fin.

References

[1] S. Geyer, B. Hetényi, S. Bosco, L. C. Camenzind, R. S. Eggli, A. Fuhrer, D. Loss, R. J. Warburton, D. M. Zumbühl, and A. V. Kuhlmann, "Two-qubit logic with anisotropic exchange in a fin field-effect transistor", (2022), arXiv:2212.02308 [cond-mat.mes-hall].

[2] L. C. Camenzind, S. Geyer, A. Fuhrer, R. J. Warburton, D. M. Zumbühl, and A. V. Kuhlmann, "A hole spin qubit in a fin field-effect transistor above 4 kelvin", Nat. Electron. **5**, 178 (2022).

[3] N. W. Hendrickx, W. I. L. Lawrie, M. Russ, F. van Riggelen, S. L. de Snoo, R. N. Schouten, A. Sammak, G. Scappucci, and M. Veldhorst, "A four-qubit germanium quantum processor", Nature **591**, 580 (2021).

[4] N. Piot, B. Brun, V. Schmitt, S. Zihlmann, V. P. Michal, A. Apra, J. C. Abadillo-Uriel, X. Jehl, B. Bertrand, H. Niebojewski, L. Hutin, M. Vinet, M. Urdampilleta, T. Meunier, Y.-M. Niquet, R. Maurand, and S. D. Franceschi, "A single hole spin with enhanced coherence in natural silicon", Nat. Nanotechnol. **17**, 1072 (2022).

[5] D. Jirovec, A. Hofmann, A. Ballabio, P. M. Mutter, G. Tavani, M. Botifoll, A. Crippa, J. Kukucka, O. Sagi, F. Martins, J. Saez-Mollejo, I. Prieto, M. Borovkov, J. Arbiol, D. Chrastina, G. Isella, and G. Katsaros, "A singlet-triplet hole spin qubit in planar Ge", Nat. Mater. **20**, 1106 (2021).

[6] D. Jirovec, P. M. Mutter, A. Hofmann, A. Crippa, M. Rychetsky, D. L. Craig, J. Kukucka, F. Martins, A. Ballabio, N. Ares, D. Chrastina, G. Isella, G. Burkard, and G. Katsaros, "Dynamics of hole singlet-triplet qubits with large g-factor differences", Phys. Rev. Lett. **128**, 126803 (2022).

[7] M. T. Mądzik, S. Asaad, A. Youssry, B. Joecker, K. M. Rudinger, E. Nielsen, K. C. Young, T. J. Proctor, A. D. Baczewski, A. Laucht, V. Schmitt, F. E. Hudson, K. M. Itoh, A. M. Jakob, B. C. Johnson, D. N. Jamieson, A. S. Dzurak, C. Ferrie, R. Blume-Kohout, and A. Morello, "Precision tomography of a three-qubit donor quantum processor in silicon", Nature **601**, 348 (2022).

[8] L. Petit, M. Russ, G. H. G. J. Eenink, W. I. L. Lawrie, J. S. Clarke, L. M. K. Vandersypen, and M. Veldhorst, "Design and integration of single-qubit rotations and two-qubit gates in silicon above one Kelvin", Commun. Mater. **3**, 82 (2022).

[9] S. G. J. Philips, M. T. Mądzik, S. V. Amitonov, S. L. de Snoo, M. Russ, N. Kalhor, C. Volk, W. I. L. Lawrie, D. Brousse, L. Tryputen, B. P. Wuetz, A. Sammak, M. Veldhorst, G. Scappucci, and L. M. K. Vandersypen, "Universal control of a six-qubit quantum processor in silicon", Nature **609**, 919 (2022).

[10] F. K. Unseld, M. Meyer, M. T. Mądzik, F. Borsoi, S. L. de Snoo, S. V. Amitonov, A. Sammak, G. Scappucci, M. Veldhorst, and L. M. K. Vandersypen, "A 2d quantum dot array in planar ^{28}Si/SiGe", (2023), arXiv:2305.19681 [cond-mat.mes-hall].

[11] A. O. Denisov, S. W. Oh, G. Fuchs, A. R. Mills, P. Chen, C. R. Anderson, M. F. Gyure, A. W. Barnard, and J. R. Petta, "Microwave-frequency scanning gate microscopy of a Si/SiGe double quantum dot", Nano Lett. **22**, 4807 (2022).

[12] K. Takeda, A. Noiri, J. Yoneda, T. Nakajima, and S. Tarucha, "Resonantly driven singlet-triplet spin qubit in silicon", Phys. Rev. Lett. **124**, 117701 (2020).

[13] X. Xue, M. Russ, N. Samkharadze, B. Undseth, A. Sammak, G. Scappucci, and L. M. K. Vandersypen, "Quantum logic with spin qubits crossing the surface code threshold", Nature **601**, 343 (2022).

[14] K. M. Itoh and H. Watanabe, "Isotope engineering of silicon and diamond for quantum computing and sensing applications", MRS Commun. **4**, 143 (2014).

[15] M. Veldhorst, J. C. C. Hwang, C. H. Yang, A. W. Leenstra, B. de Ronde, J. P. Dehollain, J. T. Muhonen, F. E. Hudson, K. M. Itoh, A. Morello, and A. S. Dzurak, "An addressable quantum dot qubit with fault-tolerant control-fidelity", Nat. Nanotechnol. **9**, 981 (2014).

[16] K. Takeda, J. Kamioka, T. Otsuka, J. Yoneda, T. Nakajima, M. R. Delbecq, S. Amaha, G. Allison, T. Kodera, S. Oda, and S. Tarucha, "A fault-tolerant addressable spin qubit in a natural silicon quantum dot", Sci. Adv. **2**, e1600694 (2016).

[17] J. Yoneda, K. Takeda, T. Otsuka, T. Nakajima, M. R. Delbecq, G. Allison, T. Honda, T. Kodera, S. Oda, Y. Hoshi, N. Usami, K. M. Itoh, and S. Tarucha, "A quantum-dot spin qubit with coherence limited by charge noise and fidelity higher than 99.9%", Nat. Nanotechnol. **13**, 102 (2018).

[18] M. Veldhorst, C. H. Yang, J. C. C. Hwang, W. Huang, J. P. Dehollain, J. T. Muhonen, S. Simmons, A. Laucht, F. E. Hudson, K. M. Itoh, A. Morello, and A. S. Dzurak, "A two-qubit logic gate in silicon", Nature **526**, 410 (2015).

[19] D. M. Zajac, T. M. Hazard, X. Mi, E. Nielsen, and J. R. Petta, "Scalable gate architecture for a one-dimensional array of semiconductor spin qubits", Phys. Rev. Appl. **6**, 054013 (2016).

[20] T. F. Watson, S. G. J. Philips, E. Kawakami, D. R. Ward, P. Scarlino, M. Veldhorst, D. E. Savage, M. G. Lagally, M. Friesen, S. N. Coppersmith, M. A. Eriksson, and L. M. K. Vandersypen, "A programmable two-qubit quantum processor in silicon", Nature **555**, 633 (2018).

[21] W. Huang, C. H. Yang, K. W. Chan, T. Tanttu, B. Hensen, R. C. C. Leon, M. A. Fogarty, J. C. C. Hwang, F. E. Hudson, K. M. Itoh, A. Morello, A. Laucht, and A. S. Dzurak, "Fidelity benchmarks for two-qubit gates in silicon", Nature **569**, 532 (2019).

[22] X. Xue, T. Watson, J. Helsen, D. Ward, D. Savage, M. Lagally, S. Coppersmith, M. Eriksson, S. Wehner, and L. Vandersypen, "Benchmarking gate fidelities in a Si/SiGe two-qubit device", Phys. Rev. X **9**, 021011 (2019).

[23] A. Sigillito, J. Loy, D. Zajac, M. Gullans, L. Edge, and J. Petta, "Site-selective quantum control in an isotopically enriched $^{28}Si/Si_{0.7}Ge_{0.3}$ quadruple quantum dot", Phys. Rev. Appl. **11**, 061006(R) (2019).

[24] X. Mi, M. Benito, S. Putz, D. M. Zajac, J. M. Taylor, G. Burkard, and J. R. Petta, "A coherent spin-photon interface in silicon", Nature **555**, 599 (2018).

[25] N. Samkharadze, G. Zheng, N. Kalhor, D. Brousse, A. Sammak, U. C. Mendes, A. Blais, G. Scappucci, and L. M. K. Vandersypen, "Strong spin-photon coupling in silicon", Science **359**, 1123 (2018).

[26] T. Bonsen, P. Harvey-Collard, M. Russ, J. Dijkema, A. Sammak, G. Scappucci, and L. M. K. Vandersypen, "Probing the Jaynes-Cummings ladder with spin circuit quantum electrodynamics", Phys. Rev. Lett. **130**, 137001 (2023).

[27] R. Li, L. Petit, D. P. Franke, J. P. Dehollain, J. Helsen, M. Steudtner, N. K. Thomas, Z. R. Yoscovits, K. J. Singh, S. Wehner, L. M. K. Vandersypen, J. S. Clarke, and M. Veldhorst, "A crossbar network for silicon quantum dot qubits", Sci. Adv. **4**, eaar3960 (2018).

[28] A. R. Mills, D. M. Zajac, M. J. Gullans, F. J. Schupp, T. M. Hazard, and J. R. Petta, "Shuttling a single charge across a one-dimensional array of silicon quantum dots", Nat. Commun. **10**, 1063 (2019).

[29] A. Noiri, K. Takeda, T. Nakajima, T. Kobayashi, A. Sammak, G. Scappucci, and S. Tarucha, "A shuttling-based two-qubit logic gate for linking distant silicon quantum processors", Nat. Commun. **13**, 5740 (2022).

[30] I. Seidler, T. Struck, R. Xue, N. Focke, S. Trellenkamp, H. Bluhm, and L. R. Schreiber, "Conveyor-mode single-electron shuttling in Si/SiGe for a scalable quantum computing architecture", npj Quantum Inf. **8**, 10.1038/s41534-022-00615-2 (2022).

[31] K. Takeda, A. Noiri, T. Nakajima, J. Yoneda, T. Kobayashi, and S. Tarucha, "Quantum tomography of an entangled three-qubit state in silicon", Nat. Nanotechnol. **16**, 965 (2021).

[32] A. Mills, C. Guinn, M. Feldman, A. Sigillito, M. Gullans, M. Rakher, J. Kerckhoff, C. Jackson, and J. Petta, "High-fidelity state preparation, quantum control, and readout of an isotopically enriched silicon spin qubit", Phys. Rev. Appl. **18**, 064028 (2022).

[33] A. Noiri, K. Takeda, T. Nakajima, T. Kobayashi, A. Sammak, G. Scappucci, and S. Tarucha, "Fast universal quantum gate above the fault-tolerance threshold in silicon", Nature **601**, 338 (2022).

[34] T. Tanttu, W. H. Lim, J. Y. Huang, N. D. Stuyck, W. Gilbert, R. Y. Su, M. Feng, J. D. Cifuentes, A. E. Seedhouse, S. K. Seritan, C. I. Ostrove, K. M. Rudinger, R. C. C. Leon, W. Huang, C. C. Escott, K. M. Itoh, N. V. Abrosimov, H.-J. Pohl, M. L. W. Thewalt, F. E. Hudson, R. Blume-Kohout, S. D. Bartlett, A. Morello, A. Laucht, C. H. Yang, A. Saraiva, and A. S. Dzurak, "Stability of high-fidelity two-qubit operations in silicon", (2023), arXiv:2303.04090 [quant-ph].

[35] T. Ando, A. B. Fowler, and F. Stern, "Electronic properties of two-dimensional systems", Rev. Mod. Phys. **54**, 437 (1982).

[36] F. A. Zwanenburg, A. S. Dzurak, A. Morello, M. Y. Simmons, L. C. L. Hollenberg, G. Klimeck, S. Rogge, S. N. Coppersmith, and M. A. Eriksson, "Silicon quantum electronics", Rev. Mod. Phys. **85**, 961 (2013).

[37] R. Ruskov, M. Veldhorst, A. S. Dzurak, and C. Tahan, "Electron g-factor of valley states in realistic silicon quantum dots", Phys. Rev. B **98**, 245424 (2018).

[38] M. G. Borselli, R. S. Ross, A. A. Kiselev, E. T. Croke, K. S. Holabird, P. W. Deelman, L. D. Warren, I. Alvarado-Rodriguez, I. Milosavljevic, F. C. Ku, W. S. Wong, A. E. Schmitz, M. Sokolich, M. F. Gyure, and A. T. Hunter, "Measurement of valley splitting in high-symmetry Si/SiGe quantum dots", Appl. Phys. Lett. **98**, 123118 (2011).

[39] Z. Shi, C. B. Simmons, J. R. Prance, J. K. Gamble, M. Friesen, D. E. Savage, M. G. Lagally, S. N. Coppersmith, and M. A. Eriksson, "Tunable singlet-triplet splitting in a few-electron Si/SiGe quantum dot", Appl. Phys. Lett. **99**, 233108 (2011).

[40] D. M. Zajac, T. M. Hazard, X. Mi, K. Wang, and J. R. Petta, "A reconfigurable gate architecture for Si/SiGe quantum dots", Appl. Phys. Lett. **106**, 223507 (2015).

[41] A. Hollmann, T. Struck, V. Langrock, A. Schmidbauer, F. Schauer, T. Leonhardt, K. Sawano, H. Riemann, N. V. Abrosimov, D. Bougeard, and L. R. Schreiber, "Large, tunable valley splitting and single-spin relaxation mechanisms in a Si/Si_xGe_{1-x} quantum dot", Phys. Rev. Appl. **13**, 034068 (2020).

[42] E. H. Chen, K. Raach, A. Pan, A. A. Kiselev, E. Acuna, J. Z. Blumoff, T. Brecht, M. D. Choi, W. Ha, D. R. Hulbert, M. P. Jura, T. E. Keating, R. Noah, B. Sun, B. J. Thomas, M. G. Borselli, C. Jackson, M. T. Rakher, and R. S. Ross, "Detuning axis pulsed spectroscopy of valley-orbital states in Si/Si-Ge quantum dots", Phys. Rev. Appl. **15**, 044033 (2021).

[43] P. Scarlino, E. Kawakami, T. Jullien, D. R. Ward, D. E. Savage, M. G. Lagally, M. Friesen, S. N. Coppersmith, M. A. Eriksson, and L. M. K. Vandersypen, "Dressed photon-orbital states in a quantum dot: intervalley spin resonance", Phys. Rev. B **95**, 165429 (2017).

[44] X. Mi, S. Kohler, and J. R. Petta, "Landau-zener interferometry of valley-orbit states in Si/SiGe double quantum dots", Phys. Rev. B **98**, 161404(R) (2018).

[45] X. Mi, C. G. Péterfalvi, G. Burkard, and J. Petta, "High-resolution valley spectroscopy of Si quantum dots", Phys. Rev. Lett. **119**, 176803 (2017).

[46] M. Friesen, S. Chutia, C. Tahan, and S. N. Coppersmith, "Valley splitting theory of SiGe/Si/SiGe quantum wells", Phys. Rev. B **75**, 115318 (2007).

[47] S. Chutia, S. N. Coppersmith, and M. Friesen, "Multiscale theory of valley splitting in the conduction band of a quantum well", Phys. Rev. B **77**, 193311 (2008).

[48] A. L. Saraiva, M. J. Calderón, X. Hu, S. D. Sarma, and B. Koiller, "Physical mechanisms of interface-mediated intervalley coupling in Si", Phys. Rev. B **80**, 081305(R) (2009).

[49] A. Hosseinkhani and G. Burkard, "Electromagnetic control of valley splitting in ideal and disordered Si quantum dots", Phys. Rev. Res. **2**, 043180 (2020).

[50] A. Hosseinkhani and G. Burkard, "Relaxation of single-electron spin qubits in silicon in the presence of interface steps", Phys. Rev. B **104**, 085309 (2021).

[51] J. R. F. Lima and G. Burkard, "Interface and electromagnetic effects in the valley splitting of si quantum dots", Mater. Quantum. Technol. **3**, 025004 (2023).

[52] B. P. Wuetz, M. P. Losert, S. Koelling, L. E. A. Stehouwer, A.-M. J. Zwerver, S. G. J. Philips, M. T. Mądzik, X. Xue, G. Zheng, M. Lodari, S. V. Amitonov, N. Samkharadze, A. Sammak, L. M. K. Vandersypen, R. Rahman, S. N. Coppersmith, O. Moutanabbir, M. Friesen, and G. Scappucci, "Atomic fluctuations lifting the energy degeneracy in Si/SiGe quantum dots", Nat. Commun. **13**, 7730 (2022).

[53] C. H. Yang, R. C. C. Leon, J. C. C. Hwang, A. Saraiva, T. Tanttu, W. Huang, J. C. Lemyre, K. W. Chan, K. Y. Tan, F. E. Hudson, K. M. Itoh, A. Morello, M. Pioro-Ladrière, A. Laucht, and A. S. Dzurak, "Operation of a silicon quantum processor unit cell above one kelvin", Nature **580**, 350 (2020).

[54] T. McJunkin, B. Harpt, Y. Feng, M. P. Losert, R. Rahman, J. P. Dodson, M. A. Wolfe, D. E. Savage, M. G. Lagally, S. N. Coppersmith, M. Friesen, R. Joynt, and M. A. Eriksson, "SiGe quantum wells with oscillating Ge concentrations for quantum dot qubits", Nat. Commun. **13**, 7777 (2022).

[55] B. D. Woods, M. A. Eriksson, R. Joynt, and M. Friesen, "Spin-orbit enhancement in Si/SiGe heterostructures with oscillating Ge concentration", Phys. Rev. B **107**, 035418 (2023).

[56] C. H. Yang, A. Rossi, R. Ruskov, N. S. Lai, F. A. Mohiyaddin, S. Lee, C. Tahan, G. Klimeck, A. Morello, and A. S. Dzurak, "Spin-valley lifetimes in a silicon quantum dot with tunable valley splitting", Nat. Commun. **4**, 2069 (2013).

[57] A. Saraiva, W. H. Lim, C. H. Yang, C. C. Escott, A. Laucht, and A. S. Dzurak, "Materials for silicon quantum dots and their impact on electron spin qubits", Adv. Funct. Mater. **32**, 2105488 (2021).

[58] J. D. Cifuentes, T. Tanttu, W. Gilbert, J. Y. Huang, E. Vahapoglu, R. C. C. Leon, S. Serrano, D. Otter, D. Dunmore, P. Y. Mai, F. Schlattner, M. Feng, K. Itoh, N. Abrosimov, H.-J. Pohl, M. Thewalt, A. Laucht, C. H. Yang, C. C. Escott, W. H. Lim, F. E. Hudson, R. Rahman, A. Saraiva, and A. S. Dzurak, "Bounds to electron spin qubit variability for scalable CMOS architectures", (2023), arXiv:2303.14864 [quant-ph].

[59] R. R. Reeber and K. Wang, "Thermal expansion and lattice parameters of group IV semiconductors", Mater. Chem. Phys. **46**, 259 (1996).

[60] J. C. Hensel, H. Hasegawa, and M. Nakayama, "Cyclotron resonance in uniaxially stressed silicon. II. nature of the covalent bond", Phys. Rev. **138**, A225 (1965).

[61] Z. Stanojevic, O. Baumgartner, V. Sverdlov, and H. Kosina, "Electronic band structure modeling in strained Si-nanowires: two band k·p versus tight binding", in 2010 14th international workshop on computational electronics (Oct. 2010).

[62] V. Sverdlov, G. Karlowatz, S. Dhar, H. Kosina, and S. Selberherr, "Two-band k·p model for the conduction band in silicon: impact of strain and confinement on band structure and mobility", Solid-State Electron. **52**, 1563 (2008).

[63] M. V. Fischetti and S. E. Laux, "Band structure, deformation potentials, and carrier mobility in strained Si, Ge, and SiGe alloys", J. Appl. Phys. **80**, 2234 (1996).

[64] C. G. V. de Walle and R. M. Martin, "Theoretical calculations of heterojunction discontinuities in the Si/Ge system", Phys. Rev. B **34**, 5621 (1986).

[65] L. D. Laude, F. H. Pollak, and M. Cardona, "Effects of uniaxial stress on the indirect exciton spectrum of silicon", Phys. Rev. B **3**, 2623 (1971).

[66] S. Bosco and D. Loss, "Hole spin qubits in thin curved quantum wells", Phys. Rev. Appl. **18**, 044038 (2022).

[67] C. Kloeffel, M. Trif, and D. Loss, "Acoustic phonons and strain in core/shell nanowires", Phys. Rev. B **90**, 115419 (2014).

[68] A. M. Kosevich, E. M. Lifshitz, 1. Landau L. D., and L. P. Pitaevskii, *Theory of elasticity, Theoretical physics*, Vol. 7 (Butterworth-Heinemann, Boston, 1986).

[69] Y.-M. Niquet, C. Delerue, and C. Krzeminski, "Effects of strain on the carrier mobility in silicon nanowires", Nano Lett. **12**, 3545 (2012).

[70] S. Bosco, M. Benito, C. Adelsberger, and D. Loss, "Squeezed hole spin qubits in Ge quantum dots with ultrafast gates at low power", Phys. Rev. B **104**, 115425 (2021).

[71] L. A. Terrazos, E. Marcellina, Z. Wang, S. N. Coppersmith, M. Friesen, A. R. Hamilton, X. Hu, B. Koiller, A. L. Saraiva, D. Culcer, and R. B. Capaz, "Theory of hole-spin qubits in strained germanium quantum dots", Phys. Rev. B **103**, 125201 (2021).

[72] R. Maurand, X. Jehl, D. Kotekar-Patil, A. Corna, H. Bohuslavskyi, R. Laviéville, L. Hutin, S. Barraud, M. Vinet, M. Sanquer, and S. D. Franceschi, "A CMOS silicon spin qubit", Nat. Commun. **7**, 13575 (2016).

[73] *COMSOL Multiphysics® v. 6.1. www.comsol.com. COMSOL AB, Stockholm, Sweden.*

[74] K.-H. Hong, J. Kim, S.-H. Lee, and J. K. Shin, "Strain-driven electronic band structure modulation of Si nanowires", Nano Lett. **8**, 1335 (2008).

[75] P. Huang and X. Hu, "Spin relaxation in a Si quantum dot due to spin-valley mixing", Phys. Rev. B **90**, 235315 (2014).

[76] T. B. Boykin, G. Klimeck, M. A. Eriksson, M. Friesen, S. N. Coppersmith, P. von Allmen, F. Oyafuso, and S. Lee, "Valley splitting in strained silicon quantum wells", Appl. Phys. Lett. **84**, 115 (2004).

[77] H. J. McSkimin and P. Andreatch, "Elastic moduli of silicon vs hydrostatic pressure at 25.0°c and - 195.8°c", J. Appl. Phys. **35**, 2161 (1964).

[78] H. J. McSkimin and P. Andreatch, "Elastic moduli of germanium versus hydrostatic pressure at 25.0°c and -195.8°c", J. Appl. Phys. **34**, 651 (1963).

[79] C. X. Yu, S. Zihlmann, J. C. Abadillo-Uriel, V. P. Michal, N. Rambal, H. Niebojewski, T. Bedecarrats, M. Vinet, É. Dumur, M. Filippone, B. Bertrand, S. D. Franceschi, Y.-M. Niquet, and R. Maurand, "Strong coupling between a photon and a hole spin in silicon", Nat. Nanotechnol. **18**, 741 (2023).

[80] M. F. Gonzalez-Zalba, S. de Franceschi, E. Charbon, T. Meunier, M. Vinet, and A. S. Dzurak, "Scaling silicon-based quantum computing using CMOS technology", Nat. Electron. **4**, 872 (2021).

[81] F. Borjans, D. Zajac, T. Hazard, and J. Petta, "Single-spin relaxation in a synthetic spin-orbit field", Phys. Rev. Appl. **11**, 044063 (2019).

[82] H. T. Mengistu and A. García-Cristóbal, "The generalized plane piezoelectric problem: theoretical formulation and application to heterostructure nanowires", Int. J. Solids Struct. **100-101**, 257 (2016).

Acknowledgments

First and foremost, I would like to thank my esteemed supervisors, Prof. Daniel Loss and Prof. Jelena Klinovaja, for their invaluable guidance and support throughout my four-year journey of my Ph.D. They generously shared all their experience which allowed me to develop into a proficient researcher in theoretical condensed matter physics. The successful completion of several intriguing projects under their supervision has been a truly fulfilling experience.

I also thank Prof. Georgios Katsaros for graciously serving as the external expert for my thesis and defense.

My time at the Condensed Matter Theory and Quantum Computing group in Basel has been enriched by the company of outstanding colleagues and friends. All of them are excellent researchers with expertise in numerous fields. I appreciate all the enlightening discussions we had and I am grateful for everything that I could learn from you. Besides the physics you also provided an enjoyable social atmosphere at work but also at many social activities. My cordial thanks go to each of the following individuals: Mónica Benito González, Stefano Bosco, Denis Chevallier, Renato Dantas, Oindrila Deb, Sebastian Diaz, Olesia Dmytruk, Carlos Egues, Pierre Fromholz, Tamás Haidekker Galambos, Richard Heß, Bence Hetényi, Tomoki Hirosawa, Silas Hoffman, Zhe Hou, Joel Hutchinson, Maximilian Hünenberger, Peter Johannsen, Geo Jose, Vardan Kaladzhyan, Christoph Klöffel, Aksel Kobiałka, Valerii Kozin, Denis Kurlov, Katharina Laubscher, Henry F. Legg, Anatoliy Lotkov, Melina Lüthi, Dmitry Miserev, Alexander Mook, Poliana Penteado, Kirill Plekhanov, Marko Rančić, Falvio Ronetti, Ferdinand Schulz, Maria Spethmann, Aleksandr Svetogorov, Even Thingstad, Yanick Volpez, Xianpeng Zhang, Yuhao Zhao, and Ji Zou.

In particular I want to thank Stefano Bosco with whom I worked on most of my projects and from whom I learned the most during my PhD.

Special thanks are due to Bence Hetényi and Katharina Laubscher for their valuable feedback and constructive comments on the introduction to my thesis.

Last but not least, I want to express my deep gratitude to my family and friends, in particular my parents Christine and Klaus, and my partner Anna, for her unwavering and unconditional support throughout this endeavor.